SPECTROSCOPIC STUDIES OF PHOTO REAGENTS FOR PRECISION CHEMISTRY

By

Jurick Lahiri

A DISSERTATION

Submitted to
Michigan State University
in partial fulfillment of the requirements
for the degree of

Chemistry—Doctor of Philosophy

2022

ABSTRACT

SPECTROSCOPIC STUDIES OF PHOTO REAGENTS FOR PRECISION CHEMISTRY

By

Jurick Lahiri

Precision chemistry offers temporal and spatial control of reaction and requires active photo reagents. In this dissertation, the excited state dynamics of photo reagents is discussed. This is part of a collaboration that included synthesis, theory, and spectroscopic characterization with the goal of developing more active super photobases. The rotational dynamics study revealed significantly slower rotational diffusion of FR0-HSB^{+*} than FR0-SB*. The microscopic solvent interactions play a crucial role in the excited state proton transfer. The spatial resolution can be improved from one-photon excitation (OPE) by utilizing two-photon excitation (TPE). The spectroscopy of FR0-SB following TPE revealed higher reactivity in comparison to OPE. The quantum mechanical aspects of two-photon excitation were examined to demonstrate that the dipolar pathway plays an important role in these transitions even though it is far from resonance. Finally, the efforts to stabilize the higher excited states of cyanine dyes, with the goal of harnessing the energy of photons to achieve greater reactivity, have been described. Using this as inspiration, the S2 spectroscopy of a similar cyanine dye has been used to monitor the binding of the dye with human serum albumin protein.

ACKNOWLEDGEMENTS

First and foremost, I would like to express my greatest appreciation for my PhD advisor Prof. Marcos Dantus. I had the privilege of working very closely with him from the very beginning of my graduate school, which has allowed me to realize the value of time and resources, and inspired me to stay productive in lab. It has been a great learning experience not just in terms of science but also several aspects of life in general. I would also like to thank my committee members, Dr. Gary Blanchard, Dr. Warren Beck, and Dr. Richard Lunt. Your guidance and constructive criticism has been of great value and motivated me to be a better thinker.

I am extremely grateful to my collaborators Mehdi Moemeni, Jessica Kline, Dr. Ilias Magoulas, Dr. Stephen Yuwono, Maryann Laboe, Shawn Sandhu, Moaid Shaikh, Dr. Jun Shen, Nila Mohan, Fanchung Liang, and Arnab Chakraborty. It has been an enriching experience as I have learnt so much from working together on different projects. The collaborating research advisors, within and outside the department, including Dr. Gary Blanchard, Dr. Babak Borhan, Dr. Piotr Piecuch, Dr. Warren Beck, Dr. Benjamin Levine, Dr. James Jackson, and Dr. Ehud Pines have had significant contributions in my learning process.

I am privileged to have worked with several talented scientists in the Dantus group from whom I have learnt a great deal. The former members of the group include Dr. Muath Nairat, Dr. Gabrielle Murashova, Dr. Nagitha Ekanayake, Dr. Shuai Li, Jessica Kline, Maryann Laboe, Matthew Michie, Patrick Pawlaczyk, Diego Sierra, Benjamin Farris, and Nicholas Weigartz. I would also like to thank the current group members Dr. Bethany Jochim, Jacob Stamm, Shawn Sandhu, Moaid Shaikh, Alondra Negron, Lindsey Dejesus, Dr. Gabriel Rona, Farha Mime, Clayton Wicka, Leo Suguimoto, and Evan Adamski.

Finally, to my wonderful family. My parents Rinku and Jayanta have worked so hard and sacrificed so much to support me throughout my career. I will forever be indebted to them for everything I am today as they have always encouraged me to be an honest and hard-working person. Even through the hardest times, they have always kept a smile on their face and kept cheering me. To my wife, Grace, who is my biggest cheerleader and would do anything to bring a smile on my face. She has supported me through every step of graduate school, first as my best friend, then fiancée, and finally as my wife! We have come a long way and I would not have been able to get here without her unwavering support. To my in-laws who have accepted me into their family; Amy and Joe treat me as their own son and everyone in the family shower me with all the love there is. I couldn't have asked for more loving in-laws. And lastly, my cats Obie and Frank, who have been my work buddies at home, have the most trust in me and love me unconditionally. I don't know how I would get through graduate school since 2020 without my furry friends.

TABLE OF CONTENTS

LIST OF TAI	BLES	vii
LIST OF FIG	URES	ix
LIST OF SCH	IEMES	xvii
KEY TO ABI	BREVIATIONS	xviii
Chanter 1	Introduction	1
	Reagents	
	hoton Excitation	
	Fluorescence and Harnessing Higher Excited States	
Chapter 2	Rotational Dynamics and Excited States of FR0-SB	15
	uction and Background	
	mental and Theoretical Methods	
2.2.1	Materials	
2.2.2	Steady-State Absorbance and Emission Spectroscopy	19
2.2.3	Time-Resolved Fluorescence Measurements	
2.2.4	Computational Details	
2.3 Result	s and Discussion	
	usion	
Chapter 3	Steric Effects in Light-Induced Solvent Proton Abstraction	40
3.1 Introd	uction and Background	
3.2 Experi	mental and Theoretical Methods	45
3.2.1	Materials	45
3.2.2	Steady-State Absorbance and Emission Spectroscopy	45
3.2.3	Time-Resolved Fluorescence Measurements	
3.2.4	Computational Details	46
3.3 Result	s and Discussion	49
3.4 Conclu	usion	68
Chapter 4	Isoenergetic Two-Photon Excitation Enhances Solvent-to-Solute	Excited-State
Proton Transf		
4.1 Introd	uction and Background	
	mental and Theoretical Methods	
4.2.1	Experimental Details	
4.2.2	Computational Details	
4.3 Result	s and Discussion	
4.4 Conclu	icion	102

Chapt	er 5	Controlling Quantum Interference between Virtual and Dipole Two-pho	oton Optical
Excita	tion Pa	thways using Phase-shaped Laser Pulses	104
5.1	Intro	luction and Background	105
5.2	Theo	ry	108
5.3	Expe	rimental and Theoretical Methods	122
5.4	-	ts and Discussion	
5.5		lusion	
Chapt	er 6	Controlling S ₂ and S ₁ Fluorescence of Cyanines IR140 and IR144	134
6.1	Intro	luction and Background	
6.2	Expe	rimental and Theoretical Methods	142
6.3		ts	
6	.3.1	Experimental Results	145
6	.3.2	<u> </u>	
6	.3.3	Numerical Simulations.	163
6.4	Discu	ission	169
6.5	Conc	lusion	173
Chapt	er 7	Human Serum Albumin Dimerization Enhances S ₂ Emission of Bound	Cyanine
7.1	Intro	luction and Background	175
7.2		rimental and Theoretical Methods	
7.3		ts and Discussion	
7.4	Conc	lusion	194
Chapt	er 8	Summary and Future Outlook	195
8.1	Super	Photobase for Precision Chemistry	197
8.2		ed Dynamics and Photochemistry of Cyanines	
APPE	NDIX.		200
RIRI	IOGR A	PHY	202

LIST OF TABLES

Table 2.1. Fluorescence anisotropy and lifetime components 30
Table 2.2. The orbital character, vertical excitation energies $\mathcal{O}_n^{(\text{EOMCC})}$, oscillator strengths, and electronic dipole moment values μ_n of the four lowest-energy excited singlet electronic states S_n of FR0-SB , as obtained in the EOMCC calculations described in the Computational Details section. The CCSD value of the dipole moment in the ground electronic state is 2.6 D32
Table 3.1. Analysis of the steady-state spectroscopy results. Relative -OH concentration for the different alcohols, K_{eq} obtained as the ratio between FR0 -SB* and FR0 -HSB ^{+*} , and derived ΔG^0 values for proton abstraction from steady-state data
Table 3.2. Fluorescence lifetimes obtained from time-correlated single photon counting experiments. The time constants are as defined in Figure 5. Uncertainties are $\pm \sigma$. The χ^2 values across all fits were below 0.47
Table 3.3. Temperature-dependent steady-state data in n-propanol (n-PrOH) and i-propanol (i-PrOH)
Table 3.4. Temperature-dependent fluorescence lifetimes in <i>n</i> -propanol (<i>n</i> -PrOH) and <i>i</i> -propanol (<i>i</i> -PrOH) obtained from time-correlated single photon counting experiments. Uncertainties are $\pm \sigma$. The χ^2 values across all fits were below 0.460
Table 4.1. Quantitative assessment of the extent of protonation following OPE and TPE from steady-state fluorescence measurements for FR0 -SB. The ratio of the extent of protonation expressed as TPE/OPE shows the enhancement in ESPT resulting from TPE experiments compared to their OPE counterparts
Table 4.2. Fluorescence lifetime measurements following one- and two-photon isoenergetic excitation of FR0 -SB in methanol, ethanol, and acetonitrile. The initial state, FR0 -SB*, decays with a fast τ_{SB1} and a slow τ_{SB2} biexponential lifetimes. The numbers in parentheses indicate the amplitude of the fast decay component (a_1). The protonated state FR0 -HSB** shows a fast rise time τ_X and a slow decay time τ_{HSB} . In acetonitrile, no proton transfer takes place, thus one observes only a single exponential decay of the FR0 -SB* state that is identical for OPE and TPE within the measurement errors. All numbers are given in picoseconds
Table 4.3. The vertical transition energies ω_{0} (abs.) (in eV) and transition dipole moments μ_{10} (in Debye) corresponding to the $S_0 \rightarrow S_1$ absorption, along with the μ_0 and μ_1 dipoles characterizing the S_0 and S_1 states (in Debye) and their ratios for FR0 -SB in the gas phase and in selected alcohol solvents calculated at the respective S_0 minima following the CC/EOMCC-based protocol described in Computational Details.

Table 4.4. The vertical transition energies $\omega_{l_0}(em.)$ (in eV) and transition dipole moments μ_{l_0} (in Debye) corresponding to the $S_1 \rightarrow S_0$ emission, along with the μ_0 and μ_1 dipoles characterizing the S_0 and S_1 states (in Debye) and their ratios for FR0 -SB in the gas phase and in selected alcohol solvents calculated at the respective S_1 minima following the CC/EOMCC-based protocol described in Computational Details
Table 4.5 . A comparison of the calculated S_0 – S_1 adiabatic transition energies without $[\omega_{10}(ad.)]$ and with $[\omega_{10}(0-0)]$ zero-point energy (ZPE) vibrational corrections (in eV), along with the differences and ratios of the μ_0 and μ_1 dipoles characterizing the S_0 and S_1 states at the respective minima (in Debye) for FR0 -SB in the gas phase and in selected alcohol solvents obtained following the CC/EOMCC-based protocol described in Computational Details with the corresponding experimentally derived data
Table 6.1. Fluorescence lifetimes obtained from time-correlated single photon counting experiments. The time constants are as defined in Figure 6.2 and 6.3
Table 6.2. Fitted chirped S ₂ fluorescence curves were fitted with a Lorentzian line-shape
Table 6.3. S ₂ /S ₁ integrated fluorescence intensity ratios
Table 7.1. Fluorescence lifetimes obtained from time-correlated single photon counting experiments. The time constants are as defined by the fitting equation $f(t) = a \exp(-t/\tau_1) + (1-a) \exp(-t/\tau_2)$

LIST OF FIGURES

Figure 1.1. Förster cycle for ESPT of photobases. The blue and red color labels demonstrate the energy states and the transitions for the non-protonated and protonated system, respectively3
Figure 1.2. Simultaneous OPE and TPE of sample solution in cuvette. The objective on the right for TPE is producing fluorescence only at the focal point (shown with the white arrow). Photographed by Amos W.B. and Cipollone M, MRC Cambridge
Figure 1.3. Jablonski diagram showing the ground and the excited electronic and vibrational states. The solid arrows indicate radiative transitions while dashed arrows indicate non-radiative transitions. The different transitions include absorption, VR, IC, and fluorescence shown by blue, dark yellow, purple, and green arrows, respectively
Figure 1.4. Representative structures of organic dyes showing S ₂ emission
Figure 1.5. The fluorescence for S ₁ (red) and S ₂ (black) states as a function of linear chirp for (a) IR144 and (b) mPi-IR806. The top axis shows the corresponding chirped pulse duration. TL pulses lead to greater S ₂ fluorescence, while chirped pulses lead to greater S ₁ fluorescence. Data obtained from ref. 1 with permission
Figure 2.1. (a) FR0- SB super photobase. (b) The structure of the isolated FR0- SB molecule in its ground electronic (S ₀) state and the dipole moments characterizing the S ₀ (shorter orange vector $\vec{\mu}_{S_0}$) and electronically excited S ₁ (longer magenta vector $\vec{\mu}_{S_1}$) states, as calculated in this work
Figure 2.2. The normalized absorption (left) and fluorescence (right) spectra of FR0 -SB in linear alcohols from methanol to <i>n</i> -octanol. Absorbance spectra are normalized to a maximum of 1.0 and integrated emission band areas are normalized for area
Figure 2.3. Reorientation times of FR0- SB* and FR0- HSB** in the primary <i>n</i> -alcohols, methanol through 1-octanol, and ethylene glycol plotted <i>vs.</i> solvent viscosity. The purple and blue dashed lines indicate the slip and stick limit from the modified DSE equation, Eq. 2.3, respectively. The green points represent the result of solvent "attachment" to the chromophore
Figure 2.4. Schematic of proton exchange between SB* and solvent28
Figure 2.5. Kinetic population model for excited state proton transfer between FR0 -SB and the solvent
Figure 2.6. (a) Dependence of lifetimes τ_{SB} , τ_{X} and τ_{HSB} on solvent viscosity. (b) Dependence of the same lifetimes on solvent [-OH]

Figure 3.1. The FR0-SB molecule and how its electronic density changes upon excitation. (a) FR0-SB super photobase. (b) The structure of the isolated FR0-SB molecule in its ground electronic S_0 state, the dipole moments characterizing the S_0 (shorter orange vector) and electronically excited S_1 (longer magenta vector) states, and the $S_1 - S_0$ total electronic density difference, resulting from the CC/EOMCC calculations described in the main text. The red/blue color indicates an increase/decrease in the electron density upon the $S_0 \rightarrow S_1$ excitation
Figure 3.2. Steady-state absorption and fluorescence spectra of FR0 -SB in alcohols. (a) The normalized absorption and emission spectra of FR0 -SB in primary alcohols from methanol to <i>n</i> -octanol. (b) The absorption and emission spectra of FR0 -SB in various solvents to compare steric hindrance. The long wavelength emission near 630 nm (~15,870 cm ⁻¹) corresponds to FR0 -HSB ^{+*} , while the short wavelength emission near 460 nm (~21,740 cm ⁻¹) corresponds to FR0 -SB*
Figure 3.3. Steady-state absorption and fluorescence spectra of FR0 -SB in alcohols. (a) The normalized absorption and emission spectra of FR0 -SB in primary alcohols from methanol to <i>n</i> -octanol. (b) The absorption and emission spectra of FR0 -SB in various solvents to compare steric hindrance. The long wavelength emission near 630 nm (~15,870 cm ⁻¹) corresponds to FR0 -HSB ^{+*} , while the short wavelength emission near 460 nm (~21,740 cm ⁻¹) corresponds to FR0 -SB*
Figure 3.4. The fluorescence decay responses plotted on a \log_{10} scale of FR0 -HSB ^{+*} detected at 630 nm in (a) primary alcohols and (b) selected primary and secondary alcohols. The fitting function used was $f(t) = b_1 \exp(-t/\tau_{\text{HSB}}) - b_2 \exp(-t/\tau_{\text{X}})$. For the time constants reported in Table 3.2, the IRF has been deconvoluted using a convolute-and-compare method
Figure 3.5. Kinetic model for the ESPT reaction between FR0 -SB and the alcohol solvent ROH
Figure 3.6. Trends in dynamics and free energy as a function of relative [-OH]. (a) The ratio of the time constants τ_X and τ_{HSB} is plotted as a function of relative [-OH]. (b) ΔG^0 for proton abstraction obtained from the ratio of FR0 -SB* to FR0 -HSB ^{+*} emission as a function of relative [-OH]. We note good agreement between the time-resolved and the steady-state data for the linear alcohols
Figure 3.7. Temperature-dependent proton transfer data for n - and i -propanol. (a) Concentration ratio of the protonated and unprotonated $\mathbf{FR0}$ -SB* following photoexcitation obtained from steady-state spectra. (b) Temperature-dependent $\overline{\tau}_{SB}$ for $\mathbf{FR0}$ -SB* obtained from time-resolved measurements. From these steady-state band ratio data, we can determine the temperature-dependent equilibrium constant for protonation/deprotonation of $\mathbf{FR0}$ -SB*
Figure 3.8. Schematic representation of the r_1 and r_2 N–H internuclear distances needed to create the grid defining the ESPT reaction pathway

Figure 3.9. Results from the reaction pathway calculations showing ground- and excited-state
energy differences as a function of proton abstraction. The SMD/CAM-B3LYP/6-31+G* ground-
state (S_0) and excited-state (S_1) reaction pathways corresponding to the proton abstraction from n -
propanol (blue) and i-propanol (orange) by FR0-SB along the internuclear distance between the
imine nitrogen and the alcohol proton being transferred. The energies ΔE are shown relative to the
ground-state minimum of the respective pathways. The dashed line in each pathway indicates the
excited-state geometry relaxation following the $S_0 \rightarrow S_1$ excitation of FR0 -SB64

Figure 4.3. Extent of proton transfer determined following OPE and TPE for FR0 -SB in a number of alcohols. The TPE over OPE ratio is given by the gray bars (left y-axis). In all the solvents but <i>i</i> -propanol, enhanced proton transfer is observed following TPE. The ratios between the fluorescence bands [FR0 -HSB ^{+*}]/[FR0 -SB*], corrected for fluorescence quantum yield, are plotted as bars OPE (blue) and TPE (red); each ratio is indicated on a logarithmic scale (right y-axis). Abbreviations: MeOH = methanol, EtOH = ethanol, <i>n</i> -PrOH = <i>n</i> -propanol, <i>n</i> -HxOH = <i>n</i> -hexanol, <i>i</i> -PrOH = <i>i</i> -propanol
Figure 4.4. EEM spectra showing the dependence of protonation as a function of excitation wavelength for methanol (left) and ethanol (right). The absorption spectrum for both molecules is shown as a bold black line. Emission from FR0 -SB* is observed at ~450 nm and emission from FR0 -HSB** is observed at ~650 nm
Figure 4.5 . Laser intensity dependence of the fluorescence following two-photon excitation for FR0-SB in (a) methanol and (b) acetonitrile, measured for laser pulses from a Ti:Sapphire oscillator. The fitting function (red line) and the experimental points (black squares) are plotted on a log-log scale. The exponent obtained from the fit, of ~2, indicates two-photon excitation and shows no indication of three-photon excitation
Figure 4.6. Isoenergetic two-photon enhanced ESPT as a function of excited-state lifetime prior to proton transfer for (in order of greater to lower enhancement) methanol, ethanol, <i>n</i> -propanol, <i>n</i> -hexanol, and <i>i</i> -propanol. The dashed line is included as a guide to the eye
Figure 4.7. OPE and TPE spectra for FR0 -SB in cyclohexane (<i>c</i> -Hexane), acetonitrile (ACN), and methanol (MeOH). The solid line shown for the two-photon spectra is the result of 3-point smoothing and is included as a guide to the eye
Figure 4.8. Absorption spectra of FR0 -SB in methanol (MeOH), ethanol (EtOH), <i>n</i> -propanol (<i>n</i> -PrOH), and <i>i</i> -propanol (<i>i</i> -PrOH) (solid lines) and difference between these spectra and the absorption in <i>i</i> -propanol (dotted lines). We find a significant difference between the spectra in the 25,000 cm ⁻¹ energy region where the experiment was performed
Figure 5.1 . (a) A 40 nm wide spectral phase window centered on the spectrum of 16.6 fs Gaussian pulses at 811 nm resulting from the phase scanning from 0 to 2π . (b) Calculated SOPS resulting from scanning the phase window from -2π to 2π . (c) Experimental SHG spectrum as a function of the same phase window scan as used in (b). In panels (b) and (c), areas where constructive and partial destructive interferences take place are colored red and blue, respectively
Figure 5.2 . (a) The TPE spectrum of FR0 -SB in methanol (black squares), based on the data points reported in ref. 2, along with the SOPS for the 40 nm wide phase window at selected amplitudes. Note that as the phase amplitude changes the SOPS remains centered at 405.5 nm. (b) The results of simulations of the TL-normalized overlap integral between the SOPS and the TPE spectrum of FR0 -SB in methanol (black open squares), the TL-normalized SHG signal (blue circles), and the ratio of the two signals (red diamonds) as functions of the spectral phase of the 40 nm window

Figure 5.3 . (a) Simulation of the TL-normalized TPEF signal based on Eq. 5.7 (black squares), the TL-normalized SHG signal based on Eq. 5.8 (blue circles), and the ratio of the two signals (red triangles) as functions of the spectral phase. The simulation parameters are given in the Theory section. (b) Experimental data corresponding to (a) obtained following TPE of FR0 -SB in methanol using 16.6 fs pulses and a 40 nm window as a function of the spectral phase. The TL-normalized TPEF signal is shown in black squares, the TL-normalized SHG signal is shown in blue circles, and the ratio between the two signals is shown in red triangles
Figure 5.4 . Experimental results for the frequency integrated TPEF signal for FR0- SB in methanol (black squares) and the reference SHG signal of the laser (blue circles), along with the TPEF/SHG signal ratios with error bars (red triangles), plotted as functions of the spectral phase for window widths of (a) 10 nm, (b) 20 nm, (c) 30 nm, (d) 40 nm, and (e) 50 nm. The TPEF/SHG signal ratios for all window sizes examined in (a)–(e) are shown in (f)
Figure 5.5 . Simulation results for the frequency integrated TPEF signal for FR0 -SB in methanol (black squares) and the reference SHG signal of the laser (blue circles), along with the TPEF/SHG signal ratios (red triangles), based on Eq's. 5.7 and 5.8, plotted as functions of the spectral phase for window widths of (a) 10 nm, (b) 20 nm, (c) 30 nm, (d) 40 nm, and (e) 50 nm. The simulated TPEF/SHG signal ratios for all window sizes examined in (a)–(e) are shown in (f). The simulation parameters are given in the Theory section
Figure 5.6 . Calculated [panels (a) and (b)] and experimentally determined [panel (c)] TPEF/SHG ratios as functions of phase values for different window widths. (a) Results obtained assuming that the interference between the virtual and dipole pathways in the TPEF signal can be neglected, as in Eq. 5.9. (b) Results obtained assuming that the TPEF signal can be simulated using a linear combination of Eq. 5.7, which assumes interference, and Eq. 5.9, where interference is absent, with the contribution from Eq. 5.7 being increased linearly with the window width (see text for details). (c) Experimental data, as shown in Figure 5.4f, reproduced here to facilitate comparison
Figure 6.1. IR144 and IR144' represent two commonly understood conformations of IR144. IR140 mainly forms a cyanine-like conformation
Figure 6.2. The interaction of chirped laser pulses with the S ₁ state of a molecule. (top) Relative changes in fluorescence and stimulated emission from the S ₁ state as a function of chirp (bold line and dashed line, respectively), according to ref. 3 (bottom) Albrecht ladder diagrams representing the laser-molecule interaction for TL and chirped pulses. Pathways (1 ⁻ and 1 ⁺) are independent of chirp, pathway (2 ⁻) is responsible for the enhanced stimulated emission and decrease in fluorescence. Pathway (2 ⁺) causes no effect because it is energetically forbidden. Solid/dashed arrows indicate ket/bra interactions. Blue/red arrows indicate high/low frequency portion of the spectrum. Green arrows indicate non-radiative transitions including wavepacket motion139
Figure 6.3. The interaction of chirped laser pulses with the S_2 state of a molecule. (top) Relative changes in fluorescence from the S_1 and S_2 states, (light and bold lines, respectively) as a function

of chirp, according to ref. 1 (bottom) Albrecht ladder diagrams representing the laser-molecule interaction for TL and chirped pulses. Pathway (TPE) where two-photon excitation to an upper

excited state S _n is accessible in this case, leading to enhanced S ₂ fluorescence. Pathways (1 ⁻ and 1 ⁺) are independent of chirp. Pathways (2 ⁻) is responsible for a decrease in fluorescence observed for negative chirp, however, non-radiative relaxation via IC leads to decreased S ₂ fluorescence that is essentially symmetric with chirp sign. Solid/dashed arrows indicate ket/bra interactions. Blue/red arrows indicate high/low frequency portion of the spectrum. Green arrows indicate non-radiative transitions including wavepacket motion
Figure 6.4. Steady-state absorption and fluorescence spectra for (a) IR144 and (b) IR140. The normalized absorption of both IR144 and IR140 is represented with thin lines whereas the normalized emission with thicker lines. Methanol, ethanol, <i>n</i> -propanol, ethylene glycol and glycerol are represented by black, red, blue, pink and green lines, respectively
Figure 6.5. The integrated fluorescence ratio of S ₂ /S ₁ from steady state spectra for IR144 and IR140 as a function of varying solvent viscosity (logarithmic scale). The numbers have been normalized such that the ratios are 1 for the respective methanol samples
Figure 6.6. Excitation emission matrix spectra of (a) IR144 and (b) IR140 in propanol. The diagonal indicates scattered excitation light when both excitation energy and emission energy are equal
Figure 6.7. The fluorescence decay of IR144 detected at (a) $S_2 \rightarrow S_0$ fluorescence maxima and (b) $S_1 \rightarrow S_0$ fluorescence maxima in methanol (blue dots), ethylene glycol (green dots), and glycerol (red dots). The fluorescence lifetimes for (a) have been obtained from the function $f(t) = a_1 \exp(-t/\tau_1) + a_2 \exp(-t/\tau_2)$ while for (b) have been obtained from the function $f(t) = -b_1 \exp(-t/\tau_3) + b_2 \exp(-t/\tau_4)$. The time constants have been obtained post deconvolution of the IRF from the fluorescence decay signals. $(a_1 + a_2 = 1; b_1 + b_2 = 1)$
Figure 6.8. The fluorescence decay of IR140 detected at (a) $S_2 \rightarrow S_0$ fluorescence maxima and (b) $S_1 \rightarrow S_0$ fluorescence maxima in methanol (blue dots), ethylene glycol (green dots), and glycerol (red dots). The fluorescence lifetimes for (a) have been from the function $f(t) = a_1 \exp(-t/\tau_1) + a_2 \exp(-t/\tau_2)$ while for (b) have been obtained from the function $f(t) = -b_1 \exp(-t/\tau_3) + b_2 \exp(-t/\tau_4)$. The time constants have been obtained post deconvolution of the IRF from the fluorescence decay signals. $(a_1 + a_2 = 1; b_1 + b_2 = 1)$
Figure 6.9. Chirp dependence scans conducted on (a) IR144 and (b) IR140 from -5000 fs ² to +5000 fs ² at constant laser power for each molecule. A lower laser power intensity was used for IR140. The thinner and thicker lines show the relative fluorescence intensity as a function of chirp compared to its TL value (I-I _{TL})/ I _{TL} for S ₁ and S ₂ , respectively. Methanol, ethanol and <i>n</i> -propanol are represented by black, red and blue lines, respectively. S ₁ and S ₂ data are represented by thin and thick lines, respectively.
Figure 6.10. Chirp dependence scans carried out as a function of laser intensity for (a) IR144 and (b) IR140 in methanol. The thinner and thicker lines show the relative fluorescence intensity as a function of chirp compared to its TL value (I- I_{TL})/ I_{TL} for S_1 and S_2 , respectively. Laser excitation power of 15mW, 10mW and 5mW are represented by black, red and blue lines, respectively. S_1 and S_2 data are represented by thin and thick lines, respectively

Figure 6.11. Normalized S ₂ fluorescence spectra are plotted as a function of chirp and power value for (a) IR144 and (b) IR140. The blue line (positive chirp) considers chirp values from +4000 fs ² to +5000 fs ² , while the red line (negative chirp) averages the fluorescence spectrum from -4000 fs ² to -5000 fs ² . The black line (transform-limited pulses) stays relatively the same as the power increases for both dyes. The (b) IR140 fluorescence spectrum is not dependent upon chirp or power. 15mW and 10mW S ₂ spectra are shown for the three differing pulse descriptions, with relatively no change. The data have been normalized to the highest value within the S ₂ fluorescence emission band
Figure 6.12. Computed state energies of IR140 in glycerol at corresponding geometries. S_0 , S_1 , S_1 , and S_2 energies are shown by black, red, blue and green lines, respectively. Energies for S_1 , S_1 , and S_2 are shifted as described in the text
Figure 6.13. Computed state energies of IR144 in glycerol at corresponding geometries. S ₀ , S ₁ , S ₁ , and S ₂ energies are shown by black, red, blue and green lines, respectively. Energies for S ₁ , S ₁ , and S ₂ are shifted as described in the text
Figure 6.14. Schematic model representing potential energy curves that illustrate the different processes involved in the femtosecond chirped pulse experiments. As indicated in the theory section, two S ₂ states were identified. The S ₂ state under adiabatic representation can be considered as having a double well potential that leads to emission at two different wavelengths165
Figure 6.15. Results from numerical simulations of the S_1 and S_2 populations plotted as a function of chirp and viscosity. The viscosity of the solvent affects the rate k_2 , and this is reflected in the chirp dependence. Results shown for methanol (black), ethanol (red), and propanol (blue), where the only parameter changed in these simulations was the viscosity of the solvent
Figure 6.16. Results from numerical simulations of the S ₁ and S ₂ populations as a function of chirp for three different laser intensities: weak pulses (blue), higher intensity (red), and saturation (black); as described in the text
Figure 6.17. Laser intensity dependence of S ₂ fluorescence upon 520 nm excitation for (a) IR144 and (b) IR140 in <i>n</i> -propanol
Figure 7.1. Steady-state absorption and fluorescence spectra. (a) Normalized absorption of IR806 and IR806-HSA samples prepared in pH 7.4 buffer. The IR806 concentration was kept constant at 5 μ M. (b) EEM spectrum of IR806 in the buffer. (c) EEM spectrum of IR806-HSA at 1:15 relative concentration. Please note that the scale for the z-axis in the EEM spectra is logarithmic182
Figure 7.2. (a) Steady-state fluorescence of IR806 and IR806-HSA samples, with increasing HSA concentration, excited at 16667 cm ⁻¹ . The IR806 concentration was kept constant at 2 μ M. We normalized the data to keep the integrated emission under the two fluorescence bands constant. (b) The integrated fluorescence ratio of S_2^L/S_2^H , excited at 16667 cm ⁻¹ , as a function of the HSA concentration. Note the difference in slope for concentrations above 10 μ M, the concentration where dimerization becomes favorable. (c) The fluorescence decay of IR806 and IR806-HSA samples, with a constant IR806 concentration of 5 μ M, excited at 16500 cm ⁻¹ and detected at

$14500~\text{cm}^{-1}$. (d) Rotational anisotropy decays associated with S_2 fluorescence for the samples in (c)
Figure 7.3. (a) Fluorescence following excitation at the absorption maximum for each solution. (b) The fluorescence decay of IR806 and IR806–HSA samples excited at 16500 cm^{-1} and detected at 12000 cm^{-1} . The concentration of IR806 was kept constant at $5 \mu \text{M}$
Figure 7.4. Molecular docking study of IR806. (a) IR806 (spheres) bound to HSA (ribbons). The different subdomains are depicted by different colors: IA - gray, IB - purple, IIA - blue, IIB - green, IIIA - salmon, and IIIB- red. The atoms of IR806 are shown by different colors as well: C - orange, Cl - green, O - red, S - yellow, and N - blue. (b) The geometry of IR806, when bound to HSA186
Figure 7.5. Results of the TD-DFT calculations showing energies for the different states corresponding to different geometries. The top row of molecular geometries depicts the molecules to be in the plane of paper while the bottom row is a visualization of the same system, with the Chlorine atom coming out of the plane of paper. The energies for S_0 , S_1 , and S_2 are shown in black, red, and blue, respectively
Figure 7.6. Principal IR806 isomers. The bonds in Z configuration are highlighted in red189
Figure 7.7. The excitation spectrum normalized for IR806 and IR806–HSA samples detecting fluorescence at 14190 cm $^{-1}$. The concentration of IR806 was kept constant at 5 μ M190
Figure 7.8. S_1 fluorescence maxima as a function of HSA concentration. IR806 concentration is kept constant at (a) 2 μ M and (b) 5 μ M
Figure 7.9. S ₁ integrated emission spectra at the emission maxima, as a function of HSA concentration. The data was obtained from raw spectra without normalization. IR806 concentration is kept constant at 2 μM

LIST OF SCHEMES

Scheme 1.1. Molecular structure of FR0-SB	4
Scheme 5.1. Molecular structure of the FR0-SB super photobase	107
Scheme 7.1. Molecular structure of (a) IR806 and (b) IR125	176

KEY TO ABBREVIATIONS

β-BBO Beta Barium Borate

ACN Acetonitrile

ADT AutoDockTools

CC Coupled-Cluster

C-PCM Conductor-Like Polarizable Continuum Model

c-PeOH Cyclopentanol

DFT Density Functional Theory

DSE Debye–Stokes–Einstein

EEM Excitation–Emission Matrix

EFP Effective Fragment Potentials

EG Ethylene Glycol

EOM Equation-Of-Motion

ESPT Excited State Proton Transfer

EtOH Ethanol

FDA Food and Drug Administration

FWHM Full Width at Half Maxima

Gl Glycerol

HSA Human serum albumin

IC Internal Conversion

i-PrOH *i*-Propanol

IRF Instrument Response Function

MeOH Methanol

MIIPS Multiphoton Intrapulse Interference Phase Scan

n-BuOH *n*-Butanol

n-HpOH *n*-Heptanol

n-HxOH *n*-Hexanol

n-OcOH *n*-Octanol

n-PeOH *n*-Pentanol

n-PrOH *n*-Propanol

OPE One-Photon Excitation

PDB Protein Data Bank

PES Potential Energy Surface

RHF Restricted Hartree–Fock

SB Schiff Base

SHG Second Harmonic Generation

SOPS Second-Order Power Spectrum

TAA *t*-Amyl Alcohol

TCSPC Time-Correlated Single Photon Counting

TD-DFT Time-Dependent Density Functional Theory

TL Transform Limited

TPE Two-Photon Excitation

TPEF Two-Photon Excited Fluorescence

VR Vibrational Relaxation

WL White Light

Chapter 1 Introduction

Precision chemistry is the ability of controlling chemical reactions with high spatial and temporal resolution. Research in precision chemistry is of utmost importance and affords applications in the field of chemistry, material science and biology. The spatial and temporal resolution may be achieved by the use of light to trigger chemical reactions at the focus of the light source by utilizing photo reagents. Additionally, higher spatial resolution can be achieved by taking advantage of two-photon excitation (TPE). TPE is a highly sought after method especially in biological imaging deeper tissue penetration, efficient light detection, and reduced photobleaching. My research addressed three important aspects required for achieving precision chemistry. First, I introduce the concepts and important properties of photo reagents, focusing on photoacids and photobases. I then introduce the concept of two-photon excitation for triggering excited state reactivity. Finally, I describe how certain molecules have long lived higher excited states and how those could be useful for designing photo reagents or applied as sensors.

1.1 Photo Reagents

Photochemistry is highly dependent on several intra- and intermolecular properties of the excited photo reagent and its surrounding environment. A general understanding of the physical organic properties and the excited state dynamics of photo reagents is essential for the development of newer, more active molecules. One important class of reactions for precision chemistry is excited state proton transfer (ESPT) involving photoacids or photobases. Photoacids are molecules that exhibit a significant decrease in pK_a upon activation by light, generating a more acidic system in the excited state in comparison to the ground state. The literature on photoacids is extensive starting with the observation of dual-fluorescence by Weber (1932) upon variation of the pH of solution.⁴ This was followed by Förster's studies of excited state proton transfer and developing the theory to calculate the excited state pK_a (pK_a^*) of a photoacid for the proton transfer from the photoacid to the solvent, also known as the Förster cycle.^{5–7} Similarly, photobases are compounds that undergo a substantial increase in pK_a (or decrease in pK_b) upon photoexcitation. Unfortunately, there are limited examples of reversible intermolecular photobases in literature in comparison to photoacids.

The energetic cycle for ESPT was outlined by Förster and the cycle for a photobase has been depicted below in Figure 1.1. Starting from the ground state, the photobase B, upon activation by light, reaches the excited state designated by B*. The significantly more basic species B* is now capable of proton abstraction from the surrounding protic solvent environment to form the excited protonated photobase BH⁺*. BH⁺* is capable of radiative decay, similar to B*, leading to the formation of the protonated photobase BH⁺ which spontaneously converts to the photobase. In the ground and excited state proton transfer processes, the entropy change is negligible. The drastic

change in the reactivity of photo reagents is attributed to the differences in the electronic structures between their ground and excited electronic states.^{5–8}

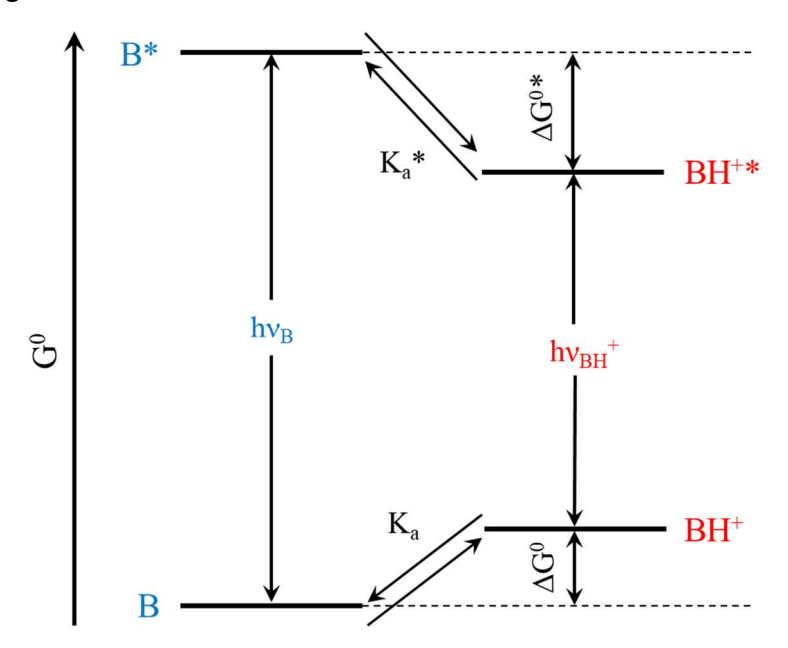


Figure 1.1. Förster cycle for ESPT of photobases. The blue and red color labels demonstrate the energy states and the transitions for the non-protonated and protonated system, respectively.

The 0-0 electronic transition energies for B and BH⁺ are $hv_{\rm B}$ and $hv_{\rm BH^+}$, respectively. Since the energy in the Förster cycle is conserved, (Figure 1.1) we have the following:

$$hv_{\rm B} + \Delta G^0 = hv_{\rm BH^+} + \Delta G^0 * (1.1)$$

For a Brønsted-type equilibrium proton exchange in solution, the equilibrium constants K_a and K_a * for the ground and excited states, respectively, are given as,

$$K_{a} = [B][H]/[BH^{+}], K_{a}^{*} = [B^{*}][H]/[BH^{+*}]$$
 (1.2)

The standard change in Gibb's free energy for proton transfer in the ground state is given by ΔG^0 , which is related to the dissociation constant K_a and pK_a as:

$$\Delta G^0 = -RT \ln K_a = 2.303RT \text{ pK}_a$$
 (1.3)

Similarly, the standard change in Gibb's free energy for proton transfer in the excited state is depicted as ΔG^0 * and connected to the dissociation constant K_a * and pK_a * as:

$$\Delta G^{0*} = -RT \ln K_a^{*} = 2.303RT \text{ p}K_a^{*}$$
 (1.4)

Upon combining Eq. 1.1 with Eq.'s 1.3 and 1.4, we obtain the Förster equation for photobases, which can predict the basicity of the excited state (pK_a^*) as follows:

$$\Delta p K_a = p K_a * -p K_a = (h V_B - h V_{BH^+}) / 2.3RT$$
 (1.5)

The change in pK_a can be calculated from the spectral shift upon deprotonation and protonation of photoacids and photobases, respectively. Solntsev et al. introduced the term "super" photoacid for cyano-substituted 2-naphthols capable of donating protons in non-aqueous medium. Similarly, Sheng et al. coined the term "super" photobase for their fluorene-based photobase **FR0**-SB (Scheme 1), capable of abstracting protons from alcohols that have significantly lower acidity than water. Substituted quinolines are also capable of exhibiting "super" photobasic activity but are limited to smaller alcohols as the highest pK_a * recorded for substituted quinolines is 15.9 for 5-amino-quinoline.

Scheme 1.1 Molecular structure of FR0-SB.

The super photobase **FR0**-SB, reported by Sheng et al., is a Schiff base obtained from the reaction of fluorene-based aldehyde **FR0**¹⁶ and *n*-butylamine. The ground state pK_a of **FR0**-SB was estimated using α -naphthylamine as a reference, which yielded a pK_a value of 6.7 in ethanol. Using the steady-state spectroscopy of **FR0**-SB and protonated **FR0**-HSB^{+*}, the pK_a was

estimated at \sim 21 for **FR0-SB*** using the Förster equation. The photobasicity might be taken advantage of for photo-initiated protonation, pH-based sensing, and imaging in biological and material science realms, similar to the applications of photoacids. ^{17–23}

1.2 Two-photon Excitation

Spatial control, in addition to temporal control, can be achieved by TPE. TPE was first introduced as a theoretical prediction by Maria Göppert-Mayer in her PhD thesis in 1931.²⁴ However, experimental demonstration of TPE could only be possible in 1961 by Kaiser and Garrett, ²⁵ owing to the discovery of the visible maser. 26,27 Over time, with the advent of pulsed lasers, TPE became more feasible as its probability is dependent on the peak power of the laser beam, where peak power is the energy of the pulse divided by the pulse duration. ^{28–31} TPE has the ability to initiate reactions only at the focal point of the laser giving it the higher spatial resolution in comparison to one-photon excitation (OPE) which can cause photoactivation in areas other than the focal point (Figure 1.2). Additionally, since several dyes have excitation energies in the UV region, the use of UV light can cause damage of tissues. Conversely, TPE activation of the dyes by near-IR light will not be absorbed by tissues and can only activate molecules at the focus. Also, the depth of penetration at a higher frequency (OPE) is reduced due to scattering and absorption from samples. Obtaining fluorescence signal from the same sample at half the frequency (TPE) affords higher signal-to-noise ratio allowing for wider applications involving diagnostics and therapy. 32,33 TPE has been utilized in different applications in biology, including bioimaging and photodynamic therapy. Similar to the biological applications, TPE is of significant importance in material science and chemistry including photopolymerization, heterogeneous catalysis, microfabrication,³⁴ and three-dimensional optical data storage. 35-37 In order to explore the scope of two-photon excited photo reagents, the photo-physics of the ESPT of **FR0**-SB upon TPE is studied in detail.



Figure 1.2. Simultaneous OPE and TPE of sample solution in cuvette. The objective on the right for TPE is producing fluorescence only at the focal point (shown with the white arrow). Photographed by Amos W.B. and Cipollone M, MRC Cambridge.

Considering the importance of TPE for different applications, there have been significant efforts to design and synthesize molecules with high two-photon absorption cross-section. 30,38,39 Attempts at controlling the TPE efficiency have been made for molecules in solution by modulating the ultrafast laser pulse. The Dantus group has been successful in exhibiting control of one- or multiphoton excitation processes by taking advantage of the principle of multiphoton intrapulse interference. 40-43 TPE progresses through two pathways namely the virtual and the dipole pathways, which emerges from the two-photon absorption cross section term. The virtual pathway involves virtual states in between the ground and excited state, whereas the dipole pathway is a non-resonant one-photon transition. Spectral phase shaping has been used to modulate the phase difference between the virtual and the dipole pathways. It is important to choose the spectral phase function such that the enhancement is not due to the tuning of the second-order power spectrum with the two-photon absorption spectrum. The quantum control of TPE in

condensed phase may lead to an enhanced signal at a lower intensity in two-photon microscopy, which can be crucial for biological samples by preventing photocytotoxicity.

1.3 Dual Fluorescence and Harnessing Higher Excited States

Excitation of molecules in condensed phase to electronic excited states higher than S₁ leads to fast relaxation through non-radiative pathways and hence fluorescence from the lowest state of the same parity as the ground state, a process known as Kasha's rule. 44 The basis of this rule is that the non-radiative pathways, which include internal conversion (IC) and vibrational relaxation (VR) from higher excited states, are typically faster than the rate of fluorescence. The energy progression upon excitation to the S₂ potential energy surface (PES) is shown below with the help of a Jablonski diagram in Figure 1.3. It should be noted that not only does a decrease in the rate of IC potentially lead to increased higher excited state fluorescence, but also excited state reactivity from higher excited states. Interestingly, there are few compounds that violate Kasha's rule and exhibit fluorescence from higher excited states. There have been significant efforts to obtain such molecules as they may have the potential to achieve more efficient photochemistry. A dye molecule with a longer-lived higher excited state will be capable of more efficiently transferring electrons or holes (n-type or p-type semiconductor, respectively) from the higher excited state, by harnessing the higher energy photons. A longer-lived higher excited state may also be employed for phototheranostics, a term which combines phototherapy and diagnosis. A higher energy excited state, which has a longer lifetime can allow for more efficient photochemistry, causing the release of reactive oxygen species to kill cancerous cells. The photo physics upon direct excitation of organic dyes to higher excited states is discussed in this thesis.

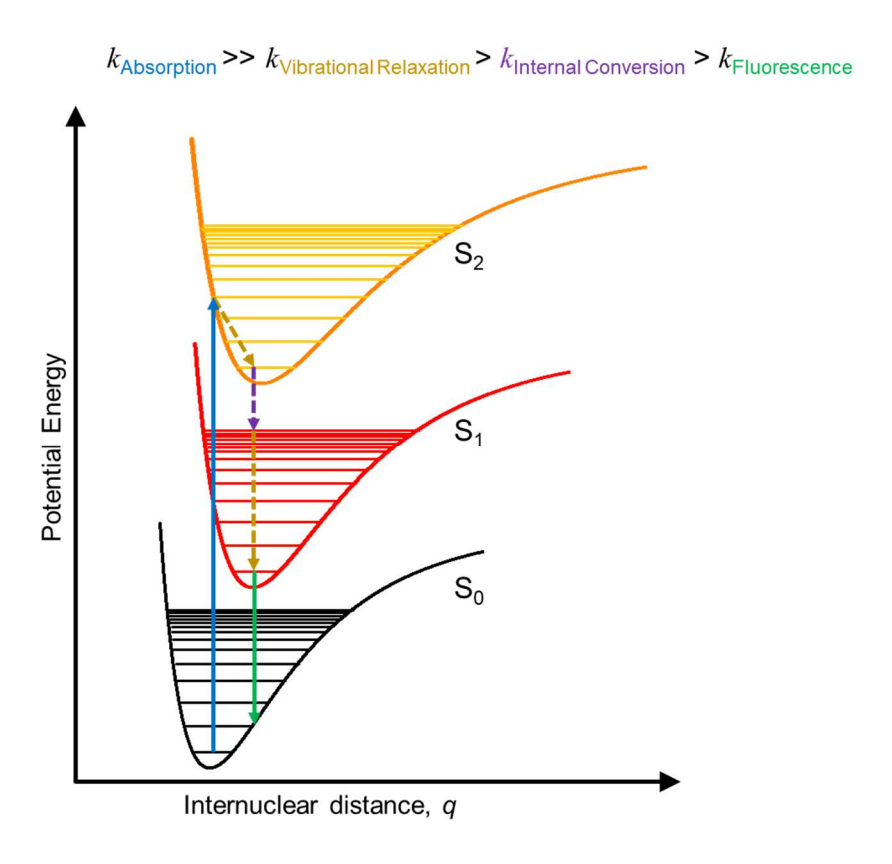


Figure 1.3. Jablonski diagram showing the ground and the excited electronic and vibrational states. The solid arrows indicate radiative transitions while dashed arrows indicate non-radiative transitions. The different transitions include absorption, VR, IC, and fluorescence shown by blue, dark yellow, purple, and green arrows, respectively.

Fluorescence from higher energy electronic states of organic molecules has been observed in some molecules (Figure 1.4), which may be enhanced by altering their substitution. Additionally, one can achieve higher S_2 fluorescence by altering the experimental conditions including, temperature, pressure, and viscosity. Fluorescence is observed from higher excited state of substituted azulenes, pseudoazulenes, acenes, and polyenes. One of the first examples of dual fluorescence to be reported is in the case of azulene, where the quantum yield of $S_2 \rightarrow S_0$ fluorescence is higher than $S_1 \rightarrow S_0$ fluorescence. This is primarily due to a significantly high energy difference between the S_2 and S_1 states, presumably leading to a lower Franck–Condon factor for $S_2 \rightarrow S_1$ transition and lower rates of IC.

Azulene 1,2-Benzanthracene
$$\beta$$
-Carotene β -Carotene β -Carotene β -Cyanines

Figure 1.4. Representative structures of organic dyes showing S₂ emission.

The blue fluorescence from the higher excited state of cryptocyanine was observed along with the red fluorescence from S₁ upon TPE using a ruby laser.⁵⁰. Blue fluorescence was also observed from DTTC (3,3'-diethyl-2,2'-thiatricarbocyanine iodide), which has a relatively strong S₂ absorption and emission.⁵¹ The time-resolved picosecond spectroscopy upon S₂ excitation of DTTC and HITC (1,3,3,1',3',3'-hexamethyl-2,2'-indotricarbocyanie iodide) in alcohols was performed which revealed the rate of IC.⁵² The excited state dynamics of the dyes appeared to be highly dependent on the solvent viscosity when excited to the S₂ state, which stems from the differences in geometry of the excited electronic states. The time-resolved study of the blue emission in tri-, penta-, and heptamethine cyanine dyes showed the kinetics being highly dependent on the solvent viscosity.⁵³ In addition, an ultrafast study was carried out to unravel the optical properties and excited state dynamics of a number of carbocyanines.⁵⁴ Further research have been conducted to comprehend the S₂ dynamics of cyanine dyes and the relationship with their structure.^{55,56} The Dantus group recently investigated the S₂ spectroscopy of some substituted heptamethine cyanine dyes, where they probe and control the IC using linear chirp.¹

The S_2 fluorescence is highly dependent on the solvent viscosity due to the difference in conformations between S_1 and S_2 states, similar to the cyanines DTTC and HITC.⁵² A high dependence of the rate of IC, and hence the S_2 fluorescence intensity, on the value of linear chirp was revealed (Figure 1.5). The higher value of chirp led to a higher extent of IC conversion in comparison to the transform limited (TL) condition (zero chirp), leading to the highest relative S_2 fluorescence at TL. Additionally, there seems to be two different higher excited states revealed from the emission spectra for the cyanine molecules with emissions separated by ~ 1000 cm⁻¹. Considering cyanine dyes already have extensive application in solar cells and phototheranostics, a more efficient photochemistry through S_2 excitation may lead to a broader range of applications.

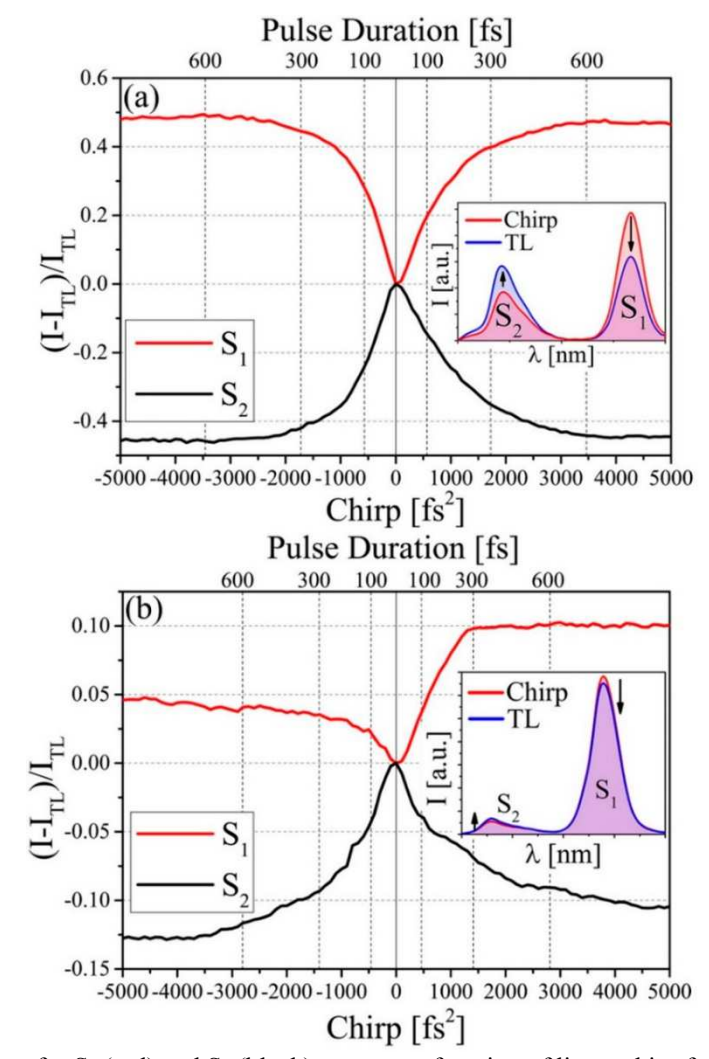


Figure 1.5. The fluorescence for S_1 (red) and S_2 (black) states as a function of linear chirp for (a) IR144 and (b) mPi-IR806. The top axis shows the corresponding chirped pulse duration. TL pulses lead to greater S_2 fluorescence, while chirped pulses lead to greater S_1 fluorescence. Data obtained from ref. 1 with permission.

The binding of fluorescent dyes with biomolecules for different biological applications is probed predominantly using S₁ fluorescence.^{57–62} The scope of S₂ fluorescence has been considered to track the binding of cyanine IR806 with human serum albumin (HSA), the most abundant plasma protein in the human body. HSA is responsible for maintaining osmotic blood pressure and transporting a multitude of ligands (fatty acids, steroids, metals, and pharmaceuticals) throughout the body. The occurrence of excessive HSA dimers in the body are a biomarker for

oxidative stress and cirrhosis of liver. Steady-state and time-resolved experiments, protein docking, and quantum calculations are able to detect the non-covalent dimer formation of HSA.

Chapter 2 Rotational Dynamics and Excited States of FR0-SB

We report on the motional and proton transfer dynamics of the super photobase FR0-SB in the series of normal alcohols C1 (methanol) through C8 (n-octanol) and ethylene glycol. Steady-state and time-resolved fluorescence data reveal that the proton abstraction dynamics of excited FR0-SB depend on the identity of the solvent and that the transfer of the proton from solvent to FR0-SB*, forming FR0-HSB^{+*}, fundamentally alters the nature of interactions between the excited molecule and its surroundings. In its unprotonated state, solvent interactions with FR0-SB* are consistent with slip limit behavior, and in its protonated form, intermolecular interactions are consistent with a much stronger interaction of FR0-HSB^{+*} with the deprotonated solvent RO⁻. We understand the excited-state population dynamics in the context of a kinetic model involving a transition state wherein FR0-HSB+* is still bound to the negatively charged alkoxide, prior to solvation of the two charged species. Data acquired in ethylene glycol confirm the hypothesis that the rotational diffusion dynamics of FR0-SB* are largely mediated by solvent viscosity while proton transfer dynamics are mediated by the lifetime of the transition state. Taken collectively, our results demonstrate that FR0-SB* extracts solvent protons efficiently and in a predictable manner, consistent with a ca. 3-fold increase in dipole moment upon photoexcitation as determined by *ab initio* calculations based on the equation-of-motion coupled-cluster theory.

This chapter has been adapted with permission from (*J. Phys. Chem. B* **2019**, *123*, 8448-8456) Copyright © 2019, American Chemical Society.

2.1 Introduction and Background

The ability to activate chemical reagents to perform spatially and temporally localized reactions affords many opportunities in areas ranging from materials science to the modulation of intracellular phenomena. Central to such precision chemistry is the use of photoinitiated reactive species, with the most common type being super photoacids. 63,64 Such species exhibit a large negative change in the pK_a of an acidic proton upon excitation, typically to the first excited electronic state. The reactive counterpart to a super photoacid is a super photobase. Presently there are two known examples of super photobases: 5-methoxyquinoline (5MQ)⁶⁵ and FR0-SB (Figure 2.1), a compound that exhibits a large negative change in p K_b of an imine upon excitation to its S_1 state.¹¹ While the unique properties of this molecule show much promise for future work on localized photoinitiated chemical reactions, a detailed understanding of the factors responsible for this behavior and of the dynamics of solvent interactions and proton abstraction remains to be elucidated. Among the reasons for the need for this information is to design other photobases with tailored properties (e.g., $\Delta pK_a = pK_a^* - pK_a$) and to understand the structural and electronic factors that control the photobase lifetime, because it is this property that determines the diffusionmediated resolution of any photoinitiated reaction using such reagents. We report here on the lifetime and solvent-interaction dynamics for FR0-SB in a series of normal alcohols and ethylene glycol.

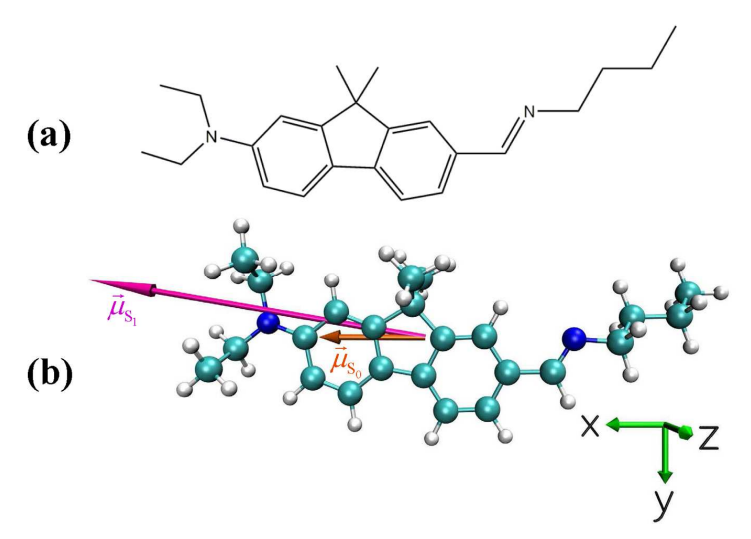


Figure 2.1. (a) **FR0-**SB super photobase. (b) The structure of the isolated **FR0-**SB molecule in its ground electronic (S_0) state and the dipole moments characterizing the S_0 (shorter orange vector $\vec{\mu}_{S_0}$) and electronically excited S_1 (longer magenta vector $\vec{\mu}_{S_0}$) states, as calculated in this work.

For any condensed phase chemical reaction, the interactions of the reactant(s) with their immediate environments typically play a critical role in the rate and specificity of the reaction. For FR0-SB, photoexcitation leads to proton abstraction from its local environment in protic solvents. There are multiple consequences to this abstraction event, ranging from the generation of another strong base, i.e., RO⁻, to structural and electronic changes in the photobase that occur due to the addition of a proton. These excitation-induced changes can be characterized using time-resolved spectroscopy, and we provide a detailed discussion of results from such measurements. First, however, we consider the steady-state spectroscopic properties of FR0-SB and how these data can be explained in the context of a simple kinetic model. With this understanding in place, we can interpret the time-resolved fluorescence data in the context of proton transfer processes. These results indicate that the addition of a proton to FR0-SB* alters the nature of its interactions with its immediate surroundings in a pronounced manner, pointing to the importance of solvent—solute interactions in understanding condensed phase dynamics and providing insight into molecular design strategies to gain direct control over proton transfer processes.

2.2 Experimental and Theoretical Methods

2.2.1 Materials

Anhydrous alcohols from methanol to *n*-octanol and ethylene glycol were obtained from MilliporeSigma in their highest purity grade available and used without further purification.

The compound FR0-SB was synthesized from FR0 and n-butylamine as described below.

7-(Diethylamino)-9,9-dimethyl-9H-fluorene-2-carbaldehyde (FR0). The synthesis of FR0 followed the procedure reported previously and is described briefly here. The synthesis commenced with the bromination of fluorene at C2 with N-bromosuccinimide (NBS). The gemdimethyl group at C9 was installed with the reaction of the brominated fluorene with iodomethane in the presence of NaOH. Nitration with fuming nitric acid yielded 2-bromo-9,9-dimethyl-7-nitro-9H-fluorene, which was subsequently reduced to the corresponding amine with iron powder suspended in an aqueous ammonium chloride solution. The resulting product was heated with ethyl iodide and potassium carbonate to introduce the diethyl substituents on the amine. FR0 was obtained upon formylation of the resultant metal/halogen exchanged intermediate (exchange promoted by the addition of n-butyllithium) as a yellow solid.

FR0-SB. **FR0** (10.5 mg, 35.8 μmol) was dissolved in ethanol (3.0 mL), and *n*-butylamine (100 μL, 28.2 equiv) was added. The resulting solution was stirred at room temperature for 2 h, after which the solvent and excess *n*-butylamine were removed under reduced pressure, affording a light yellow solid (**FR0-SB**) as an analytically pure product (12.5 mg, 99%). ¹H NMR (CDCl₃, 500 MHz), δ (ppm): 8.30 (s, 1H), 7.83 (d, J = 1.3 Hz, 1H), 7.61–7.51 (m, 3H), 6.74–6.65 (m, 2H), 3.67–3.60 (m, 2H), 3.45 (q, J = 7.1 Hz, 4H), 1.72 (p, J = 7.2 Hz, 2H), 1.50 (s, 6H), 1.47–1.39 (m, 2H), 1.23 (t, J = 7.0 Hz, 6H), 0.98 (t, J = 7.4 Hz, 3H). ¹³C NMR (CDCl₃, 125 MHz), δ (ppm):

161.52, 156.42, 153.14, 148.22, 142.73, 133.14, 128.59, 126.33, 121.49, 120.85, 118.09, 110.74, 105.49, 61.64, 46.70, 44.70, 33.22, 27.43, 20.52, 13.97, 12.64. ESI-MS: (calcd) (m/z) calcd for $C_{24}H_{33}N_2$ [M + H]⁺ 349.2644; found 349.2643.

2.2.2 Steady-State Absorbance and Emission Spectroscopy

UV-vis absorption spectra were recorded by using a Shimadzu UV-2600 UV-vis spectrometer. The spectral resolution was 1 nm for all measurements reported here. The concentration of the samples was 10 μ M in all the solvents. By use of a 1 cm cuvette, the OD of the samples at the absorbance maximum was 0.82 ($\varepsilon_{max} \sim 81500 \, \text{M}^{-1} \, \text{cm}^{-1}$). While this OD is somewhat higher than usual, we acquired steady-state and time-resolved data for **FR0**-SB in several solvents at OD 0.1 and obtained results that are identical to those acquired by using the 10 μ M samples. All absorbance and emission data were acquired at room temperature (20 ± 1 °C). Fluorescence spectra for the dye while dissolved in the solvents were obtained by using a Hitachi FL-4500 fluorescence spectrometer with excitation at maximum absorption. Spectral resolution was 1 nm for all measurements reported here.

2.2.3 Time-Resolved Fluorescence Measurements

The time-correlated single photon counting (TCSPC) instrument used in this work has been described elsewhere⁶⁶ in detail, and we highlight its salient features here. The light source for this instrument is a passively mode-locked Nd:YVO₄ laser (Spectra-Physics Vanguard) that produces 13 ps pulses at 1064 nm with 80 MHz repetition rate. The second and third harmonic outputs of this laser provide 2.5 W average power at 532 and 355 nm, respectively, with nominally the same 13 ps pulse width. The second harmonic output of this laser was used to excite a synchronously pumped cavity-dumped dye laser (Coherent 701-3) operating at 700 nm (LDS 698 laser dye,

Exciton). The fundamental output of the dye laser was frequency-doubled by using a Type I SHG crystal (LiIO₃, 1 mm) to produce 350 nm excitation pulses (ca. 5 ps pulse, 120 ns interpulse spacing) to excite the **FR0**-SB samples. The average power at the sample was 0.5 mW or less for all measurements, and the sample temperature was maintained at room temperature (20 ± 1 °C). A portion of the 700 nm pulse train was sent to a reference photodiode (B&H). Sample fluorescence was collected using a 40× reflecting microscope objective (Ealing) and sent to a polarization-selective beamsplitter (Newport). Each polarized emission component was polarization-scrambled and sent through a subtractive double monochromator (CVI Digikrom CM112) to a microchannel plate photomultiplier (Hamamatsu RG3809). The output of each detection channel was sent to one channel of a TCSPC system (B&H Simple Tau 152) and to a personal computer. Data were acquired and stored by using software written in-house using National Instruments LabVIEW. For each individual data set, the maximum signal channel contained at least 1500 counts, and at least three individual data sets were acquired for **FR0**-SB in each solvent studied.

The experimental fluorescence lifetime $(I_{||}(t) + 2I_{\perp}(t))$ and anisotropy decay functions, R(t), were constructed from raw polarized fluorescence transients that were tail-matched at times long relative to the anisotropy decay time. The resulting experimental anisotropy decay function data were fitted to either one- or two-component exponential decays by using Microcal Origin 9.0 software. The instrumental response function for the TCSPC instrument (ca. 40 ps) is sufficiently short that it was not necessary to deconvolute it from the fluorescence transients.

2.2.4 Computational Details

The purpose of the electronic structure calculations reported in this work was to determine some of the key properties of the ground (S_0) and low-lying excited singlet electronic (S_n , n > 0) states

of the isolated **FR0**-SB molecule, which are relevant to this work, including the ground-state geometry, the excitation energies and oscillator strengths characterizing the vertical $S_0 \rightarrow S_n$ transitions, and the electronic dipole moments of the calculated states. With the exception of the molecular geometry, which was optimized using the Kohn–Sham formulation⁶⁷ of the density functional theory (DFT),⁶⁸ all of the characteristics of the calculated electronic states were obtained by using high-level *ab initio* methods of quantum chemistry based on the coupled-cluster (CC) theory⁶⁹ and its equation-of-motion (EOM) extension⁷⁰ to excited states.

Given the relatively large size of the **FR0**-SB molecule, which consists of 58 atoms and 190 electrons, to use the CC and EOMCC methods as fully as possible and to make sure that the higher-order many-electron correlation effects beyond the basic EOMCC singles and doubles $(EOMCCSD)^{70}$ level are properly accounted for we used the following composite approach to determine the vertical excitation energies corresponding to the $S_0 \rightarrow S_n$ transitions:

$$\omega_n^{(\text{EOMCC})} = \omega_n^{(\text{EOMCCSD/6-31+G*})} + [\omega_n^{(\delta-\text{CR-EOMCC}(2,3)/6-31G)} - \omega_n^{(\text{EOMCCSD/6-31G})}]. \tag{2.1}$$

The first term on the right-hand side of Eq. 2.1 denotes the vertical excitation energy obtained in the EOMCCSD calculations using the 6-31+G* basis set,^{71–73} which was the largest basis set we could afford in such computations. The next two terms on the right-hand side of Eq. 2.1, which represent the difference between the δ -CR-EOMCC(2,3) and EOMCCSD vertical excitation energies obtained by using a smaller 6-31G basis,⁷¹ correct the EOMCCSD/6-31+G* results for the higher-order many-electron correlation effects due to triple excitations. We recall that the δ -CR-EOMCC(2,3) approach⁷⁴ is a rigorously size-intensive modification of the completely renormalized EOMCC methodology, abbreviated as CR-EOMCC(2,3),^{75–77} which provides a recipe how to correct EOMCCSD energies for the leading triple excitations in a robust manner and

which is an extension of the CR-CC(2,3) triples correction^{75,76,78,79} to CCSD⁸⁰ to excited electronic states. For example, in a report⁸¹ where about 200 excited states of 28 organic molecules were examined by using a variety of EOMCC methods, it was shown that one needs triples corrections, such as those of the δ -CR-EOMCC(2,3) approach, on top of EOMCCSD to obtain a quantitative description (errors reduced to an ~0.1–0.2 eV level). The size intensivity of the EOMCCSD and δ -CR-EOMCC(2,3) excitation energies entering our composite computational protocol defined by Eq. 2.1, combined with the size extensivity of the underlying CCSD and CR-CC(2,3) approaches, is important, too, since without reinforcing these formal theory features one risks losing accuracy with growing molecular size.

The CCSD/6-31+G* and EOMCCSD/6-31+G* calculations were also used to determine the dipole moments in the ground and excited states and the oscillator strengths characterizing the vertical $S_0 \to S_n$ (in general, $S_m \to S_n$) transitions. As usual, this was done by solving both the right and the left EOMCCSD eigenvalue problems and constructing the relevant one-electron reduced density and transition density matrices.^{70,82} While triples corrections, such as those of CR-CC(2,3) and δ -CR-EOMCC(2,3), are important to improve the energetics, the description of one-electron properties, such as dipole moments and oscillator strengths characterizing one-electron transitions examined in this study, by the CCSD and EOMCCSD approaches is generally quite accurate.

All single-point CC and EOMCC calculations reported in this work relied on the groundstate geometry of **FR0**-SB, which we optimized using the analytic gradients of the CAMB3LYP DFT approach⁸³ employing the 6-31+G* basis set. We chose the CAMB3LYP functional because the extension of this functional to excited states using the time-dependent (TD) DFT formalism⁸⁴ provided vertical excitation energies closest to those obtained with EOMCC. Furthermore, the ground-state geometry of the **FR0**-SB molecule resulting from the CAMB3LYP/6-31+G* calculations turned out to be virtually identical (to within 0.004 Å on average and not exceeding 0.02 Å for the bond lengths) to that obtained with the second-order Møller–Plesset perturbation theory (MP2) approach using the same basis.

All of the electronic structure calculations for the **FR0**-SB molecule reported in this study, including the CAMB3LYP and MP2 geometry optimizations and the CC/EOMCC single-point calculations, were performed by using the GAMESS package. The relevant CCSD, EOMCCSD, and δ -CR-EOMCC(2,3) computations using the restricted Hartree–Fock (RHF) determinant as a reference and the corresponding left-eigenstate CCSD and EOMCCSD calculations, which were needed to determine the triples corrections of δ -CR-EOMCC(2,3) and the one-electron properties of interest, including the dipole moments and oscillator strengths, were performed by using the CC/EOMCC routines developed by the Piecuch group, 75,77–79,82,86,87 which form part of the GAMESS code. In all of the post-RHF calculations, the core orbitals associated with the 1s shells of C and N atoms were kept frozen, i.e., we correlated 138 electrons. In the calculations employing the 6-31+G* basis set, we used spherical d-type polarization functions. The visualization of the optimized structure of **FR0**-SB in its ground electronic state shown in Figure 1b was accomplished by using VMD software. 88

2.3 Results and Discussion

The central issue of concern is how the excited state of the super photobase **FR0**-SB interacts with the surrounding solvent before and after photoexcitation. We initiate our study by surveying the steady-state fluorescence spectra of **FR0**-SB in normal alcohols, which show two prominent emission bands. One band is associated with the (initially) unprotonated form, **FR0**-SB* (ca. 460 nm), and the other is associated with the protonated form, **FR0**-HSB^{+*} (ca. 630 nm). As can be seen from the spectra (Figure 2.2), the relative intensities of the two emission bands depend on the solvent medium.

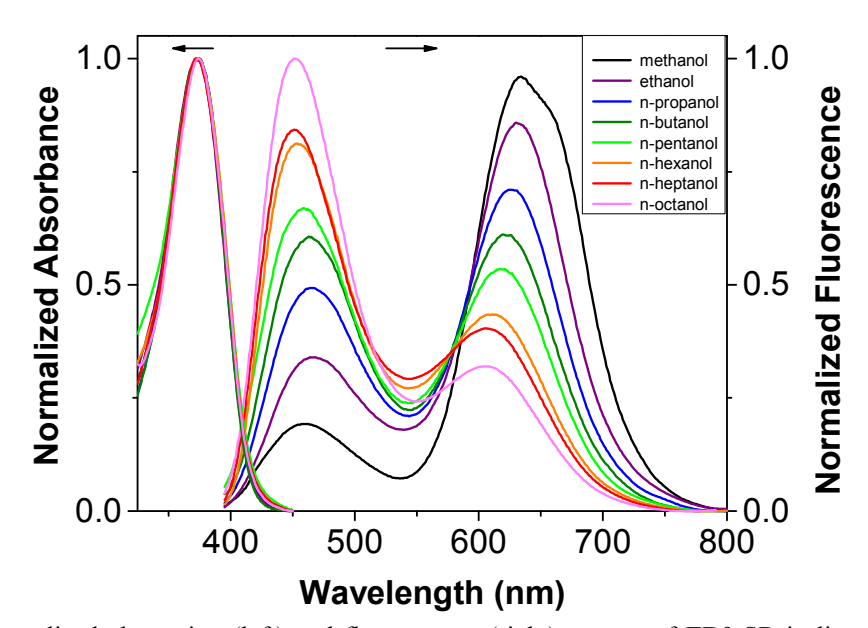


Figure 2.2. The normalized absorption (left) and fluorescence (right) spectra of **FR0**-SB in linear alcohols from methanol to *n*-octanol. Absorbance spectra are normalized to a maximum of 1.0 and integrated emission band areas are normalized for area.

To examine the interactions between the super photobase and its immediate environment, we measure the rotational diffusion dynamics of both **FR0**-SB* and **FR0**-HSB^{+*}. For such measurements, we acquired fluorescence transients for polarizations parallel and perpendicular to the excitation polarization in each solvent ($I_{||}(t)$ and $I_{\perp}(t)$, respectively). The transients are combined to produce the induced orientational anisotropy decay function,

$$R(t) = \frac{I_{\square}(t) - I_{\perp}(t)}{I_{\square}(t) + 2I_{\perp}(t)}.$$
 (2.2)

The chemical and physical information of interest lies in the functional form and decay time constant(s) of R(t), and there is a well-established theoretical framework in place for the interpretation of these data. ^{89–92} The relationship between the anisotropy decay function and the Cartesian components of the rotational diffusion constant $(D_i, i = x, y, z)$ have been described by Chuang and Eisenthal. ⁸⁹ For the experimental conditions of relevance here, the transition dipole moment between the ground state and the first excited singlet state lies approximately along the long molecular axis (x), which is taken to be unique relative to the short molecular axes (y, z) (see Figure 1b). Such motion is described in the context of a prolate rotor $(D_x \neq D_y = D_z)$, and R(t) decays as a single exponential. The recovered anisotropy decay time constant is inversely related to D_z .

Under these experimental conditions, the rotational diffusion decay time constant is related to chromophore and system properties through the modified Debye–Stokes–Einstein (DSE) equation, 90–92

$$\tau_{\rm OR} = \frac{1}{6D_a} = \frac{\eta V f}{k_{\rm B} TS},\tag{2.3}$$

where τ_{OR} is the decay time constant of R(t), η is the (bulk) solvent viscosity, V is the hydrodynamic volume of the rotating entity, calculated by using the method of van der Waals increments, ^{93}f is a frictional interaction term that describes the boundary condition between solvent and solute, $^{91}k_{B}T$ is the thermal energy term, and S is a shape factor related to the ellipsoidal shape of the rotating molecule, calculated via Perrin's equations. 92 Using molecular mechanics, we estimated the major axis length of **FR0**-SB to be 18.2 Å and the minor axis to be 6.2 Å, yielding a hydrodynamic volume of 363 Å³, in agreement with the estimate from the method of van der Waals increments.

From the ratio of the axes, $\rho = 0.34$, and using Perrin's equation for a prolate ellipsoid, we recover S = 0.43. The choice of a prolate ellipsoid was based on the observed single-exponential anisotropy decay in all cases (vide infra). For strong intermolecular interactions, f is set to 1, the so-called stick limit. For conditions where the interactions between solvent and chromophore are less strong, f can range from 0 to <1, depending on the value of S. For a prolate rotor with S = 0.43, $f_{\rm slip} = 0.44$. This is the so-called slip limit. In our consideration of solvent—chromophore interactions, we do not attempt to correct for changes in S because any such correction would lead to only small changes in the model results, and there is no experimental means of evaluating any such change.

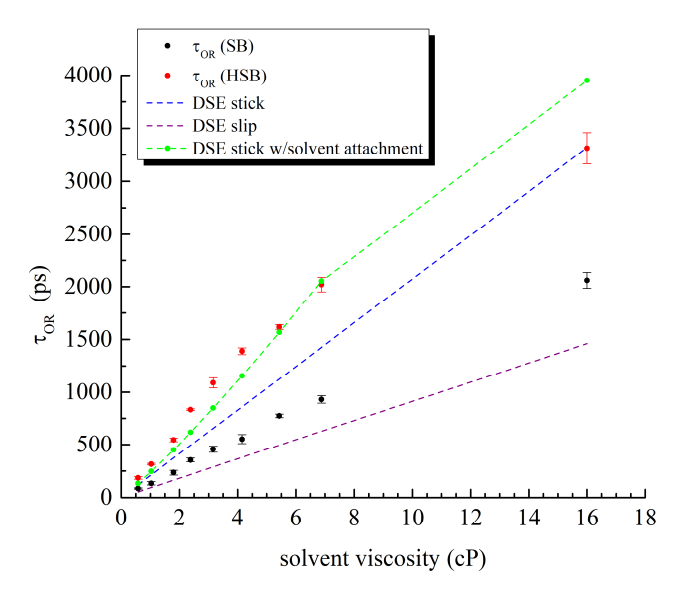


Figure 2.3. Reorientation times of **FR0-**SB* and **FR0-**HSB^{+*} in the primary *n*-alcohols, methanol through 1-octanol, and ethylene glycol plotted *vs.* solvent viscosity. The purple and blue dashed lines indicate the slip and stick limit from the modified DSE equation, Eq. 2.3, respectively. The green points represent the result of solvent "attachment" to the chromophore.

Despite the fact that the modified DSE model assumes the solvent to be a continuum, it has proven to be a relatively accurate predictor of rotational diffusion behavior. For the experiments reported here, the rotational diffusion dynamics for the unprotonated **FR0**-SB* system are measured at 450 nm, and the rotational diffusion dynamics of the protonated **FR0**-HSB** species are measured at 650 nm. The normalization for the total excited-state population (the denominator

in Eq. 2.2 ensures that the fluorescence decay or the fluorescence rise in the case of the protonated species does not distort the motional information content of R(t). We show in Figure 2.3 the experimental reorientation times for **FR0**-SB* and **FR0**-HSB^{+*} as a function of solvent viscosity along with the predictions of the modified DSE model in both the stick and slip limits. We find that the anisotropy decay time constant varies linearly with solvent viscosity for both species; however, the slope of the dependence is different by a factor of slightly more than 2 (291 ps/cP for **FR0**-HSB^{+*} vs 134 ps/cP for **FR0**-SB*). We consider this difference in more detail next.

As can be seen from the lines in Figure 2.3 calculated by using the modified DSE model in the stick and slip limits, the reorientation behavior of FR0-HSB^{+*} appears to be slower than the stick limit, while that of FR0-SB* is intermediate between stick and slip limits. Following proton transfer, FR0-HSB^{+*} is positively charged and there is a negatively charged RO— species nearby. The difference in behavior between FR0-SB* and FR0-HSB^{+*} is consistent with the difference predicted by the stick and slip limits. We believe this to be largely fortuitous. The modified DSE model in either limit does not account for intermolecular interactions between chromophore and solvent that are central to the data we report here.

Despite the apparent appeal of the stick and slip limit predictions, it is important to also consider the process that is relevant to our observations. Specifically, the process under consideration is a proton transfer event from the ROH solvent to the **FR0**-SB* chromophore. The products of this process are described as RO⁻ and **FR0**-HSB^{+*}, with the necessary involvement of a transition state (see Figure 2.4). This representation has been made previously for **FR0**-SB*, where the excited-state proton transfer reaction coordinate is indicated as having a local minimum intermediate between **FR0**-SB* and **FR0**-HSB^{+*}. The open issue is the time scale of the transition from unprotonated to protonated form (Figure 2.4) and the ability to distinguish a "shared" proton

from a contact ion pair (FR0-HSB^{+*}-TOR) based on the data reported here. In fact, the reorientation data cannot provide explicit information about the nature of the solvent–solute pair. If the solvent–(excited) solute complex (Figure 2.4) is stable on a time scale similar to the rotational time of the chromophore, the complex, including both the chromophore and solvent molecule hydrodynamic volume, would contribute to the hydrodynamic volume of the rotating species. Such a solvent–solute complex can be modeled by $V = V_{FR0-SB^*} + V_{ROH}$, which is presented as the green dots and connecting line in Figure 2.3. In such a system it is expected that for sufficiently slow reorientation there would be a negative deviation of the experimental data from the volume-based prediction because the complex would not persist as an entity for as long as τ_{OR} . In other words, the hydrodynamic volume would be represented by that of the chromophore and a fraction of the solvent volume, with the fraction being related to the ratio of the complex lifetime to τ_{OR} . Such an explanation is not without precedent. The formation of a persistent complex between chromophore and solvent has been invoked previously to explain state-dependent rotational diffusion behavior in oxazines in hydrogen-bonding solvents.

$$SB^* \cdots H - OR \rightleftharpoons SB^* \cdots H \cdots OR \rightleftharpoons SB^* - H \cdots OR$$

Figure 2.4. Schematic of proton exchange between SB* and solvent.

In an attempt to clarify this assertion, we acquired anisotropy decay data for **FR0**-HSB^{+*} in acidified methanol and ethanol solutions. Acidification of **FR0**-SB in methanol and ethanol produces **FR0**-HSB^{+*}, which has a characteristic absorption band centered at ca. 480 nm. Direct excitation of this band yielded anisotropy decay time constants that are identical to those for **FR0**-HSB⁺ in the nonacidified solvents. We attribute this result to the limitations of the experiment. The addition of sufficient acid to produce **FR0**-HSB⁺ is practical only in methanol and ethanol, and the

hydrodynamic volumes of these solvents are small relative to the chromophore. Thus, any difference between the reorientation of protonated **FR0**-HSB^{+*} and the same chromophore interacting with the solvent is not resolvable within our experimental uncertainty.

A brief word is in order regarding the zero-time anisotropy decay data shown in Table 2.1. These data reflect the angle between the excited and emitting transition dipole moments. For **FR0**-SB* there appears to be a monotonic decline in R(0) with increasing solvent viscosity while for **FR0**-HSB*+ R(0) appears to be independent of solvent. For **FR0**-SB* the angle between the excited and emitting transition dipole moment varies between 15° and 49°, while for **FR0**-HSB*+ the angle is essentially constant at ~30°. The angle between the excited and emitting transition dipole moments depends on the structure of the emitting species and on the symmetries of the vibronic transitions accessed by the emission. As the details of solvation change with solvent, the specific vibronic transitions accessed over the detected emission window will vary. While interesting, there simply is not enough information contained in R(0) to be able to extract additional detailed chemical information.

We consider next the details of the proton exchange process. It is important to note at the outset that the primary factors mediating molecular rotation are different than those which mediate proton transfer. As noted above, the two emission bands shown in Figure 2.2 correspond to FR0-SB* (ca. 460 nm) and FR0-HSB+* (ca. 630 nm). We can explain the changes in the area of the two fluorescence emission bands in the context of a kinetic model, which can be evaluated by using time-resolved measurements. The relative intensities of the two bands are expected to scale with the corresponding lifetimes of the unprotonated and protonated species in the different solvents, after considering differences in the fluorescence quantum yield between the unprotonated and protonated species. Table 2.1 summarizes the fluorescence lifetime decays obtained from

fitting the isotropic quantity ($I_{\parallel}(t)+2I_{\perp}(t)$) to an exponential decay function. The lifetime data for **FR0**-HSB^{+*} (630 nm) exhibit two components: a rise time and a decay time. For the *n*-alcohols, we observe that all the lifetimes increase as a function of solvent aliphatic chain length. This dependence cannot be accounted for in terms of the solvent pKa, which varies over a narrow range, from 15.5 to 17. Rather, the change in observed rates is seen to depend on the concentration of -OH functionality in the solvents.

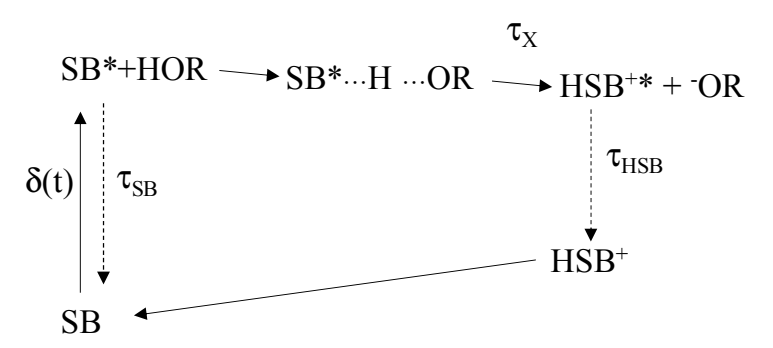


Figure 2.5. Kinetic population model for excited state proton transfer between FR0-SB and the solvent.

Table 2.1. Fluorescence anisotropy and lifetime components.

Solvent	460 nm emission (SB*)				630 nm emission (HSB+*)			
	R(0)	$\tau_{\rm OR}$ (ps)	$ au_{\mathrm{SB1}}\left(\mathrm{ps}\right)$	$\tau_{\mathrm{SB2}}(\mathrm{ps})$	R(0)	$\tau_{\mathrm{OR}}\left(\mathrm{ps}\right)$	$\tau_{\rm X} ({\rm ps})$	$\tau_{\rm HSB} ({\rm ps})$
MeOH	0.36	86 ± 6	48 ± 4	_	0.24	186 ± 13	96 ± 4	1048 ± 2
EtOH	0.31	134 ± 16	74 ± 5	301 ± 24	0.24	315 ± 8	208 ± 13	1262 ± 15
PrOH	0.23	235 ± 23	94 ± 3	306 ± 6	0.25	544 ± 17	296 ± 10	1443 ± 6
BuOH	0.19	355 ± 19	213 ± 5	617 ± 31	0.25	834 ± 8	426 ± 63	1585 ± 30
PeOH	0.14	456 ± 29	361 ± 41	2201 ± 753	0.24	1090 ± 49	610 ± 53	1604 ± 26
HxOH	0.10	552 ± 43	437 ± 12	2824 ± 212	0.24	1389 ± 32	739 ± 40	1663 ± 32
НрОН	0.06	774 ± 17	605 ± 64	_	0.26	1618 ± 22	773 ± 9	1774 ± 13
ОсОН	0.11	931 ± 36	691 ± 72		0.25	2020 ± 69	933 ± 17	1701 ± 55
EG	0.11	2061 ± 76	57 ± 1	1328 ± 30	0.29	3312 ± 146	100 ± 12	1133 ± 104

All time constants are in ps. Uncertainties are reported as $\pm 1 \sigma$ for at least three determinations. Abbreviations: MeOH = methanol, EtOH = ethanol, PrOH = 1-propanol, BuOH = 1-butanol, PeOH = 1-pentanol, HxOH = 1-hexanol, HpOH = 1-heptanol, OcOH = 1-octanol, EG = ethylene glycol.

A kinetic model, consistent with the steady-state emission data, is presented in Figure 2.5. In this model, excitation ($\delta(t)$) is at 350 nm, producing **FR0**-SB*. This species either can relax radiatively to **FR0**-SB (τ_{SB} , $\lambda_{\text{em}} \approx 460$ nm) or can interact with a solvent molecule through hydrogen bonding, leading to a transition state [**FR0**-SB*···H···OR][‡] and subsequent proton abstraction to

produce FR0-HSB^{+*} and -OR. Radiative relaxation of FR0-HSB^{+*} (τ_{HSB}) is observed at ca. 630 nm. For the proton transfer process, we identify two different rate constants. The first rate constant is associated with hydrogen bonding between the solvent and FR0-SB*. We believe the formation of the H-bond to be fast. We assert that the rise time pertaining to the FR0-HSB^{+*} population is associated with the formation of the complex (Figure 4) and progression to the products, FR0-HSB^{+*} + RO⁻. To assist the interpretation of the experimental data, we show some of the key properties of the low-lying singlet electronic states of the FR0-SB molecule in Table 2.2 obtained in the ab initio EOMCC calculations described in the Computational Details section. They include the excitation energies and oscillator strengths characterizing the vertical $S_0 \rightarrow S_n$ (n = 1-4) transitions and the electronic dipole moments of the calculated ground and excited states. To verify the reliability of our EOMCC-based computational protocol defined by Eq. 2.1, we compared our theoretical gas-phase value of the $S_0 \rightarrow S_1$ vertical excitation energy of FR0-SB with the corresponding experimental photoabsorption energy characterizing FR0-SB dissolved in hexane, which is the least polar solvent considered in our experiments that will be reported in a future publication. Our best ab initio EOMCC value based on Eq. 2.1, of 3.70 eV, matches closely the experimentally derived $S_0 \rightarrow S_1$ transition energy corresponding to the maximum of the photoabsorption band characterizing FR0-SB dissolved in hexane, which is 3.52 eV. If we did not correct the EOMCCSD/6-31+G* excitation energy for the triples using Eq. 2.1, we would obtain 4.10 eV, which shows that high-order many-electron correlation effects beyond the EOMCCSD level, estimated in this study with the help of the δ -CR-EOMCC(2,3) approach, are significant. We should also mention that our best TD-DFT result for the $S_0 \rightarrow S_1$ vertical excitation energy of FR0-SB, obtained using the CAMB3LYP functional, of 3.92 eV, is not as good as the EOMCC value shown in Table 2.2.

Table 2.2. The orbital character, vertical excitation energies ω_n^{EOMCC} , oscillator strengths, and electronic dipole moment values μ_n of the four lowest-energy excited singlet electronic states S_n of **FR0**-SB, as obtained in the EOMCC calculations described in the Computational Details section. The CCSD value of the dipole moment in the ground electronic state is 2.6 D.

State	Orbital character	ω_n^{EQ}	DMCC)	Oscillator strength	μ_n (D)
	Character	(eV)	(nm)		
S_1	$\pi \to \pi^*$	3.70	335	0.74	8.6
S_2	$\pi \to \pi^*$	3.96	313	0.35	6.7
S_3	$\pi \to \pi^*$	4.23	293	0.02	5.4
S_4	$\pi \to \pi^*$	4.45	279	0.03	4.3

Moving to our main theoretical findings summarized in Table 2.2, we can see that of the four lowest-energy singlet excited states of FR0-SB calculated in this study, two, namely, S_1 and S₂, can be accessed by photoabsorption. The remaining two states, S₃ and S₄, are characterized by negligible oscillator strengths. In a future computational study, we will show that the positions and relative intensities of the $S_0 \rightarrow S_1$ and $S_0 \rightarrow S_2$ transitions closely match those observed in highresolution photoabsorption experiments for **FR0**-SB in nonpolar solvents, such as hexane. What is most important for this study are the observations that both S_1 and S_2 have similar peak positions and intensities on the same order, resulting in broadening of the FR0-SB → FR0-SB* photoabsorption band, and that the electronic dipole moment of FR0-SB increases significantly upon photoexcitation, from 2.6 D in the ground electronic state to 8.6 D for S₁ and to 6.7 D for S₂. This more-or-less 3-fold increase in the dipole moment as a result of the $S_0 \to S_1$ and $S_0 \to S_2$ optical transitions in FR0-SB, observed in our EOMCC calculations and shown in Figure 1b for S₁, demonstrates that the deprotonation of protic solvent molecules by the photoactivated **FR0-SB** species is indeed possible, since there is an accumulation of the net negative charge on the imine nitrogen. While the decay time constant corresponding to the second excited singlet state, τ_{SB2} , represents only a small fraction of the total population decay of FR0-SB*, and in some cases (methanol, n-heptane, and n-octane) this component cannot be even resolved, i.e., the S₂ state does

not appear to play a direct role in proton exchange, the presence of this strongly dipolar state in the vicinity of S_1 , which has a similarly large dipole, may be important for understanding the state-dependent modulation of electron density in FR0-SB. In extracting the decay time constants τ_{SB1} and τ_{SB2} in Table 2.1, we made the assumption that the $S_1 \rightarrow S_0$ and $S_2 \rightarrow S_0$ fluorescence processes are independent of each other and that the radiative $S_2 \rightarrow S_1$ transition can be neglected, and our ab initio EOMCC calculations confirm the validity of these assumptions. The oscillator strength characterizing the transition between the S_1 and S_2 states resulting from our calculations is only about 0.01, making the $S_2 \rightarrow S_1$ fluorescence highly unlikely. Gaining a detailed understanding of the role of each excited state in the optical response and proton transfer clearly requires more experimental investigation. We are presently investigating both the one- and two- photon excited emission data and will report on those data in a future publication.

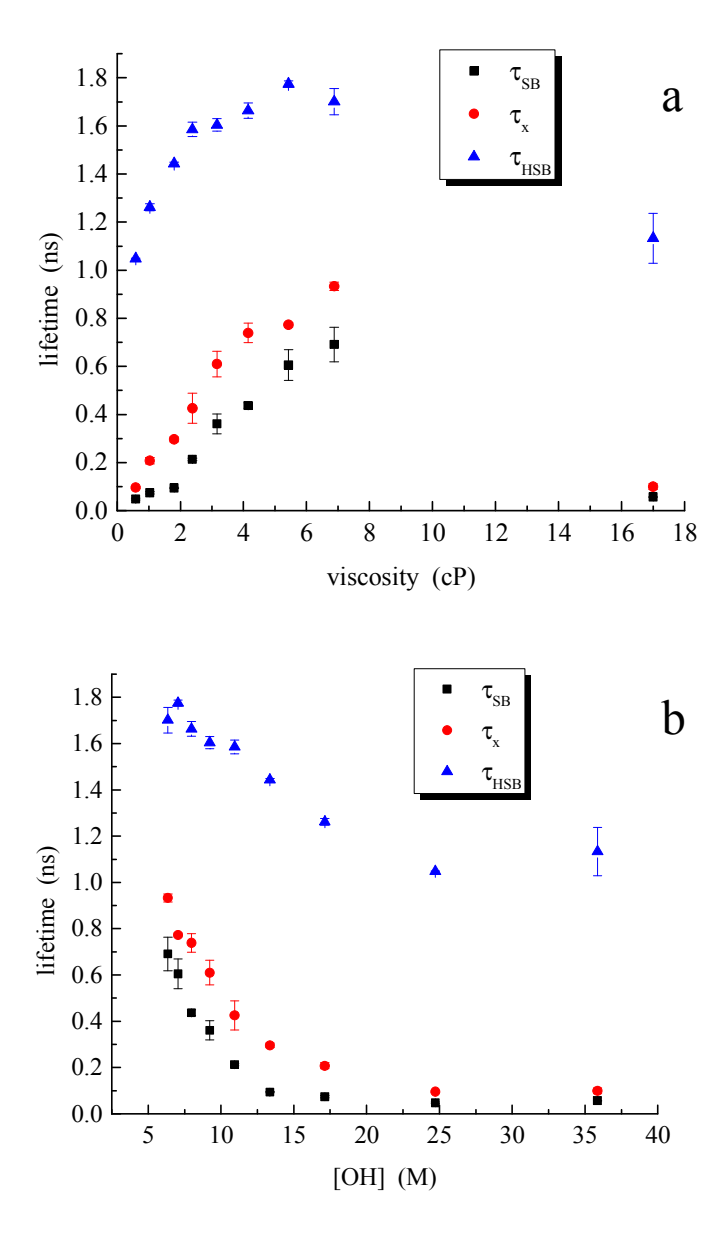


Figure 2.6. (a) Dependence of lifetimes τ_{SB} , τ_{X} and τ_{HSB} on solvent viscosity. (b) Dependence of the same lifetimes on solvent [-OH].

The solvent dependence of the fluorescence lifetimes is shown in Figure 2.6 as a function of solvent viscosity (Figure 2.6a) and as a function of the solvent [OH] (Figure 2.6b). The dependence on [OH] is similar to the dependence on dielectric constant (not shown). The dependence of the radiative lifetimes of **FR0**-SB* and **FR0**-HSB** on viscosity indicates that relaxation for both is mediated by the ability of the chromophore to access out-of-plane

conformations to activate nonradiative decay pathways. The dependence of τ_x on viscosity suggests that some level of solvent–solute alignment is required to facilitate the formation of the transition state.

Examining the lifetimes as a function of [-OH] reveals that all of the lifetimes are affected by the proton transfer process. For the highest proton concentrations (ethylene glycol and methanol) it appears that the formation of the transition state and the subsequent proton transfer event occurs on a time scale that is on the order of our experimental time resolution (ca. 40 ps) or faster. This result is expected based on the high concentration of -OH functionality that is present. The [-OH] dependence becomes more clear for solvents ethanol through n-octanol, where the concentration of [-OH] is lower. Such findings are consistent with the model shown in Figure 5.

We note correlation between the population decay of **FR0**-SB* and buildup of **FR0**-HSB^{+*}. The time constant associated with the transition from **FR0**-SB* to **FR0**-HSB^{+*} (τ_X) is longer in all cases than the decay time of **FR0**-SB*. These data demonstrate there is necessarily a transition state with a finite lifetime associated with the proton transfer process.

Because the series of n-alcohols provide a correlation between solvent molecular structure and viscosity, with an inverse dependence on [-OH], it is important to test which of these properties dominates the several processes we consider in this paper. For the rotational diffusion data there is a known viscosity dependence (Eq. 2.3), and we observe this experimentally. For the lifetime data, ethylene glycol (furthest right points in Figure 2.6a) does not follow the trend for the normal alcohols. As can be seen in Figure 2.6b, however, the lifetime data exhibits a dependence on [-OH] that holds for both ethylene glycol and the n-alcohols, and such a finding is consistent with the kinetic model shown in Figure 2.5.

It is also useful to consider the dependence of our lifetime data on the dielectric constant of the solvent. This dependence follows the same trend as shown in Figure 2.6b for [-OH]. The dielectric constant is related to the ability of the environment to solvate charged species. The rise time of the protonated species τ_X decreases as the dielectric constant of the solvent increases. The stabilization of the solvent–solute complex as well as the formation of the charged species is mediated by the dielectric response of the system, which implies that both the transition state and the reaction products (FR0-HSB^{+*} and RO⁻) are more polar than the neutral FR0-SB* and ROH reactants. While this is obviously the case for the final products, the dependence of τ_X on dielectric constant sheds some light on the nature of the transition state.

It is also important to consider the dominant factor that mediates the relaxation of FR0-HSB^{+*}. As can be seen from the steady-state emission data (Figure 2.2), the emission of FR0-HSB^{+*} shifts to the blue with increasing solvent aliphatic chain length, consistent with the polar (ionic) nature of the excited chromophore. On the basis of this observation, one would expect on simple polarity grounds that the lifetime of FR0-HSB^{+*} would decrease with increasing solvent aliphatic chain length. Experimentally, the opposite trend is observed (Table 2.1). The lifetime of FR0-HSB^{+*} is seen to be proportional to [-O⁻], indicating that back-donation of the proton from FR0-HSB^{+*} to the alkoxide RO⁻ mediates the relaxation of the protonated chromophore. Consequently, the species FR0-HSB^{+*} shown in Figure 2.5 may have a vanishingly small concentration, which is not surprising.

It is important to make a clear distinction between the rotational diffusion dynamics and the proton exchange dynamics seen here. Indeed, these two phenomena, which both play important roles in the data we report here, depend on the solvent properties in different ways. Specifically, the rotational diffusion dynamics are known to depend on the viscosity of the solvent system

according to the modified DSE model. The proton exchange dynamics, in contrast, may depend on the solvent viscosity to a limited extent in the context of the time required to achieve intermolecular alignment to facilitate proton transfer and solvation dynamics. The dominant contributions to proton transfer dynamics, however, are the available –OH concentration and the solvent dielectric constant. The data for **FR0**-SB* and **FR0**-HSB** in ethylene glycol underscore the difference in the factors that dominate the two processes.

2.4 Conclusion

We have examined the rotational diffusion and excited-state protonation/deprotonation dynamics of both FR0-SB* and FR0-HSB^{+*} species as a function of solvent viscosity and dielectric constant for a series of n-alcohols C1 (methanol) through C8 (n-octanol) and ethylene glycol. The rotational diffusion behavior of FR0-SB* and FR0-HSB** is seen to be substantially different and approximated by the modified DSE model in the slip and stick limits, respectively. It is the protonation of the FR0-SB* molecule that leads to a chromophore possessing formal charge and exhibiting substantially stronger solvent-solute interactions. We find better agreement when we consider that the solvent interacts with the excited chromophore over a time scale that is similar to the chromophore rotational diffusion time. This finding provides strong evidence for the formation of a relatively stable transition state, as schematized in Figure 2.4. The lifetime of the excited states of both FR0-SB* and FR0-HSB^{+*} correlate with the [-OH] and the dielectric constant, which is consistent with the kinetic model presented in Figure 5 and with the structure of the transition state being more polar than the neutral reactants. The dependence of each process on solvent parameters is different, and we expect that there are steric issues in addition to those we report here that can be revealed through the study of these processes in secondary and tertiary alcohols and in diols. Taken collectively, these data demonstrate that the FR0-SB* super photobase extracts solvent protons efficiently and in a predictable manner. This is consistent with the significant, ca. 3-fold, increase in the dipole moment upon photoexcitation to the two lowest-energy singlet excited states of FR0-SB* observed in our high-level ab initio EOMCC calculations. While our decay time measurements suggest that the second excited singlet state, which has a large dipole moment similar to the first excited singlet state, does not play a direct role in proton exchange, its presence may be important for understanding the state-dependent modulation of electron density in FR0SB. Our experiments reported in this work find the protonation step to be highly dependent on the ability of the solvent to solvate the resulting charged species. The use of photoinitiated reagents in precision chemistry applications can proceed with greater predictive power with the information gained from this work. In the future, we will explore other aspects of the complex interactions between **FR0**-SB* and its local environment to more fully understand the chemical and physical factors that mediate its photoinduced reactive properties.

Chapter 3 Steric Effects in Light-Induced Solvent Proton Abstraction

The significance of solvent structural factors in the excited-state proton transfer (ESPT) reactions of Schiff bases with alcohols is reported here. We use the super photobase FR0-SB and a series of primary, secondary, and tertiary alcohol solvents to illustrate the steric issues associated with solvent to photobase proton transfer. Steady-state and time-resolved fluorescence data show that ESPT occurs readily for primary alcohols, with a probability proportional to the relative –OH concentration. For secondary alcohols, ESPT is greatly diminished, consistent with the barrier heights obtained using quantum chemistry calculations. ESPT is not observed in tertiary alcohols. We explain ESPT using a model involving an intermediate hydrogen-bonded complex where the proton is "shared" by the Schiff base and the alcohol. The formation of this complex depends on the ability of the alcohol solvent to achieve spatial proximity to and alignment with the FR0-SB* imine lone pair stabilized by the solvent environment.

This chapter has been reproduced from (*Phys. Chem. Chem. Phys.* **2020**, *22*, 19613-19622), with permission from PCCP owner societies.

3.1 Introduction and Background

The development and characterization of reversible photoactivated reagents is central to the advancement of precision chemistry. The goal of this emerging area is to control the execution of a chemical reaction spatially and temporally through the use of photo-activated reactive chemical species. Applications for such precision chemistry are numerous, ranging from high-precision photolithography to the development of near-field chemical-reaction-based sensing and imaging of complex surfaces, including, for example, heterogeneous catalysts.

The vast majority of chemical reactions are either acid–base or redox processes, and the key to the development of precision chemistry is the ability to design photoinitiated reagents for specific purposes. Some of the best-known members of this class of molecules are photoacids and super photoacids, where a chemical functionality on a chromophore, typically an alcohol or carboxylic acid moiety, undergoes a substantial decrease in pK_a upon photoexcitation.

Even though there are several known families of super photoacids, such as the cyanonaphthols, 9,10 only a limited number of molecules are known to function as photobases, capable of abstracting protons from alcohols. Among them are 5-methoxyquinoline⁶⁵ and (E)-7-((butylimino)methyl)-N,Ndiethyl-9,9-dimethyl-9H-fluoren-2-amine (**FR0**-SB)¹¹ (Figure 1) with excited-state pK_a values of 15.5 and 21, respectively. These two species are examples of molecules that exhibit excited-state intermolecular proton transfer (ESPT) rather than excited-state intramolecular proton transfer. 97,98 It is worth pointing out that unlike hydroxyquinoline, aminoquinoline, and azaindole photobases, **FR0**-SB lacks labile protons and must undergo explicit intermolecular proton transfer, as opposed to tautomerization or other net intramolecular rearrangements. Studies carried out on 5-methoxyquinoline have concluded that a cluster of at least two solvent molecules is required to enable ESPT. 99,100 However, these investigations were

not able to assess steric restrictions posed by secondary and tertiary alcohols given the fact that 5-methoxyquinoline deprotonates only low-p K_a primary alcohols (e.g., halogenated ethanol).⁶⁵ To that end, we focus here on the steric properties of the solvent–solute complex, required for ESPT to occur, using the much stronger photobase **FR0**-SB as an example.

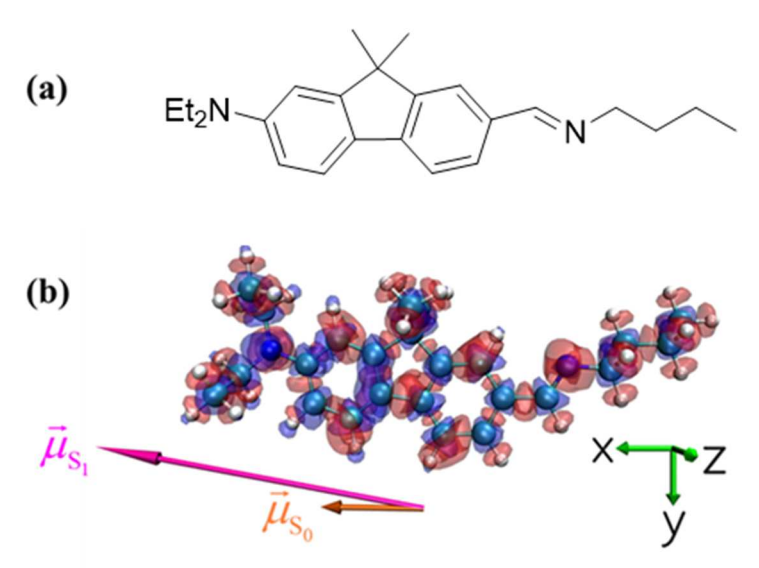


Figure 3.1. The FR0-SB molecule and how its electronic density changes upon excitation. (a) FR0-SB super photobase. (b) The structure of the isolated FR0-SB molecule in its ground electronic S_0 state, the dipole moments characterizing the S_0 (shorter orange vector) and electronically excited S_1 (longer magenta vector) states, and the S_1 – S_0 total electronic density difference, resulting from the CC/EOMCC calculations described in the main text. The red/blue color indicates an increase/decrease in the electron density upon the $S_0 \rightarrow S_1$ excitation.

In a recent report, we presented experimental evidence for the formation of a persistent interaction between solvent primary alcohols and **FR0**-SB* based on rotational diffusion dynamics measurements. The high-level *ab initio* calculations presented in that report, based on the coupled-cluster (CC) theory and its equation-of-motion (EOM) excited-state extension, indicated that this persistent interaction, which leads to ESPT, is a consequence of the *ca*. 3-fold increase in the static dipole moment of **FR0**-SB upon excitation from its ground electronic state (S₀) to its first-excited singlet state (S₁) (cf. Figure 3.1b). As shown in Figure 3.1b, where we plot the S₁ – S₀ total electron density difference, calculated using the CC/EOMCC one-electron reduced density matrices resulting from our earlier computations, the cause of this significant

increase in dipole moment upon photoexcitation is an overall intramolecular migration of a relatively small amount of electron density over a long distance, from the diethylamino nitrogen to the imine nitrogen.

Even though our earlier work demonstrated that the rate of formation of the complex between FR0-SB* and the solvent ROH was controlled by the concentration of –OH functional groups in the solvent for primary alcohols, the details of the excited Schiff base–alcohol complex formation was left unresolved. In particular, the steric effect arising from the structure of the alcohol and the details of the associated proton-transfer reaction pathways remained unclear. Among the factors that contribute to the proton transfer process is the highly associative nature of the solvent and the role that solvent molecular structure plays in the ability to engage in an ESPT reaction with the Schiff base.

The transfer of protons between excited chromophores and their surrounding media carries different spatial and reaction coordinate implications depending on the direction of proton transfer. Photoacids require a lesser extent of solvent organization than photobases to execute the proton transfer event. Photoexcitation of photoacids leads to the ejection of a proton from the chromophore into a highly associative bath where intermolecular proton exchange operates under an equilibrium condition. Photobases, on the other hand, require the alignment of the proton-donating solvent molecule with the excited Schiff base receptor, which is mediated by the solvent's associative network. Studies of hydroxyquinolines and azaindoles have explored the net isomerization processes in which one terminus of an excited chromophore becomes strongly basic and the other end becomes acidic, releasing a proton. In such systems, two or more alcohol molecules are needed in a hydrogen bonded "proton wire" to mediate the proton transfer process. 102–113 Much less common are photobases such as 5-methoxyquinoline or FR0-SB that

carry no labile protons. In these systems, the above-mentioned bridging is unnecessary; the key role of the hydroxylic solvent molecules or clusters is simply to serve as a source of protons in response to the enhanced basicity engendered by photoexcitation.

The purpose of this work is to provide insights into the effect of solvent steric factors on the ESPT process. The experimental data we report are time-resolved and steady-state fluorescence measurements of **FR0**-SB in primary, secondary, and tertiary alcohols, with an emphasis on the kinetics and equilibria of the ESPT reaction. We also report the details of the ESPT reaction pathways between **FR0**-SB and representative primary and secondary alcohols predicted by quantum chemistry calculations. Our data show that primary alcohols exhibit facile proton transfer to the excited chromophore **FR0**-SB*, with secondary alcohols being much less efficient and tertiary alcohols not exhibiting measurable proton transfer. These data demonstrate collectively the existence of an intermediate complex where **FR0**-SB* and alcohol solvent molecules share the alcohol proton and mediate the ESPT process.

3.2 Experimental and Theoretical Methods

3.2.1 Materials

The alcohols methanol, ethanol, propan-1-ol (*n*-propanol), propan-2-ol (*i*-propanol), butan-1-ol (*n*-butanol), pentan-1-ol (*n*-pentanol), cyclopentanol, 2-methylbutan-2-ol (*t*-amyl alcohol, TAA), hexan-1-ol (*n*-hexanol), heptan-1-ol (*n*-heptanol), and octan-1-ol (*n*-octanol) were obtained from Millipore-Sigma in their highest purity grade available and were used as received. Acetonitrile (ACN) was purchased from Millipore-Sigma in its highest purity grade and used as received. The compound **FR0**-SB was synthesized from **FR0** and *n*-butylamine as described previously.^{11,101}

3.2.2 Steady-State Absorbance and Emission Spectroscopy

UV-visible absorption spectra were recorded using a Shimadzu UV-2600 spectrometer. Spectral resolution was 1 nm for all measurements. The concentration of the samples was 2 μ M in all the solvents. The molar absorptivity of **FR0**-SB is $\varepsilon_{\text{max}} = 81500 \text{ M}^{-1}\text{cm}^{-1}$ (ca. 370 nm). Fluorescence spectra of **FR0**-SB dissolved in each solvent were recorded using a Hitachi FL-4500 fluorescence spectrometer with excitation at the absorption maximum in each solvent. Excitation and emission spectral resolution was 1 nm for all measurements. Temperature-dependent steady-state spectra of **FR0**-SB in n- and i-propanol were acquired using a Horiba Duetta spectrofluorometer with a Quantum Northwest temperature controller (QNW TC 1). Analysis of the spectra was performed using Microcal Origin 9.0 software.

3.2.3 Time-Resolved Fluorescence Measurements

The time-correlated single photon counting (TCSPC) instrument used in this work has been described elsewhere⁶⁶ in detail and we provide only a brief synopsis here. The pump laser is a passively mode-locked Nd:YVO₄ laser (Spectra-Physics Vanguard) that operates at 1064 nm

producing 13 ps pulses at 80 MHz repetition rate. The second harmonic (532 nm) and third harmonic (355 nm) outputs are 2.5 W average power with the same pulse width and repetition rate as the fundamental laser output. The 532 nm output of the Nd:YVO₄ laser excites synchronously a cavity-dumped dye laser (Coherent 701-3) operating at 700 nm (LDS 698 laser dye, Exciton). The output of the dye laser was frequency-doubled using a Type I LiIO₃ SHG crystal to produce 350 nm excitation pulses (ca. 5 ps pulses, 250 ns inter-pulse spacing) to excite the samples. Average power at the sample was less than 1 mW for all measurements. A portion of the dye laser fundamental output (700 nm) was sent to a reference photodiode (B&H). Sample fluorescence was collected using a 40× reflecting microscope objective (Ealing) and sent to a polarization-selective cube beamsplitter (Newport). Each polarized emission component was polarization-scrambled and sent through a subtractive double monochromator (CVI Digikrom CM112) equipped with a microchannel plate photomultiplier detector (MCP-PMT, Hamamatsu RG3809). The output of each MCP-PMT detector was input to one channel of a two-channel TCSPC system (B&H Simple Tau 152) with instrument control performed with a personal computer. Data were acquired and stored using a program written in-house using National Instruments LabVIEW® software. Temperature-dependent time-resolved data were recorded by TCSPC as described above, the only differences being that the excitation wavelength was 430 nm and that the temperature was controlled using a Thermo Fisher Scientific bath circulator connected to the cuvette-holder. For the temperature-dependent measurements, data were collected at every 10 K between 273 K and 323 K while the sample was stirred.

3.2.4 Computational Details

All of the geometry optimizations relied on the Kohn–Sham formulation⁶⁷ of density functional theory (DFT)⁶⁸ using, in the case of the structures along the excited-state proton transfer reaction

pathway, the time-dependent (TD)⁸⁴ extension of DFT to excited states combined with the SMD continuum solvation model, ¹¹⁴ to account for the bulk solvation effects (the analogous protocol employing SMD was used in the DFT ground-state optimizations). All of the calculations reported in this work employed the 6-31+G* basis set^{71–73} using spherical components of d functions and the CAM-B3LYP functional.⁸³ As explained in our previous work, ¹⁰¹ among the several benchmarked functionals, CAM-B3LYP provides the gas-phase vertical excitation energies of **FR0-**SB closest to those obtained in the high-level *ab initio* EOMCC calculations using the δ -CR-EOMCC(2,3) triples correction to EOMCCSD.⁷⁴ For example, the CAM-B3LYP/6-31+G* S₀ \rightarrow solvertical excitation energy of 3.92 eV is close to the 3.70 eV value obtained with δ -CR-EOMCC(2,3), which is, in turn, within 0.2 eV from the experimental excitation energy of 3.52 eV. In addition, the CAM-B3LYP functional provides the ground-state geometry of **FR0-**SB that is essentially identical to that obtained using the second-order Møller–Plesset perturbation theory, when the 6-31+G* basis set is employed.¹⁰¹

All of the electronic structure calculations reported in this study, including the DFT and TD-DFT geometry optimizations using the CAM-B3LYP functional and the accompanying single-point DFT and TD-DFT calculations employing the same functional and the SMD continuum solvation model, were performed using the GAMESS package. In the case of the optimized ground-state geometries, the $S_0 \rightarrow S_1$ vertical excitation energies, which, from the fundamental physics perspective, correspond to a very fast process resulting in an abrupt change in the solute electron density, were computed by taking advantage of the nonequilibrium solvation effects associated with the solvent relaxation delay, incorporating a fast component of the solvent dielectric constant in addition to its bulk value, 115 as implemented in GAMESS. All visualizations

of optimized molecular structures presented in this work were performed using the VMD software.⁸⁸

In what follows, we provide the SMD/CAM-B3LYP/6-31+G* optimized geometries, labeled A–L, obtained in this work, characterizing the interaction between **FR0**-SB and a cluster of three n-propanol molecules in a continuum solvation model of n-propanol. In particular, geometry A corresponds to the optimized structure of the [**FR0**-SB···HOR] complex in the ground electronic state (S₀), B corresponds to the optimized structure of the [**FR0**-SB*···HOR] reactant, *i.e.*, **FR0**-SB in its first-excited singlet state (S₁) hydrogen-bonded to a cluster of three n-propanol molecules, and L is the optimized geometry of the [**FR0**-HSB⁺*···-OR] product of the excited-state proton transfer reaction. The partially optimized geometries C–K are the structures along the minimum-energy pathway defining the proton exchange process in the S₁ state, obtained using the procedure outlined in the main text. For each of the A–L structures, we also provide the total electronic energies of the S₀ and S₁ states, denoted as E_{S_0} and E_{S_0} , respectively.

3.3 Results and Discussion

The ability of **FR0**-SB to abstract a proton from an alcohol can be evaluated using steady-state fluorescence spectroscopy. The absorption and fluorescence spectra of **FR0**-SB dissolved in a series of solvents are shown in Figure 3.2a and b. The absorption spectra are relatively independent of solvent. Fluorescence of **FR0**-SB exhibits two emission bands, one centered around 630 nm (~15870 cm⁻¹) and the other near 460 nm (~21740 cm⁻¹), which have been assigned to the protonated **FR0**-HSB^{+*} species and its non-protonated form **FR0**-SB*, respectively. The **FR0**-HSB^{+*} emission band appears as a result of ESPT.¹¹ Fluorescence spectra have been divided by the frequency cubed, according to the transition dipole representation, which makes fluorescence intensity proportional to the population of emitters according to the Einstein coefficient of spontaneous emission.¹¹⁶ In Figure 3.2a we have normalized the protonated emission intensities for all solvents allowing a facile comparison of the extent of ESPT for **FR0**-SB* as a function of solvent alcohol identity.

Shown in Figure 3.2b is the normalized absorption and fluorescence spectra of **FR0**-SB in primary, secondary, and tertiary alcohols. Included is acetonitrile, an aprotic solvent, which is not capable of undergoing ESPT and thus exhibits no **FR0**-HSB^{+*} emission. Fluorescence spectra are normalized to the most intense emission intensity to facilitate comparison of the extent of ESPT by **FR0**-SB* in the selected solvents. We find a substantial decrease in the probability of ESPT relative to the primary alcohols for secondary alcohols (*i*-propanol and cyclopentanol) and observe no ESPT emission in the case of the tertiary alcohol *t*-amyl alcohol (TAA).

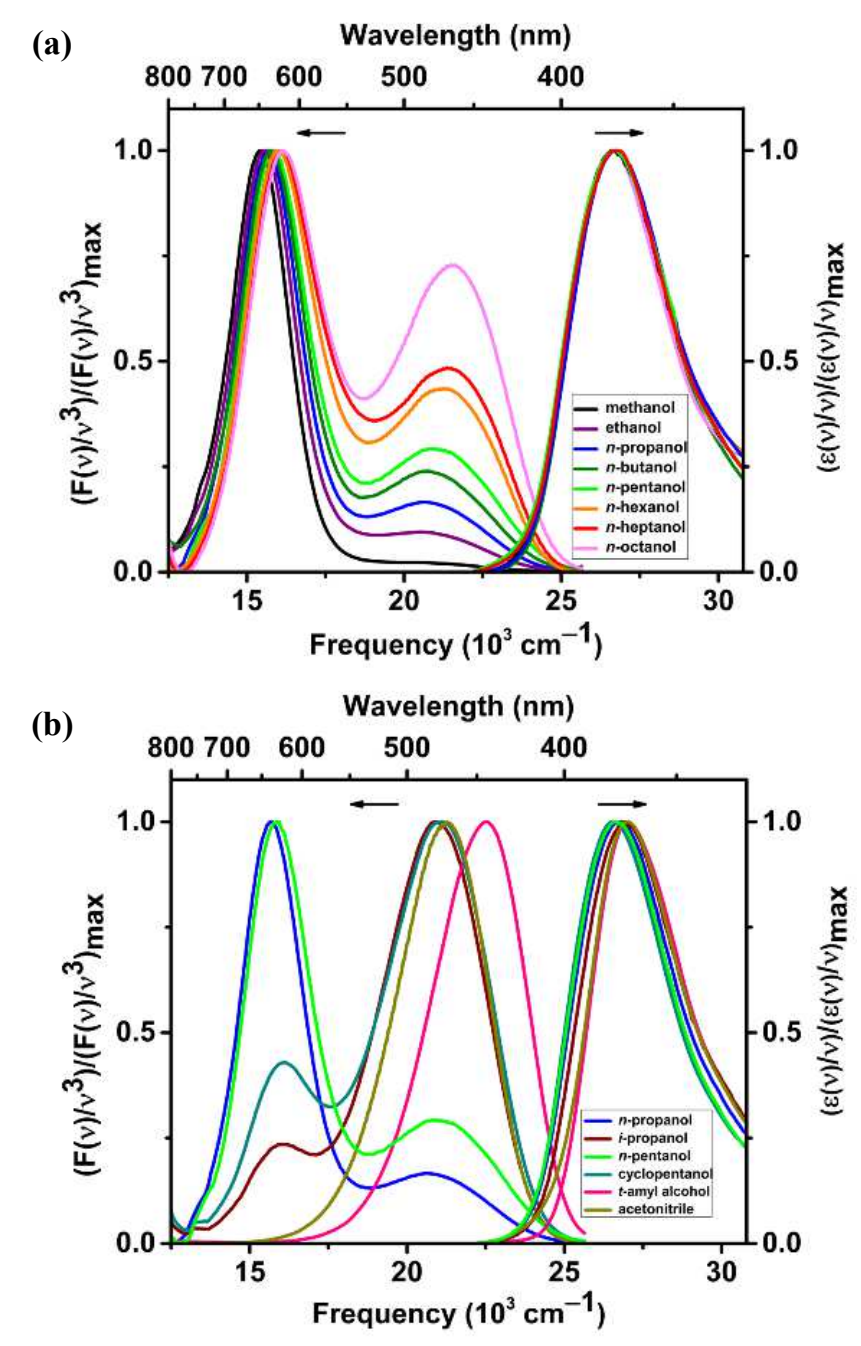


Figure 3.2. Steady-state absorption and fluorescence spectra of **FR0**-SB in alcohols. (a) The normalized absorption and emission spectra of **FR0**-SB in primary alcohols from methanol to *n*-octanol. (b) The absorption and emission spectra of **FR0**-SB in various solvents to compare steric hindrance. The long wavelength emission near 630 nm (~15,870 cm⁻¹) corresponds to **FR0**-HSB^{+*}, while the short wavelength emission near 460 nm (~21,740 cm⁻¹) corresponds to **FR0**-SB*.

The ratio of the areas of the two emission bands for a given solvent can be used to estimate the fraction of **FR0**-SB that undergoes ESPT, after correcting for the fluorescence quantum yields

 (Φ_{fl}) of the non-protonated and protonated species. 11 Fluorescence measurements were taken in acetonitrile and acidified acetonitrile to quantify the difference in $\Phi_{\rm fl}$ for FR0-SB* and FR0- HSB^{+*} . This comparison was repeated with acetone as the solvent to obtain the ratio of Φ_{fl} for the nonprotonated to protonated forms of FR0-SB in a different solvent system. The unprotonated species FR0-SB* exhibits a 1.5 times greater $\Phi_{\rm fl}$ than FR0-HSB^{+*}, in agreement with previous results.¹¹ However, here we use the transition-dipole representation to ensure emission is proportional to the number of emitters. 116 Table 3.1 summarizes the equilibrium constant and free energy of proton abstraction data as a function of solvent. For the primary alcohol solvents there is a monotonic decrease in FR0-HSB^{+*} fluorescence intensity with increasing solvent aliphatic chain length, which is directly proportional to solvent [-OH]. 101 Secondary alcohols exhibit a markedly reduced propensity for proton donation relative to that seen for primary alcohols, despite the fact that the pK_a values of primary and secondary alcohols, differing by structural isomerism, are similar (e.g., $pK_a = 16.1$ for *n*-propanol¹¹⁷ and 16.5 for *i*-propanol¹¹⁸). We note that cyclopentanol has a higher protonation probability than i-propanol despite the lower -OH concentration. The tertiary alcohol TAA appears to not participate in ESPT to within our ability to detect FR0-HSB^{+*}. Assuming that FR0-SB* and FR0-HSB^{+*} are in equilibrium, we can derive the free energy of the process.

$$\mathbf{FR0}\text{-SB*} + \mathrm{ROH} = \mathbf{FR0}\text{-HSB**} + \mathrm{RO}^{-}$$

$$\Delta G^{0} = -RT \ln K_{eq}$$
(3.1)

The free energy values derived from the steady-state data are included in Table 3.1.

Table 3.1 Analysis of the steady-state spectroscopy results. Relative -OH concentration for the different alcohols, K_{eq} obtained as the ratio between **FR0**-SB* and **FR0**-HSB^{+*}, and derived ΔG^0 values for proton abstraction from steady-state data.

Solvent ^a	[-OH] (M)	$K_{\mathrm{eq}} pprox rac{[\mathbf{FR0}\text{-HSB}^{+*}]}{[\mathbf{FR0}\text{-SB*}]}$	ΔG^0 (kJ/mol)
MeOH	24.7	35.6 ± 3.0	-8.7 ± 0.2
EtOH	17.0	7.6 ± 0.5	-4.9 ± 0.2
<i>n</i> -PrOH	13.4	3.5 ± 0.1	-3.1 ± 0.1
<i>n</i> -BuOH	10.9	2.5 ± 0.1	-2.2 ± 0.1
n-PeOH	9.2	2.0 ± 0.1	-1.7 ± 0.1
n-HxOH	8.0	1.6 ± 0.1	-1.1 ± 0.1
<i>n</i> -HpOH	7.0	1.4 ± 0.1	-0.9 ± 0.1
n-OcOH	6.4	1.1 ± 0.1	-0.2 ± 0.1
<i>i</i> -PrOH	13.1	0.2 ± 0.1	4.2 ± 0.1
$c ext{-PeOH}$	11.0	0.3 ± 0.1	2.6 ± 0.1
TAA	9.2		
ACN		-	<u> </u>

 $[\]overline{a}$ Abbreviations: MeOH = methanol, EtOH = ethanol, n-PrOH = n-propanol, n-BuOH = n-butanol, n-PeOH = n-pentanol, n-HxOH = n-hexanol, n-HpOH = n-heptanol, n-OcOH = n-octanol, i-PrOH = i-propanol, c-PeOH = cyclopentanol, TAA = t-amyl alcohol, ACN = acetonitrile.

In addition to the steady-state measurements, we also performed picosecond time-resolved fluorescence lifetime measurements for **FR0**-SB* and **FR0**-HSB^{+*} in the same solvents to relate the population relaxation dynamics of these species to the ESPT process. Figure 3.3a shows the emission decay of **FR0**-SB* for the series of linear alcohols, where a monotonic increase in fluorescence lifetime was observed with increasing solvent aliphatic chain length. Figure 3.3b shows the same emission decay data for **FR0**-SB* in selected primary, secondary, and tertiary alcohols. There is a significantly longer fluorescence lifetime for **FR0**-SB* decay in secondary and tertiary alcohols, suggesting less efficient proton abstraction from the alcohol in these media. For comparison, the decay of **FR0**-SB* in acetonitrile, which is incapable of participating in proton transfer, is also shown in Figure 3.3b. The trends observed in the primary alcohols can be understood in terms of the relative concentration of –OH in each solvent. ¹⁰¹ The time-resolved emission increase and subsequent decay for **FR0**-HSB^{+*} in the primary alcohols, methanol through *n*-octanol, is shown in Figure 3.4a. A monotonic increase in the time constants of both processes with increasing solvent aliphatic chain length is evident. The data in Figure 3.4b provide

a comparison of the time-resolved emission transients for **FR0**-HSB^{+*} for selected primary and secondary alcohols. Because the extent of ESPT for tertiary alcohols is beneath the detection limit, there are no data for **FR0**-HSB^{+*} in TAA.

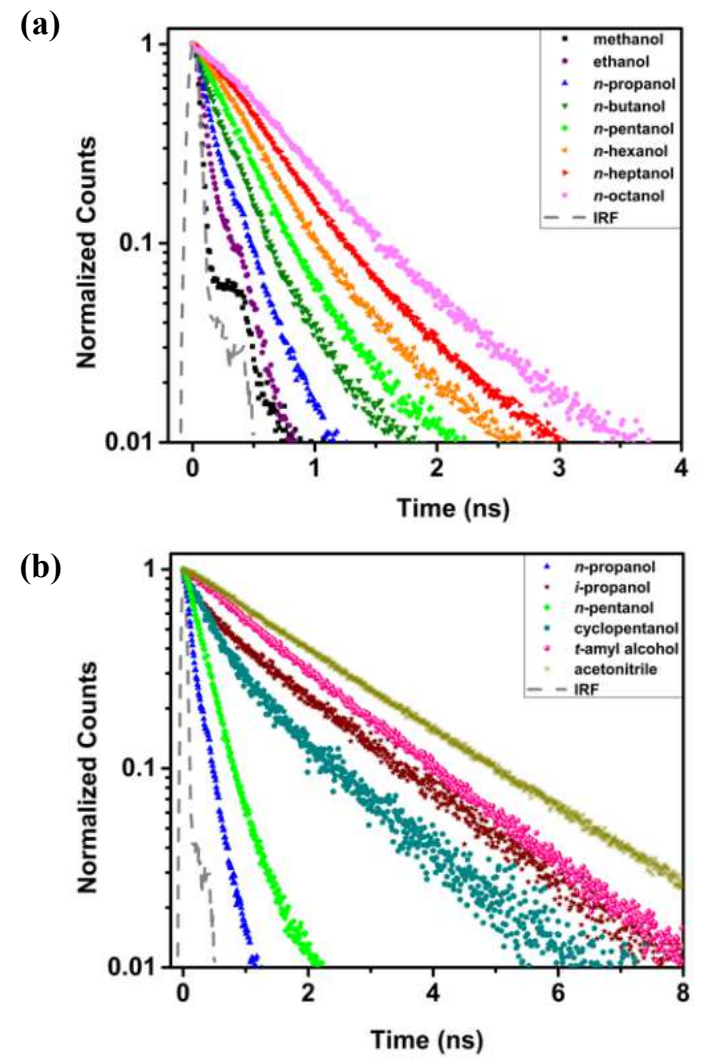


Figure 3.3. Steady-state absorption and fluorescence spectra of **FR0**-SB in alcohols. (a) The normalized absorption and emission spectra of **FR0**-SB in primary alcohols from methanol to *n*-octanol. (b) The absorption and emission spectra of **FR0**-SB in various solvents to compare steric hindrance. The long wavelength emission near 630 nm (~15,870 cm⁻¹) corresponds to **FR0**-HSB^{+*}, while the short wavelength emission near 460 nm (~21,740 cm⁻¹) corresponds to **FR0**-SB*.

The time constants for the processes discussed above are summarized in Table 3.2. As expected, linear alcohols exhibit a smooth trend. Secondary alcohols show significantly longer lifetimes, indicating lower probability for proton transfer. In the case of cyclopentanol, we observe

a faster **FR0**-SB* decay than for *i*-propanol, suggesting a slightly higher probability of proton transfer, in agreement with the steady-state emission spectroscopic data (Figure 3.2b). It is important to note that cyclopentanol shows a slower rise of **FR0**-HSB^{+*} emission as compared to *i*-propanol. This finding is currently under investigation and may provide insight into the details of the reaction coordinate for proton transfer in secondary alcohols.

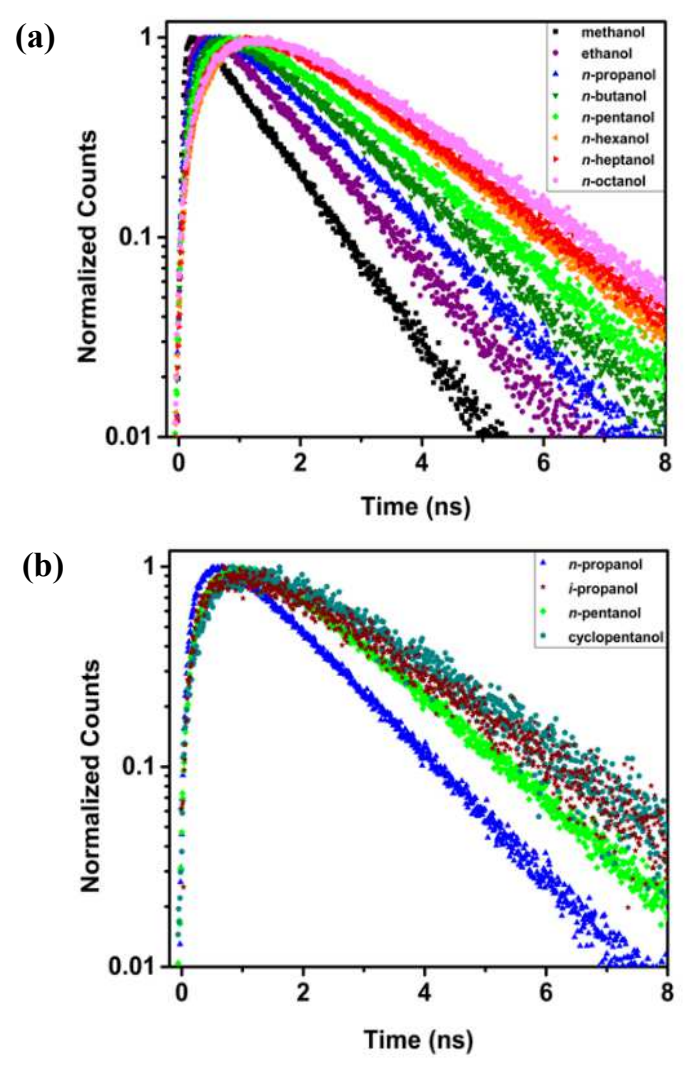


Figure 3.4. The fluorescence decay responses plotted on a \log_{10} scale of **FR0**-HSB^{+*} detected at 630 nm in (a) primary alcohols and (b) selected primary and secondary alcohols. The fitting function used was $f(t) = b_1 \exp(-t/\tau_{\rm HSB}) - b_2 \exp(-t/\tau_{\rm X})$. For the time constants reported in Table 3.2, the IRF has been deconvoluted using a convolute-and-compare method.

Table 3.2 Fluorescence lifetimes obtained from time-correlated single photon counting experiments. The time constants are as defined in Figure 5. Uncertainties are $\pm \sigma$. The χ^2 values across all fits were below 0.47.

Solvent ^a	a_1	$\tau_{\mathrm{SB1}} \left(\mathrm{ps} \right)$	a_2	$ au_{\mathrm{SB2}}\left(\mathrm{ps}\right)$	$\overline{\tau}_{SB}^{b}$ (ps)	$\tau_{\rm X} ({\rm ps})$	$\tau_{\rm HSB}$ (ps)
MeOH	0.99	18 ± 8	0.01	478 ± 185	23 ± 9	42 ± 4	1050 ± 10
EtOH	0.93	57 ± 6	0.07	232 ± 26	68 ± 15	150 ± 5	1280 ± 10
<i>n</i> -PrOH	0.92	104 ± 15	0.08	463 ± 38	134 ± 22	244 ± 4	1470 ± 10
<i>i</i> -PrOH	0.70	110 ± 16	0.30	1760 ± 20	612 ± 13	375 ± 24	2290 ± 50
<i>n</i> -BuOH	0.86	147 ± 5	0.14	504 ± 23	198 ± 13	391 ± 5	1610 ± 30
n-PeOH	0.90	272 ± 35	0.10	1040 ± 80	347 ± 53	589 ± 8	1630 ± 20
$c ext{-PeOH}$	0.74	231 ± 6	0.26	1580 ± 30	582 ± 17	630 ± 32	2200 ± 10
n-HxOH	0.94	336 ± 51	0.06	1420 ± 240	401 ± 141	755 ± 13	1640 ± 30
<i>n</i> -HpOH	0.97	470 ± 8	0.03	1690 ± 120	502 ± 137	749 ± 7	1800 ± 10
n-OcOH	0.95	536 ± 8	0.05	1850 ± 90	602 ± 50	846 ± 18	1870 ± 20

^a Abbreviations: MeOH = methanol, EtOH = ethanol, n-PrOH = n-propanol, i-PrOH = i-propanol, n-BuOH = n-butanol, n-PeOH = n-pentanol, c-PeOH = cyclopentanol, n-HxOH = n-hexanol, n-HpOH = n-heptanol, n-OcOH = n-octanol. ${}^{b}\bar{\tau}_{SB} = a_{1}\tau_{SB1} + a_{2}\tau_{SB2}$.

Our analysis of the time-resolved data is based on a kinetic scheme used in our previous work involving linear alcohols, ¹⁰¹ modified slightly and schematized in Figure 3.5. The excitation function, $\delta(t)$, is a ca. 5 ps for the 350 nm laser pulse, which produces the electronically excited FR0-SB* molecule. The photoexcited chromophore, FR0-SB*, relaxes either radiatively back to **FR0-SB** (τ_{SB2} , $\lambda_{\text{em}} \approx 460 \text{ nm}$) or non-radiatively, along a reaction coordinate on the excited-state potential energy surface, producing an intermediate complex [FR0-SB*...H-OR] in the early stages of the ESPT process. This complex undergoes a transformation that results in proton abstraction from the alcohol and formation of the **FR0**-HSB^{+*} and $^-$ OR products (τ_X). Emission from the protonated FR0-HSB^{+*} species near 630 nm competes with deprotonation (τ_{HSB}).

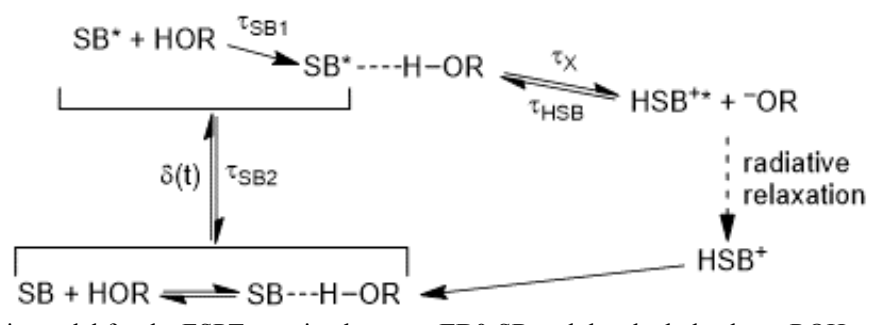


Figure 3.5. Kinetic model for the ESPT reaction between **FR0**-SB and the alcohol solvent ROH.

Considering τ_X and τ_{HSB} as lifetimes that reflect the protonation and deprotonation processes in the equilibrium between the intermediate complex [FR0-SB*···H–OR] and FR0-HSB**, then the ratio of the time constants τ_X/τ_{HSB} (Figure 3.6a) can be compared to the free energy values (Table 3.1) derived from the steady-state band intensity ratio (Figure 3.6b). The correspondence between steady-state and time-resolved measurements provides confidence in assigning an equilibrium between the intermediate and the protonated species. However, the free energy for the process cannot be derived from the latter equilibrium given the existence of the intermediate. The large deviation observed for the secondary alcohols in Figure 3.6a does not translate into a difference in the time domain data in Figure 3.6b. We consider this as an indication that formation of the transient solvent organization required for proton transfer is more challenging on structural grounds for secondary alcohols than it is for the primary ones.

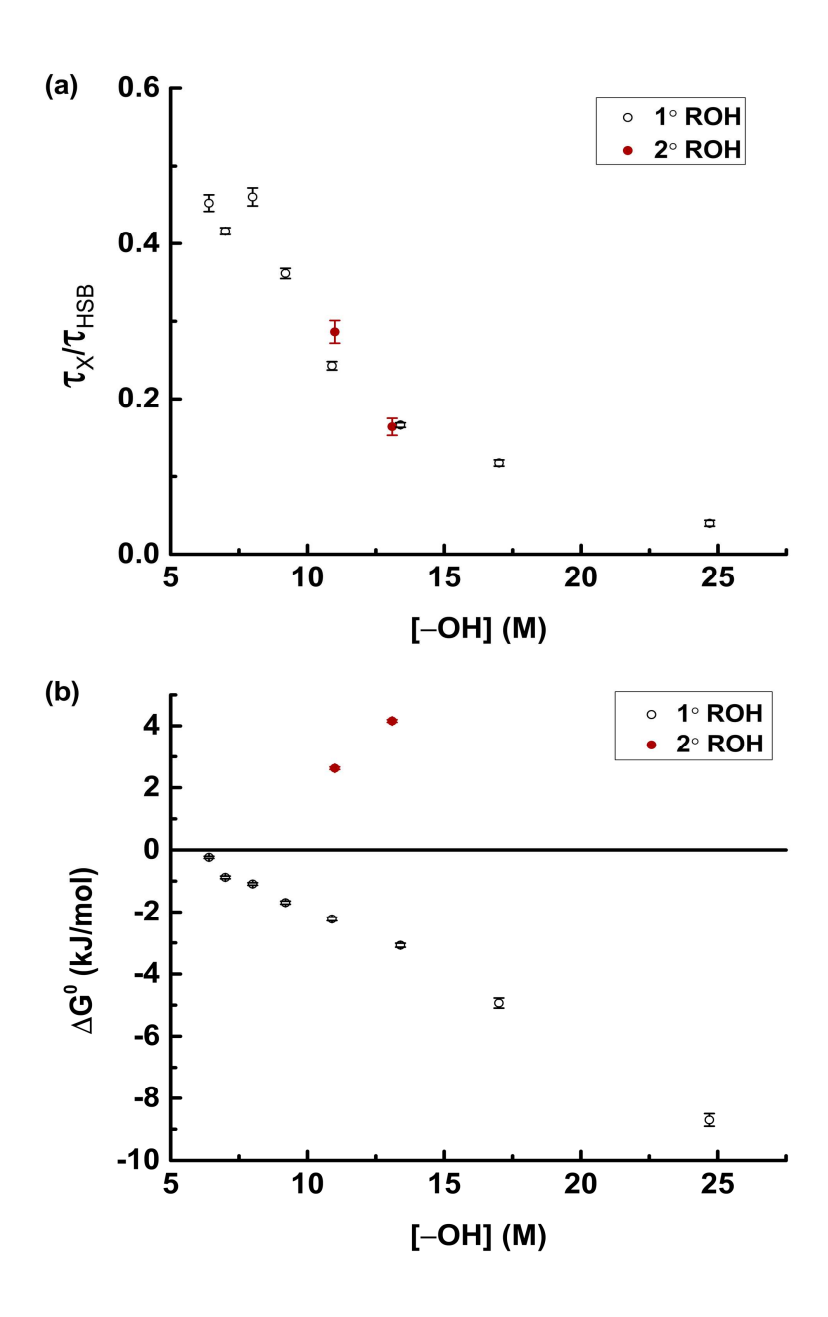


Figure 3.6. Trends in dynamics and free energy as a function of relative [-OH]. (a) The ratio of the time constants τ_X and τ_{HSB} is plotted as a function of relative [-OH]. (b) ΔG^0 for proton abstraction obtained from the ratio of **FR0**-SB* to **FR0**-HSB^{+*} emission as a function of relative [-OH]. We note good agreement between the time-resolved and the steady-state data for the linear alcohols.

The data plotted in Figure 3.6b make it clear that secondary alcohols deviate drastically from the linear trend observed for primary alcohols as a function of [–OH], underscoring the important role of solvent molecular structure in the proton abstraction reaction. We postulate that for secondary alcohols the initial formation of an excited Schiff base–solvent complex may be an

activated process, which is a testable hypothesis. The extent of proton abstraction in *n*- and *i*-propanol as a function of temperature was measured, following excitation at 430 nm, in order to minimize the excess energy in the excited state; these measurements were corrected by the independently measured change in fluorescence quantum yield as a function of temperature. The results from these measurements are shown in Figure 3.7a with the equilibrium constants and the free energy of protonation values listed in Table 3.3. We observe no significant temperature dependence for *n*-propanol, but do observe a decrease in proton abstraction in *i*-propanol with increasing temperature. Table 3.4 and Figure 3.7b show the lifetimes of FR0-SB* as a function of temperature for the *n*- and *i*-propanol. These data suggest that conversion of FR0-SB* to FR0-HSB+* along the reaction coordinate resulting in the deprotonation of *n*-propanol is a process characterized by a low-energy barrier, which is lower than the analogous process with *i*-propanol. No discernable temperature-dependent changes were observed in the absorption spectra for FR0-SB in these two solvents (not shown), consistent with the protonation occurring exclusively in the excited electronic state.

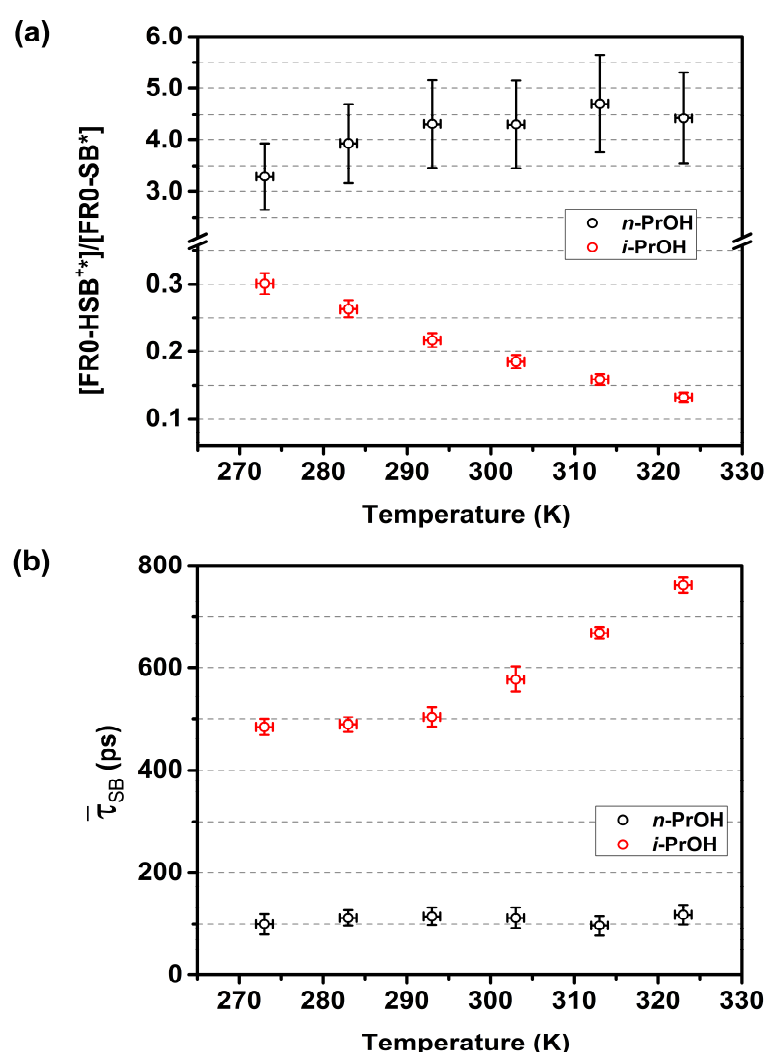


Figure 3.7. Temperature-dependent proton transfer data for n- and i-propanol. (a) Concentration ratio of the protonated and unprotonated **FR0**-SB* following photoexcitation obtained from steady-state spectra. (b) Temperature-dependent $\bar{\tau}_{SB}$ for **FR0**-SB* obtained from time-resolved measurements. From these steady-state band ratio data, we can determine the temperature-dependent equilibrium constant for protonation/deprotonation of **FR0**-SB*.

While explicit thermodynamic information is not extracted from the above data, given the existence of an intermediate, it is clear that the negative slope of the temperature dependence shown in Figure 3.7a implies a distinctly negative entropy term for ESPT in the case of the secondary alcohol, with entropic factors being less significant for the primary ones. This finding is consistent with the proton transfer reaction coordinate depending on a solvent configuration that is more difficult to access on steric grounds for the secondary alcohol than for the primary alcohol.

It is important to note that τ_X is longer than τ_{SB1} for both primary and secondary alcohols, implying the existence of an intermediate state between **FR0-SB*** and **FR0-HSB****, originally postulated by Lahiri et al.¹⁰¹ and consistent with the scheme shown in Figure 3.5.

Table 3.3 Temperature-dependent steady-state data in *n*-propanol (*n*-PrOH) and *i*-propanol (*i*-PrOH).

Solvent	T (K)	$K_{\rm eq} pprox rac{[{ m FR0\text{-}HSB}^{+*}]}{[{ m FR0\text{-}SB*}]}$	$\Delta G^0 ext{ (kJ/mol)}$
	273 ± 1	3.3 ± 0.6	-2.7 ± 0.4
	283 ± 1	3.9 ± 0.8	-3.2 ± 0.5
n-PrOH	293 ± 1	4.3 ± 0.9	-3.6 ± 0.5
n-PIOH	303 ± 1	4.3 ± 0.8	-3.7 ± 0.5
	313 ± 1	4.7 ± 0.9	-4.0 ± 0.5
	323 ± 1	4.4 ± 0.9	-4.0 ± 0.5
	273 ± 1	0.25 ± 0.01	3.1 ± 0.1
	283 ± 1	0.22 ± 0.01	3.5 ± 0.1
<i>i</i> -PrOH	293 ± 1	0.18 ± 0.01	4.2 ± 0.1
l-PIOH	303 ± 1	0.15 ± 0.01	4.7 ± 0.1
	313 ± 1	0.13 ± 0.01	5.2 ± 0.1
	323 ± 1	0.11 ± 0.01	5.9 ± 0.1

Table 3.4 Temperature-dependent fluorescence lifetimes in *n*-propanol (*n*-PrOH) and *i*-propanol (*i*-PrOH) obtained from time-correlated single photon counting experiments. Uncertainties are $\pm \sigma$. The χ^2 values across all fits were below 0.4.

Solvent	T (K)	a_1	τ_{SB1} (ps)	a_2	$\tau_{\mathrm{SB2}}\left(\mathrm{ps}\right)$	$\overline{\tau}_{SB}^{a}(ps)$	τ_{X} (ps)	τ _{HSB} (ps)
D OH	273 ± 1	0.94	80 ± 10	0.06	420 ± 30	100 ± 20	220 ± 10	2560 ± 20
	283 ± 1	0.93	90 ± 10	0.07	450 ± 20	112 ± 15	210 ± 10	2360 ± 20
	293 ± 1	0.91	86 ± 8	0.09	392 ± 28	115 ± 17	181 ± 4	2250 ± 20
<i>n</i> -PrOH	303 ± 1	0.95	86 ± 9	0.05	562 ± 34	112 ± 20	160 ± 5	2230 ± 30
	313 ± 1	0.94	67 ± 5	0.06	582 ± 33	97 ± 19	133 ± 3	2400 ± 20
	323 ± 1	0.96	82 ± 6	0.04	894 ± 26	118 ± 19	110 ± 6	2380 ± 10
i-PrOH	273 ± 1	0.75	116 ± 5	0.25	1590 ± 20	485 ± 15	258 ± 6	3050 ± 20
	283 ± 1	0.75	111 ± 11	0.25	1640 ± 20	490 ± 14	233 ± 8	3070 ± 30
	293 ± 1	0.75	102 ± 6	0.25	1710 ± 30	504 ± 18	199 ± 11	3070 ± 30
	303 ± 1	0.72	95 ± 13	0.28	1820 ± 30	578 ± 24	160 ± 5	2970 ± 10
	313 ± 1	0.68	101 ± 8	0.32	1860 ± 10	669 ± 11	127 ± 6	3090 ± 20
	323 ± 1	0.63	101 ± 11	0.37	1890 ± 20	762 ± 16	106 ± 9	2940 ± 30

 $[\]overline{\overline{\tau_{SB}}} = a_1 \tau_{SB1} + a_2 \tau_{SB2}.$

The issue that is central to understanding the light-induced proton abstraction reactions examined in this work is whether or not there is a resolvable intermediate [FR0-SB*···H-OR] complex along the reaction coordinate that undergoes the ESPT leading to the formation of the

[FR0-HSB^{+*}····OR] product. To address this issue and to provide deeper insights into the role of steric effects in the proton transfer reactions between the excited FR0-SB* chromophore and alcohol solvent molecules, we augmented the experimental effort by performing electronic structure calculations focusing on the ground, S_0 , and first excited singlet, S_1 , electronic states of the solvated FR0-SB system. In the calculations reported in this work, we focused on the reactions of FR0-SB* with n- and i-propanol. The n- and i-propanol molecules are the smallest alcohol species in the primary and secondary categories considered in our experiments that permit structural isomerism.

In modeling the ESPT process, we considered the interaction between **FR0**-SB* and a cluster of three alcohol molecules, which, according to our computations, is the minimum number of explicit solvent molecules necessary for the proton transfer to occur. In trying to use complexes consisting of **FR0**-SB* bound to fewer alcohol molecules, our calculations could not detect the presence of the second minimum corresponding to ESPT. The remaining, i.e., bulk, solvation effects were incorporated using the universal continuum solvation model based on solute electron density (SMD).¹¹⁴ For the details of our electronic structure computations, which were based on density functional theory and its time-dependent extension to excited states.

In constructing the reaction pathways characterizing the proton transfer between **FR0**-SB* and *n*- and *i*-propanol, the following protocol was adopted. For each of the two alcohols, the geometries of the electronically excited reactant and product complexes were optimized. The reactant complex is the **FR0**-SB* chromophore hydrogen-bonded to the cluster of three solvent molecules, i.e., the [**FR0**-SB*···HOR] species with two ROH molecules attached to the alcohol bonded to **FR0**-SB*. The product of the proton transfer reaction is the [**FR0**-HSB^{+*}····OR] complex with two ROH molecules attached to it. Having established the internuclear distances

between the proton being transferred and the imine nitrogen of **FR0**-SB* in the reactant and the product complexes, designated in Figure 3.8 as r_1 and r_2 , respectively, we probed the [**FR0**-SB*···HOR] \rightarrow [**FR0**-HSB⁺*···-OR] reaction pathway by introducing an equidistant grid of N–H separations using the step size defined as $(r_1 - r_2)/10$. The molecular structure at each point along the above ESPT reaction pathway was obtained by freezing the N–H distance at the respective grid value and reoptimizing the remaining geometrical parameters. We also optimized the geometry of **FR0**-SB hydrogen-bonded to the cluster of three alcohol molecules in the ground electronic state, needed to calculate the S₀ – S₁ vertical excitation energy.

Figure 3.8. Schematic representation of the r_1 and r_2 N–H internuclear distances needed to create the grid defining the ESPT reaction pathway.

The results of our quantum chemistry computations, shown in Figure 3.9–3.11, reveal the intricacies of the excited-state proton abstraction process initiated by the formation of the [FR0-SB*···H–OR] complex. In Figure 3.9, we present the calculated minimum-energy pathways characterizing the ESPT reactions involving FR0-SB in its first-excited singlet S₁ state and the *n*-and *i*-propanol molecules along the internuclear distance between the imine nitrogen of FR0-SB and the proton being transferred. For completeness, the energetics characterizing the corresponding S₀ ground states as well as the S₀ and S₁ energies obtained at the optimized ground-state structures of the relevant [FR0-SB···H–OR] complexes are also provided (the leftmost points in Figure 3.9). As shown in Figure 3.9, the ground-state energy monotonically increases as the alcohol proton approaches the imine nitrogen of FR0-SB, indicating that the proton abstraction occurs in the excited state of FR0-SB, not in the ground state, in agreement with the experimental

observations. As elaborated on above, in the experiments reported in this work, the excited state of **FR0**-SB is populated by photoabsorption from the ground electronic state. Our calculated $S_0 \rightarrow$ S_1 excitation energies of FR0-SB in n- and i-propanol of ~3.6 eV agree quite well with their corresponding experimental values of ~3.3 eV (see Figure 3.2b and 3.9–3.11). Upon relaxing the excited-state geometries (see the dashed lines in Figure 3.9), the difference in the behavior of the bulkier i-propanol species in the [FR0-SB*...H-OR] complex relative to its n-propanol counterpart becomes apparent already in the early stages of the deprotonation process. In particular, the internuclear distance between the imine nitrogen of FR0-SB and the alcohol proton that is hydrogen-bonded to it is ~ 0.1 Å larger in *i*-propanol than in *n*-propanol (cf. Figure 3.9– 3.11). Furthermore, Figure 3.9 reveals that even though the ESPT process takes place in both nand i-propanol, the barrier height characterizing the reaction involving the secondary alcohol ipropanol species is ~50% higher than the analogous barrier associated with its primary alcohol npropanol counterpart, consistent with the larger distance between the proton being transferred and the oxygen of the alcohol in *i*-propanol relative to that in *n*-propanol in the corresponding transition states (see Figure 3.10 and 3.11). At the same time, the barrier for the reverse process, i.e., deprotonation of FR0-HSB^{+*}, in *i*-propanol is about 35% lower than that characterizing the analogous process in *n*-propanol.

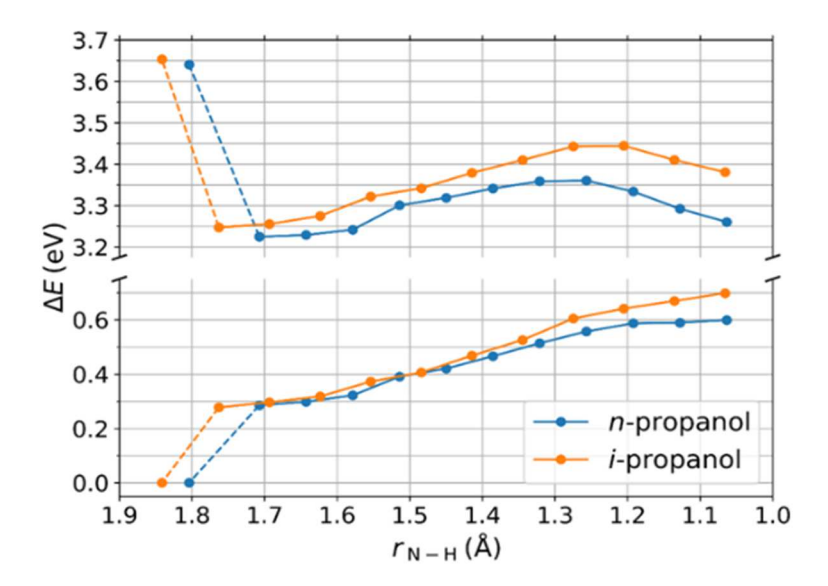


Figure 3.9. Results from the reaction pathway calculations showing ground- and excited-state energy differences as a function of proton abstraction. The SMD/CAM-B3LYP/6-31+G* ground-state (S_0) and excited-state (S_1) reaction pathways corresponding to the proton abstraction from *n*-propanol (blue) and *i*-propanol (orange) by **FR0**-SB along the internuclear distance between the imine nitrogen and the alcohol proton being transferred. The energies ΔE are shown relative to the ground-state minimum of the respective pathways. The dashed line in each pathway indicates the excited-state geometry relaxation following the $S_0 \rightarrow S_1$ excitation of **FR0**-SB.

At first glance, the observed decrease in ESPT as a function of increasing temperature seems to contradict the need to overcome a higher-energy barrier, but there is no contradiction here. Indeed, as the thermal energy of the system is increased, the individual solvent molecules spend less and less time oriented along the reaction coordinate, resulting in a decrease in the efficiency of proton transfer. This explanation implies that in order for the ESPT to occur, the intermediate [FR0-SB*···HOR] complex involving the alcohol molecule, with the additional alcohol molecules around it, must achieve spatial proximity and alignment of the alcohol's –OH group with the FR0-SB* imine lone pair, shown in Figure 3.10 and 3.11. These steric requirements for the formation of the intermediate [FR0-SB*···HOR] complex result in a large negative entropy component. Our analysis of the temperature-dependent data corroborates the large negative entropy associated with *i*-propanol.

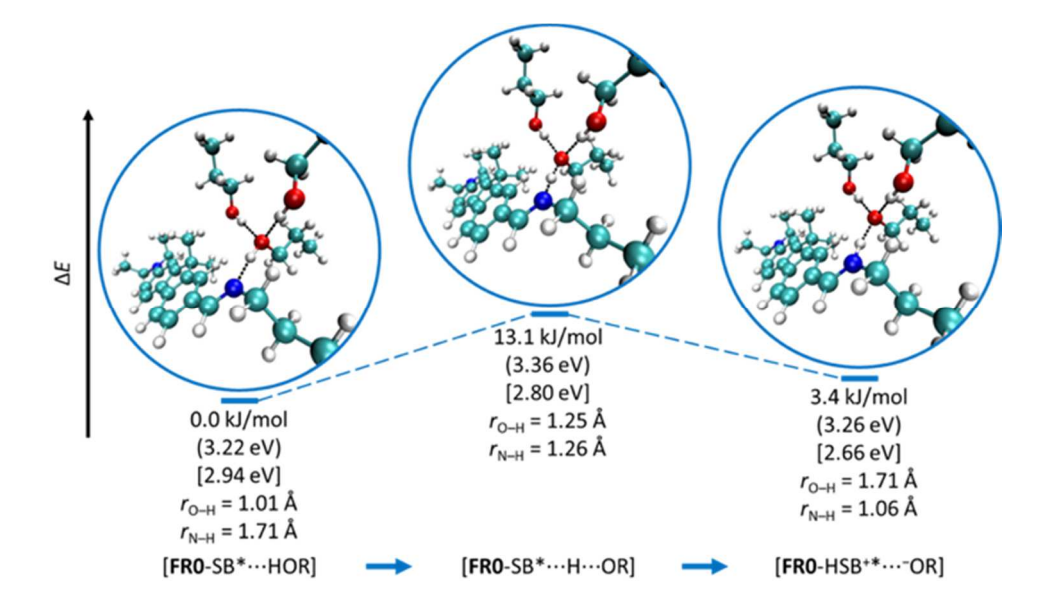


Figure 3.10. Snapshots of the proton abstraction process from n-propanol. The SMD/CAM-B3LYP/6-31+G* optimized geometries of the [**FR0**-SB*···HOR] reactant, [**FR0**-SB*···H···OR] transition state, and [**FR0**-HSB⁺*···-OR] product of the ESPT process between **FR0**-SB in its S₁ electronic state and three n-propanol molecules. The ΔE values in kJ/mol are given relative to the reactant energy. The energies inside parentheses, in eV, are given relative to the [**FR0**-SB···HOR] minimum in the ground electronic state S₀, while those inside square brackets correspond to the S₀-S₁ vertical transitions at each respective geometry. The $r_{\text{O-H}}$ and $r_{\text{N-H}}$ distances at each geometry represent the internuclear separations between the proton being transferred and the oxygen of n-propanol and the imine nitrogen of **FR0**-SB, respectively.

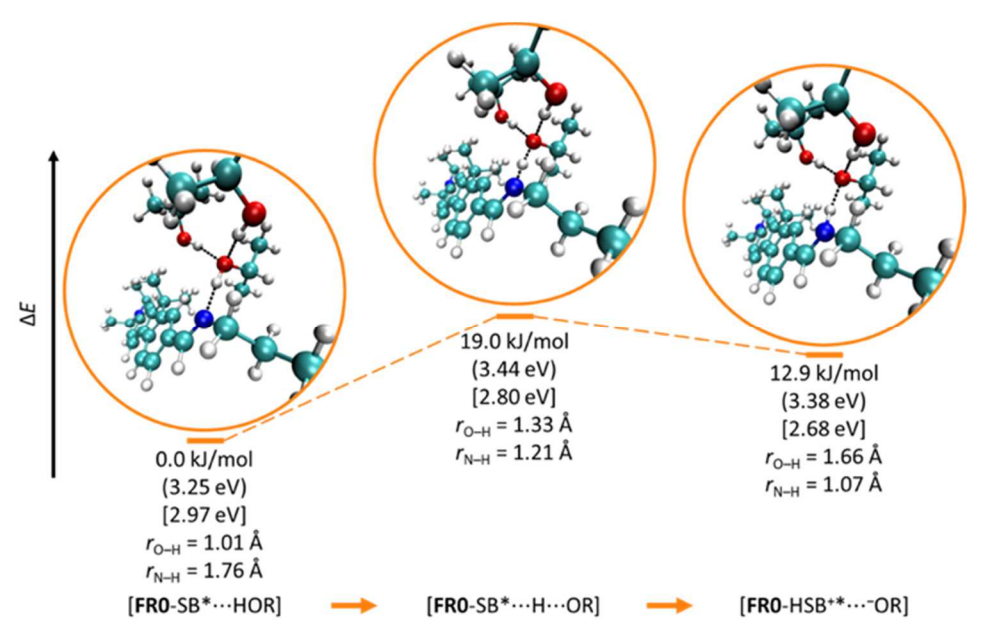


Figure 3.11. Snapshots of the proton abstraction process from *i*-propanol. The SMD/CAM-B3LYP/6-31+G* optimized geometries of the [**FR0**-SB*···HOR] reactant, [**FR0**-SB*···H···OR] transition state, and [**FR0**-HSB⁺*···⁻OR] product of the ESPT process between **FR0**-SB in its S₁ electronic state and three *i*-propanol molecules. The ΔE values in kJ/mol are given relative to the reactant energy. The energies inside parentheses, in eV, are given relative to the [**FR0**-SB···HOR] minimum in the ground electronic state S₀, while those inside square brackets correspond to the S₀–S₁ vertical transitions at each respective geometry. The $r_{\text{O-H}}$ and $r_{\text{N-H}}$ distances at each geometry represent the internuclear separations between the proton being transferred and the oxygen of *i*-propanol and the imine nitrogen of **FR0**-SB, respectively.

The reluctance of **FR0**-SB* to abstract protons from branched (secondary) alcohols, such as i-propanol, despite the similarity of its bulk properties (e.g., dielectric constant, viscosity, pK_a) to n-propanol, appears to be a consequence of steric factors that may significantly affect the initial formation of the [**FR0**-SB*···HOR] complex. The higher degree of solvent organization required to accomplish ESPT in i-propanol, as observed in Figure 3.11, results in a negative entropy contribution that leads to the reduced proton transfer yield, as reflected in the temperature-dependent weighted protonation time data in i-propanol (Figure 3.7 and Table 3.4). The inability of **FR0**-SB* to form a complex with TAA is consistent with a steric explanation of our findings. ESPT requires proximity of the hydroxyl group to the imine group of the photobase.

Our calculations summarized in Figures 3.10 and 3.11 imply that there is a need for a complex with two hydrogen bonds to the –OH group of the alcohol that transfers the proton. This "branched" arrangement is unusual; X-ray diffraction structures of the n-alkanols ethanol and butanol, congeners of n-propanol, show only linear structures of –OH moieties, in which each oxygen accepts only one hydrogen bond. However, the "structure" of n-propanol in the liquid phase has been studied and consists of chains of various lengths with modest amounts (a few percent) of branching. For i-propanol, which has a stronger preference for cyclic clusters, such configurations are unlikely and again, are not observed in the crystal structure of the pure solvent.

Indeed, for both *n*- and *i*-propanol, our computations predict the linear alcohol clusters to be about 8–12 kJ/mol lower in energy compared to the branched arrangements, not only for the ground-state [**FR0**-SB···HOR] species, but also in the case of the [**FR0**-SB*···HOR] ESPT reactant. Nevertheless, the situation changes dramatically, in favor of the branched alcohol conformations, when one considers the [**FR0**-HSB^{+*}···-OR] product of the ESPT reaction. In the

case of *n*-propanol, for example, the branched [FR0-HSB $^{+*}$ ····OR] structure is lower in energy than the linear one by about 2 kJ/mol. This is related to the fact that the branched alcohol arrangement solvates the RO species more effectively. Consequently, the $E_{product} - E_{reactant}$ energy difference in the case of the linear *n*-propanol configuration, of 14.3 kJ/mol, is higher than the 13.1 kJ/mol activation barrier characterizing the branched conformation (see Figure 3.10), implying that the activation energy characterizing the linear arrangement is even larger. The difference between the branched and linear conformations is pronounced even more when one considers ipropanol. In this case, the $E_{product} - E_{reactant}$ energy difference in the linear cluster is about 8 kJ/mol higher than the activation barrier characterizing the branched arrangement (cf. Figure 3.11). Based on our calculations we can conclude that the branched structures adopted in modeling of the ESPT reactions, while unusual in the case of the pure solvents, are a more realistic representation of the $[FR0-SB^*\cdots HOR] \rightarrow [FR0-HSB^{+*}\cdots OR]$ process, since they lead to smaller activation energies compared to the linear arrangements of alcohol molecules bound to FR0-SB*. Last, but not least, the difficulty in achieving the configurations shown in Figure 3.11 is consistent with the greatly diminished protonation yield observed for i-propanol and the lack of protonation observed for tertiary alcohols.

3.4 Conclusion

We have reported on the ESPT dynamics in the reactions of the super photobase FR0-SB with a wide variety of alcohol solvents. Steady-state and time-resolved fluorescence spectroscopy data from a series of primary, secondary, and tertiary alcohols, combined with carefully calibrated quantum chemistry calculations, demonstrate that the efficiency of solvent proton abstraction by the electronically excited FR0-SB* species depends on the alcohol structure. Our results for FR0-SB, a photobase lacking labile protons, are in contrast with those obtained for azaindole and quinoline photobases, where the distance between a labile proton in the molecule and the protonation site is at most three bond-lengths away. While for primary alcohols the efficiency of proton abstraction by FR0-SB* displays a simple -OH concentration-dependence, the efficiency of proton abstraction from secondary alcohols is largely determined by steric factors preventing the formation of reactive solvent configurations, in agreement with the barrier heights resulting from quantum chemistry calculations. Proton transfer from solvent to FR0-SB* is not detectable in the tertiary t-amyl alcohol, which strengthens the validity of our analysis emphasizing the significance of steric factors further. Our experimental and theoretical results show that a prerequisite for proton transfer is the formation of an intermediate [FR0-SB*...HOR] complex. They also suggest that in order for the ESPT to occur, the [FR0-SB*···HOR] complex must achieve spatial proximity between the FR0-SB* and HOR fragments and alignment of the alcohol's -OH group with the FR0-SB* imine lone pair, stabilized by solvation effects.

Chapter 4 Isoenergetic Two-Photon Excitation Enhances Solvent-to-Solute Excited-State Proton Transfer

Two-photon excitation is an attractive means for controlling chemistry in both space and time. Isoenergetic one- and two-photon excitations (OPE and TPE) in non-centrosymmetric molecules are often assumed to reach the same excited state and, hence, to produce similar excited-state reactivity. We compare the solvent-to-solute excited-state proton transfer of the super photobase FR0-SB following isoenergetic OPE and TPE. We find up to 62% increased reactivity following TPE compared to OPE. From steady-state spectroscopy, we rule out the involvement of different excited states and find that OPE and TPE spectra are identical in non-polar solvents but not in polar ones. We propose that differences in the matrix elements that contribute to the two-photon absorption cross sections lead to the observed enhanced isoenergetic reactivity, consistent with the predictions of our high-level coupled-cluster-based computational protocol. We find that polar solvent configurations favor greater dipole moment change between ground and excited states, which enters the probability for two-photon excitations as the absolute value squared. This, in turn, causes a difference in the Franck-Condon region reached via TPE compared to OPE. We conclude that a new method has been found for controlling chemical reactivity via the matrix elements that affect two-photon cross sections, which may be of great utility for spatial and temporal precision chemistry.

This chapter has been reproduced from (*J. Chem. Phys.* **2020**, *153*, 224301), with the permission of AIP Publishing.

4.1 Introduction and Background

Two-photon excitation²⁴ (TPE) is an attractive means of chemical activation because it allows one to control chemical processes in space and time with resolution limited only by the laser pulse used, typically sub-micron spatial resolution and sub-picosecond temporal resolution. The high spatial resolution achieved via TPE led to the development of multi-photon microscopy, which is capable of providing sub-micron resolution through scattering biological tissues. ^{31,32,125–128} These advantages are particularly important when imaging strongly absorbing samples, such as blood, or highly sensitive tissues, *e.g.*, the retina. ^{129,130} Similarly, TPE has been adopted as a valuable method for sub-micron photolithography. ^{131–135} As part of an effort to develop the tools required for precision chemistry, where chemical reactions can be activated and deactivated with high temporal and spatial control, we have evaluated if strong photobases ¹¹ can be made better photo reagents through the use of TPE.

Precision chemistry of light-induced acid-base reactions requires controlling the underlying excited-state proton transfer (ESPT) processes. ^{136–140} This broad category of chemical reactions can generally be divided into reversible and irreversible and intramolecular and intermolecular. Here, we focus on reversible intermolecular processes that may be amenable to precision chemistry. From the point of view of the photo-activated reagent, there are numerous proton-donating species, called photoacids, essentially hydroxylated aromatic compounds, while proton-abstracting molecules, *i.e.*, photobases, are less common. The present work examines the super photobase **FR0-SB** (7-((butylimino)methyl)-*N,N*-diethyl-9,9-dimethyl-9*H*-fluoren-2-amine), a non-centrosymmetric fluorene Schiff base shown in Figure 4.1a, capable of abstracting protons from alcohols ranging from methanol to *n*-octanol. ^{11,101} While other compounds, primarily quinoline derivatives, have been found to undergo ESPT in methanol, with 5-methoxyquinoline

reaching an excited-state pK_a value of 15.5, $^{65,110,141-146}$ our work has focused on **FR0**-SB because of its stronger photobasicity (pK_a* = 21). Reversible photobases are relatively scarce, because their reactivity depends on having a high excited-state pK_a and the ability to abstract a proton from the solvent within the lifetime of the excitation and the relevant solvent reorganization time. In particular, solvation of the resulting ions has been found to require two or more solvent molecules in a specific configuration. $^{104,110,141,147-153}$

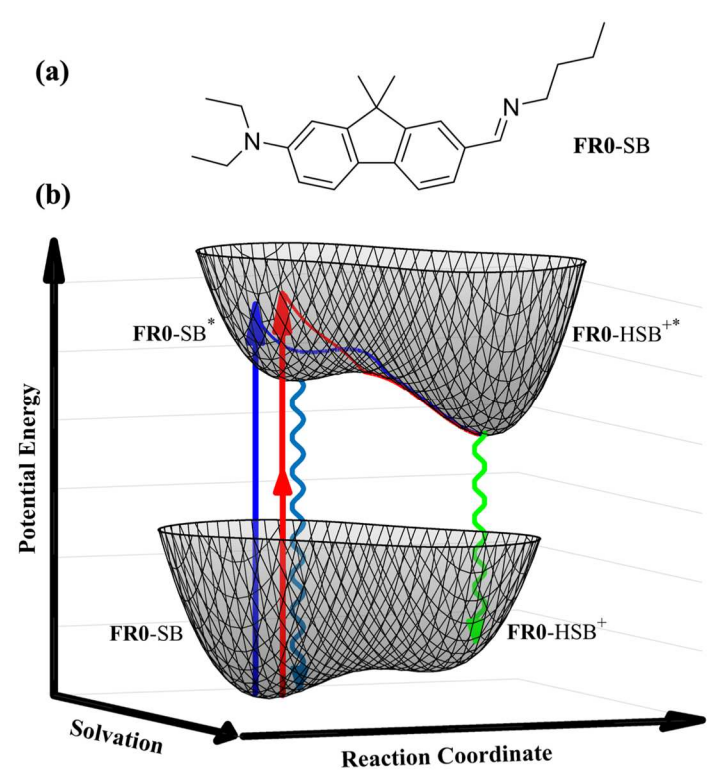


Figure 4.1. (a) Structural formula of FR0-SB. (b) Schematic representation of the ground- and excited-state potential energy surfaces of FR0-SB along the solvation and ESPT reaction coordinates. We illustrate how OPE (blue) and TPE (red) to the first excited singlet S_1 state of FR0-SB may favor differently solvated molecules from the inhomogeneous ensemble and result in accessing different Franck–Condon regions. Note that OPE and TPE are accessing the same excited electronic state. Different entries into the S_1 potential energy surface lead to different reaction trajectories toward protonation, with different dynamics and different probability to reach the protonated excited state. Fluorescence from both the non-protonated (blue wiggly line) and protonated (green wiggly line) excited states provide information on the progress of the reaction.

The primary focus of this work is to explore the reactivity of **FR0**-SB upon two-photon photo-activation. **FR0**-SB lacks a center of inversion, so Laporte's symmetry rule preventing one-and two-photon transitions to the same excited state does not apply. Therefore, both one-photon

excitation (OPE) and TPE to the first excited singlet (S₁) state of **FR0**-SB are allowed. While the excitation efficiencies for OPE and TPE are quite different, one might reasonably expect similar reactivity following isoenergetic (in the case of this work, $\omega_{\text{OPE}} = 2 \omega_{\text{TPE}}$) excitation. For **FR0**-SB in alcohol solvents, however, we find the extent of solvent-to-solute ESPT following TPE to be as much as 62 % greater than that following OPE. We present direct evidence for this surprising finding through steady-state and time-resolved spectroscopic data. We discuss several hypotheses and support or refute them based on experimental findings and theoretical calculations. Finally, we conclude that the molecular properties governing TPE, which we estimate from the spectroscopic data as well as using high-level quantum chemistry computations, lead to the formation of an excited-state wave packet at a different Franck–Condon region compared to OPE, thus changing the entry point onto the excited-state potential energy surface and, consequently, giving rise to a different trajectory along the reaction coordinate (see Figure 1).

4.2 Experimental and Theoretical Methods

4.2.1 Experimental Details

For the OPE and TPE fluorescence measurements, tunable ~50 fs pulses centered at 800 nm were obtained from a noncolinear optical parametric amplifier (Orpheus-N-3H, Light Conversion) pumped by the third-harmonic of a Pharos Yb:KGW laser producing 50 mJ of pulse energy at a repetition rate of 200 kHz centered at 1030 nm. For OPE, the output was frequency doubled by a β-BBO crystal to produce excitation light centered at 400 nm focused by a 10 cm focal length convex lens onto a 1 cm cuvette. The sample solutions had a ~3 μM concentration, corresponding to an optical density of less than 0.2. For TPE, the output was focused by a 20 cm focal length convex lens to the same sample. The fluorescence was captured with an optical fiber with detection using an Ocean Optics QE PRO spectrometer for measurements in methanol and ethanol, while an Ocean Optics QE 65000 instrument was used in the case of *n*-propanol, *i*-propanol, and *n*-hexanol.

For time-resolved fluorescence measurements, a Ti:Sapphire oscillator (Coherent Vitara-S) producing pulses at 80 MHz centered at 800 nm was used for laser excitation. For OPE, the frequency doubling of the laser output was achieved with a β-BBO crystal and the sample was excited with linearly polarized (vertical) laser pulses. For TPE, the laser pulses were polarization-rotated by 90° with a half-wave plate to maintain the same linear (vertical) polarization between TPE and OPE excitation. The **FR0**-SB sample with an optical density of 0.2 or below was contained in a 1 cm cuvette. Fluorescence emitted at right angles was acquired at parallel and perpendicular polarizations with respect to the vertically polarized excitation pulse using a polarizer followed by detection with a 16-multiplier time-correlated single-photon counting (TCSPC) system (SPC-830 TCSPC, Becker-Hickl, GmBH). The reported time constants were obtained after extracting the isotropic component from the fluorescence decays and fitting with a

convolute-and-compare routine to account for the instrument response function. Measurements were repeated at least 5 times for each solvent to quantify uncertainties.

The TPE spectra of **FR0**-SB in methanol, acetonitrile, and cyclohexane were measured in the same optical setup as the TPE fluorescence, except for a glass slide, which was introduced in the path of the excitation beam before the converging lens, to reflect part of the beam to be scattered on a diffuser and detected with a compact Ocean Optics spectrometer. The scattered integrated spectrum was used as a reference laser intensity to normalize the TPE spectra. The spectra were recorded for excitation wavelengths between 650 nm to 860 nm with data acquired every 10 nm. The setup was calibrated against a coumarin 540 (Exciton) solution, which exhibits similar TPE and OPE spectra. The TPE absorption cross section for **FR0**-SB in methanol is estimated to be 6 GM at 800 nm and 24 GM at its maximum at ~770 nm.

4.2.2 Computational Details

In order to provide further insights into the enhancement of ESPT between **FR0**-SB and alcohol solvent observed in the case of TPE vs OPE, we augmented our experimental effort by quantum chemistry computations examining the electronic structure of the solvated **FR0**-SB system in the ground (S₀) and first excited singlet S₁ states involved in the ESPT process.¹⁰¹ We focused on analyzing the role of solvation effects on the S₀-S₁ vertical and adiabatic transition energies and vertical transition dipole moments, along with the electronic dipoles characterizing the individual S₀ and S₁ states of **FR0**-SB, which are key quantities in comparing the one- and two-photon S₀ \rightarrow S₁ absorption cross sections. In doing so, we relied on the coupled-cluster (CC) theory,⁶⁹ which provides an accurate and size-extensive description of molecular systems, and its extension to excited states using the equation-of-motion (EOM) CC formalism,⁷⁰ focusing on the EOMCC approach with singles and doubles (EOMCCSD)⁷⁰ and the δ -CR-EOMCC(2,3) triples correction⁷⁴

to EOMCCSD, which is a rigorously size-intensive modification to the CR-EOMCC(2,3)^{75–77} methodology capable of determining excitation energies to within ~0.1–0.2 eV.⁸¹ In modeling the solvated **FR0-SB** chromophore, we considered the complex of **FR0-SB** hydrogen-bonded to a cluster of three alcohol solvent molecules, designated as [**FR0-SB···HOR**], which, according to our previous investigation of the steric effects on the ESPT process involving **FR0-SB** and *n*- and *i*-propanol, is the minimum number of explicit solvent molecules required for the proton transfer to occur.¹⁵³ Following ref. 153, we used the "branched" arrangement of the three alcohol solvent molecules treated in our modeling explicitly, with one of them hydrogen-bonded to **FR0-SB** and the other two solvating it, since such an arrangement leads to the lowest energy barriers for the ESPT reactions involving **FR0-SB** (see ref. 153 for further details). The remaining, bulk, solvation effects were described using the continuum solvation model based on the solute electron density (SMD) approach.¹¹⁴ The alcohol solvents considered in our computations were methanol, ethanol, *n*-propanol, and *i*-propanol.

For each of the alcohol solvents considered in our calculations, the geometry optimization of the [FR0-SB···HOR] complex in its S_0 state, used in the subsequent CC/EOMCC calculations, was performed using density functional theory (DFT)⁶⁸ employing the Kohn-Sham formulation of DFT.⁶⁷ To obtain the corresponding minimum-energy structures of the [FR0-SB···HOR] species in the S_1 state, we used the time-dependent (TD)⁸⁴ extension of DFT to excited electronic states. In carrying out these geometry optimizations, we used the CAM-B3LYP functional, ⁸³ which, as elaborated on in our earlier studies, ^{101,153} provides vertical excitation energies of FR0-SB that are closer to those resulting from the EOMCC calculations using the δ -CR-EOMCC(2,3) triples correction to EOMCCSD than the excitation energies obtained with other tested functionals. All

geometry optimizations of the [**FR0**-SB···HOR] complex employed the 6-31+G* basis set^{71–73} and accounted for the bulk solvation effects using the aforementioned SMD model.

To provide accurate information about the transition energies and transition dipole moments characterizing the absorption $(S_0 \to S_1)$ and emission $(S_1 \to S_0)$ processes involving the solvated **FR0**-SB species and the corresponding dipoles in the S_0 and S_1 states, which are all needed to model the one- and two-photon cross sections for each of the alcohol solvents considered in our calculations, we performed the following series of single-point CC and EOMCC computations at the aforementioned CAM-B3LYP/6-31+G*/SMD optimized geometries. First, we determined the S_0 - S_1 electronic transition energies

$$\omega_0^{\text{EOMCC})} = E_{S_1}^{\text{(EOMCC)}} - E_{S_0}^{\text{(CC)}}$$
(4.1)

corresponding to the [FR0-SB···HOR] complex in the absence of the SMD continuum solvation, where the total electronic energies of the S_0 and S_1 states entering Eq. 4.1 were computed as

$$E_{\rm S_0}^{\rm (CC)} = E_{\rm S_0}^{\rm (CCSD/6-31+G*)} + \left[E_{\rm S_0}^{\rm (CR-CC(2,3)/6-31G)} - E_{\rm S_0}^{\rm (CCSD/6-31G)} \right] \tag{4.2}$$

for the ground state and

$$E_{\rm S_{\rm l}}^{\rm (EOMCC)} = E_{\rm S_{\rm l}}^{\rm (EOMCCSD/6-31+G*)} + \left[E_{\rm S_{\rm l}}^{\rm (\delta-CR-EOMCC(2,3)/6-31G)} - E_{\rm S_{\rm l}}^{\rm (EOMCCSD/6-31G)} \right] \tag{4.3}$$

for the first excited singlet state. The first term on the right-hand side of Eq. 4.2 denotes the total electronic energy of the S_0 state computed at the CCSD⁸⁰ level utilizing the largest basis set considered in this study, namely, 6-31+G*. The term in the square brackets on the right-hand side of Eq. 4.2 corrects the CCSD/6-31+G* energy for the many-electron correlation effects due to triply excited clusters obtained in the CR-CC(2,3)^{75,76,78,79} calculations employing the smaller and more affordable 6-31G basis.⁷¹ Similarly, the first term on the right-hand side of Eq. 4.3 designates the EOMCCSD/6-31+G* energy of the S_1 state and the expression in the square brackets represents the triples correction to EOMCCSD obtained in the δ -CR-EOMCC(2,3)/6-31G

calculations. Ideally, one would like to use basis sets larger than 6-31+G* and, in particular, incorporate polarization and diffuse functions on hydrogen atoms, but such calculations at the CC and EOMCC levels used in this work turned out to be prohibitively expensive. Nevertheless, we tested the significance of the polarization⁷² and diffuse functions⁷³ on hydrogen atoms by performing the CAM-B3LYP/6-31++G**/SMD calculations for the [FR0-SB···HOR] complexes which show that neither the excitation energies nor the dipole and transition dipole moment values change by more than 1 % compared to the CAM-B3LYP/6-31+G*/SMD results.

Before describing the remaining elements of our computational protocol, it is important to emphasize that the composite approach defined by Eq's. 4.1-4.3 is more general than the analogous expressions shown in ref. 101 where we focused on the vertical excitation processes only. Eq.'s 4.1–4.3 encompass both the vertical and adiabatic transition energies. Indeed, if $E_{S_0}^{\rm (CC)}$ and $E_{S_1}^{(EOMCC)}$ are calculated at the minimum on the S_0 potential energy surface, $a_0^{(EOMCC)}$ given by Eq's. 4.1–4.3 becomes the vertical excitation energy $\omega_{l0}^{\text{EOMCC)}}(abs.)$ characterizing the $S_0 \to S_1$ absorption defined by Eq. 4.1 of ref. 101. If $E_{\rm S_0}^{\rm (CC)}$ and $E_{\rm S_1}^{\rm (EOMCC)}$ are determined at the minimum characterizing the [FR0-SB···HOR] complex in the S₁ state, we obtain the vertical transition energy $a_0^{\text{(EOMCC)}}$ (em) corresponding to the $S_1 \to S_0$ emission. The $a_0^{\text{(EOMCC)}}$ energy defined by Eq. 4.1 becomes the adiabatic transition energy, abbreviated as ω_0^{EOMCC} (ad.), when $E_{s_0}^{\text{(CC)}}$ and $E_{\rm S_{\rm I}}^{\rm (EOMCC)}$ are computed at their respective minima. As far as the transition dipole moments characterizing the vertical absorption and emission processes involving the solvated FR0-SB species are concerned, they were calculated from the one-electron transition density matrices obtained at the EOMCCSD level of theory employing the 6-31+G* basis set. Similarly, we used

the CCSD/6-31+G* and EOMCCSD/6-31+G* one-electron reduced density matrices to determine the dipole moments of the S_0 and S_1 states at each of the two potential minima.

Given the large computational costs associated with the EOMCCSD and δ -CR-EOMCC(2,3) calculations for the [FR0-SB···HOR] system, which consists of three alcohol molecules bound to the FR0-SB chromophore and which requires correlating as many as 216 electrons and 758 molecular orbitals in the case of the *n*- or *i*-propanol solvents when the 6-31+G* basis set is employed, we replaced the three explicit alcohol molecules with the corresponding effective fragment potentials (EFPs). 154 We were able to do this because, based on our CAM-B3LYP/6-31+G*/SMD calculations for the [FR0-SB···HOR] complexes, the S₀-S₁ electronic transition does not involve charge-transfer between the photobase and its solvent environment. Indeed, the S₀–S₁ transition in the bare¹⁰¹ and solvated **FR0**-SB species has a predominantly π – π * character with the π and π^* orbitals localized on the **FR0**-SB chromophore, *i.e.*, the alcohol solvent molecules are mere spectators to this excitation process. The use of EFPs to represent the cluster of three alcohol molecules bonded to FR0-SB in our CC/EOMCC computations allowed us to reduce the system size to that of the bare FR0-SB species embedded in the external potential providing a highly accurate description of the intermolecular interactions between FR0-SB and solvent molecules in the [FR0-SB···HOR] complex, including electrostatic, polarization, dispersion, and exchange repulsion effects. 154

Once the electronic transition energies and the corresponding one-electron properties of the [FR0-SB···HOR] complex were determined, we proceeded to the second stage of our modeling protocol, which was the incorporation of the remaining bulk solvation effects that turned out to be non-negligible as well. As in the case of the aforementioned geometry optimizations, the bulk solvation effects were calculated with the help of the implicit solvation SMD approach. Due to

limitations of the computer codes available to us, we could not perform the CC/EOMCC computations in conjunction with the SMD model, so we estimated the SMD effects using the *a posteriori* corrections $\mathcal{S}_X^{(SMD)}$ to the various CC/EOMCC properties X of the [FR0-SB···HOR] complex, such as transition energies and dipole moments, using DFT and TD-DFT. These corrections were constructed in the following way. First, for each of the four alcohol solvents considered in our calculations, we performed single-point DFT/TD-DFT calculations for the [FR0-SB···HOR] complex at the previously optimized S_0 and S_1 geometries accounting for the bulk solvation effects using SMD. As in the case of the geometry optimizations, we used the CAM-B3LYP functional and the 6-31+G* basis set and, in analogy to the CC/EOMCC computations, replaced the cluster of three explicit alcohol solvent molecules bound to FR0-SB by the corresponding EFPs. We then repeated the analogous calculations without SMD. This allowed us to determine the desired $\mathcal{S}_X^{(SMD)}$ corrections using the formula

$$\mathcal{S}_{X}^{\text{(SMD)}} = X^{\text{(CAM-B3LYP/6-31+G*/SMD)}} - X^{\text{(CAM-B3LYP/6-31+G*)}}, \tag{4.4}$$

where the first and second terms on the right-hand side of Eq. 4.4 designate property *X* obtained in the CAM-B3LYP/6-31+G* calculations with and without SMD, respectively. The final SMD-corrected EOMCC electronic transition energies were computed as

$$\boldsymbol{\alpha}_0 = \boldsymbol{\alpha}_0^{\text{EOMCC}} + \boldsymbol{\delta}_{\boldsymbol{\alpha}_0}^{\text{(SMD)}}, \tag{4.5}$$

where ω_0^{EOMCC} is the transition energy for the [FR0-SB···HOR] complex defined by Eq's. 4.1–4.3, whereas the SMD-corrected one-electron properties were determined using the formula

$$X = X^{[\text{(EOM)CCSD/6-31+G*}]} + \delta_X^{\text{(SMD)}}, \tag{4.6}$$

with $X^{[\text{EOM})\text{CCSD}/6-31+G*]}$ denoting the value of property X calculated at the (EOM)CCSD/6-31+G* level. If the property of interest was a vector, such as dipole or transition dipole moment, we used Eq. 4.6 for each of the Cartesian components of the vector.

Finally, to gauge the effects of solvation on the various calculated properties, including transition energies and dipole and transition dipole moments, we also performed single-point CC/EOMCC calculations for the bare super photobase, *i.e.*, **FR0**-SB without the presence of explicit solvent molecules or equivalent EFPs and SMD implicit solvation, at the gas-phase geometry of the S₁ state optimized using CAM-B3LYP/6-31+G*. In the case of the S₀ minimum-energy structure, we relied on our previous gas-phase CC/EOMCC results reported in ref. 101.

All of the electronic structure calculations reported in this work, including the CAM-B3LYP geometry optimizations with and without the SMD continuum solvation, the CC/EOMCC single-point calculations without implicit SMD solvation, and the CAM-B3LYP single-point calculations with and without SMD, needed to estimate the SMD corrections to CC/EOMCC properties, were performed using the GAMESS package^{85,155} (we used the 2019 R2 version of GAMESS). In the case of the $S_0 \rightarrow S_1$ absorption process, whenever the SMD implicit solvation model was utilized, we incorporated the nonequilibrium solvation effects associated with the solvent relaxation delay, as implemented in GAMESS. The relevant CCSD, CR-CC(2,3), EOMCCSD, and δ -CR-EOMCC(2,3) computations using the restricted Hartree-Fock (RHF) determinant as a reference and the corresponding left-eigenstate CCSD and EOMCCSD calculations, which were needed to determine the triples corrections of CR-CC(2,3) and δ -CR-EOMCC(2,3) and the one-electron properties of interest, including the dipole and transition dipole moments, were carried out using the CC/EOMCC routines developed by the Piecuch group, 75–79,82,86,87 which form part of the GAMESS code as well. In all of our CC/EOMCC calculations, the

core orbitals associated with the 1s shells of C and N atoms of **FR0**-SB were kept frozen. The EFPs that were used to replace the cluster of three explicit alcohol solvent molecules bound to **FR0**-SB in the CC/EOMCC single-point calculations and the CAM-B3LYP computations aimed at determining the SMD solvation effects were generated using the RHF approach and the 6-31+G* basis set. Thanks to the use of EFPs, our frozen-core CC/EOMCC calculations for the [**FR0**-SB···HOR] complex correlated only 138 electrons of the **FR0**-SB system. In all of the calculations employing the 6-31+G* basis set, we used spherical components of d orbitals.

4.3 Results and Discussion

Steady-state fluorescence spectra following isoenergetic OPE (400 nm) and TPE (2×800 nm) for a number of alcohols are presented in Figure 4.2. These spectra have been divided by the frequency cubed according to the transition dipole moment representation, which makes fluorescence intensity proportional to population according to the Einstein coefficient of spontaneous emission. The Upon excitation, **FR0**-SB reaches the first excited singlet state (denoted **FR0**-SB*), which emits at $\sim 21,000$ cm⁻¹. Following proton transfer, the **FR0**-HSB+* excited protonated state is reached, which emits at $\sim 15,000$ cm⁻¹. The probability of proton transfer is observed to decrease as the alkane chain of the linear alcohols increases. This observation was found to correlate with the relative \sim OH concentration. Interestingly, for *i*-propanol, significantly less proton transfer takes place, an aspect related to steric hindrance in the formation of an appropriate solvent configuration for proton transfer that has been addressed elsewhere.

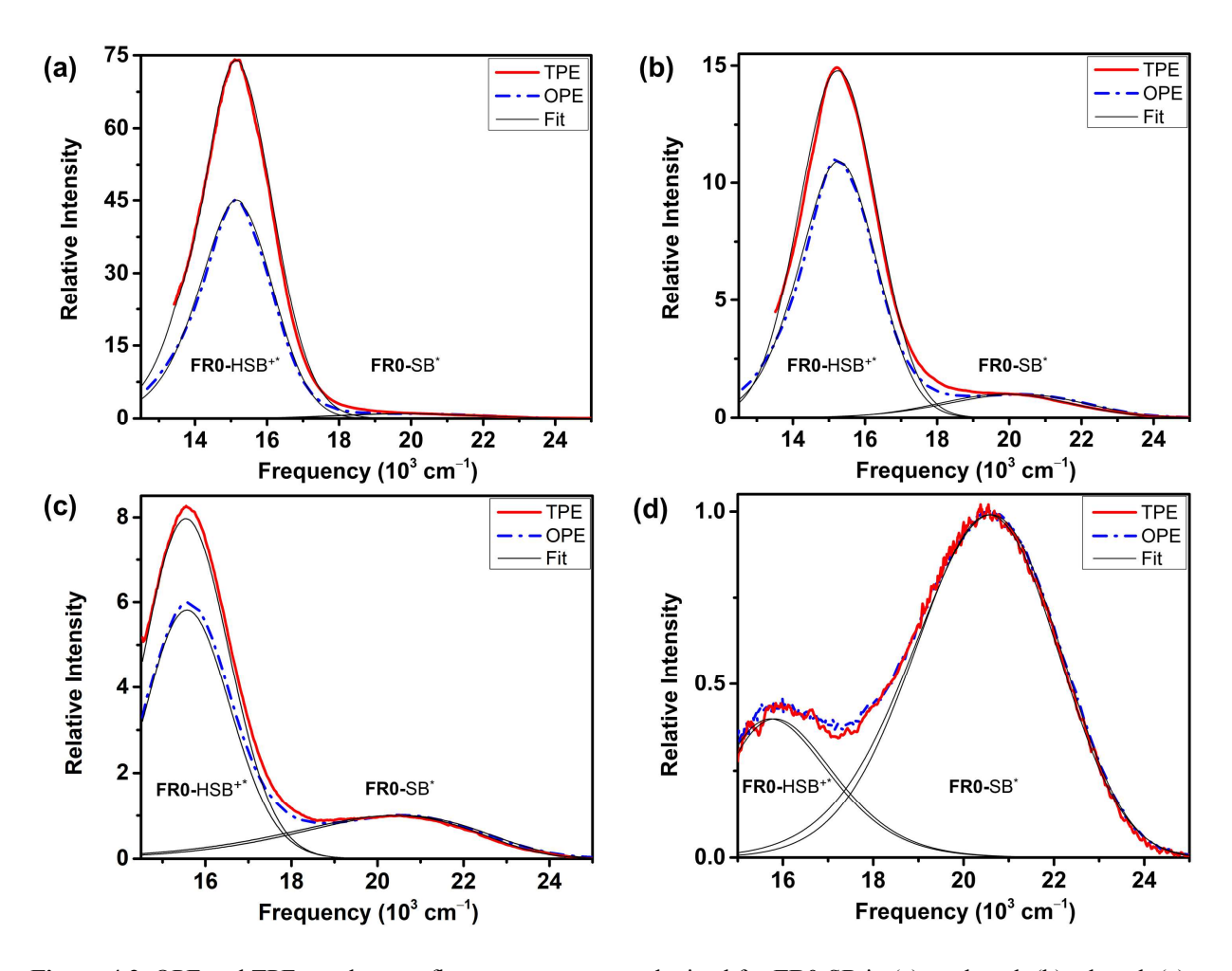


Figure 4.2. OPE and TPE steady-state fluorescence spectra obtained for **FR0**-SB in (a) methanol, (b) ethanol, (c) *n*-propanol, and (d) *i*-propanol. In each of the panels, OPE (blue line) is compared with TPE (red line). The fluorescence spectra are normalized to the non-protonated emission intensity. The ratio between the areas for **FR0**-HSB⁺⁺ (\sim 15,000 cm⁻¹) and **FR0**-SB* (\sim 21,000 cm⁻¹) emission following OPE and TPE is determined by fits to log-normal functions (thin black lines).

Of particular interest in this work is how the probability for proton transfer, *i.e.*, the reactivity of the Schiff base, is affected by the excitation process. For this purpose, we quantify the extent of proton transfer as the [FR0-HSB^{+*}]/[FR0-SB*] ratio for linear and nonlinear excitation by fitting the fluorescence areas to log-normal functions as shown in Figure 4.2, and then correcting the results for differences in the fluorescence quantum yield of the protonated and non-protonated excited-state species in the different solvents. The results, summarized in Table 4.1, are presented in Figure 4.3 for both OPE (blue) and TPE (red); note that the vertical axis on

the right is a logarithmic scale so differences between the two modes of excitation seem less prominent than they actually are. While both OPE and TPE proton-transfer rates change proportionally for the different solvents, we consistently observe greater proton transfer following TPE compared to OPE. The ratio between the two modes of observed excitation, *i.e.*, the ratio of ratios, is shown as gray bars in Figure 3. We find that for methanol TPE leads to 62 ± 20 % greater reactivity than OPE. Greater reactivity following TPE vs OPE is also observed for ethanol (42 ± 13 %), n-propanol (36 ± 4 %), and n-hexanol (24 ± 3 %), although the percent enhancement decreases with alcohol aliphatic chain length. The large error bars, especially for methanol, result from the difficulty in measuring the very small **FR0**-SB* signal, which amounts to one part in 58. In the case of i-propanol, no excess reactivity is found within the uncertainty of the measurements.

Table 4.1. Quantitative assessment of the extent of protonation following OPE and TPE from steady-state fluorescence measurements for **FR0-SB**. The ratio of the extent of protonation expressed as TPE/OPE shows the enhancement in ESPT resulting from TPE experiments compared to their OPE counterparts.

	ε		1
Solventa	OPE ratio	TPE ratio	TPE/OPE
МеОН	36 ± 3	58 ± 5	1.62 ± 0.20
EtOH	7.6 ± 0.5	10.9 ± 0.7	1.42 ± 0.13
<i>n</i> -PrOH	3.85 ± 0.06	5.2 ± 0.1	1.36 ± 0.04
n-HxOH	1.72 ± 0.02	2.13 ± 0.04	1.24 ± 0.03
<i>i</i> -PrOH	0.37 ± 0.01	0.35 ± 0.02	0.94 ± 0.06

^a Abbreviations: MeOH = methanol, EtOH = ethanol, n-PrOH = n-propanol, n-HxOH = n-hexanol, i-PrOH = i-propanol.

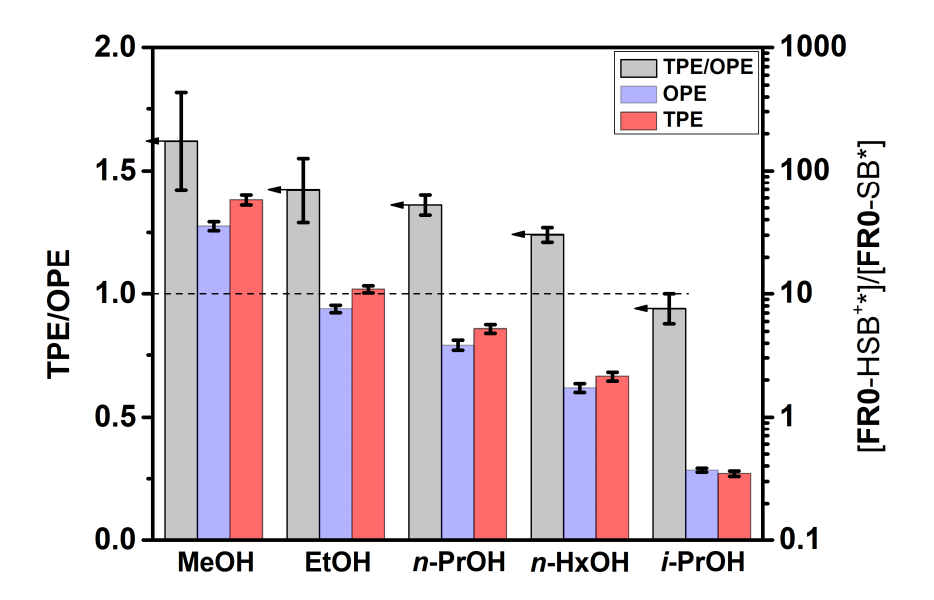


Figure 4.3. Extent of proton transfer determined following OPE and TPE for **FR0**-SB in a number of alcohols. The TPE over OPE ratio is given by the gray bars (left y-axis). In all the solvents but i-propanol, enhanced proton transfer is observed following TPE. The ratios between the fluorescence bands [**FR0**-HSB^{+*}]/[**FR0**-SB^{*}], corrected for fluorescence quantum yield, are plotted as bars OPE (blue) and TPE (red); each ratio is indicated on a logarithmic scale (right y-axis). Abbreviations: MeOH = methanol, EtOH = ethanol, n-PrOH = n-propanol, n-HxOH = n-hexanol, i-PrOH = i-propanol.

The enhanced reactivity following isoenergetic TPE is unexpected. Therefore, we explore the possible involvement of an additional dark state that lies within the absorption band associated with S_1 or a higher excited singlet state S_n that is reached via three-photon excitation (3 × 800 nm). These possible contributions are addressed as follows. Excitation–emission matrix (EEM) spectra were obtained for **FR0-SB** in methanol and ethanol and are shown in Figure 4.4. The absorption spectrum is shown as a bold black line. From the spectra in Figure 4.4, we observe no evidence for the existence of an additional state within the 325–450 nm S_1 region. However, we do see evidence for absorption to S_n with n > 1 in the 225–290 nm region which is also associated with **FR0-HSB**^{+*} and **FR0-SB*** emission following S_n to S_1 internal conversion. We measured the excitation intensity dependence of the TPE integrated fluorescence for the different solvents. The exponent associated with the laser intensity dependence indicates the number of photons associated with the excitation process (Figure 4.5). The exponent measured was ~1.9, indicating

that three-photon excitation, if it occurs, contributes minimally. Thus, to summarize, we exclude the participation of a dark state near S_1 based on the EEM spectra. Furthermore, given the near quadratic laser power dependence combined with the observation that the probability for proton transfer following 266 nm excitation is similar to that following 400 nm excitation, we rule out contributions to the observed ESPT enhancement from three-photon excitation processes. In particular, we can exclude the involvement of excited-state absorption in which two-photon $S_0 \rightarrow S_1$ transition is followed by a one-photon $S_1 \rightarrow S_n$ excitation in the observed reactivity enhancement. When normalizing for proton transfer emission, we find that maximum proton transfer for OPE is observed at 400 nm excitation, the wavelength chosen for this study.

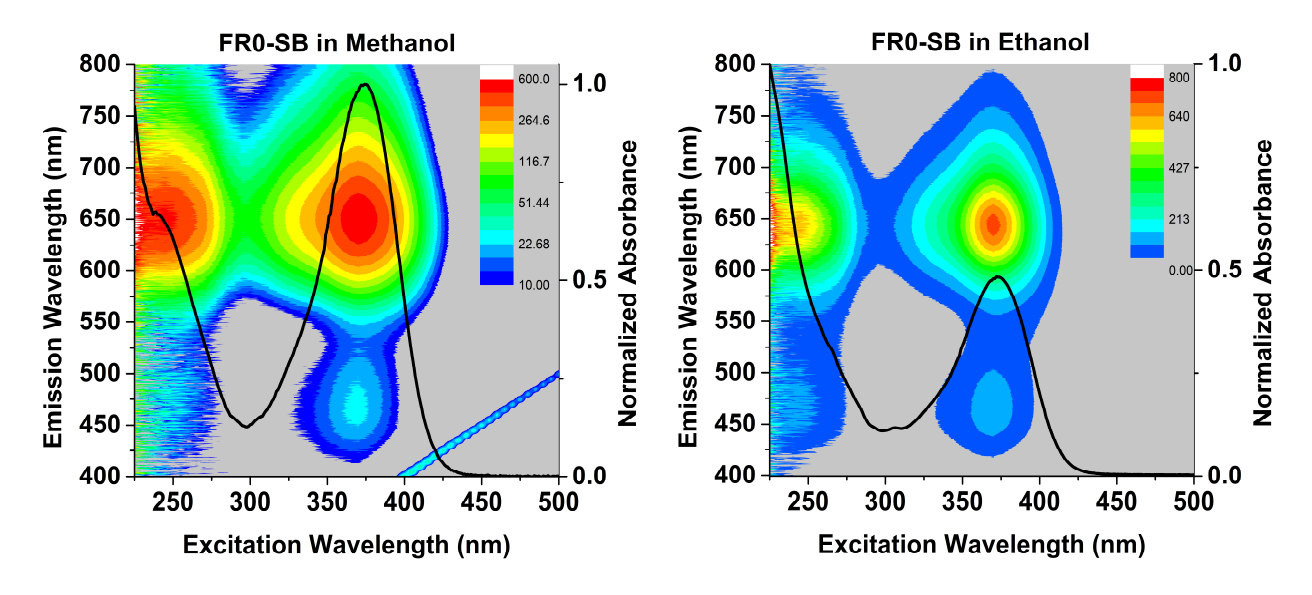


Figure 4.4. EEM spectra showing the dependence of protonation as a function of excitation wavelength for methanol (left) and ethanol (right). The absorption spectrum for both molecules is shown as a bold black line. Emission from **FR0-SB*** is observed at \sim 450 nm and emission from **FR0-HSB*** is observed at \sim 650 nm.

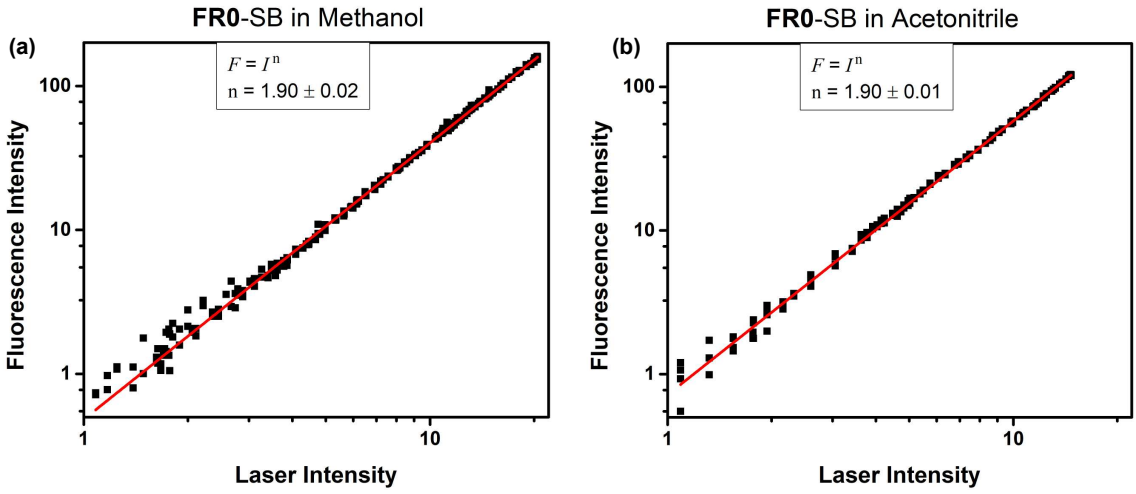


Figure 4.5. Laser intensity dependence of the fluorescence following two-photon excitation for **FR0**-SB in (a) methanol and (b) acetonitrile, measured for laser pulses from a Ti:Sapphire oscillator. The fitting function (red line) and the experimental points (black squares) are plotted on a log-log scale. The exponent obtained from the fit, of \sim 2, indicates two-photon excitation and shows no indication of three-photon excitation.

The striking solvent dependence observed for the enhanced two-photon reactivity implies that the underlying process depends on the dynamics of proton transfer and solvation. To explore this dependence, we can first rely on our previous time-resolved TCSPC results for the solvents studied here. In Figure 4.6, we plot the TPE/OPE enhancement as a function of the measured **FR0**-SB* lifetime. We observe an inverse correlation, shorter **FR0**-SB* lifetimes correlate with greater enhancement. When the **FR0**-SB* lifetime is longer, the observed enhancement decreases. We interpret this finding as follows. Although **FR0**-SB has a high pK_a^* , the ability of **FR0**-SB* to abstract a proton depends on the solvent configuration. We know from our quantum chemistry calculations reported in ref. 153 that the minimum of three solvent molecules, with one of them directly hydrogen-bonded to **FR0**-SB, are needed to enable the ESPT process. Achieving such a configuration is easiest for small molecules, such as methanol, and much less probable for secondary alcohols, *e.g.*, *i*-propanol and cyclopentanol. The prepares

the molecule at a point on the excited-state reaction coordinate that enhances reactivity, but such propensity is lost within a few hundred picoseconds or less.

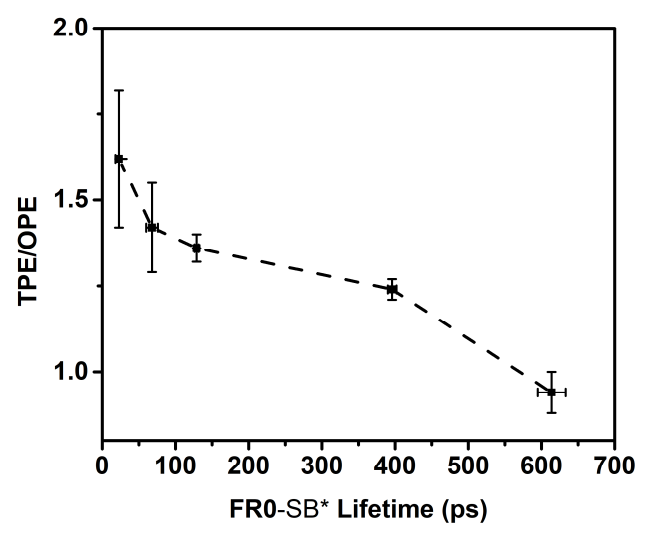


Figure 4.6. Isoenergetic two-photon enhanced ESPT as a function of excited-state lifetime prior to proton transfer for (in order of greater to lower enhancement) methanol, ethanol, *n*-propanol, *n*-hexanol, and *i*-propanol. The dashed line is included as a guide to the eye.

From the previous observations, it appears that TPE leads to a more reactive species than OPE. We performed fluorescence lifetime measurements following isoenergetic OPE and TPE detecting at both the **FR0**-SB* and **FR0**-HSB⁺* wavelength regions. Results from these measurements are summarized in Table 4.2. In the case of aprotic solvents, such as acetonitrile, the average excited-state lifetime $\bar{\tau}_{SB}$ is ~2 ns. The much shorter values for $\bar{\tau}_{SB}$ in alcohols are associated with the formation of the [**FR0**-SB*···HOR] complex where the proton is already shared by **FR0**-SB* and ROH, which precedes the separation and solvation of the protonated **FR0**-HSB⁺* and the deprotonated solvent RO⁻ species characterized by the rise time τ_{X} . The latter process has a timescale that is much less dependent on the method of excitation. We find that the first step in protonation, namely, the loss of population in **FR0**-SB* and the rise of the **FR0**-HSB⁺* emission are approximately two times faster for TPE than for OPE. This observation is consistent with the enhanced reactivity and with the conclusion that TPE leads to a more reactive species.

Measurements carried out in acetonitrile in the **FR0**-SB* and **FR0**-HSB^{+*} wavelength regions showed no OPE *vs* TPE difference, indicating that the enhancement depends on the hydrogen-bonding capabilities of protic solvents.

Table 4.2. Fluorescence lifetime measurements following one- and two-photon isoenergetic excitation of **FR0-**SB in methanol, ethanol, and acetonitrile. The initial state, **FR0-**SB*, decays with a fast τ_{SB1} and a slow τ_{SB2} biexponential lifetimes. The numbers in parentheses indicate the amplitude of the fast decay component (a_1). The protonated state **FR0-**HSB** shows a fast rise time τ_X and a slow decay time τ_{HSB} . In acetonitrile, no proton transfer takes place, thus one observes only a single exponential decay of the **FR0-**SB* state that is identical for OPE and TPE within the measurement errors. All numbers are given in picoseconds.

Solvent ^a	OPE					TPE				
	$ au_{\mathrm{SB1}}$	τ_{SB2}	$\overline{\tau}_{SB}{}^b$	$ au_{\mathrm{X}}$	$\tau_{\rm HSB}$	$ au_{\mathrm{SB1}}$	τ_{SB2}	$\overline{\tau}_{SB}{}^b$	τ_{X}	$ au_{ ext{HSB}}$
МеОН	23 ± 7 (0.99)	1259 ± 14	35 ± 7	31 ± 1	1116 ± 2	12 ± 6 (0.99)	811 ± 30	20 ± 6	28 ± 9	1106 ± 11
EtOH	59 ± 4 (0.84)	220 ± 6	85 ± 4	103 ± 2	1241 ± 33	35 ± 3 (0.89)	212 ± 20	54 ± 5	90 ± 4	1232 ± 1
ACN	_	2121 ± 10	2121 ± 10	_	_	_	2138 ± 8	2138 ± 8	_	

^a Abbreviations: MeOH = methanol, EtOH = ethanol, ACN = acetonitrile.

Having ruled out the involvement of an additional excited state, or excitation to a higher S_n excited state with n > 1, we now turn to the possibility of reaching a more reactive species via TPE. We begin by comparing the expressions for the absorption cross sections associated with OPE and TPE arising from the first- and second-order time-dependent perturbation theory, respectively (see, *e.g.*, ref. 156). The $0 \rightarrow f$ OPE absorption cross section, with 0 and f denoting the initial and final electronic states, respectively, is 156

$$\sigma_{f0}^{(1)}(\boldsymbol{\omega}) = A \left| \mu_{f0} \right|^2 g_{\text{MI}}(\boldsymbol{\omega}), \tag{4.7}$$

where ω is the frequency of the exciting photon (in our case, the frequency of a 400 nm laser), A is a constant, μ_{f0} denotes the magnitude of the transition dipole moment between the ground and excited electronic states, and $g_{MI}(\omega)$ is the OPE distribution function or linewidth associated with the molecular system of interest. In presenting Eq. 4.7, we have assumed an isotropic averaging

^b For protic solvents (MeOH and EtOH), $\bar{\tau}_{SB} = a_1 \tau_{SB1} + a_2 \tau_{SB2}$, where $a_2 = 1 - a_1$. In the case of ACN, for which there is no ESPT, $\bar{\tau}_{SB} = \tau_{SB2}$.

over the directions of the transition dipole moment vector μ_{f0} . To arrive at an expression for the absorption cross section associated with the isoenergetic one-color TPE, where the laser frequency is half of its OPE counterpart, we take advantage of the fact that no resonance at 800 nm is observed in our experiments, in agreement with our electronic structure calculations. Under these conditions, the absorption cross section for TPE becomes 157

$$\sigma_{f0}^{(2)}(\omega/2) = B \left| \sum_{\nu} \frac{\mu_{f\nu} \mu_{\nu 0}}{\omega_{\nu 0} - \omega/2 + i\Gamma_{\nu}(\omega/2)} \right|^{2} g_{M2}(\omega), \tag{4.8}$$

where B is a constant, ω_{v0} is the frequency needed to reach the intermediate state v from the ground state 0, $i\Gamma_v(\omega/2)$ is a damping factor that is inversely proportional to the lifetime of a given intermediate state v, and $g_{M2}(\omega)$ is the TPE line shape function. In analogy to the OPE absorption cross section, we have performed an isotropic averaging over the directions of the transition dipole moment vectors μ_{fv} and μ_{v0} .

Eq. 4.8 is useful, but in this work we are interested in relating the TPE absorption cross section with the change in the dipole moment upon $0 \rightarrow f$ photoexcitation. One can derive such a relationship if we perform the following mathematical manipulations. First, we separate the v = 0 and v = f terms from the sum over states in Eq. 4.8. Next, we take advantage of the fact that in our case 0 and f correspond to the electronically bound S_0 and S_1 states of **FR0**-SB, respectively. This allows us to eliminate the $i\Gamma_v(\omega/2)$ term in the v = 0 and v = f denominators in Eq. 8. In the final step, we replace ω_{f0} in the v = f denominator by ω and combine the v = 0 and v = f contributions to obtain v = f

$$\sigma_{f0}^{(2)}(\omega/2) = B \left| \sum_{\nu \neq 0, f} \frac{\mu_{f\nu} \mu_{\nu 0}}{\omega_{\nu 0} - \omega/2 + i\Gamma_{\nu}(\omega/2)} + \frac{\mu_{f0} \Delta \mu_{f0}}{\omega/2} \right|^{2} g_{M2}(\omega). \tag{4.9}$$

It is customary to refer to the first term in Eq. 4.9 as the 'virtual' pathway and to the second one, which relies on the transition dipole moment μ_{f0} and the difference between the permanent ground- and excited-state dipoles $\Delta\mu_{f0} \equiv \mu_{ff} - \mu_{00}$, as the 'dipole' pathway. ¹⁵⁹ Eq. 4.9 shows that for centrosymmetric molecules, for which $\Delta\mu_{f0}$ vanishes identically, the virtual pathway is the only contributing term to the TPE absorption cross section. However, FR0-SB is not centrosymmetric and, thus, it is interesting to examine the extent to which each pathway contributes to the $S_0 \rightarrow S_1$ one-color TPE considered here. For the first term in Eq. 4.9 to be large, the following three conditions would have to be satisfied: (1) the ω_{v_0} frequency characterizing the $0 \rightarrow v$ transition would have to be close to the frequency $\omega/2$ of each of the two photons associated with TPE, (2) the $i\Gamma_{\nu}(\omega/2)$ damping factor would have to be very small, i.e., the intermediate state v would have to be sufficiently long-lived, and (3) the $0 \rightarrow v$ and $v \rightarrow f$ transitions would have to be allowed, giving rise to larger μ_{v0} and μ_{fv} transition dipole moments. In the case of the TPE experiments performed in this work, it is unlikely that conditions (1), (2), and (3) can be simultaneously satisfied. Indeed, since there are no dipole-allowed electronic states between S_0 and S_1 , the intermediate state ν satisfying condition (1) would have to be a rovibrational resonance supported by the ground-state electronic potential. It is unlikely that such resonances are long-lived and characterized by large $0 \rightarrow v$ and $v \rightarrow f$ transition dipole moments. It is possible that the intermediate states v characterized by larger $\mu_{v,0}$ and μ_{fv} values exist, but those would have to be electronic states higher in energy than S₁, which cannot satisfy the resonant condition (1). Furthermore, as demonstrated in ref. 101, the low-lying electronically excited states above S₁ are characterized by small or even negligible transition dipole moments from the ground state. In other words, while the virtual pathway contributes to the TPE cross section, the probability that it dominates it seems low, especially when we realize that there are reasons for the dipole pathway to play a substantial role in the case of the molecular systems considered in this work. Indeed, as shown in our earlier studies, 101,153 and as further elaborated on below, the $S_0 \rightarrow S_1$ excitations in the isolated and solvated **FR0-SB** are characterized by large transition dipole moments and significant changes in the permanent dipoles. This suggests that the second term in Eq. 4.9 plays a major role, which is consistent with the well-established fact that the dipole pathway becomes critical when TPE involves charge-transfer associated with substantial change in the permanent dipole upon photoexcitation. $^{160-165}$ Although the $S_0 \rightarrow S_1$ transition in **FR0-SB** is accompanied by a migration of a small amount of charge, 101,153 this migration happens over a very large distance, giving rise to more than a three-fold increase in dipole moment and a substantial enhancement of the second term in Eq. 4.9. Given the above analysis, from this point on we focus on the dipole pathway and assume that we can approximate the TPE absorption cross section by the second term in Eq. 4.9, *i.e.*, 163

$$\sigma_{f_0}^{(2)}(\omega/2) \approx B' |\mu_{f_0}|^2 |\Delta \mu_{f_0}|^2 g_{M_2}(\omega),$$
 (4.10)

where $B' = 4B / \omega^2$.

As illustrated in Eq's. 4.7 and 4.10, the absorption cross sections for both one- and twophoton excitation processes depend on the square of the absolute value of the transition dipole moment μ_{f0} characterizing the $0 \to f$ vertical electronic excitation, which in our case is the transition dipole μ_{10} corresponding to the $S_0 \to S_1$ photoabsorption for the **FR0**-SB system in various solvents. However, in the case of TPE, the absorption cross section also depends on the difference between the electronic dipole moments of the f and 0 states, $\Delta \mu_{f0}$, which in our case is the difference $\Delta \mu_{10} \equiv \mu_1 - \mu_0$ between the dipole moment μ_1 characterizing the first excited singlet S_1 state of **FR0**-SB and its S_0 counterpart μ_0 . Consequently, $\Delta \mu_{10}$ and its dependence on the solvent environment hold the key to understanding the enhancement of the ESPT reactions between the **FR0**-SB photobase and alcohol solvents observed in the case of TPE. To provide insights into the effect of solvation on $\Delta \mu_{10}$ and other properties characterizing the S_0 and S_1 states of the solvated **FR0**-SB chromophore and transitions between them, we performed electronic structure calculations using the CC/EOMCC-based composite approach described in the Computational Details section. As mentioned in that section, the alcohol solvents considered in our computations were methanol, ethanol, n-propanol, and i-propanol.

In Table 4.3, we report the vertical transition energies $\omega_{10}(abs.)$ and transition dipole moments $\mu_{\scriptscriptstyle 10}$ characterizing the $S_0 \to S_1$ photoabsorption process, along with the dipoles corresponding to the S_0 and S_1 states, μ_0 and μ_1 , respectively, and their ratios resulting from our calculations for FR0-SB in the gas phase and in the aforementioned four solvents determined at the minima on the respective S₀ potential energy surfaces. The analogous information for the S₁ \rightarrow S₀ emission and the dipole moment values of the S₀ and S₁ states determined at the S₁ minima characterizing the isolated and solvated FR0-SB is presented in Table 4.4. We begin our discussion of computational results by comparing the vertical absorption and emission energies characterizing the solvated FR0-SB species obtained with the CC/EOMCC-based protocol adopted in this work against their experimental counterparts. The vertical excitation energies for the [FR0-SB···HOR] complexes calculated at the respective S₀ minima, shown in Table 4.3, are essentially identical to the locations of the peak maxima in the corresponding experimental photoabsorption spectra reported in ref. 153, which are 3.32, 3.33, 3.32, and 3.34 eV for methanol, ethanol, *n*-propanol, and *i*-propanol, respectively. The same accuracies are also seen in the case of the vertical emission energies calculated at the S₁ minima of the [FR0-SB···HOR] species reported in Table 4.4, which can hardly be distinguished from the maxima in the experimental emission peaks for **FR0**-SB in methanol, *n*-propanol, and *i*-propanol of 2.57, 2.61, 2.62, and 2.65 eV, respectively. These observations corroborate the accuracy of the computational protocol used in this study to model the interactions of the **FR0**-SB photobase with the various alcohol solvents. The observed good agreement between the theoretical vertical transition energies reported in Tables 4.3 and 4.4 and the corresponding experimental data can largely be attributed to the use of high-level *ab initio* CC/EOMCC approaches in describing the [**FR0**-SB···HOR] complexes. This becomes apparent when one considers the errors relative to experiment characterizing the vertical transition energies obtained in the single-point CAM-B3LYP/6-31+G*/SMD computations, which are about 0.2–0.3 eV (9–11 %).

Table 4.3. The vertical transition energies ω_{10} (abs.) (in eV) and transition dipole moments μ_{10} (in Debye) corresponding to the $S_0 \to S_1$ absorption, along with the μ_0 and μ_1 dipoles characterizing the S_0 and S_1 states (in Debye) and their ratios for **FR0**-SB in the gas phase and in selected alcohol solvents calculated at the respective S_0 minima following the CC/EOMCC-based protocol described in Computational Details.

Solventa	ω_{10} (abs.)	$\mu_{\!\scriptscriptstyle 10}$	$\mu_{\scriptscriptstyle 0}$	$\mu_{\scriptscriptstyle 1}$	$\mu_{\scriptscriptstyle 1}$ / $\mu_{\scriptscriptstyle 0}$
None (gas phase) ^b	3.70	6.9	2.6	8.6	3.3
MeOH	3.30	9.6	4.4	16.4	3.8
EtOH	3.32	9.5	4.3	15.9	3.7
n-PrOH	3.32	9.5	4.2	15.9	3.7
<i>i</i> -PrOH	3.33	9.4	4.2	15.7	3.7

^a Abbreviations: MeOH = methanol, EtOH = ethanol, *n*-PrOH = *n*-propanol, *i*-PrOH = *i*-propanol.

Table 4.4. The vertical transition energies $\omega_{l_0}(em.)$ (in eV) and transition dipole moments μ_{l_0} (in Debye) corresponding to the $S_1 \to S_0$ emission, along with the μ_0 and μ_1 dipoles characterizing the S_0 and S_1 states (in Debye) and their ratios for **FR0**-SB in the gas phase and in selected alcohol solvents calculated at the respective S_1 minima following the CC/EOMCC-based protocol described in Computational Details.

Solventa	$\omega_{10}(em.)$	$\mu_{\!\scriptscriptstyle 10}$	$\mu_{\scriptscriptstyle 0}$	$\mu_{\scriptscriptstyle 1}$	$\mu_{\scriptscriptstyle 1}$ / $\mu_{\scriptscriptstyle 0}$
None (gas phase)	3.26	8.9	3.4	10.9	3.2
MeOH	2.68	11.8	6.6	20.0	3.0
EtOH	2.69	11.8	6.5	19.7	3.0
n-PrOH	2.70	11.8	6.5	19.6	3.0
<i>i</i> -PrOH	2.72	11.7	6.4	19.1	3.0

^a Abbreviations: MeOH = methanol, EtOH = ethanol, *n*-PrOH = *n*-propanol, *i*-PrOH = *i*-propanol.

^b Taken from our previous gas-phase CC/EOMCC calculations reported in ref. 101.

Having established the accuracy of our quantum chemistry protocol, we proceed to the discussion of our computational findings regarding the dipole moments of the S₀ and S₁ states and the transition dipoles between them, which are the key quantities for the one- and two-photon absorption cross sections given by Eq's. 4.7 and 4.10, respectively. In the absence of direct experimental information, our computations provide insights into the effects of solvation on these quantities. To begin with, as reported in our earlier work for the bare FR0-SB species, 101 and as shown in Table 4.3, there is a large, by a factor of more than 3, increase in the electronic dipole moment following $S_0 \rightarrow S_1$ photoabsorption, giving rise to the superbase character of **FR0**-SB*. Upon solvation, both S₀ and S₁ dipole moments of the **FR0**-SB chromophore are significantly enhanced, becoming approximately twice as large as their gas-phase counterparts. This can be attributed to the polarization of the electron cloud of the FR0-SB photobase by the alcohol molecules surrounding it. Furthermore, the fact that the electronic dipole moment characterizing the S_1 state is much larger than its S_0 counterpart translates into a stronger stabilization of the S_1 state relative to S_0 , leading to lower $S_0 \to S_1$ vertical excitation energies in the case of FR0-SB in alcohol solvents when compared to the bare FR0-SB system. The transition dipole moment characterizing the $S_0 \rightarrow S_1$ photoabsorption process is amplified by solvation as well (by about 40 %), which results in larger OPE and TPE absorption cross sections for the solvated FR0-SB species relative to their gas-phase values. Similar trends are observed when we examine the dipoles and transition dipoles shown in Table 4.4. It is also interesting to note that the dipole moments characterizing the S₀ and S₁ states and the corresponding transition dipoles increase upon geometrical relaxation from the S₀ to S₁ minima, with a concomitant red shift in the vertical transition energies. This bathochromic shift is more pronounced in the case of the solvated FR0SB species as a consequence of μ_1 being much larger than μ_0 , implying a stronger stabilization of the S_1 state due to the polar solvent environment compared to the S_0 state.

As already alluded to above, the transition dipole moments characterizing the S₀-S₁ absorption and emission processes and the S₀ and S₁ dipoles at the respective potential minima could not be determined from our experiments. However, by analyzing the solvatochromic shift of the absorption and fluorescence bands in sixteen different solvents as a function of solvent dielectric constant and index of refraction, we could estimate the magnitude of the transition dipole moment μ_{0} and the change in the dipole moment, $\Delta \mu_{10}$, associated with the $S_0 \to S_1$ adiabatic excitation. Based on our analysis, we found $_{\Delta \mu_{10}}$ of **FR0**-SB in the alcohol solvents considered in our experiments to be ~15 Debye, a magnitude usually associated with substantial charge-transfer, and $\mu_{\text{\tiny 10}}$ to be about 10 Debye. Having access to the dipole moments characterizing the S₀ and S₁ states at their respective minimum-energy structures and the vertical transition dipole moments associated with the S₀–S₁ transitions resulting from our quantum chemistry computations (see Tables 3 and 4) allowed us to assess the quality of our experimentally derived values of μ_{10} and $_{\Delta \mu_{10}}$. As shown in Tables 4.3 and 4.4, the vertical transition dipole moments $_{\mu_{10}}$ characterizing the FR0-SB chromophore in the alcohol solvents included in our calculations range from 9.4 to 11.8 Debye, in very good agreement with the experimentally derived value of about 10 Debye. According to the data collected in Table 4.5, the calculated and experimentally derived changes in the dipole moment associated with the $S_0 \rightarrow S_1$ adiabatic transition, which are about 15 Debye in both cases, are virtually identical. Given that both theory and experiment point to the large values of μ_{10} and $\Delta \mu_{10}$ as a result of solvation and that the dipole pathway defined by the second term in Eq. 4.9 is anticipated to be the dominant TPE pathway, as discussed above, we can

conclude that using Eq. 4.10 in approximating the TPE absorption cross section of **FR0**-SB in alcohol solvents is justified.

Table 4.5. A comparison of the calculated S_0 – S_1 adiabatic transition energies without $[\omega_{10}(ad.)]$ and with $[\omega_{10}(0-0)]$ zero-point energy (ZPE) vibrational corrections (in eV), along with the differences and ratios of the μ_0 and μ_1 dipoles characterizing the S_0 and S_1 states at the respective minima (in Debye) for **FR0**-SB in the gas phase and in selected alcohol solvents obtained following the CC/EOMCC-based protocol described in Computational Details with the corresponding experimentally derived data.

	Theory			Experiment				
Solventa	$\omega_{10}(ad.)$	$\omega_{10}(0-0)^{b}$	$\Delta \mu_{10}$	μ_1 / μ_0^c	Solventa	$\omega_{10}(0-0)$	$\Delta \mu_{ 1 0}^{ \mathrm{d}}$	$\mu_{\scriptscriptstyle 1}$ / $\mu_{\scriptscriptstyle 0}{}^{^{ m d}}$
None (gas phase)	3.42	3.33	8.3	4.2	c-Hexane	3.4	_	_
MeOH	2.88	2.80	15.6	4.6	МеОН	2.9	15.2 ± 0.2	4.4 ± 0.1
EtOH	2.89	2.80	15.4	4.6	EtOH	3.0	15.3 ± 0.3	4.6 ± 0.1
n-PrOH	2.89	2.81	15.3	4.6	n-PrOH	3.0	15.3 ± 0.3	4.6 ± 0.1
<i>i</i> -PrOH	2.88	2.80	14.9	4.5	<i>i</i> -PrOH	3.0	15.5 ± 0.5	4.7 ± 0.1

^a Abbreviations: MeOH = methanol, EtOH = ethanol, n-PrOH = n-propanol, i-PrOH = i-propanol, c-Hexane = cyclohexane.

By forming the ratio of Eq's. 4.7 and 4.10, we can obtain a new expression that summarizes the difference between OPE and TPE, in which the change in permanent dipole moment acts as an amplification factor,

$$\frac{\sigma_{f_0}^{(2)}(\omega/2)}{\sigma_{f_0}^{(1)}(\omega)} = \frac{B'}{A} \frac{\left|\Delta\mu_{f_0}\right|^2 \left|\mu_{f_0}\right|^2 g_{M_2}(\omega)}{\left|\mu_{f_0}\right|^2 g_{M_1}(\omega)} = C \frac{\left|\Delta\mu_{f_0}\right|^2 g_{M_2}(\omega)}{g_{M_1}(\omega)},$$
(4.11)

where C = B'/A. The difference between OPE and TPE typically arises from differences in the expressions for the line shapes, which in the case of large organic molecules in solution, are the Franck-Condon distribution convolved with the extensive homogeneous and inhomogeneous broadening. We have acquired these spectra for **FR0**-SB in cyclohexane, acetonitrile, and

^b Calculated as ω_{10} (ad.) + Δ ZPE , where Δ ZPE is the difference between the zero-point vibrational energies characterizing the S₁ and S₀ electronic states of the bare **FR0**-SB molecule in the gas phase computed at the CAM-B3LYP/6-31+G* level of theory. Our calculations with and without solvent indicate that the effect of solvation on Δ ZPE is negligible (less than 0.01 eV).

^c Calculated using the μ_0 values reported in Table 4.3 and the μ_1 values reported in Table 4.4.

^d Calculated using the theoretical values of μ_0 reported in Table 4.3 and based on the analysis of the experimental solvatochromic shifts.

methanol, as shown in Figure 4.7. From these spectra, we can obtain the ratio of the spectral line shapes for OPE and TPE.

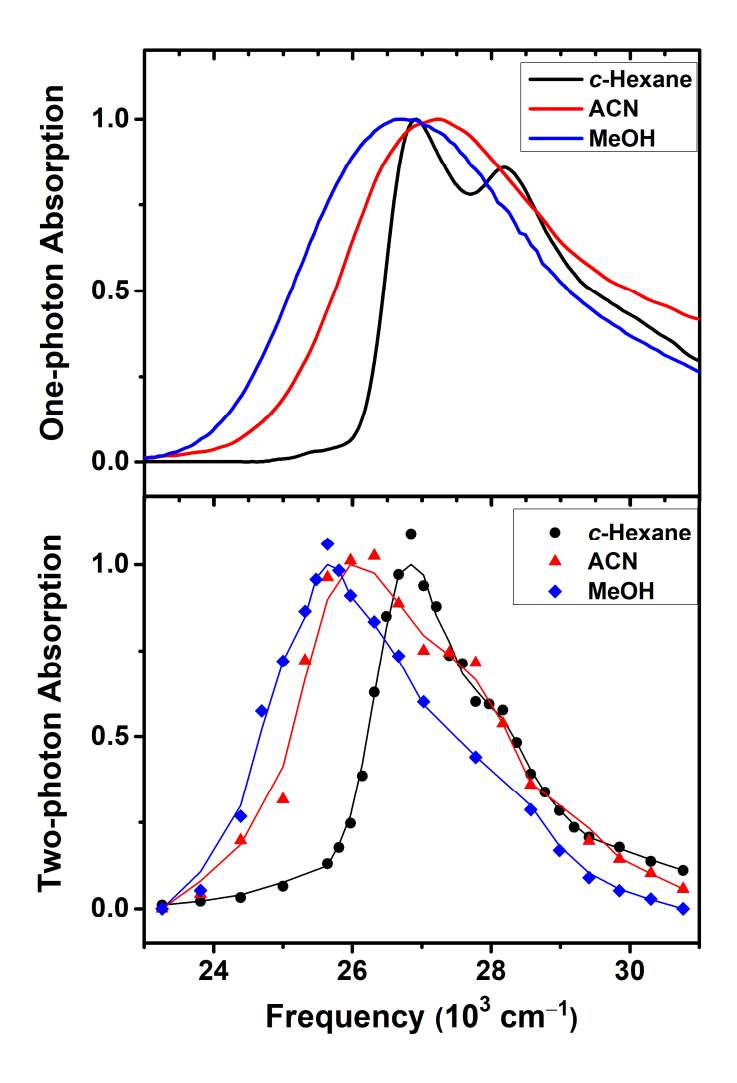


Figure 4.7. OPE and TPE spectra for **FR0**-SB in cyclohexane (*c*-Hexane), acetonitrile (ACN), and methanol (MeOH). The solid line shown for the two-photon spectra is the result of 3-point smoothing and is included as a guide to the eye.

For cyclohexane, a non-polar solvent for which the change in permanent dipole moment is smallest, the excitation maximum for OPE and TPE coincide, and the ratio between the line shapes can be fit to a line with a negative slope from the peak to higher energies, indicating a steeper decline of the spectrum as a function of excitation energy for TPE. The steeper decline is consistently observed for acetonitrile and for methanol. However, for acetonitrile and methanol

we also see that the two-photon absorption peaks appear at significantly lower energies than their OPE counterparts. The largest shift of the TPE absorption maximum compared to OPE, of ~1,140 cm⁻¹, is observed for methanol. Differences between OPE and TPE have been observed experimentally, in particular as blue shifts in the TPE of the green fluorescent protein, ¹⁶⁸ and have been explained as non-Condon contributions to TPE. ¹⁶⁹ However, the large red shift observed in this work appears to be unprecedented.

Having strong evidence that TPE must be reaching parts of the S₁ potential surface that enhance reactivity compared to the isoenergetic OPE and that the initial state wave packet following TPE is different than that following OPE, we turn our attention to the relationship between the ESPT enhancement, the inhomogeneous broadening, and the significant red shift observed in our TPE experiments. It is well-established that polar solvents, in particular those capable of forming hydrogen bonds, are responsible for significant inhomogeneous broadening in absorption spectra. 170,171 The inhomogeneous broadening can further be amplified when the solute has hydrogen-bond acceptor and/or donor functional groups and undergoes large permanent dipole changes upon photoexcitation. 170 From Eq. 4.10, we learn that TPE is greatly enhanced by the $\left|\Delta\mu_{f0}\right|^2$ term, favoring chromophore molecules whose local solvation environment gives rise to larger $\Delta\mu_{f0}$ values compared to OPE. The substantial increase in the dipole moment upon photoexcitation should result in the different configurations in which protic solvents can be arranged to solvate FR0-SB, giving rise to inhomogeneous broadening. At the same time, larger $\Delta\mu_{f0}$ results in the additional stabilization of the [FR0-SB···HOR] complex in the S₁ state relative to the ground state, manifesting itself in the observed red shift in the absorption maximum. While this hypothesis needs additional thorough investigations using, for example, two-dimensional

spectroscopy and molecular dynamics simulations of the observed excited-state reactivity, it is conceivable that the dynamical restructuring of the solvent around the chromophore molecules following TPE, promoting larger $\Delta\mu_{f0}$ values compared to OPE, results in stronger charge-transfer between the amine and imine nitrogens of **FR0**-SB, the additional accumulation of negative charge on the imine nitrogen, and, subsequently, the enhancement of the ESPT process, which is what we attempted to schematically illustrate in Figure 4.1(b). This is in contrast to some intramolecular ESPT reactions, such as in diethylaminohydroxyflavone, where solvation is inversely correlated with proton transfer.¹⁷² The differences observed in **FR0**-SB following OPE or TPE are caused by the large change in permanent dipoles influencing the probability for TPE of some molecules. Molecules with a solvent configuration that is more likely to result in proton transfer would then be favored to undergo TPE because of their larger $|\Delta\mu_{f0}|^2$ values.

We find support for the role of inhomogeneous broadening in protic solvents in the experimental data. We note that there is essentially no shift between the maxima for OPE and TPE for cyclohexane, a non-polar molecule. There is a $\sim 1,000 \text{ cm}^{-1}$ shift observed for acetonitrile, and a $\sim 1,140 \text{ cm}^{-1}$ shift for methanol. These shifts are not predicted simply by the non-Condon vibrational makeup of the excited-state wave packet. The existence of differently solvated species, in particular those exhibiting greater dipole moment changes, can be determined experimentally by comparing the absorption spectra for **FR0**-SB in solvents that exhibit TPE enhancement (methanol, ethanol, *n*-propanol) with that of **FR0**-SB in *i*-propanol, which does not. The comparison is shown in Figure 8, where we plot the absorption spectra as well as the difference between the absorption spectrum in each solvent and that in *i*-propanol. We observe a large difference in the absorption spectra, especially at 25,000 cm $^{-1}$, where the experiment was carried out. The largest difference is found for methanol, which exhibits the largest TPE enhancement.

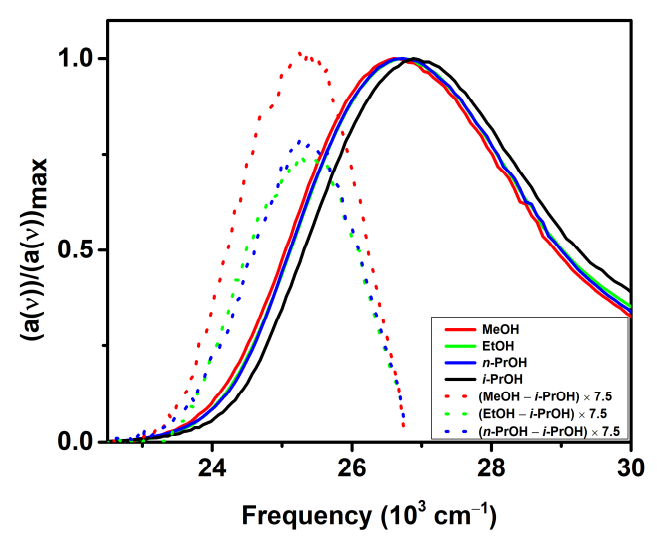


Figure 4.8. Absorption spectra of **FR0**-SB in methanol (MeOH), ethanol (EtOH), n-propanol (n-PrOH), and i-propanol (i-PrOH) (solid lines) and difference between these spectra and the absorption in i-propanol (dotted lines). We find a significant difference between the spectra in the 25,000 cm⁻¹ energy region where the experiment was performed.

From Figure 4.8, we can see significant inhomogeneous broadening toward lower energies. This supports our hypothesis that there is a clear bias toward TPE in the case of molecules primed for proton transfer, as seen in the reduction of the protonation time in methanol and ethanol by a factor of two compared to the other alcohol solvents. The effect becomes attenuated for *n*-hexanol, given that the long alkyl chain reduces the chances for two or more hydroxyl moieties to be next to the imine group where proton transfer takes place. As shown in our computations and OPE experiments reported in ref. 153, the solvent configuration leading to proton transfer in *i*-propanol is much less likely, resulting in very low efficiency of the ESPT process, and, thus, TPE can no longer enhance it, confirming our hypothesis.

4.4 Conclusion

In this paper we have presented the observation of up to 62 % enhancement in the reactivity of the super photobase **FR0**-SB following isoenergetic two-photon excitation. We have reported evidence that excitation is to the first excited singlet state, S₁, and that no other excited state contributes to proton transfer via one- or multi-photon excitation. We have found that the magnitude of the enhancement in reactivity correlates with the protonation rate; thus, it is faster for methanol, but slows down with longer chain alcohols and is not measurable for *i*-propanol.

We have reached the conclusion that the enhanced solvent-to-solute ESPT reactivity is the result of TPE creating a more reactive species than OPE. This is supported by analysis of the molecular properties that contribute to the one- and two-photon transition probabilities, namely, the transition dipole moment μ_{10} coupling the S₀ and S₁ states of **FR0**-SB and the $\Delta \mu_{10}$ difference between the dipole moments of these two states. According to our mathematical manipulations, the ratio of the TPE and OPE absorption cross sections depends on $\Delta \mu_{10}$ but not on μ_{10} . The $\Delta \mu_{10}$ values resulting from the high-level CC/EOMCC-based computations performed in this study were practically identical to those estimated from our experiments. We learned that the very large change in permanent dipoles between the ground and excited states of **FR0**-SB amplifies differences in the spectroscopic line shape, leading to non-Condon contributions and different vibrational makeups of the initial excited-state wave packet.

Finally, we have considered inhomogeneous broadening as providing an additional aspect leading to different excited-state species accessed via TPE. The permanent dipole change is highly dependent on the arrangement of polar solvent molecules, especially for protic solvents capable of hydrogen bonding. These added contributions are confirmed by the red shift observed in the TPE spectra for acetonitrile and methanol, but not for cyclohexane, and by the greater inhomogeneous

broadening toward the low energy region in the OPE spectra of solutions exhibiting TPE enhancement. The findings reported here help explain the observation by Tokumura and Itoh on the intramolecular proton transfer in 7-hydroxyquinoline in methanol solution via two-photon excitation. In that study, two-photon excitation in the 210–250 nm equivalent wavelength region leads to exclusive emission from the proton transfer state. Later measurements, based on step-wise solvation supersonic-jet spectroscopy, Italiant identified that bridging methanol structures with three methanol molecules help facilitate the proton transfer. These two separate observations support our conclusion that two-photon excitation favors structures primed for excited-state proton transfer.

In conclusion, we have reported unprecedented 62% enhancement in photochemical reactivity upon isoenergetic two-photon excitation compared to one-photon excitation. The long-term goal of our research is to develop tools for precision chemistry and our findings indicate that two-photon excitation not only provides spatial and temporal control, but it can also bring about enhanced reactivity. Future work will include quantitative determination of the two-photon absorption cross section for **FR0**-SB in different solvents and of newly developed compounds.

Chapter 5 Controlling Quantum Interference between Virtual and Dipole Two-Photon Optical Excitation Pathways using Phase-Shaped Laser Pulses

Two-photon excitation (TPE) proceeds via a "virtual" pathway, which depends on the accessibility of one or more intermediate states, and, in the case of non-centrosymmetric molecules, an additional "dipole" pathway involving the off-resonance dipole-allowed one-photon transitions and the change in the permanent dipole moment between the initial and final states. Here, we control the quantum interference between these two optical excitation pathways by using phase-shaped femtosecond laser pulses. We find enhancements by a factor of up to 1.75 in the two-photon-excited fluorescence of the photobase **FR0**-SB in methanol after taking into account the longer pulse duration of the shaped laser pulses. Simulations taking into account the different responses of the virtual and dipole pathways to external fields and the effect of pulse shaping on two-photon transitions are found to be in good agreement with our experimental measurements. The observed quantum control of TPE in condensed phase may lead to enhanced signal at a lower intensity in two-photon microscopy, multiphoton-excited photo reagents, and novel spectroscopic techniques that are sensitive to the magnitude of the contributions from the virtual and dipole pathways to multiphoton excitations.

This chapter has been adapted with permission from (*J. Phys. Chem. A* **2021**, *125*, 7534-7544) Copyright © 2021, American Chemical Society.

5.1 Introduction and Background

Control of two-photon transitions using shaped laser pulses in atomic¹⁷⁵ and condensed phase^{40,176,177} systems has primarily been accomplished by taking advantage of the direct relationship between the second-order power spectrum (SOPS) of the field and the spectral phase of the pulse. In fact, this dependence has enabled selective two-photon excitation (TPE) and the measurement of TPE spectra.^{178–183} Here, we address the quantum interference between the virtual and dipole optical pathways that connect the ground and excited electronic states of a molecule during TPE. In particular, we consider the case of a non-centrosymmetric molecule for which, in addition to the sum over intermediate "virtual" states, one is able to identify a dipole contribution which becomes significant for species with large change in the permanent dipole moment upon photoexcitation.

In their theoretical investigations, Meath and coworkers proposed how the phase difference between a pair of monochromatic pulses could be used to control two-photon transitions in isolated diatomic molecules with permanent dipoles by taking advantage of the different responses of the virtual and dipole pathways to the electric fields. ^{159,184} In a related experiment, the TPE of Rb atoms through an intermediate state was found to be favored by phase- or amplitude-shaped pulses rather than by transform-limited (TL) pulses. ¹⁸⁵ It was observed that by removing certain portions of the pulse spectrum, which decreased the peak intensity by a factor of 40, the TPE rate doubled relative to TL pulses. The observed control was due to differences in the optical response to the field by the resonant and non-resonant excitation pathways. While contributions from both virtual and dipole pathways have been implicated in the magnitude of the two-photon absorption cross section, ^{163,164} their control via phase-shaped pulses has not been reported. For a given molecule, the inherent molecular phases associated with the virtual and dipole pathways are fixed. However,

the goal of the present work is to use phase-shaped pulses designed to drive the virtual and dipole pathways with an independently adjustable phase, so that one is able to control the probability of TPE.

Here, we control the TPE pathways of the fluorescent Schiff photobase (E)-7-((butylimino)methyl)-N,N-diethyl-9,9-dimethyl-9H-fluoren-2-amine (FR0-SB, Scheme 5.1), in solution. 11,101,153 This compound, in addition to exhibiting an increase in pKa by 14 units upon photoexcitation, was recently found to become up to 62% more reactive when the first excited singlet (S₁) state was populated via TPE instead of single-photon excitation.² This is a consequence of the very large differences between the ground- and excited-state dipole moments $\Delta \mu_{10} = \mu_1 - \mu_0$ and the large values of the corresponding transition dipole moments μ_{10} (for example, $\Delta \mu_{10} = 15.6$ D and $\mu_{10} = 9.6$ D for **FR0-SB** in methanol).² In this study, we develop the theoretical basis for the effect of shaped pulses, which are far from one-photon resonance with the electronic transition to S₁ but on-resonance with TPE to the S₁ state, on the virtual and dipole pathway contributions to TPE of molecules with large permanent dipole moments. We then present experimental data showing coherent control of the virtual and dipole contributions to TPE. In particular, we find that for certain shaped pulses the ratio between TPE fluorescence and second harmonic signal can be enhanced by a factor of 1.75, in good agreement with simulations. Our study demonstrates that it is possible to use phase-shaped pulses to control the dipole and virtual contributions to TPE in larger polyatomic molecules in solution.

Scheme 5.1. Molecular structure of the **FR0-**SB super photobase.

5.2 Theory

Since the introduction of the idea of two-photon processes by Maria Göppert-Mayer in 1931^{24} (cf., also, refs ¹⁸⁶ and ¹⁸⁷), perturbation theory has been used to examine their probability and dependence on molecular symmetry. According to the second-order perturbation theory, the $0 \rightarrow f$ two-photon absorption cross section, with 0 and f designating the initial and final states, which in our case are the electronically bound ground (S₀) and excited (S₁) states of **FR0**-SB, respectively, is given by the Göppert-Mayer sum over virtual states

$$\sigma_{f0}^{(2)}(\omega/2) = A \left| \sum_{\nu} \frac{\mu_{f\nu} \mu_{\nu 0}}{\omega_{\nu 0} - \omega/2 + i\Gamma_{\nu}(\omega/2)} \right|^{2} g_{M2}(\omega), \qquad (5.1)$$

where ω is the resonance excitation frequency, A is a collection of constants, v are the intermediate states, μ_{fv} and $\mu_{v,0}$ are the transition dipole moments corresponding to the $v \to f$ and $0 \to v$ excitations, respectively, $\omega_{v,0}$ is the $0 \to v$ transition frequency, $i\Gamma_{v}(\omega/2)$ is a damping factor associated with the intermediate state v, which is inversely proportional to the lifetime of v, and $g_{M2}(\omega)$ is the TPE line shape function. Note that in presenting Eq. 5.1, we have performed an isotropic averaging over the directions of the transition dipole moment vectors $\mu_{v,0}$. For noncentrosymmetric molecules, one can separate the v0 v1 dipole contribution from the sum over states expression, Eq. 5.1, to obtain v2,158,160,163

$$\sigma_{f0}^{(2)}(\omega/2) = A \left| \sum_{\nu \neq 0, f} \frac{\mu_{f\nu} \mu_{\nu 0}}{\omega_{\nu 0} - \omega/2 + i\Gamma_{\nu}(\omega/2)} + \frac{\mu_{f0} \Delta \mu_{f0}}{\omega/2} \right|^{2} g_{M2}(\omega),$$
 (5.2)

where $\Delta \mu_{f0} = \mu_f - \mu_0$ is the difference between the dipole moments characterizing the final and initial states. To do this, we isolate the v = 0 and v = f terms in the summation over v in Eq. 5.1, $\mu_{f0}\mu_{00}/[\omega_{00}-\omega/2+i\Gamma_{0}(\omega/2)]$ and $\mu_{ff}\mu_{f0}/[\omega_{f0}-\omega/2+i\Gamma_{f}(\omega/2)]$, respectively, which involve off-resonance dipole-allowed one-photon $_{0} \rightarrow f$ transitions, recognize that $_{\omega_{00}} = 0$, replace \mathcal{O}_{f0} by the resonance frequency ω , and take advantage of the fact that the initial and final states are stationary, so that the damping factors $i\Gamma_0(\omega/2)$ and $i\Gamma_f(\omega/2)$ can be assumed to be zero. The resulting $\mu_{f0}\mu_{00}/(-\omega/2)$ and $\mu_{ff}\mu_{f0}/(\omega/2)$ contributions can be recombined into the expression $\mu_{f0}(\mu_{ff}-\mu_{00})/(\omega/2)$, which is equivalent to the second term on the right-hand side of Eq. 5.2. The first term on the right-hand side of Eq. 5.2, which involves the intermediate states v between the initial and final states, is usually called the virtual pathway, while the second term, which depends on the transition dipole moment μ_{f0} and the difference between the ground- and excited-state permanent dipole moments $\Delta\mu_{f0}$, is commonly referred to as the dipole pathway. 159 It is worth mentioning that while the cross-section contributions from both pathways are proportional to the intensity of light squared, the dipole pathway, which is, in part, driven by offresonance one-photon transitions to a stationary state f, has a weaker dependence on the pulse duration compared to its virtual counterpart.

The introduction of femtosecond laser pulses has greatly contributed to the development of TPE techniques. This is because broadband femtosecond pulses enable contributions from a very large number of possible intermediate states, ensuring that some frequencies $\omega_{v,0}$ in Eq's. 5.1 and 5.2 are close to ω / 2, and the high peak intensity of such pulses reduces the need for the

 $_{i\Gamma_{v}(\omega/2)}$ damping factors to become small to result in a measurable TPE signal. It should also be noted that non-centrosymmetric molecules, such as **FR0**-SB examined in this work, have a non-zero $\Delta\mu_{f0}$, so that both the virtual and dipole pathways present in Eq. 5.2 can contribute to TPE, further enhancing the two-photon absorption cross sections. ¹⁶⁴

The two pathways available for TPE have a phase difference that arises from the complex nature of the different matrix elements in Eq. 5.2. This phase difference may lead to quantum interference that could modulate the two-photon absorption cross section. Jagatap and Meath considered the competition between the virtual and dipole pathways and derived an expression for the orientationally averaged probability of TPE. 159 Based on their calculations for the LiH molecule, the quantum interference between the virtual and dipole pathways can be constructive or destructive. While TPE is fundamentally different than Young's double slit experiment or quantum control of molecular excitations, one might try to adopt a heuristic approach and use analogies with these phenomena to explain the possibility of modulating the probability for TPE through quantum interference of the virtual and dipole pathways. For example, if $_{\phi}$ and $_{\phi_2}$ designate phases associated with interfering waves in Young's double slit experiment, the probability of constructive interference P depends on the phase difference according to $P \propto \left| e^{i\phi_1} + e^{i\phi_2} \right|^2 = 2 + 2\cos(\phi_1 - \phi_2)$. Similar interference can be observed in quantum control of molecular excitations, introduced by Brumer and Shapiro¹⁸⁸ and realized experimentally by Gordon and coworkers for one- versus three-photon transitions.¹⁸⁹ Gordon and coworkers' excitation pathways involved two laser sources with frequencies 3ω and ω . Assuming that each pathway contributes equally, the probability for reaching the final state is given by

 $P_{f0} \propto \left| e^{i\phi_1} + e^{i3\phi_1} \right|^2 = 2 + 2\cos(\phi_3 - 3\phi_1)$, where ϕ_3 and ϕ_1 are the phases of one- and three-photon excitations, respectively. Chen et al. have also examined quantum control of molecular excitation using two-photon vs. two-photon interference, where a molecule is irradiated with three interrelated frequencies ω_0 , ω_+ , and ω_- , such that $2\omega_0 = \omega_+ + \omega_-$, and where the probability for reaching the final state is given by $P_{f0} \propto \left| e^{i2\phi_0} + e^{i(\phi_0 + \phi_0)} \right|^2 = 2 + 2\cos(2\phi_0 - \phi_+ - \phi_-)$. The experimental realization of their idea was accomplished by broadband shaped femtosecond pulses, both in the gas phase 175,192,193 and in condensed phase systems. Two-photon transitions involving virtual and dipole pathways should be controllable in a similar manner. Indeed, if we assume that none of the intermediate states v in Eq. 5.2 are long lived and designate the average phase of the virtual pathway as ϕ_v and the phase associated with the dipole pathway as ϕ_d , we can use arguments similar to those presented above to re-express the $0 \to f$ two-photon absorption cross section as

$$\sigma_{f0}^{(2)}(\omega/2) \propto \left| e^{i2\phi_v} + e^{i2\phi_d} \right|^2 = 2 + 2\cos(2\phi_v - 2\phi_d). \tag{5.3}$$

This shows that one should be able to modulate the probability for TPE through quantum interference of the two pathways.

We now describe the model which will allow us to examine how the interference between the virtual and dipole pathways contributing to TPE in non-centrosymmetric molecules, such as **FR0-SB**, is affected by broadband-shaped laser pulses. Two-photon transitions in the absence of long-lived intermediate states are driven by the shaped laser field, which induces a nonlinear polarization proportional to the square of the time-dependent electric field E(t). Because pulse shapers operate in the frequency domain, ¹⁹⁴ we start with the field in the frequency domain

$$E(\omega/2) = \sqrt{I(\omega/2)}e^{i\bar{\varphi}(\omega/2)}, \tag{5.4}$$

where $I(\omega/2)$ is the spectrum of the pulse and $\overline{\varphi}(\omega/2)$ is the spectral phase, both of which can be modified by the pulse shaper. Using the field in the frequency domain and the convolution theorem, the Fourier transform of $E^2(t)$ can be written as $E^{176,195}$

$$E^{(2)}(\omega) \propto \int_{-\infty}^{\infty} \left| E(\omega/2 + \Omega) \right| \left| E(\omega/2 - \Omega) \right| \exp \left\{ i \left[\overline{\varphi}(\omega/2 + \Omega) + \overline{\varphi}(\omega/2 - \Omega) \right] \right\} d\Omega, \tag{5.5}$$

where one integrates over all the detuning frequencies from $\omega/2$ by a positive and negative amount Ω , as the two-photon frequency ω can be attained by adding the negatively detuned frequencies to the corresponding positively detuned frequencies. Eq. 5.5 is important for us, since one can use it to simulate the SOPS by determining the values of $\left|E^{(2)}(\omega)\right|^2$ in which the phase of the field at frequency ω is given by the sum inside the square brackets appearing in Eq. 5.5. The simulated SOPS can then be directly compared to the second harmonic generation (SHG) spectrum, which is also given by $\left|E^{(2)}(\omega)\right|^2$, provided that the SHG crystal is thin enough to phase match the entire bandwidth of the pulse. The dependence of SHG on spectral phase, 183 such as chirp and third-order dispersion, has been used by the Dantus group to develop a number of highly accurate pulse characterization and compression methods based on the principle of multiphoton intrapulse interference phase scan (MIIPS), 43,196-204 which is employed in this study as well.

For simulating and carrying out the control experiments reported in this work, we used well-defined spectral functions to ensure that the observed quantum control is not caused by tuning the frequency of the TPE field. The form of the spectral phase functions, which we adopted in this study and which is shown in Figure 1a, resembles a window having zero phase for all frequencies

except for a region of given width in the center of the spectrum that has a constant phase which is scanned during the experiment. By inspecting Eq. 5.5, one can obtain the phase of the field at frequency ω as the sum of the phases that are symmetrically detuned around $\omega/2$. In the present study, we report results for the phase value scanned from -2π to 2π in order to modulate the relative contributions from the dipole and virtual pathways, as further discussed below. When the phase has a value $n\pi$, with n an even integer, the pulses are of the TL type and favor the virtual pathway. For phases where n is an odd integer, the pulses are longer and favor the dipole pathway.

The expected effect of the phase scan on the SOPS, obtained as a contour plot of $\left|E^{(2)}(\omega)\right|^2$ calculated using Eq. 5.5 for 16.6 fs pulses, is shown in Figure 1b. In Figure 1c, we show the experimentally obtained SHG spectrum as a function of the 40 nm phase window being scanned from -2π to 2π . The excellent agreement between theory (Figure 5.1b) and experiment (Figure 5.1c) required careful pulse compression and a very thin SHG crystal, both described in the Experimental Details section below. The data in Figure 5.1b and c show areas where constructive (red color, when the phase window is 0 or $\pm 2\pi$) and partial destructive (blue color, when the phase window is $\pm \pi$) interferences take place.

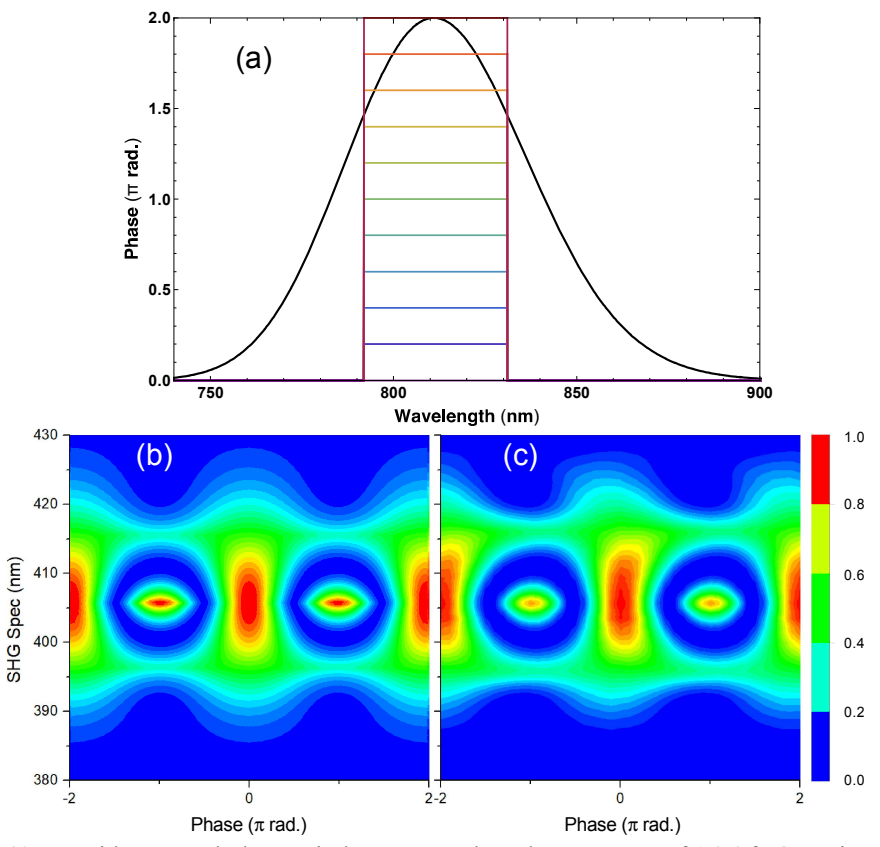


Figure 5.1. (a) A 40 nm wide spectral phase window centered on the spectrum of 16.6 fs Gaussian pulses at 811 nm resulting from the phase scanning from 0 to 2π . (b) Calculated SOPS resulting from scanning the phase window from -2π to 2π . (c) Experimental SHG spectrum as a function of the same phase window scan as used in (b). In panels (b) and (c), areas where constructive and partial destructive interferences take place are colored red and blue, respectively.

The efficiency of TPE depends not only on the phase of the pulse, but also on the overlap between the SOPS and the two-photon absorption spectrum of the chromophore. Therefore, we need to make sure that the latter factor stays constant, given that our interest is to control the interference between the virtual and dipole pathways in TPE. As mentioned above, the chosen phase window function preserves the central wavelength of the SOPS, ensuring that changes in excitation probability are minimized (Figure 5.1b and c). We provide further verification of this in Figure 5.2. Specifically, in Figure 5.2a we present the SOPS data for shaped pulses using a 40 nm wide phase window with different amplitudes, plotted together with the TPE spectrum of **FR0**-SB in methanol using the data points reported in ref. 2. As demonstrated in Figure 5.2a, the SOPS remains centered at 405.5 nm as the amplitude of the phase window changes. In Figure 5.2b we

show the SHG intensity, the simulated two-photon excited fluorescence (TPEF) corresponding to the overlap integral between the SOPS and the TPE spectrum of **FR0-**SB, and the ratio between these two quantities as functions of the phase of the 40 nm window. We find that the overlap between the SOPS and the two-photon absorption spectrum of the chromophore differs only very little from the SHG signal, as shown in Figure 5.2b. Hence, the ratio between these two quantities remains close to 1, with variations of less than 3% for all phase amplitudes. Although not shown in Figure 5.2b, the same is observed for the other window widths used in this work.

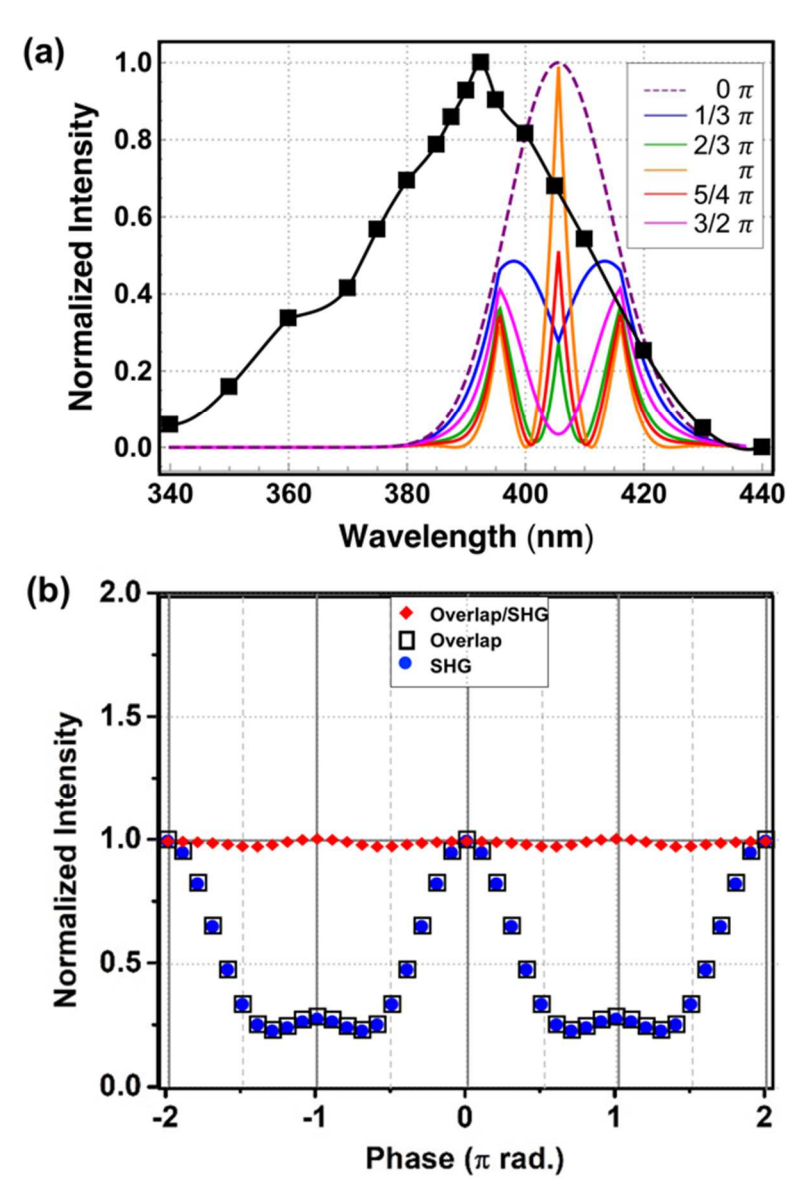


Figure 5.2. (a) The TPE spectrum of **FR0**-SB in methanol (black squares), based on the data points reported in ref. 2, along with the SOPS for the 40 nm wide phase window at selected amplitudes. Note that as the phase amplitude changes the SOPS remains centered at 405.5 nm. (b) The results of simulations of the TL-normalized overlap integral between the SOPS and the TPE spectrum of **FR0**-SB in methanol (black open squares), the TL-normalized SHG signal (blue circles), and the ratio of the two signals (red diamonds) as functions of the spectral phase of the 40 nm window.

Having demonstrated the validity of Eq. 5.5, we transform Eq. 5.2, with the help of Eq's. 5.4 and 5.5, into a formula that one can use to predict how two-photon transitions in non-centrosymmetric molecules are affected by broadband-shaped laser pulses. Given that the coherent superpositions of tens or hundreds of intermediate states v in Eq. 5.2, which are expected to have small Frank–Condon factors, are short lived, we assume that the virtual pathway behaves as a

parametric process. Thus, we describe the virtual pathway using Eq. 5.5, which is similar to the approximation adopted by Silberberg and coworkers in simulating the non-resonant TPE path. As implied by Eq. 5.2, the dipole pathway contains the action of the field on the transition dipole moment μ_{f0} and on the difference between the ground- and excited-state permanent dipoles μ_{f0} , which include the aforementioned phase lag, designated here as ϕ . Thus, given the fact that the dipole-allowed one-photon transitions between the initial and final stationary states associated with μ_{f0} are not significantly affected by pulse duration, we represent the dipole pathway contribution to Eq. 5.2 by multiplying the square of $E(\omega/2)$, as defined by Eq. 5.4, by the phase lag term $e^{i\phi}$, while incorporating the orientationally averaged μ_{f0} and μ_{f0} values in an empirical constant μ_{f0} that describes the relative contribution of the two pathways. The resulting expression for the probability of TPE, which allows us to simulate the effect of shaped laser pulses on two-photon transitions in non-centrosymmetric molecules, is as follows:

$$P_{f0}^{(2)}(\omega/2) \propto \left| E^{(2)}(\omega) + \frac{aE^2(\omega/2)e^{i\phi}}{\omega/2} \right|^2 g_{M2}(\omega).$$
 (5.6)

In transitioning from Eq. 5.2 to Eq. 5.6, we adopted a simplifying assumption where the contributions of all intermediate states v to the TPE absorption cross section, including vibronic components, are lumped into a single electronic state. While we realize the limitations of this assumption, expanding our analysis to explicitly include vibrational modes that may be accessed by the broadband pulse and the effects of homogeneous and inhomogeneous broadening caused by the solvent is outside of our present modeling capabilities. Note that because our experiments are carried out with broadband femtosecond laser pulses, the determination of the $E^{(2)}(\omega)$

contribution to Eq. 5.6 for a given spectral phase function $\overline{\varphi}(\omega/2)$ requires the integration over all Ω values in Eq. 5.5.

In the experiments reported in this work, we measured the frequency integrated TPEF signal obtained for shaped pulses, $S_{\text{shaped}}^{\text{TPEF}}$, relative to that obtained for TL pulses, $S_{\text{TL}}^{\text{TPEF}}$. Based on the considerations described above, one should be able to model the ratio of the frequency integrated TPEF signals obtained using shaped and TL pulses using the following expression:

$$S_{\text{shaped}}^{\text{TPEF}} / S_{\text{TL}}^{\text{TPEF}} = \frac{\int_{-\infty}^{\infty} \left| E^{(2)}(\omega) + aE^{2}(\omega/2)e^{i\phi} / (\omega/2) \right|_{\text{shaped}}^{2} d(\omega/2)}{\int_{-\infty}^{\infty} \left| E^{(2)}(\omega) + aE^{2}(\omega/2)e^{i\phi} / (\omega/2) \right|_{\text{TL}}^{2} d(\omega/2)}.$$

$$(5.7)$$

In writing Eq. 5.7, we assumed that the TPE line shape $g_{\text{M2}}(\omega)$ in Eq. 5.6 is a slowly varying function of ω , so that one can cancel it out. Indeed, when we included the TPE line shape function $g_{\text{M2}}(\omega)$ in the determination of the $S_{\text{shaped}}^{\text{TPEF}}/S_{\text{TL}}^{\text{TPEF}}$ values using the two-photon absorption cross section of **FR0-SB** in methanol from ref. 2, its effect on the simulated signal was very small. We used Eq. 5.7, with $E^{(2)}(\omega)$ and $E(\omega/2)$ determined using Eq's. 5.4 and 5.5, respectively, in our simulations, comparing the resulting $S_{\text{shaped}}^{\text{TPEF}}/S_{\text{TL}}^{\text{TPEF}}$ values obtained at the different phases and window widths with the experimental data. In determining the spectrum of the pulse entering Eq. 5.4, we used the expression $I(\omega/2) = e^{-[\tau_{\text{F}}(\omega/2-\omega_0)/g]^2}$, where τ_{F} is the pulse duration full-width at half maximum (FWHM) of the Gaussian pulses, $g = 2\sqrt{\log 2}$, and ω_0 is the center frequency of the laser. In the simulations shown in this work, we used $\tau_{\text{F}} = 1.6.6$ fs and $\omega_0 = 2 \, \pi \, \text{c} \, / \, \lambda$, with c being the speed of light and $\lambda = 811 \, \text{nm}$, and the phase window was centered at the center frequency of the laser pulses. The phase lag associated with the dipole pathway that best

reproduced the experimental data was $\phi = 0.46\pi$, and the value of the empirical constant a in Eq. 5.7 that worked best was 0.075. In simulating the $S_{\text{shaped}}^{\text{TPEF}}/S_{\text{TL}}^{\text{TPEF}}$ ratio as a function of the phase window, we varied the window phase from -2π to 2π and the window width from 10 nm to 50 nm. We also simulated the ratio of the frequency integrated SHG signals obtained for shaped and TL pulses as a function of the phase window using the formula

$$S_{\text{shaped}}^{\text{SHG}} / S_{\text{TL}}^{\text{SHG}} = \frac{\int_{-\infty}^{\infty} \left| E^{(2)}(\boldsymbol{\omega}) \right|_{\text{shaped}}^{2} d(\boldsymbol{\omega}/2)}{\int_{-\infty}^{\infty} \left| E^{(2)}(\boldsymbol{\omega}) \right|_{\text{TI}}^{2} d(\boldsymbol{\omega}/2)}, \tag{5.8}$$

where $_{E^{(2)}(\omega)}$ was calculated using Eq. 5.5 and the window phase and width were varied in the same way as for $S_{\text{shaped}}^{\text{TPEF}}/S_{\text{TL}}^{\text{TPEF}}$, comparing the resulting $S_{\text{shaped}}^{\text{SHG}}/S_{\text{IL}}^{\text{SHG}}$ with experiment. Finally, we calculated the ratios of the TL-normalized TPEF and SHG signals obtained using Eq's. 5.7 and 5.8, respectively, and compared them to their experimentally determined counterparts. All of the simulations reported in this work were carried out by programming Eq's. 5.4–5.8 using Wolfram Mathematica 11.

To make sure that our model predicting how two-photon transitions in non-centrosymmetric molecules are affected by shaped laser pulses is consistent with the experimental data, it is important to consider situations where the TPEF signal does not exhibit a square law dependence on laser intensity (i.e., the power dependence with n = 2) assumed in our considerations above. Such situations could be caused, for example, by saturation of the two-photon transition. Although saturation was not reached in our experiments, the deviations from a square law dependence of the TPE rate for molecules with large dipole moments have been suggested in ref. 165. We simulate such deviations assuming that no interference occurs between

the virtual and dipole pathways, i.e., the $2 \operatorname{Re} \left([E^{(2)}(\omega)]^* \times a E^2(\omega/2) e^{i\phi} / (\omega/2) \right)$ terms obtained by expanding the integrands in the numerator and denominator of Eq. 5.7 are neglected. This assumption leads to the following modification of the formula for the TL-normalized TPEF signal:

$$\widetilde{S}_{\text{shaped}}^{\text{TPEF}} / \widetilde{S}_{\text{TL}}^{\text{TPEF}} = \frac{\int_{-\infty}^{\infty} \left[\left| E^{(2)}(\omega) \right|_{\text{shaped}}^{2} + \left| aE^{2}(\omega/2)e^{i\phi} / (\omega/2) \right|_{\text{shaped}}^{2} \right] d(\omega/2)}{\int_{-\infty}^{\infty} \left[\left| E^{(2)}(\omega) \right|_{\text{TL}}^{2} + \left| aE^{2}(\omega/2)e^{i\phi} / (\omega/2) \right|_{\text{TL}}^{2} \right] d(\omega/2)}.$$
(5.9)

We found that for this case, the value of the empirical constant *a* in Eq. 5.9 that worked best was 0.18. As discussed in the Results and Discussion section, these simulations failed to simulate several features found in the experimental data, suggesting that the interference between virtual and dipole pathways is of paramount importance.

When simulating the TPEF signals and their ratios with SHG as functions of the width of the phase window, we found that the results obtained for broader windows agreed with the experimental data, but those obtained for the narrow ones did not. We considered the lack of agreement found for narrower phase windows to be caused by inhomogeneous broadening, which is quite significant in protic solutions of FR0-SB.² In doing so, we assumed that one might expect a reduction of the interference between the virtual and dipole pathways in TPE processes when the window widths become narrower. To simulate the effect of the postulated interference reduction in the TL-normalized TPEF signals as a result of inhomogeneous broadening, we formed a linear combination of Eq. 5.7, which assumes interference, and Eq. 5.9, in which interference is absent, and compared the resulting TPEF/SHG ratios with the corresponding experimental data. The relative contribution of Eq. 5.7 to the linear combination of Eq's. 5.7 and 5.9 was increased linearly from 0% for the 10 nm window width to 80% for the 50 nm window width. As shown in the Results and Discussion section, the model assuming the decrease of interference as a result of

window width reduction is in much better agreement with the experimental data obtained for all phase windows.

5.3 Experimental and Theoretical Methods

The experimental setup used a Ti:Sapphire oscillator (Coherent Vitara-S) producing pulses with a repetition rate of 80 MHz for excitation. The pulses were compressed and shaped with a pulse shaper (MIIPS Box 640, Biophotonic Solutions Inc.) using MIIPS. 43,196-204 The output beam, centered at 811 nm with a pulse duration of ~16 fs, was split with a 20:80 beam splitter (Thorlabs UFBS2080). The reflected beam (20% reflected) was frequency doubled in a β-BBO crystal to serve as our reference, which was detected with an Ocean Optics USB4000 spectrometer. The transmitted beam was focused by a 10 cm focal length convex lens onto a 1 cm cuvette containing the solutions of FR0-SB in methanol with a concentration of ~6 μM. The maximum laser power at the sample was ~ 50 mW with a peak intensity of $\sim 6 \times 10^8$ W/cm², which is at least one order of magnitude below the onset of saturation (cf. Figure 4.5). TPEF was detected perpendicular to excitation with a 2.5 cm focal length convex lens to collimate the signal followed by a 10 cm focal length convex lens to focus the signal onto an Ocean Optics QE PRO spectrometer. The pulse chirp in both the reference signal and the fluorescence excitation beam paths were matched to a value of less than 50 fs² by the introduction of glass slides in the reference beam path so that the pulses in both paths were TL after pulse compression using MIIPS. All experiments were performed multiple times to ensure reproducibility of the data. The laser power dependence for TPE for the samples measured gave a nonlinear exponent of 1.90 ± 0.02 . Deviation from the exact square law dependence is expected for molecules with significant dipole pathway contribution. 165,184

5.4 Results and Discussion

Two-photon excitation of the super photobase FR0-SB leads to the electronically excited S_1 state **FR0**-SB*, which shows emission at ~21,000 cm⁻¹. In protic solvents, excited-state proton transfer from the solvent to the photobase FR0-SB* leads to the formation of the excited protonated photobase FR0-HSB^{+*}, which emits at ~15,000 cm⁻¹. ^{2,153} Because the SHG spectrum provides an accurate measurement of $\left|E^{(2)}(\omega)\right|^2$, which, as shown by comparing Figures 1b and 1c, can be accurately modeled using Eq. 5.5, it serves in this study as a reference. In this study, we collected the frequency integrated TPEF signals using shaped and TL pulses for FR0-SB in methanol and compared them to the SHG reference data. Using the same phase functions as those utilized in Figure 1 and Eq. 5.5, we simulated the ratios of the frequency integrated TPEF signals obtained for shaped and TL pulses, defined by Eq. 5.7, and their SHG counterparts, defined by Eq. 5.8, using the window width of 40 nm and window phases varying from -2π to 2π . The results of these simulations are shown in Figure 5.3a. The corresponding experimental TPEF signals for FR0-SB in methanol and the experimental SHG reference spectra obtained using shaped pulses and normalized to their values under TL excitations are plotted in Figure 5.3b. The ratio of the fluorescence signal to the integrated laser signal amplitude reveals a maximum enhancement at $\pm 0.75\pi$ and $\pm 1.25\pi$, when the probability for TPE exceeds the value predicted by $\left|E^{(2)}(\omega)\right|^2$ alone.

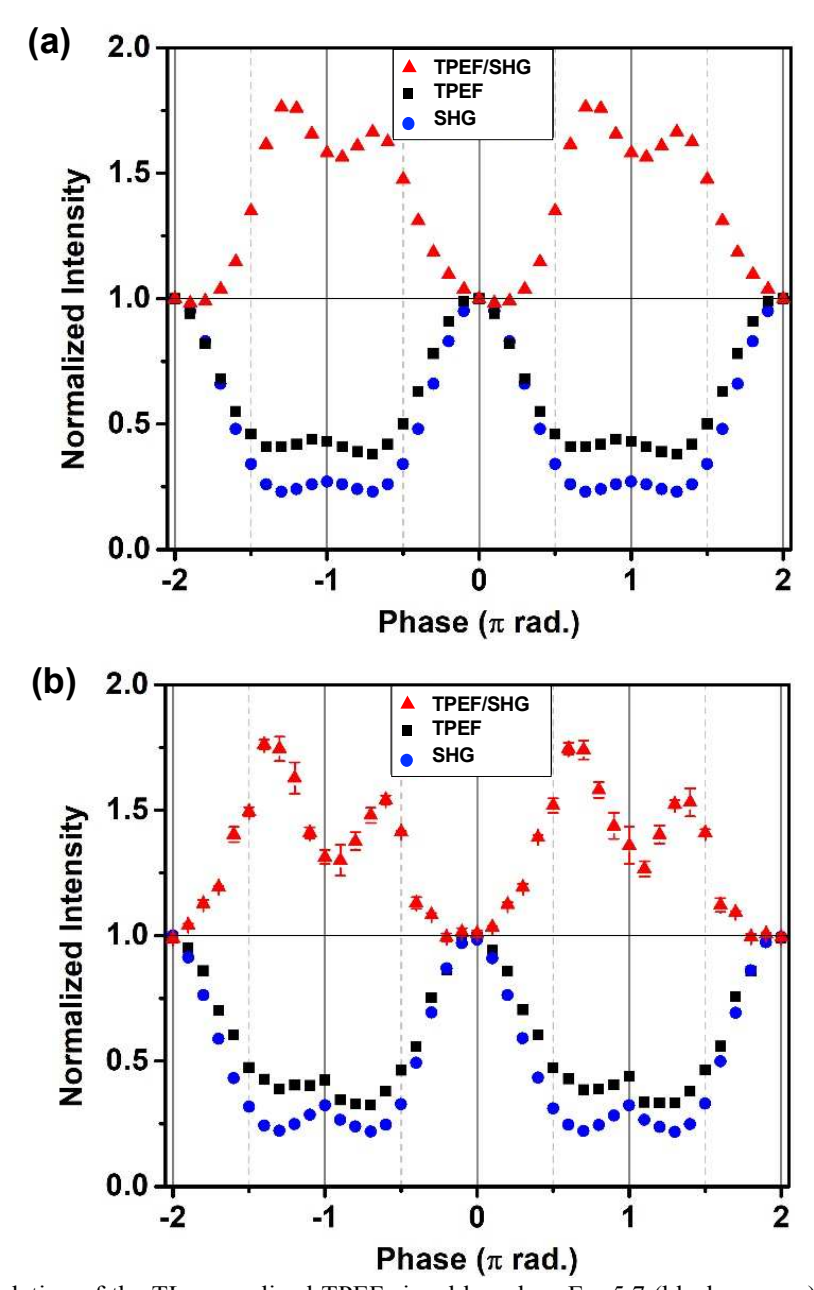


Figure 5.3. (a) Simulation of the TL-normalized TPEF signal based on Eq. 5.7 (black squares), the TL-normalized SHG signal based on Eq. 5.8 (blue circles), and the ratio of the two signals (red triangles) as functions of the spectral phase. The simulation parameters are given in the Theory section. (b) Experimental data corresponding to (a) obtained following TPE of **FR0**-SB in methanol using 16.6 fs pulses and a 40 nm window as a function of the spectral phase. The TL-normalized TPEF signal is shown in black squares, the TL-normalized SHG signal is shown in blue circles, and the ratio between the two signals is shown in red triangles.

The excellent agreement between the simulation and experimental data shown in Figure 3 demonstrates that the anticipated control of the quantum interference between the virtual and dipole pathways that contribute to TPE in large non-centrosymmetric molecules in solution is

indeed possible. To examine the possibility of controlling the interference between the two pathways, we performed a series of additional measurements in which the TPEF signals for **FR0**-SB in methanol and the corresponding SHG reference signals were obtained for several different phase window widths ranging from 10 nm to 50 nm and plotted as functions of the window phase scanned between -2π and 2π . The results of these additional measurements are shown in Figure 5.4.

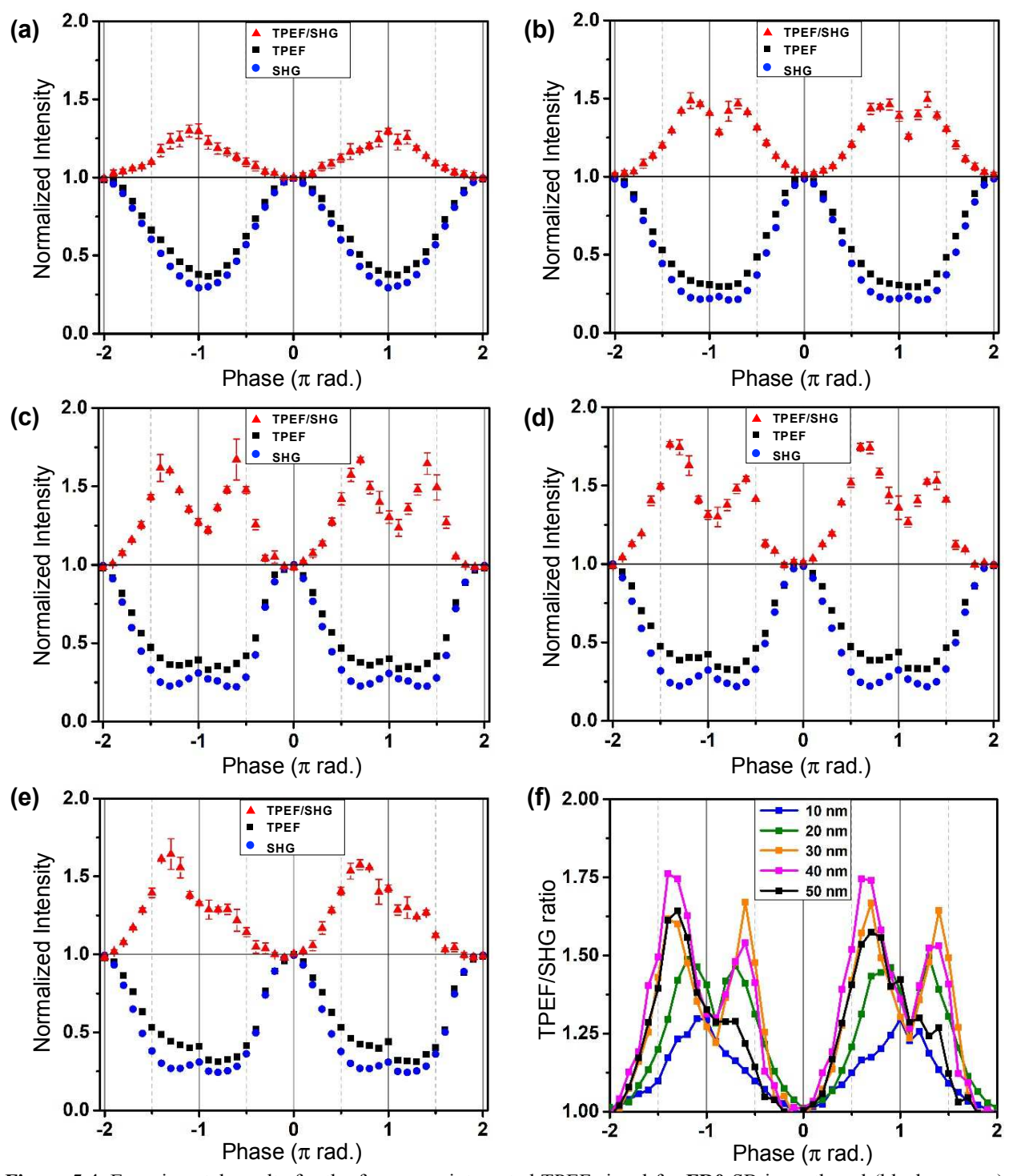


Figure 5.4. Experimental results for the frequency integrated TPEF signal for **FR0**-SB in methanol (black squares) and the reference SHG signal of the laser (blue circles), along with the TPEF/SHG signal ratios with error bars (red triangles), plotted as functions of the spectral phase for window widths of (a) 10 nm, (b) 20 nm, (c) 30 nm, (d) 40 nm, and (e) 50 nm. The TPEF/SHG signal ratios for all window sizes examined in (a)—(e) are shown in (f).

The results in Figure 4 show a clear dependence of the TPEF/SHG signal ratios on the window width. When the window is 10 nm wide, the maximum enhancement in the normalized TPEF is only 25% above that of the normalized SHG signal. However, for a window width of 40 nm we observe that TPEF can be up to 75% greater than the SHG signal. As the window width increases further to 50 nm, the observed enhancement diminishes. The optimum window width is found to be about 2/3 of the FWHM of the laser pulse spectrum (cf. Figure 5.1a).

As already mentioned in the Theory section and as implied by comparison of Figures 5.3a and 3b, the parameter a measuring the relative contribution of the dipole and virtual pathways and the phase lag ϕ characterizing the dipole pathway can be fit to closely match the experimental results shown in Figure 5.3b. However, Eq. 5.7 fails to reproduce the experimental data for some of the window widths examined in Figure 5.4. This is demonstrated in Figure 5.5, where we show the simulated TPEF and SHG signals, along with the corresponding TPEF/SHG ratios, as functions of the window phase scanned between -2π and 2π for window widths ranging from 10 nm to 50 nm, using the same parameters as used in Figure 5.3a and described in the Theory section. While the agreement between experiment and simulation is best for the larger phase window widths, the simulation results for the 10 and 20 nm windows based on Eq. 5.7 do not match the corresponding experimental data.

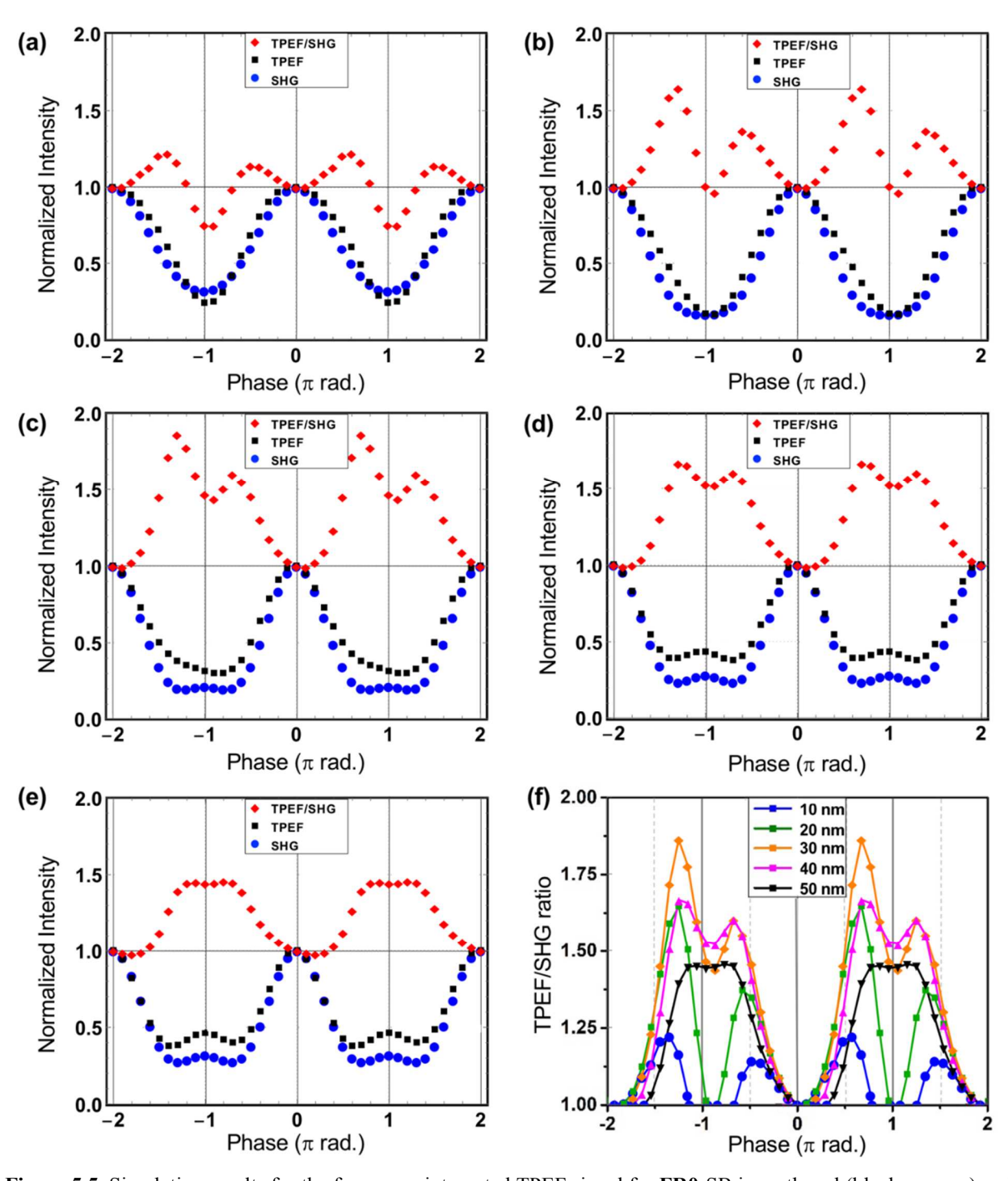


Figure 5.5. Simulation results for the frequency integrated TPEF signal for **FR0**-SB in methanol (black squares) and the reference SHG signal of the laser (blue circles), along with the TPEF/SHG signal ratios (red triangles), based on Eq's. 5.7 and 5.8, plotted as functions of the spectral phase for window widths of (a) 10 nm, (b) 20 nm, (c) 30 nm, (d) 40 nm, and (e) 50 nm. The simulated TPEF/SHG signal ratios for all window sizes examined in (a)–(e) are shown in (f). The simulation parameters are given in the Theory section.

To understand the disagreement between simulations based on Eq. 5.7 and experiment for narrower window widths, we explored two alternative explanations. In the first explanation, we assumed that there is no interference between the virtual and dipole pathways and that the presence of the dipole pathway attenuates the laser power dependence of two-photon transitions. This idea of reduced power dependence was explored by Meath who discussed the intensity dependence of two-photon absorption due to the direct permanent dipole moment excitation mechanism. 165 By employing the rotating wave approximation, Meath showed that the TPE rate due to direct permanent dipole mechanism is not necessarily proportional to the square of the laser intensity and may display a lower power dependence, which for very low intensities can be a linear function of the laser intensity. We simulated the TPEF signals assuming that no interference occurs between the virtual and dipole pathways using Eq. 5.9. We found that for these simulations the value of the empirical constant a in Eq. 5.9 that worked best was 0.18. Figure 5.6a shows the results of the simulations based on Eq. 5.9, presented as the ratio between the calculated, TL-normalized, TPEF (Eq. 5.9) and SHG (Eq. 5.8) signals. The results in Figure 6a demonstrate that the neglect of the interference between the virtual and dipole pathways fails to describe the experimental TPEF/SHG ratios shown in Figure 5.4f. In particular, the theoretical TPEF/SHG ratios simulated in this manner fail to reproduce the dip in the experimental TPEF/SHG ratios, which, as shown in Figure 5.4f, should occur when the phase is $\pm \pi$.

In the second explanation of the failures of Eq. 5.7 for the narrower window widths, we assumed that Eq. 5.7 is capable of modeling the interference, but we also postulated that the interference at smaller window widths may weaken due to inhomogeneous broadening. This could be rationalized by the fact that **FR0**-SB in methanol represents a situation where a large molecule is hydrogen-bonded to a strongly polar solvent,² so that the inhomogeneous broadening might

dominate the TPE line width(s) when dealing with narrow phase windows. The simulations shown in Figure 5.5, which do not take into account inhomogeneous broadening, show a narrow but significant interference when the amplitude of the phase window is $\pm \pi$, especially for the 10 and 20 nm windows. However, the experimental data shown in Figure 5.4 indicate that inhomogeneous broadening significantly dampens this interference and a broad background of 'unshaped' field observed for windows narrower than 30 nm becomes dominant. The effect of inhomogeneous broadening was taken into account by the simulations shown in Figure 5.6b, where the contribution from Eq. 5.7 to the linear combination of Eq. 5.7, which assumes interference, and Eq. 5.9, in which the interference is absent, was linearly increased from 0% for the 10 nm window width to 80% for the 50 nm window width. These modified simulations are in much better agreement with the experimentally observed TPEF/SHG ratios, shown in Figure 4f and reproduced in Figure 6c, than those obtained by dividing Eq. 5.7 by Eq. 5.8 or those presented in Figure 5.6a that ignore interference.

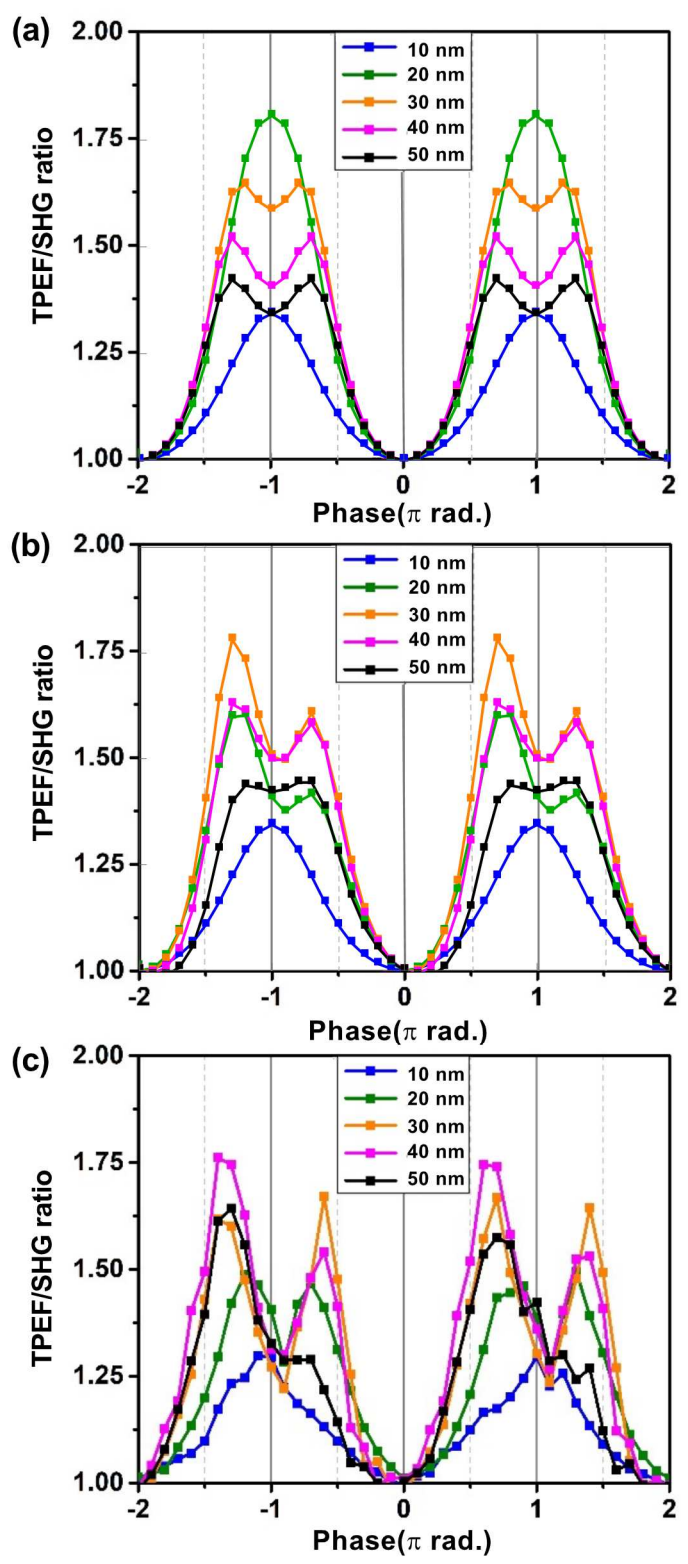


Figure 5.6. Calculated [panels (a) and (b)] and experimentally determined [panel (c)] TPEF/SHG ratios as functions of phase values for different window widths. (a) Results obtained assuming that the interference between the virtual and dipole pathways in the TPEF signal can be neglected, as in Eq. 5.9. (b) Results obtained assuming that the TPEF signal can be simulated using a linear combination of Eq. 5.7, which assumes interference, and Eq. 5.9, where

interference is absent, with the contribution from Eq. 5.7 being increased linearly with the window width (see text for details). (c) Experimental data, as shown in Figure 5.4f, reproduced here to facilitate comparison.

5.5 Conclusion

The dependence of TPEF of **FR0**-SB in methanol on the spectral phase of femtosecond broadband pulses, which reflects on the quantum interference between the dipole and virtual pathways that contribute to TPE, was examined experimentally and theoretically. When normalized for pulse duration, enhancements by a factor of up to 1.75 in the experimentally observed TPEF were found. Simulations taking into account the different responses of the virtual and dipole pathways to external fields and the effect of pulse shaping on two-photon transitions, were found to be in good agreement with the experimental measurements, but we encountered situations corresponding to narrow spectral window widths for which there were disagreements between theory and experiment. We explained these disagreements by postulating that the interference between the virtual and dipole pathways at smaller window widths weakens as a result of inhomogeneous broadening, showing that the model assuming the decrease of interference as a result of window width reduction is in very good agreement with the experimentally observed TPEF/SHG signal ratios obtained for all phase windows. At the same time, we demonstrated that simulations ignoring the interference between the virtual and dipole pathways and considering an attenuated power dependence only fail to reproduce the experimental data. Findings from the present study, in addition to their potential impact on applications that depend on TPE, may be relevant to ongoing research on the two-photon transitions induced by entangled photons, ^{205–210} where even molecules with weaker permanent dipole moments may exhibit strong quantum effects, such as transparencies.

Chapter 6 Controlling S₂ and S₁ Fluorescence of Cyanines IR140 and IR144

We report on the changes in the dual fluorescence of two cyanine dyes IR144 and IR140 as a function of viscosity and probe their internal conversion dynamics from S₂ to S₁ via their dependence on a femtosecond laser pulse chirp. Steady-state and time-resolved measurements performed in methanol, ethanol, propanol, ethylene glycol, and glycerol solutions are presented. Quantum calculations reveal the presence of three excited states responsible for the experimental observations. Above the first excited state, we find an excited state, which we designate as S₁', that relaxes to the S₁ minimum, and we find that the S₂ state has two stable configurations. Chirp-dependence measurements, aided by numerical simulations, reveal how internal conversion from S₂ to S₁ depends on solvent viscosity and pulse duration. By combining solvent viscosity, transform-limited pulses, and chirped pulses, we obtain an overall change in the S₂/S₁ population ratio of a factor of 86 and 55 for IR144 and IR140, respectively. The increase in the S₂/S₁ ratio is explained by a two-photon transition to a higher excited state. The ability to maximize the population of higher excited states by delaying or bypassing nonradiative relaxation may lead to the increased efficiency of photochemical processes.

This chapter has been adapted with permission from (*J. Phys. Chem. A* **2021**, *125*, 9770-9784) Copyright © 2021, American Chemical Society.

6.1 Introduction and Background

Fluorescence from high lying excited states is uncommon for organic molecules in solution because of the fast internal conversion (IC) to the lowest excited state of the same parity that gives rise to Kasha's rule.⁴⁴ Here, we revisit the dual fluorescence observed in cyanine dyes,^{211–213} in particular, the enhanced S₂ emission observed in studies using chirped femtosecond laser pulses.¹ Here, we endeavor to understand what leads to the unusual enhancement by restricting molecular motion via changes in solvent viscosity and shaping the laser pulses. The motivation of our work is to learn how to enable new applications of cyanine dyes through increasing the lifetime of high lying excited states.

Cyanine dyes encompass a large category of fluorescence molecules with an odd numbered conjugated π-bonding system connecting two nitrogen atoms that branch off into a range of different substituents. Cyanine dyes are used in a wide range of applications, including bioimaging,^{214–218} solar energy conversion,^{219–221} photodynamic cancer therapy,^{222,223} and textiles.²²⁴ Their spectroscopic properties are easily tuned making them useful model compounds.²²⁵ Here we focus on heptamethine cyanine dyes IR144 and IR140, shown in Figure 6.1, which differ in their amine substituent located in the center of their polymethine chain. IR144 has a piperazine substituent, while IR140 has a bulky diphenylamino group. The bulky substituent gives IR140 a higher degree of steric hindrance than IR144. Notice the two configurations for IR144 and IR144' represent the cyanine-like and bis-polar conformation of IR144, respectively; While IR140 is represented in the cyanine-like conformation.²¹⁹

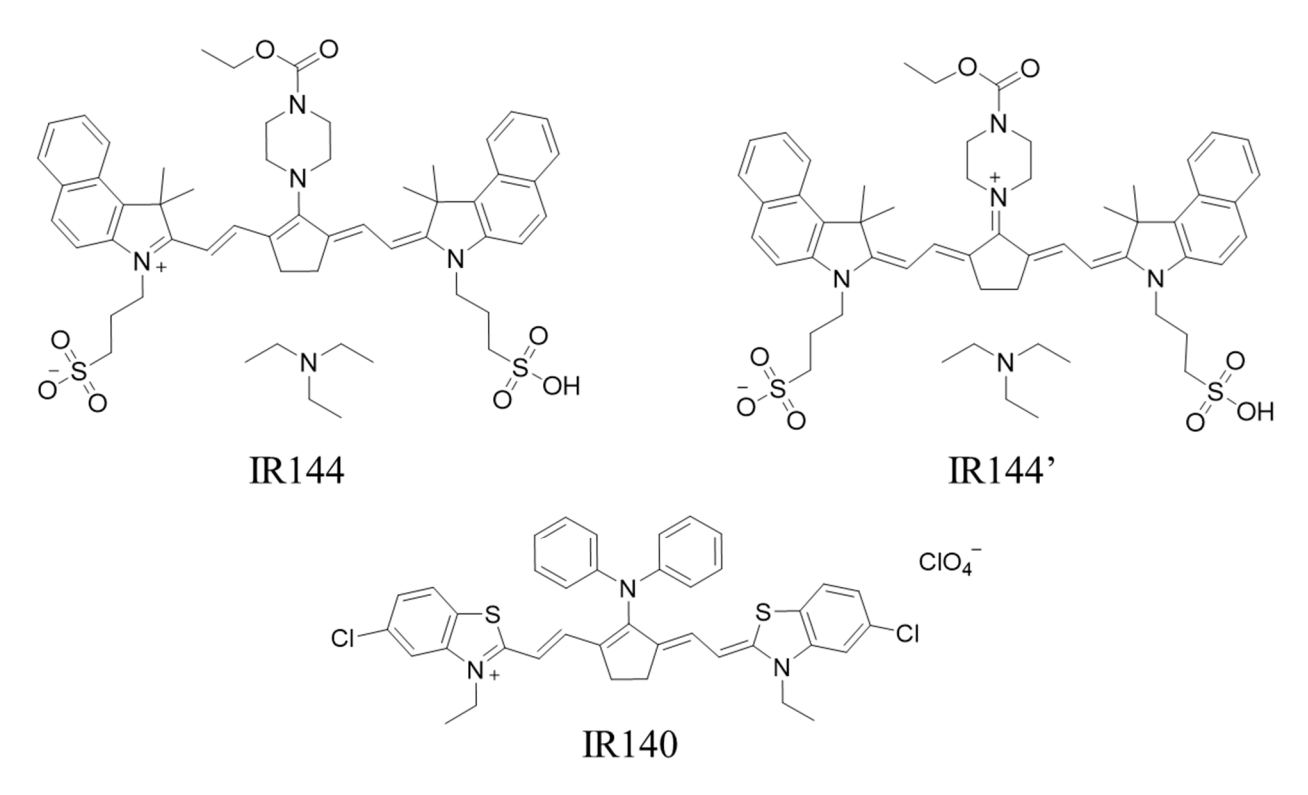


Figure 6.1. IR144 and IR144' represent two commonly understood conformations of IR144. IR140 mainly forms a cyanine-like conformation.

When a transform limited (TL) pulse is chirped, its pulse duration broadens, and its peak intensity decreases. More importantly, the instantaneous frequency sweeps from higher to lower frequencies in a pulse with negative chirp, or from lower to higher frequencies in a pulse with positive chirp. The fast sweep of the instantaneous frequency allows one to consider a chirped pulse as using a pair of pulses with different frequencies separated by a time delay that is proportional to the chirp magnitude. This analogy, and the fact that chirped pulses lack time-inversion symmetry, explains why chirped pulses are useful for following molecular dynamics. he chirp effect following S₁ excitation consists of a decreased fluorescence yield observed for negatively chirp pulses compared to positively chirped pulses. he can be supported by the Dantus group on the excitation of the S₁ state of IR144 showed that the decrease in the S₁ fluorescence was mirrored by enhanced stimulated emission in the presence of

negatively chirped pulses.²³³ For positively chirped pulses we observed enhanced S_1 fluorescence and decreased stimulated emission. Positively chirped pulses were found to be sensitive to solvation dynamics. The sensitivity of chirped pulse measurements to solvation was high enough to distinguish ~5% changes in temperature in the polar solvation response of IR144 and the non-polar solvation response of IR125. The changes observed in both fluorescence and stimulated emission were found to be quadratic in laser intensity even at laser intensities corresponding to 0.02% excitation probability corresponding to 0.02%. Nonlinear effects in laser-molecule interactions have been offered as explanations for the observation of coherent control in the 'linear regime'. We have pointed out that one must first determine that the laser pulse spectrum remains unchanged as the spectral phase is changed, otherwise changes in the spectrum can account for the observed changes in the control experiment. 236

We explain the interaction of chirped pulses with a molecule using the language of nonlinear spectroscopy.²³⁷ Instead of using double-sided Feynman diagrams, we find that Albrecht ladder diagrams²³⁸ are more instructive because one is able to show energetically why some pathways are not allowed for chirped pulses. For a review of nonlinear optical spectroscopy that includes an introduction to double-sided Feynman diagrams, ladder diagrams, and Liouville space coupling diagrams, starting from one to three field interactions which includes theory, mathematical expressions for calculating the density matrix time evolution, expected signals, and experimental results, we recommend the work of Grimberg et al.²³⁹ We start by reminding the reader that excitation from the ground to an excited state requires two laser interactions to bring both the bra (represented as dashed arrows) and ket (represented by solid arrows) from the ground state to the excited state, thus creating a population. The population in the excited state following such linear interaction is proportional to

$$P_{1\leftarrow 0} \propto \left| \left\langle e \middle| \mu \cdot E(t) \middle| g \right\rangle \right|^2 = \left\langle e \middle| \mu \cdot E(t) \middle| g \right\rangle \left\langle g \middle| \mu \cdot E(t) * \middle| e \right\rangle \tag{6.1}$$

where μ is the transition dipole and E(t) is the complex time-dependent field. In the diagrams shown in Figure 6.2, we include only two electronic states S_0 and S_1 . Excitation of the S_1 state with chirped pulses, as we have done for IR144,³ and shown in Figure 6.2, we observe that fluorescence is depleted for negative chirp values but enhanced for positive chirp values. When using TL pulses the ladder diagram for pathway (1) in Figure 6.2 populates the excited state and pathway (2) stimulates emission back to the ground state.

When using chirped pulses, we find that pathways (1⁻ and 1⁺) are independent of the timing between higher and lower energy portions of the pulse, i. e. independent of phase. Both pathways create a population in the excited state that is independent of chirp. For negatively chirped pulses, however, the higher energy portion of the pulse (blue arrow) interacts first with the ket and then the lower energy portion of the pulse (red arrow) interacts with the bra, as shown in pathway (2⁻), there is no net population created in the S₁ state. This explains the reduction in observed fluorescence and justifies the observation of enhanced vibrational coherence following negative chirp pulse excitation.^{240,241} Pathway (2⁺) for positively chirped pulses cannot take place for energetic reasons (compare with pathway (2⁻)). In summary, these diagrams (and their complex conjugates) explain the observed dependence of fluorescence and stimulated emission as a function of pulse chirp sign and magnitude as shown in Figure 6.2. Here we have illustrated the cases for two field interactions. One may add a third interaction to simulate higher-order processes, however, it is clear that the outcome will depend on the first two interactions shown here and their complex conjugates.

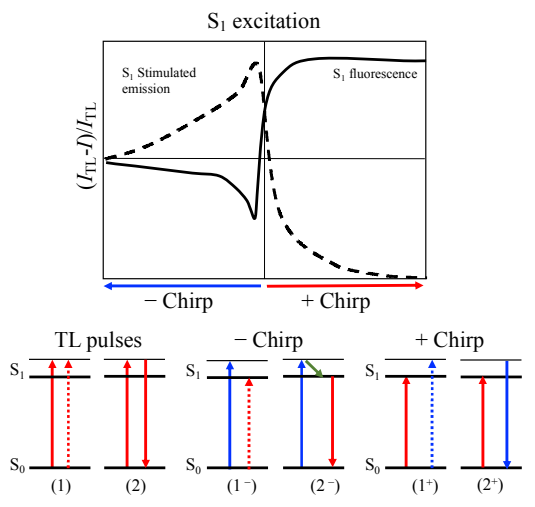


Figure 6.2. The interaction of chirped laser pulses with the S_1 state of a molecule. (top) Relative changes in fluorescence and stimulated emission from the S_1 state as a function of chirp (bold line and dashed line, respectively), according to ref. 3 (bottom) Albrecht ladder diagrams representing the laser-molecule interaction for TL and chirped pulses. Pathways (1⁻ and 1⁺) are independent of chirp, pathway (2⁻) is responsible for the enhanced stimulated emission and decrease in fluorescence. Pathway (2⁺) causes no effect because it is energetically forbidden. Solid/dashed arrows indicate ket/bra interactions. Blue/red arrows indicate high/low frequency portion of the spectrum. Green arrows indicate non-radiative transitions including wavepacket motion.

When chirp-dependence experiments were carried out on the S_2 excited state of IR144 and IR806, we found a very different molecular response, illustrated in Figure 6.3.¹ The maximum S_2 fluorescence was observed for TL pulses, while a decrease in fluorescence was found for both negatively or positively chirped pulses. In this work, we revisit this unusual behavior. The chirp dependence of the S_2 state fluorescence is illustrated in Figure 6.3. where in addition to the lasermatter interactions we show non-radiative relaxation from the different states using solid green arrows. At first glance we find that the pathways relevant to S_1 excitation are identical to those involving S_2 excitation. However, there are two main differences. First, pathway (TPE) becomes available for TL pulse excitation provided there is a state within two-photon resonance with the field and laser intensity is sufficiently high. Second, each excitation to S_2 is now competing with faster relaxation due to the excitation taking place in a region of greater density of states and due to IC to S_1 . Like the case for S_1 excitation, pathways (1⁻ and 1⁺) are independent of the timing between higher and lower energy portions. Like for S_1 excitation, pathway (2⁻) leads to a decrease

in S_2 population. The main difference in these pathways is the presence of fast relaxation that includes IC to S_1 indicated by the green arrows. These compete with optical excitation and result in signals that are fairly symmetric as a function of chirp. The expected asymmetry was observed clearly in mesopiperidine-IR806 (mPi-IR806).¹ As a result of these laser-matter interactions, we expect that chirped pulses result in a lower S_2 population but higher S_1 population. TL pulses result in higher S_2 and lower S_1 population because IC from S_2 to S_1 is slow in these cyanine molecules and because a higher excited state indicated by S_n is resonant with the laser excitation.

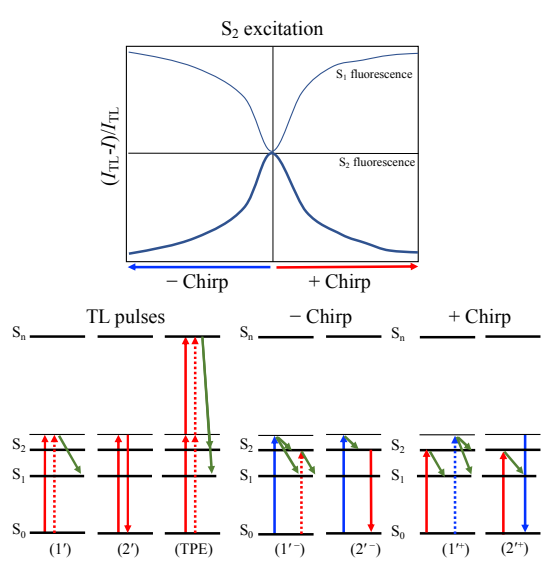


Figure 6.3. The interaction of chirped laser pulses with the S_2 state of a molecule. (top) Relative changes in fluorescence from the S_1 and S_2 states, (light and bold lines, respectively) as a function of chirp, according to ref. 1 (bottom) Albrecht ladder diagrams representing the laser-molecule interaction for TL and chirped pulses. Pathway (TPE) where two-photon excitation to an upper excited state S_n is accessible in this case, leading to enhanced S_2 fluorescence. Pathways (1⁻ and 1⁺) are independent of chirp. Pathways (2⁻) is responsible for a decrease in fluorescence observed for negative chirp, however, non-radiative relaxation via IC leads to decreased S_2 fluorescence that is essentially symmetric with chirp sign. Solid/dashed arrows indicate ket/bra interactions. Blue/red arrows indicate high/low frequency portion of the spectrum. Green arrows indicate non-radiative transitions including wavepacket motion.

Here we use femtosecond chirped pulses to better understand the time-correlated wavepacket motion that leads to IC considering linear and nonlinear light-molecule interaction. We combine chirp control and the dependence of the rate of IC on solvent viscosity^{56,242,243} to explore, in greater detail, the role of intramolecular structural changes required in cyanine dyes to enable IC. The goal of our experiments is to achieve the largest S_2/S_1 ratio to enable novel photochemistry, solar energy capture and perhaps photodynamic therapy applications.

The organization of the paper is as follows: First, we describe the experimental details including steady state spectroscopy, lifetime measurements, and chirp dependent measurements. Second, we present steady state spectroscopy of the two cyanine dyes in different solvents along with lifetime measurements. Third, we show chirp dependent measurements for different solvents obtained at different laser intensities. Fourth, we present quantum chemistry calculations performed on both molecules that identify the different excited states involved as well as their equilibrium configurations. Fifth, we present a kinetic model for the observed chirp dependence. Finally, we discuss how our experimental findings, quantum calculations, and a kinetic model come together to validate our conclusions.

6.2 Experimental and Theoretical Methods

IR144 and IR140 (Exciton, CAS Nos.: 54849-69-3 and 53655-17-7) were purchased and used without further purification. We shall assume that the presence of the diethylethanamine 1:1 in IR144 does not affect the results presented here given the complete solvation of the dye at relatively low concentrations used here. Spectrophotometric-grade methanol, ethanol, *n*-propanol, ethylene glycol and glycerol were purchased from Sigma Aldrich. Solutions made with ethylene glycol and glycerol were prepared by first dissolving the dye in 1 part methanol and then combined with 19 parts of the respective solvent. The results presented were obtained with 50 μM concentration. Measurements were repeated with different concentrations ranging from 25 to 2.5 μM concentrations, although the signal to noise ratio was poor at lower concentrations.

Steady-state spectroscopy measurements were carried out in 1 cm pathlength quartz cuvettes, polished on all four sides with UV-antireflection coating. Absorption, fluorescence with excitation at 522 nm, and excitation–emission matrix (EEM) spectra were collected using a Horiba Duetta Spectrometer. All measurements were taken at room temperature (~ 294 K).

Fluorescence lifetime measurements were acquired following excitation from a picosecond pulsed laser with a repetition rate of 80 MHz centered at 531 nm (LDH-P-FA-530XL, Picoquant). A half-wave plate was used to ensure the vertical polarization of the excitation beam. The IR144 and IR140 solutions were contained in a 1 cm cuvette. Fluorescence signal, detected perpendicular to the laser beam, was acquired at parallel and perpendicular polarizations with respect to the vertical polarization of the excitation pulse, using a polarizer. Detection was carried out with a 16-photomultiplier time-correlated single-photon counting (TCSPC) system (SPC-830 TCSPC, Becker-Hickl, GmBH). The decay times correspond to the isotropic component of the fluorescence decays and a deconvolution of the fluorescence decays was carried out to obtain the decay

lifetimes. The instrument response function (IRF) was of the order of 130 ps and was used by the convolve-and-compare deconvolution program to obtain the fluorescence lifetimes.

Chirp experiments were carried out using the Spectra–Physics Spirit-NOPA-3H pumped to the third harmonic (347 nm) of a 1040 nm Spectra–Physics Spirit-4W laser operating at a repetition rate of 100 kHz. The NOPA was tuned to generate laser pulses centered at 522 nm. Laser pulses were sent into the femtoJock P (Biophotonic Solutions, part of IPG Photonics) pulse shaper then sent through a neutral density filter and finally a lens to be focused on the sample. The chirp magnitude φ_2 is controlled in the frequency domain by introducing the spectral phase function $\varphi(\omega) = 0.5\varphi_2(\omega - \omega_0)^2$, where ω_0 is the carrier frequency of the laser pulse.

Multiphoton Intrapulse Interference Phase Scan (MIIPS) was first used to automatically compress the pulses to their TL duration 197,203 and with optimum fidelity. 244 Pulse compression was done using a thin BBO second harmonic generation (SHG) crystal that was placed in the same location where the sample would be placed. Pulse durations of 25 fs were used for all experiments. A quartz cuvette face was placed in the beam path to compensate for dispersion generated by the quartz cuvette wall when running experiments. The pulse energy was 200 nJ for IR144 experiments and around 50 nJ for IR140 experiments. The pulse energies ranged from 50 to 150 nJ during power-dependence experiments. An anti-reflective 10 cm focal length lens focused the pulses into the front of the quartz cuvette that held each sample. A multimode optical fiber was held perpendicular to the excitation beam at the location of the laser focus. The optical fiber carried the fluorescence to a QE Pro Spectrometer (Ocean Optics), and the spectra were collected by the MIIPS software and recorded. The QE spectrometer was calibrated for wavelength using a mercury lamp. The intensity was calibrated based on fluorescence spectra acquired by the Duetta spectrometer, after it was calibrated using the Raman line of water. We found this step was very

important given that the S_1 state of these dyes emit at wavelengths ranging from 800 - 1100 nm, and that wavelength range is outside the detection capability of photomultipliers. Chirp was introduced to the pulses using the pulse shaper. The chirp range over which fluorescence was collected was -5,000 fs² to +5,000 fs². The entire chirp range was divided into 300 fs² steps. At least 5 measurements were taken at each step for each of the 10 samples. Each measurement corresponded to 3 averages with an integration time of 50 ms for methanol, ethanol, and propanol solutions and 300 ms for ethylene glycol and glycerol solutions.

6.3 Results

6.3.1 Experimental Results

Steady state absorption and fluorescence spectra of IR144 and IR140 in methanol, ethanol, npropanol, ethylene glycol and glycerol are shown in Figure 6.4a and b, respectively. These spectra are plotted as the transition dipole (or oscillator) strength. 116,245 The absorption dipole strength was calculated by dividing the absorption value by its respective wavenumber $A(\nu)/\nu$. Fluorescence spectra were converted to wavenumber, multiplied by the wavelength squared and divided by the respective wavenumber cubed to calculate the fluorescence dipole strength $F(\nu)/\nu^3$. The lower energy S_0 to S_1 transition absorption band is centered around 13500 cm $^{-1}$ and 12800 cm $^{-1}$ for IR144 and IR140, respectively. The higher energy S₀ to S₂ absorption bands are associated with two configurations that we will refer to as S_2^L and S_2^H according to their lower or higher energy transitions, respectively. The S₀ to S₂ absorption bands are ~18210 and 19710 cm⁻¹ for IR144, and ~17960 and 19510 cm⁻¹ for IR140. The emission spectra for IR144 and IR140 following excitation at 19157 cm⁻¹, accessing the higher S₂ excited electronic state configuration, show three emission bands. The fluorescence bands associated with S₂^L and S₂^H for IR144 are at 15890 cm⁻¹ and 17150 cm⁻¹, respectively, while those for IR140 are centered at 15900 cm⁻¹ and 17230 cm⁻¹. The S₁ emission is centered at 11,750 cm⁻¹ for IR144 and 11,500 cm⁻¹ for IR140.

IR144 shows a solvatochromic shift for both the absorption and fluorescence of the S_1 excited state that is not linear with viscosity. Propanol gives the largest redshift, with respect to methanol, even though glycerol has the highest polarity. Both solvent viscosity and polarity play a role in IR144 absorbance and emission band positions. Similarly, IR140 shows a solvatochromic shifts for both absorption and fluorescence spectra as a function of viscosity. The S_0 to S_2 absorbance increases with solvent viscosity. For both molecules, as solvent viscosity increases, the

overall S_2/S_1 fluorescence ratio increases. Following excitation of S_2 , emission from S_2^H is favored by IR144, whereas emission from S_2^L is favored by IR140.

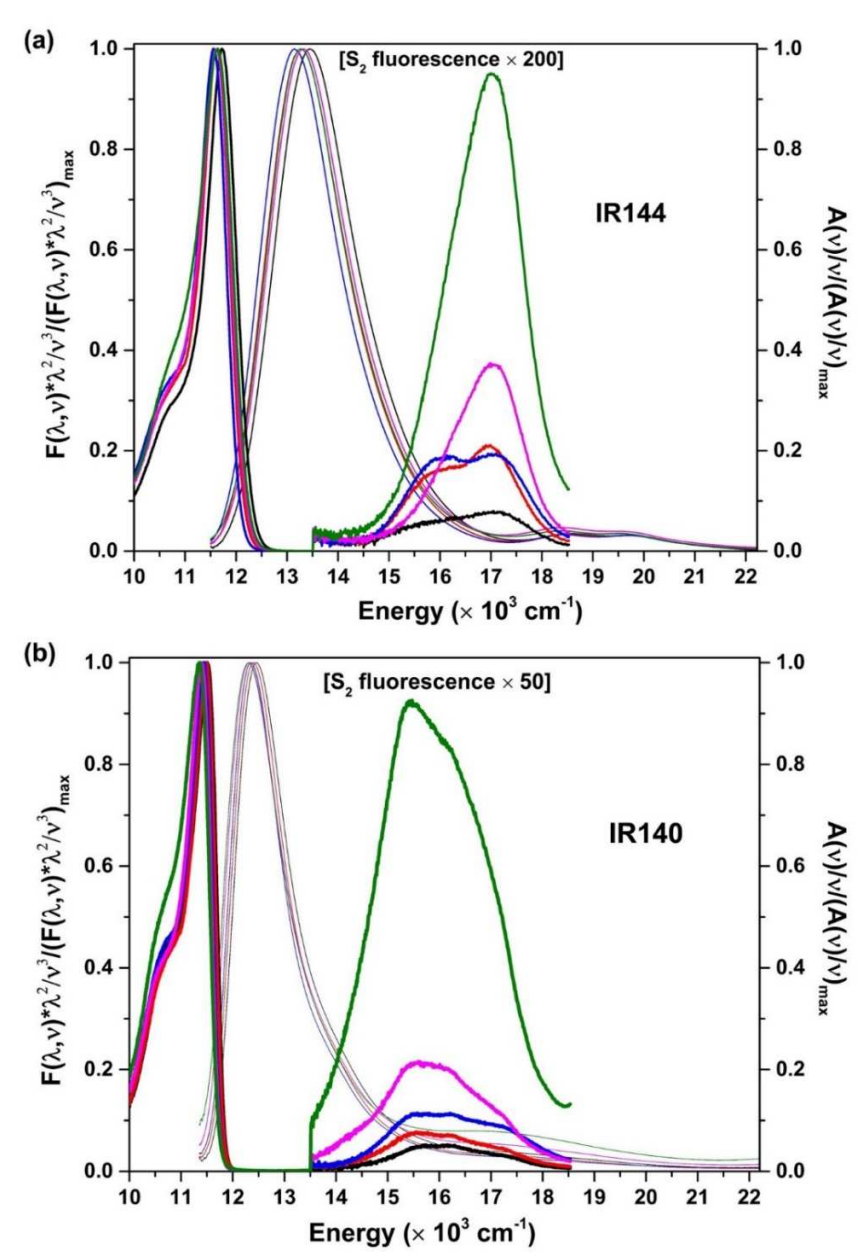


Figure 6.4. Steady-state absorption and fluorescence spectra for (a) IR144 and (b) IR140. The normalized absorption of both IR144 and IR140 is represented with thin lines whereas the normalized emission with thicker lines. Methanol, ethanol, *n*-propanol, ethylene glycol and glycerol are represented by black, red, blue, pink and green lines, respectively.

As can be observed in Figure 6.4, the intensity of the S_2 emission increases with solvent viscosity. In Figure 6.5 we plot the S_2/S_1 ratio as a function of solvent viscosity for both IR144 and IR140.

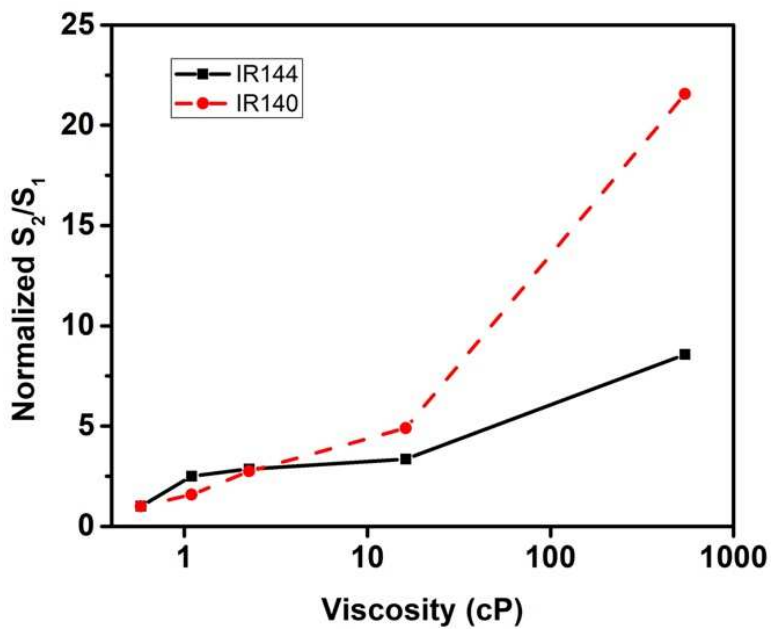


Figure 6.5. The integrated fluorescence ratio of S_2/S_1 from steady state spectra for IR144 and IR140 as a function of varying solvent viscosity (logarithmic scale). The numbers have been normalized such that the ratios are 1 for the respective methanol samples.

EEM spectra, which record the steady-state fluorescence emission intensity as a function of excitation wavelength in a 2D contour map, were collected for both IR144 and IR140 (Figure 6.6a and b). The 14085-22000 cm $^{-1}$ emission region has been enhanced by a multiplication factor of 1200 (for IR 144) and 350 (for IR140). The EEM spectra makes it clear when the S_1 and S_2 excited states are reached. We also note that excitation in the 14000-16200 cm $^{-1}$ region for IR144 and the 13500-15200 cm $^{-1}$ region of IR140, leads to bright emission from S_1 , likely indicating the presence of an excited state that quickly relaxes to S_1 .

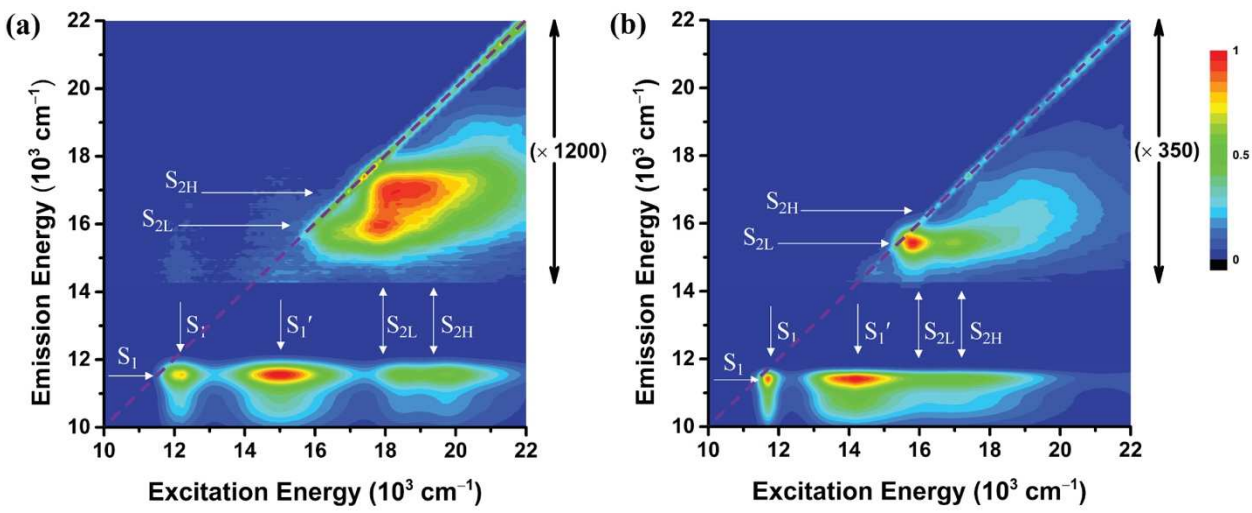


Figure 6.6. Excitation emission matrix spectra of (a) IR144 and (b) IR140 in propanol. The diagonal indicates scattered excitation light when both excitation energy and emission energy are equal.

Fluorescence lifetime measurements, with an excitation wavelength of 18832 cm⁻¹were carried out in IR144 and IR140 solutions in methanol, ethylene glycol and glycerol. Figure 6.7a and b show fluorescence lifetime measurements from IR144 S_2 and S_1 states, respectively. The population from S_2 decays via IC to S_1 and fluorescence to S_0 . However, the presence of these two decays pathways should lead to a single exponential decay with a rate corresponding to the sum of both pathways. The presence of a biexponential decay indicates that a fraction of the population remains in S_2 . As we will discuss later in the manuscript, we identify a change in the molecular structure in the S_2 state as a bottleneck that prevents IC to S_1 . The molecules that undergo that configuration change have a much slower IC to S_1 , and primarily exhibit $S_2 \rightarrow S_0$ fluorescence. The addition of a non-IC configuration to S_2 results in the biexponential fluorescence decay observed. The S_1 emission signal shows a rise followed by a decay, with both lifetimes increasing with solvent viscosity. Figure 6.8a and b show fluorescence lifetime measurements from IR140 S_2 and S_1 states, respectively, for IR140. The S_2 fluorescence lifetime increases with viscosity for IR140 and IR144. Interestingly, the IR140 S_1 fluorescence lifetime does not follow the same

viscosity trend. We find the fluorescence lifetime for IR140 in methanol to be similar to that in glycerol. The deconvoluted fluorescence lifetime values are presented in Table 6.1.

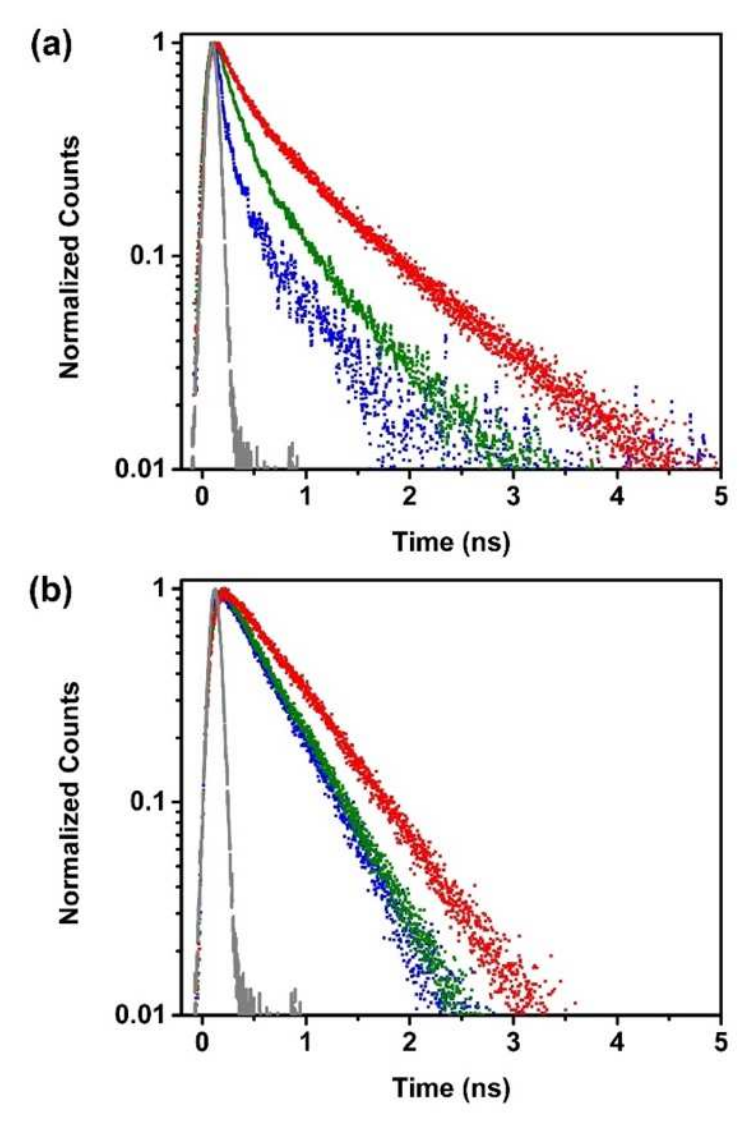


Figure 6.7. The fluorescence decay of IR144 detected at (a) $S_2 \rightarrow S_0$ fluorescence maxima and (b) $S_1 \rightarrow S_0$ fluorescence maxima in methanol (blue dots), ethylene glycol (green dots), and glycerol (red dots). The fluorescence lifetimes for (a) have been obtained from the function $f(t) = a_1 \exp(-t/\tau_1) + a_2 \exp(-t/\tau_2)$ while for (b) have been obtained from the function $f(t) = -b_1 \exp(-t/\tau_3) + b_2 \exp(-t/\tau_4)$. The time constants have been obtained post deconvolution of the IRF from the fluorescence decay signals. $(a_1 + a_2 = 1; b_1 + b_2 = 1)$

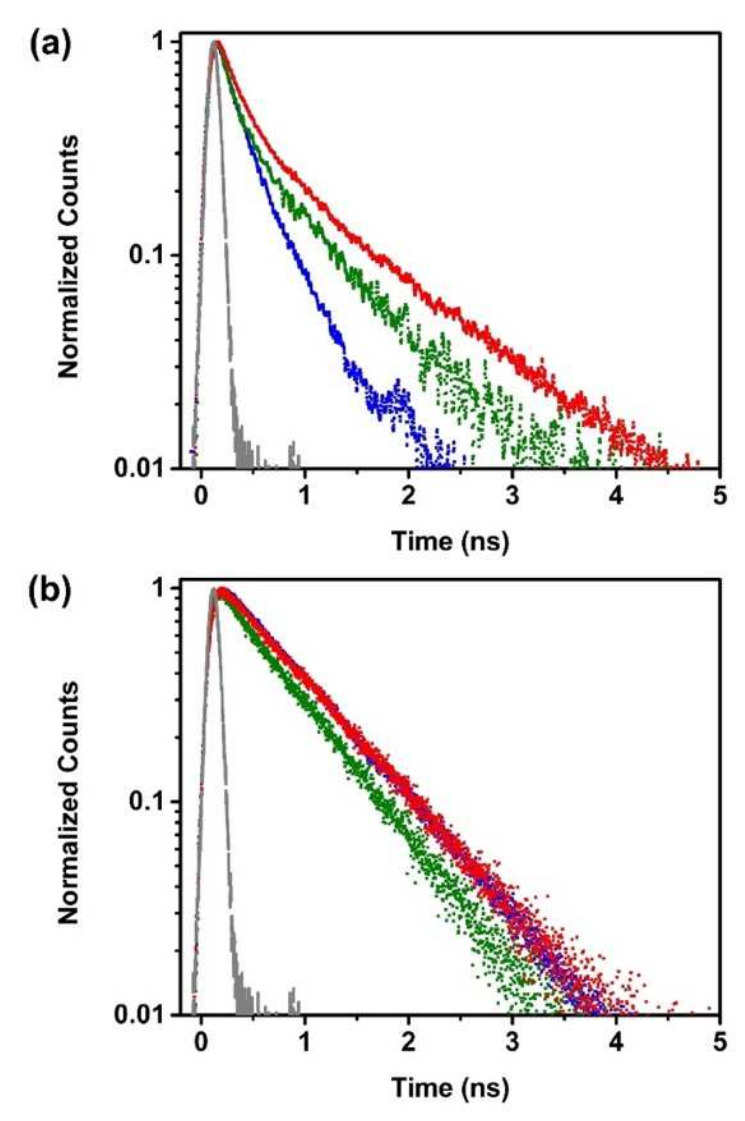


Figure 6.8. The fluorescence decay of IR140 detected at (a) $S_2 \rightarrow S_0$ fluorescence maxima and (b) $S_1 \rightarrow S_0$ fluorescence maxima in methanol (blue dots), ethylene glycol (green dots), and glycerol (red dots). The fluorescence lifetimes for (a) have been from the function $f(t) = a_1 \exp(-t/\tau_1) + a_2 \exp(-t/\tau_2)$ while for (b) have been obtained from the function $f(t) = -b_1 \exp(-t/\tau_3) + b_2 \exp(-t/\tau_4)$. The time constants have been obtained post deconvolution of the IRF from the fluorescence decay signals. $(a_1 + a_2 = 1; b_1 + b_2 = 1)$

Table 6.1 Fluorescence lifetimes obtained from time-correlated single photon counting experiments. The time constants are as defined in Figure 6.2 and 6.3.

Molecule	Solventa	a_1	$\tau_{\rm l}~({\rm ps})$	τ_2 (ps)	b_1	τ ₃ (ps)	τ ₄ (ps)
	МеОН	0.86	46 ± 1	452 ± 10	0.07	32 ± 3	455 ± 2
IR144	EG	0.78	175 ± 2	682 ± 14	0.05	43 ± 3	456 ± 1
	Gl	0.60	221 ± 4	932 ± 13	0.05	48 ± 3	630 ± 2
	МеОН	0.52	107 ± 3	347 ± 5	0.03	44 ± 1	730 ± 2
IR140	EG	0.71	124 ± 2	687 ± 9	0.06	26 ± 1	617 ± 2
	Gl	0.69	174 ± 2	914 ± 11	0.03	42 ± 1	726 ± 2

^a Abbreviations: MeOH = Methanol, EG = Ethylene Glycol, Gl = Glycerol.

Femtosecond chirp scans, from negative chirp values (higher before lower frequencies) to positive chirp values (lower before higher frequencies) were carried out on IR144 and IR140 in methanol, ethanol, and propanol. The excitation pulse, with near Gaussian spectrum and a central wavelength near the S₂ absorption band, for both IR144 and IR140 is chirped while fluorescence spectra spanning both excited states are collected. Figure 6.9a and b show the trend in S₁ and S₂ integrated fluorescence with increasing chirp for IR144 and IR140, respectively. The y-axis is the relative change in integrated fluorescence, with respect to TL fluorescence.

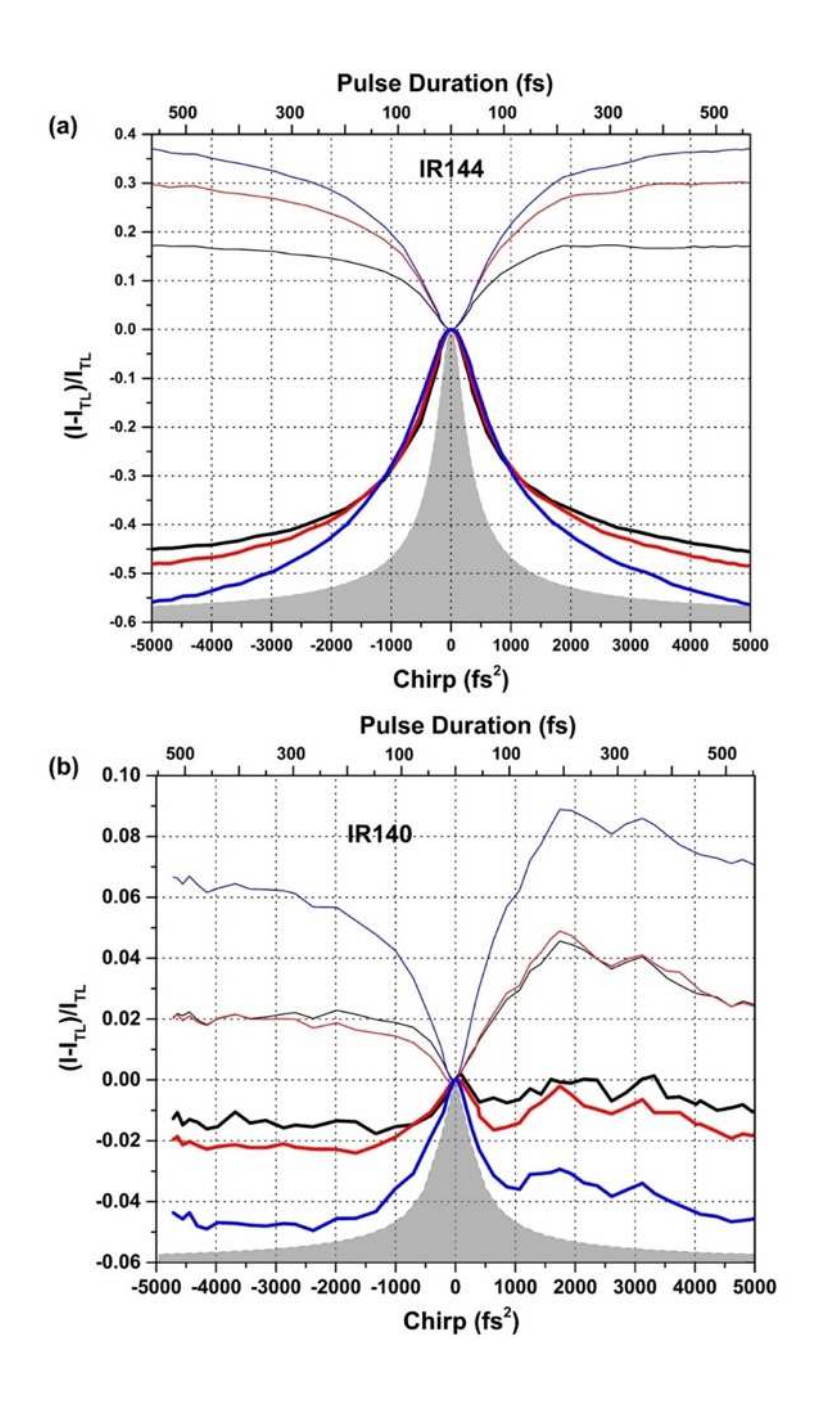


Figure 6.9. Chirp dependence scans conducted on (a) IR144 and (b) IR140 from -5000 fs² to +5000 fs² at constant laser power for each molecule. A lower laser power intensity was used for IR140. The thinner and thicker lines show the relative fluorescence intensity as a function of chirp compared to its TL value (I-I_{TL})/ I_{TL} for S₁ and S₂, respectively. Methanol, ethanol and *n*-propanol are represented by black, red and blue lines, respectively. S₁ and S₂ data are represented by thin and thick lines, respectively.

As shown in Figure 6.9, and similar to previous experiments from our group,¹ the resulting increase in S_2 and decrease in S_1 fluorescence at near zero chirp are nearly symmetrical with

respect to chirp magnitude. This chirp dependence is unusual. As mentioned in the introduction, excitation with negatively chirped pulses should lead to a pronounced decrease in fluorescence compared to excitation with positively chirped pulses. It is important to note that the total integrated S_1 fluorescence is considerably higher than the total integrated S_2 fluorescence (see Figure 6.4). The shaded gray outline, located on the bottom half of Figures 6.9a and b, represent the SHG dependence as a function of chirp obtained with the experimental pulses. The SHG intensity is proportional to the inverse of the pulse duration of the chirped pulses, τ_{out} , given by Eq. 6.2. In this equation, τ_{in} is the input pulse, $f = 4*\ln 2$, and φ_2 is the amount of chirp.

$$\tau_{out} = \tau_{in} \sqrt{1 + f^2 \left(\frac{\varphi_2}{\tau_{in}^2}\right)^2}$$
(6.2)

Because the observed response to chirped pulses following S_2 excitation in cyanines is unusual, we extend our previous work to solvents with higher viscosity values using methanol, ethanol, and propanol solutions. We find that as the viscosity increases, the effect that chirped pulses elicit on fluorescence increases in magnitude, for both S_1 and S_2 . In IR144, the same chirp dependent symmetrical S_2/S_1 enhancement for TL pulses is apparent for each solvent. For IR140 the S_2/S_1 ratio increase is observed near zero chirp, but the dynamics observed are less symmetric with respect to chirp. We note a slight increase in S_1 and S_2 emission for positively chirped pulses, as compared to negatively chirped pulses. The lower fluorescence for negatively chirped pulses is reminiscent of the chirp dependence observed in first excited states showing depleted fluorescence for negatively chirped pulses due to stimulated emission. One can understand the asymmetry by considering a negatively chirped pulse experiment as one where a higher energy pulse launches the wave packet in the S_2 excited and a lower energy pulse bringing the wavepacket back to the ground state.

One can get a sense of the wavepacket motion dynamics in the S₂ state using Eq. 6.2 to calculate the corresponding pulse duration FWHM, which corresponds to the delay between the blue and red frequency components, where τ_{in} is the laser pulse duration when TL. This operation allows us to calculate the values in fs listed on the top x-axis (Figure 6.9 and 6.10). The broadening of the chirp dependence measured for different solvents implies that the early (first 50-200 fs) wavepacket dynamics away from the FC region toward IC or toward the equilibrium geometry of the S₂ state, depend on the solvent. We can get a sense of the delayed wavepacket dynamics in the different solvents by taking the inverse of Eq. 6.2 and adding fitting parameters h, and b, corresponding to amplitude and baseline, to obtain Eq. 6.3. This equation is then used to fit the experimental S₂ chirp-dependence curves obtained for the different solvents in Figure 6.9a and obtain a fitting parameter τ_c that is then used to calculate changes in the wave packet dynamics. When $\tau_c = \tau_{in}$, we recover the experimental SHG intensity dependence. When the radical in the denominator equals 2, it implies that the chirped pulse has doubled in duration, and from then on, pulse duration increases linearly with chirp. We have chosen this point, when a chirped pulse can be considered analogous to two separate pulses with different central frequency, to define the 'wavepacket motion' time, a parameter that is proportional to the initial wavepacket motion. The resulting parameters, along with a 'wavepacket motion' obtained by solving Eq. 6.3 for each of the τ_c values when b=0 and h=1 and setting y=1/2, are listed in Table 6.2. The values reflect the delayed wavepacket dynamics in the different solvents resulting from the increased viscosity forming a solvent cage which prevents large amplitude motion.

$$y = b + \frac{h}{\sqrt{1 + f^2 \left(\frac{\varphi_2}{\tau_c^2}\right)^2}}$$

$$(6.3)$$

Table 6.2 Fitted chirped S₂ fluorescence curves were fitted with a Lorentzian line-shape.

Molecule	Solvent	$\tau_{\rm c} ({\rm fs})$	Error	Wavepacket motion (fs) ^a
IR144	Methanol	35.3	± 0.4	90
	Ethanol	38.3	± 0.36	105
	<i>n</i> -Propanol	43.4	± 0.34	133

The wavepacket motion time is calculated by solving Eq. 6.2 for the given τ_c values.

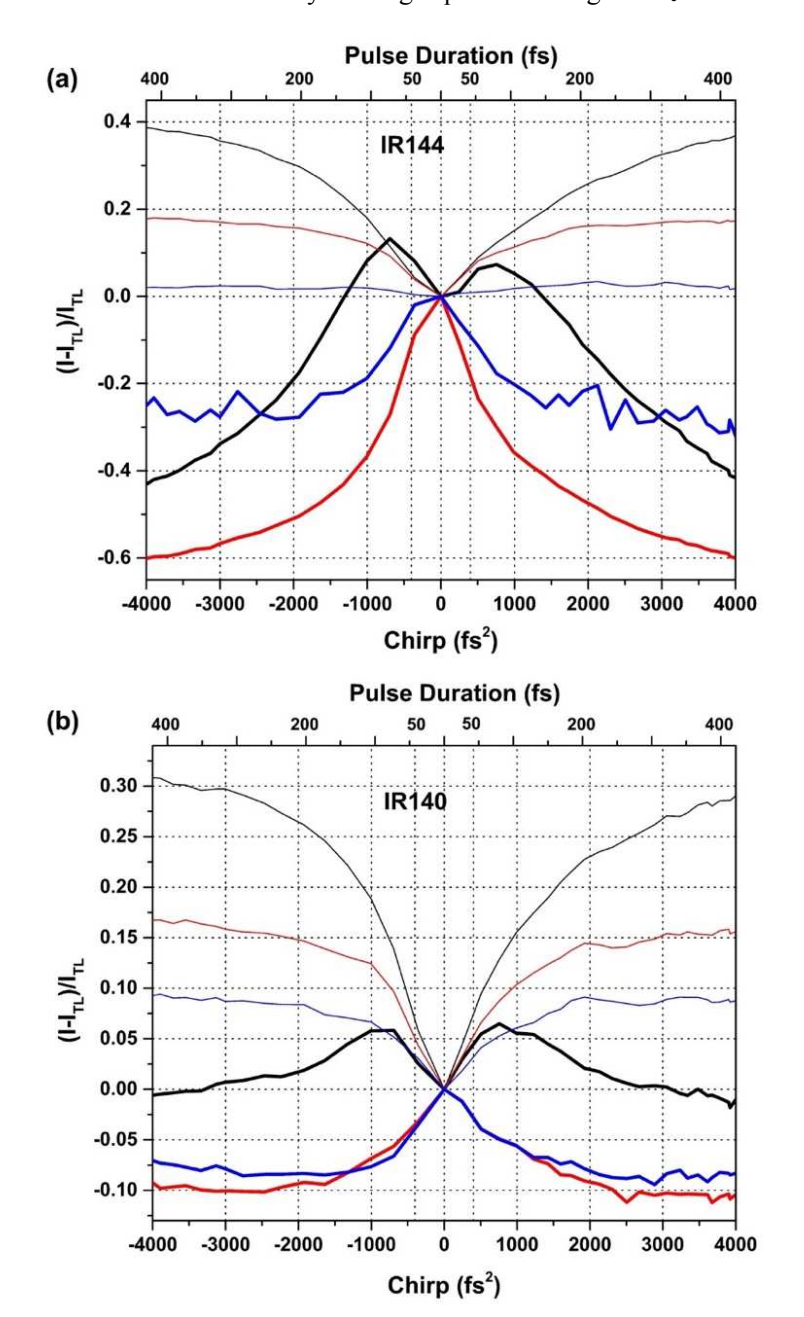


Figure 6.10. Chirp dependence scans carried out as a function of laser intensity for (a) IR144 and (b) IR140 in methanol. The thinner and thicker lines show the relative fluorescence intensity as a function of chirp compared to its TL value (I- I_{TL})/ I_{TL} for S_1 and S_2 , respectively. Laser excitation power of 15mW, 10mW and 5mW are represented by black, red and blue lines, respectively. S_1 and S_2 data are represented by thin and thick lines, respectively.

Power-dependence experiments were conducted for methanol solutions of both dyes, as shown in Figure 6.11. With the increase in laser power the S_2 intensity appears to saturate for both dyes at a laser power of 15 mW. At the highest intensity, maximum S_2 emission is no longer observed for TL pulses. Notice that saturation is not observed for S_1 fluorescence. We find the observed chirp dependence of the S_2 state in IR144 is significantly greater than the effect observed in IR140.

Having shown that viscosity causes a higher S_2/S_1 emission ratio in both IR144 and IR140, especially for TL pulses, we explore a possible relationship with chirp and laser intensity on the S_2 emission spectra of the molecules (Figures 6.11a and b). Measurements were repeated for three laser powers, 10, 15, and 20 mW. The pulses were TL (black), positively (red) or negatively (blue) chirped. For IR144, when excited by TL pulses, we find that the three intensities produce the same spectrum which corresponds to S_2^H . For chirped pulses, we find that the blue shifted S_2^H emission is less intense but increases with laser pulse intensity. This trend is not observed in IR140 (Figure 6.11b), in fact results for 10 and 15 mW for TL and chirped pulses produced identical spectra. This is consistent with IR140 preferring emission from the S_2^L configuration.

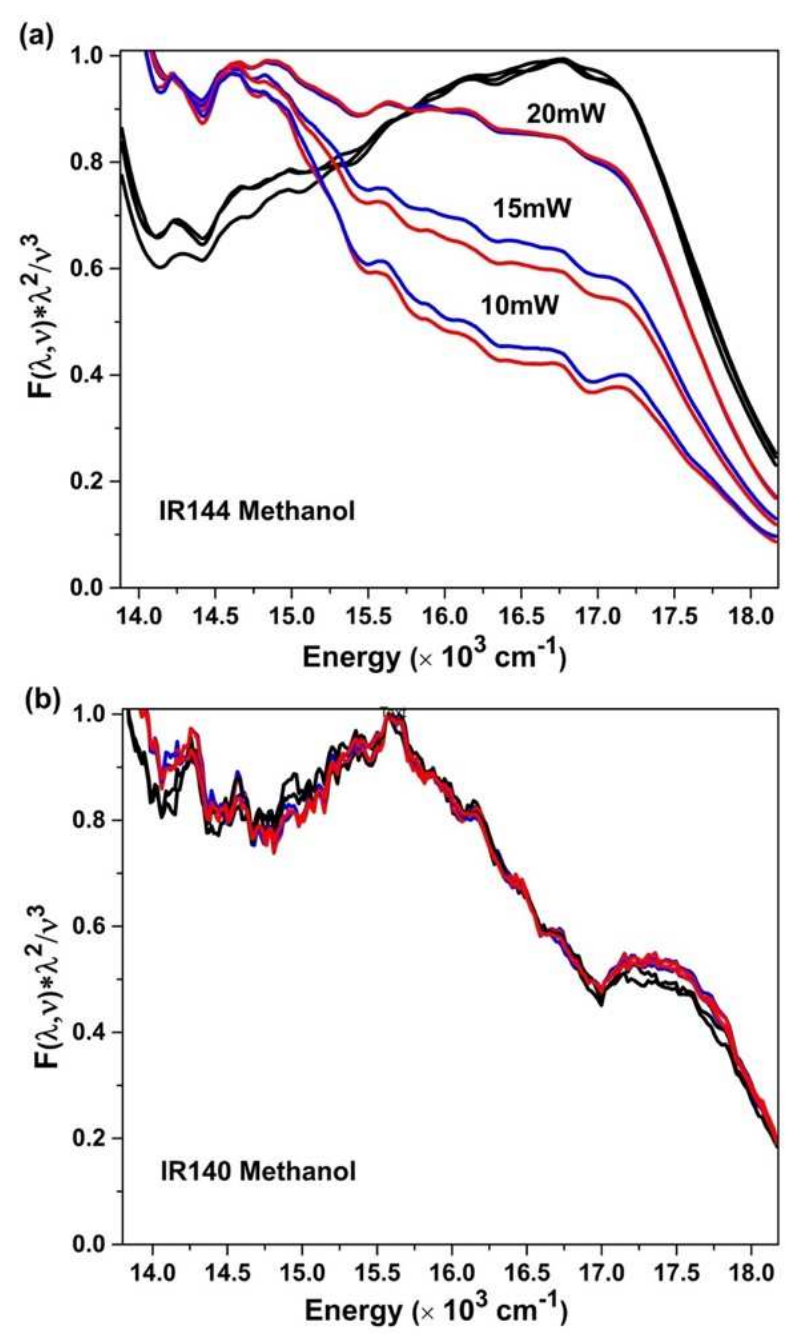


Figure 6.11. Normalized S_2 fluorescence spectra are plotted as a function of chirp and power value for (a) IR144 and (b) IR140. The blue line (positive chirp) considers chirp values from +4000 fs² to +5000 fs², while the red line (negative chirp) averages the fluorescence spectrum from -4000 fs² to -5000 fs². The black line (transform-limited pulses) stays relatively the same as the power increases for both dyes. The (b) IR140 fluorescence spectrum is not dependent upon chirp or power. 15mW and 10mW S_2 spectra are shown for the three differing pulse descriptions, with relatively no change. The data have been normalized to the highest value within the S_2 fluorescence emission band.

The motivation of this work is to maximize the lifetime of S_2 by preventing or delaying IC to S_1 so that the excess energy is available for photochemical processes such as solar energy

capture or therapeutic applications. Therefore, we quantify the integrated S_2/S_1 fluorescence ratio observed for IR144 and IR140 in the different solvents by steady state fluorescence spectroscopy as well as by femtosecond TL and chirped pulses in Table 6.3. Increasing solvent viscosity increased the S_2/S_1 ratio by a factor of 8.6 and 21 for IR144 and IR140, respectively. Femtosecond TL pulses caused even higher enhancement in the S_2/S_1 ratio by a factor of 39 and 47 for IR144 and IR140, respectively. When taking obtaining the change in the S_2/S_1 ratio obtained for femtosecond chirped pulses for methanol and TL pulses for glycerol, we obtain an overall effect of 86 and 55 for IR144 and IR140, respectively. The large difference in the effect observed for femtosecond pulse excitation compared to steady state spectroscopy indicates an additional pathway for the excitation that populates S_2 as will be discussed below.

Table 6.3 S₂/S₁ integrated fluorescence intensity ratios.

Molecule	Solvent	Viscosity (cP) ^{246–250}	Steady state	TL pulses	Chirped pulses
	Methanol	0.579	0.0014	0.022	0.010
IR144	Ethanol	1.164	0.0035	0.0342	0.013
	<i>n</i> -Propanol	2.197	0.0040	0.045	0.015
	Ethylene glycol	17.3	0.0047	0.030	0.025
	Glycerol	543	0.012	0.86	0.82
	Methanol	0.579	0.0051	0.027	0.023
IR140	Ethanol	1.164	0.0081	0.023	0.021
	<i>n</i> -Propanol	2.197	0.014	0.028	0.025
	Ethylene glycol	17.3	0.025	0.10	0.10
	Glycerol	543	0.11	1.27	1.19

6.3.2 Theory

Time-dependent density functional theory (TD-DFT) calculations were performed to identify the absorption and emission transitions of IR140 and IR144 molecules. Though TD-DFT calculations are known to predict excitations energies with errors of several tenths of an eV in cyanine dyes, the shapes of potential energy surfaces are typically found to be very accurate.^{251,252} All calculations were performed with the TeraChem software package.^{253–255} Geometries were

optimized at the CAM-B3LYP⁸³/6-31G* level. Except where noted otherwise, all calculations were performed using an implicit model of the glycerol solvent (conductor-like polarizable continuum model, C-PCM, 256,257 with dielectric constant ϵ = 46.5). All calculations were repeated in implicit methanol (ϵ = 33.0), with effectively identical results, except as noted specifically below. Alkyl chains over three carbons long and any associated sulfonate groups were replaced by methyl groups to save computational expense. Ground state optimizations show that the s-trans conformers have a lower ground state energy than the s-cis conformers for both molecules. In both molecules, the central amine group was found to rotate out of the plane of the polymethine chain. Excited state optimizations were performed to identify possible emissive geometries. The results of these optimization are presented in Figures 6.9 and 6.10 for IR140 and IR144, respectively. Three low-lying states were examined in both IR140 and IR144, which we will label S₁, S₁', and S₂. All structures were optimized in implicit solvents.

The computed S₁ vertical excitation energies at the Franck–Condon (FC) point (S₀min) are 19115 cm⁻¹ and 20486 cm⁻¹ for IR140 and IR144, respectively. These overestimate the respective experimental absorption maxima (12421 cm⁻¹ and 13469 cm⁻¹ in methanol) by 6694 and 7017 cm⁻¹, respectively. Thus, we apply respective shifts of the excited state potential energy surfaces of –6694 and –7017 cm⁻¹ in our analysis of the computational data below. These shifts account both for well-known errors in TD-DFT excitation energies and for the different environment in our calculations compared to experiment (i.e., vibronic effects, conformational flexibility, the absence of charged sulfonate groups, counterions, and hydrogen bonding interactions with solvent).

The S_1 minimum was identified in each dye, which we label S_1 min. In both cases, S_1 min is very similar to S_0 min, and has a vertical S_0 - S_1 gap less than 806 cm⁻¹ smaller than that at S_0 min.

The shifted theoretical S_1 emission energies are in excellent agreement with experiment: 11615 cm⁻¹ (18309 cm⁻¹ unshifted) and 12179 cm⁻¹ (19196 cm⁻¹ unshifted) for IR140 and IR144, respectively, compared to experimental values of 11614 cm⁻¹ and 11937 cm⁻¹. Optimization on S_1 did not yield a distinct minimum. Instead, it is found that S_1 and S_1 intersect, which likely facilitates efficient nonradiative decay from S_1 to S_1 . Thus, no emission is expected from S_1 .

In both IR140 and IR144, two distinct local minima were found on S₂, which we label S₂min-1 and S₂min-2. As detailed below, in both systems the computed S₀-S₂ energy gaps at these minima are in good agreement with the experimentally observed S₂^H and S₂^L emission peaks. In addition, in both IR140 and IR144, both S₂min-1 and S₂min-2 are significantly distorted compared to the S₀min structure. Of the two minima, S₂min-1 is more analogous to the Franck–Condon geometry; the polymethine chain remains planar, but the central amine group is twisted to 77° and 73° in IR140 and IR144, respectively (compared to 37° and 43° at S₀min). In the more distorted S₂min-2, the polymethine chain itself is twisted by 91° and 94°, relative to the planar S₀min structure. For comparison, the S₁min is less distorted, with a planar polymethine chain and respective twist angles about the central amine group of 50° and 59°.

These significant distortions of the emissive geometries compared to the S_1 min structures explain the observed solvent viscosity dependence of the ratio of S_2 to S_1 emission in both IR140 and IR144. Upon excitation to the S_2 state, molecules will be trapped at the distorted S_2 minima by more viscous solvents and emit from S_2 before nonradiative decay can occur. Thus, the ratio between S_2 and S_1 emission intensity grows larger with increasing solvent viscosity.

Careful analysis of the S_2 PES sheds light on the origin of the distinct S_{2min-1} and S_{2min-2} emission peaks. We believe that these two minima correspond to the experimentally observed S_2^H and S_2^L emission. In IR144, the predicted emission energies are 17583 and 15244 cm⁻¹ (24600 and

22261 cm⁻¹ unshifted) at S_{2min-1} and S_{2min-2} , respectively. These values are in good agreement with the experimentally observed emission peaks at 17150 and 15890 cm⁻¹, respectively. Optimization in implicit methanol solvent provides nearly identical minima and emission energies. Thus, we suggest that S_2^H and S_2^L emission correspond to the excited state structures that are twisted about either the amine substituent or the polymethine chain, respectively.

For IR140 in glycerol, two distinct minima (S_2min-1 and S_2min-2) are observed as well. The computed emission energies are 21213 and 16776 cm⁻¹ (27907 and 23471 cm⁻¹ unshifted). These likely correspond to the experimentally observed S_2^H and S_2^L emission peaks at 17230 and 15900 cm⁻¹, though agreement with the computationally predicted feature at 21213 cm⁻¹ is only qualitative. In addition, only a single minimum (similar to S_2min-2) was observed upon optimization in implicit methanol solvent. Given the large number of degrees of freedom on the molecule, there may be an additional minimum on S_2 that we have not found in our study. However, given the similarity of both the experimental emission spectra and the computed PESs of IR140 and IR144, it appears likely that the S_2^H and S_2^L emission peaks arise from distinct minima on S_2 in both systems.

Comparison of the S_2 – S_1 ' energy gaps at the optimized S_2 minima provides insights into the relative ratios of S_2 to S_1 emission in these systems. In IR144, relatively small gaps of 4355 and 1694 cm⁻¹ are predicted at the S_2 min-1 and S_2 min-2, respectively. This suggests relatively fast non-radiative relaxation to S_1 ', and subsequently to S_1 (through the above-mentioned intersection), which is consistent with the relatively low ratio of S_2 emission to S_1 emission in this system. The gaps are larger in IR140 (10082 and 5565 cm⁻¹), consistent with the higher yield of S_2 emission relative to S_1 .

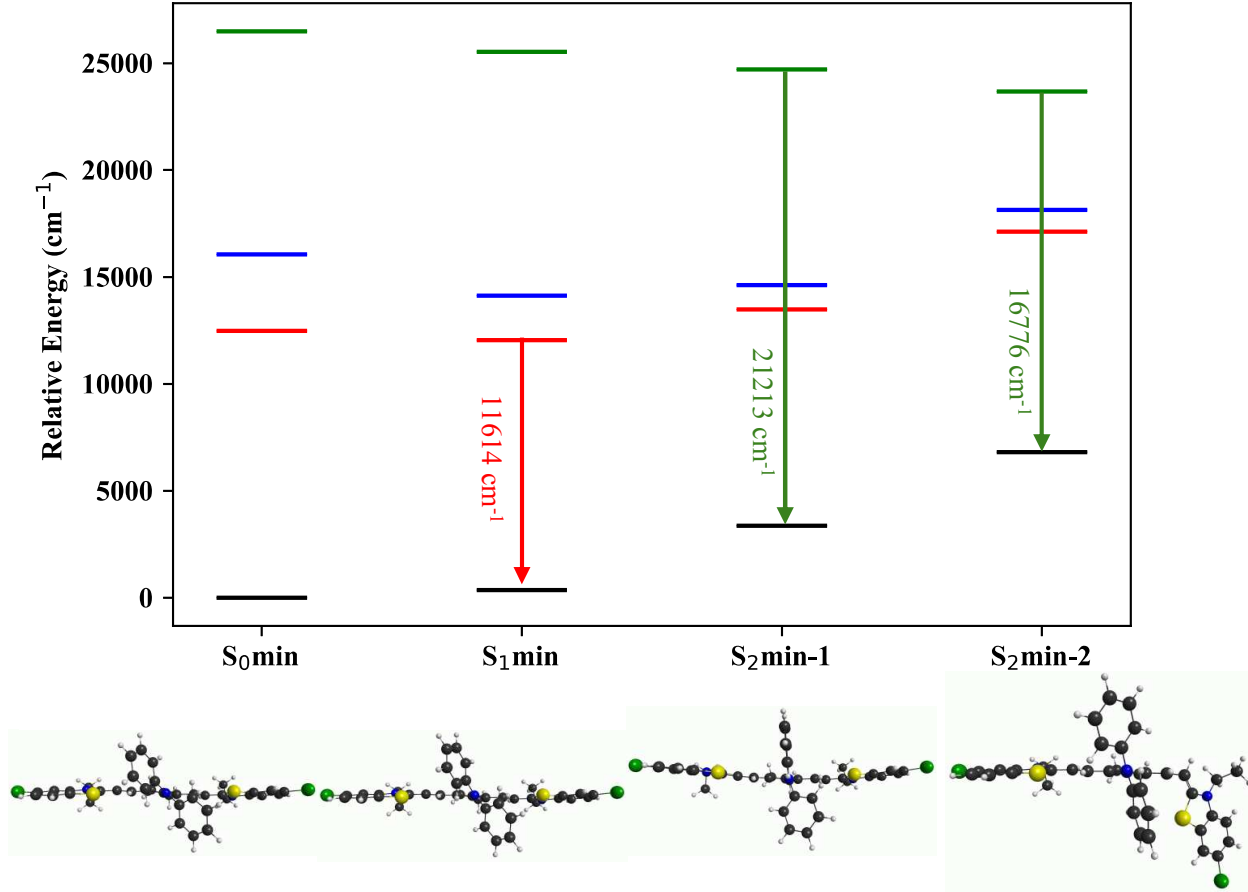


Figure 6.12. Computed state energies of IR140 in glycerol at corresponding geometries. S_0 , S_1 , S_1 , and S_2 energies are shown by black, red, blue and green lines, respectively. Energies for S_1 , S_1 , and S_2 are shifted as described in the text.

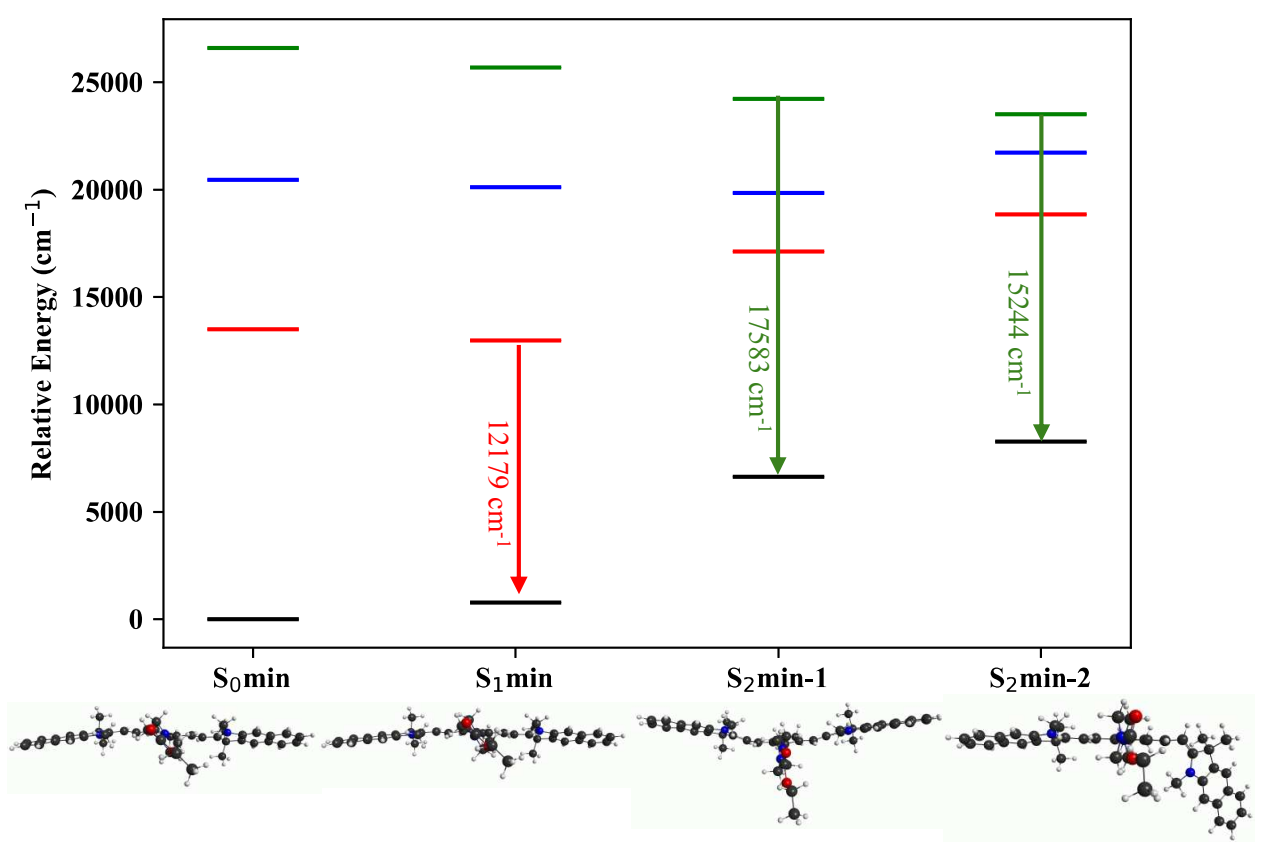


Figure 6.13. Computed state energies of IR144 in glycerol at corresponding geometries. S_0 , S_1 , S_1 , and S_2 energies are shown by black, red, blue and green lines, respectively. Energies for S_1 , S_1 , and S_2 are shifted as described in the text.

6.3.3 Numerical Simulations

Numerical simulations were carried out to understand the chirp dependence observed experimentally, and how that dependence varies with the solvent viscosity and laser intensity. The simulations are based on the scheme shown in Figure 6.14. Before addressing the chirp dependence, the first goal was to simulate the fluorescence lifetime measurements shown in Figures 6.7 and 6.8, whose fit parameters are listed in Table 6.1. For both molecules we find that the fluorescence decay from S_2 shows biexponential behavior, with viscosity dependent fast and slow components. Emission from S_1 shows an initial rise that does not vary significantly with viscosity followed by a single exponential decay. We thus assume that k_{IC} is independent of

viscosity. Following the model in Figure 6.14, the first step is the excitation from S_0 to the FC region of S_2 , forming the wavepacket shown in red. From there, the wave packet relaxes to either of the S_2 state configurations (S_2^H or S_2^L) with rate k_2 or crosses over to S_1 , by way of a conical intersection between the two states, with an IC rate k_{IC} . The S_2 emission has two contributions, soon after excitation the population can be considered 'hot' and is indicated as S_2^* , following relaxation and a likely structural change as discussed in the quantum calculations presented above, emission is from a configuration that is much less likely to undergo IC, indicated as S_2 . The briefest system of differential equations that describes the data is:

$$\frac{d[S_{2^*}]}{dt} = -(k_{IC}[S_{2^*}] + k_2[S_{2^*}] + k_{fl}[S_{2^*}])$$

$$\frac{d[S_2]}{dt} = k_2[S_{2^*}] - k_{fl}[S_2]$$

$$\frac{d[S_1]}{dt} = k_{IC}[S_{2^*}] - k_{fl}[S_1]$$
(6.3)

The system of equations is solved using Mathematica®. For these calculations, the population starts in S_2 and the times associated with the rates $1/k_{\rm IC}$, $1/k_2$ are 32 ps, 46 ps for methanol, respectively. To keep the model as compact as possible, we did not include in these equations the fact that some of the excitation goes directly into S_1 given that its higher vibrational states overlap with S_2 , and we did not introduce the state S_1 , which is even closer to S_2 . However, the initial excitation causes initial populations, which we designate S_{1_nat} and S_{2_nat} . No efforts were made to differentiate the model between IR144 and IR140. The fluorescence lifetimes for S_2 and S_1 were obtained from Table 6.1.

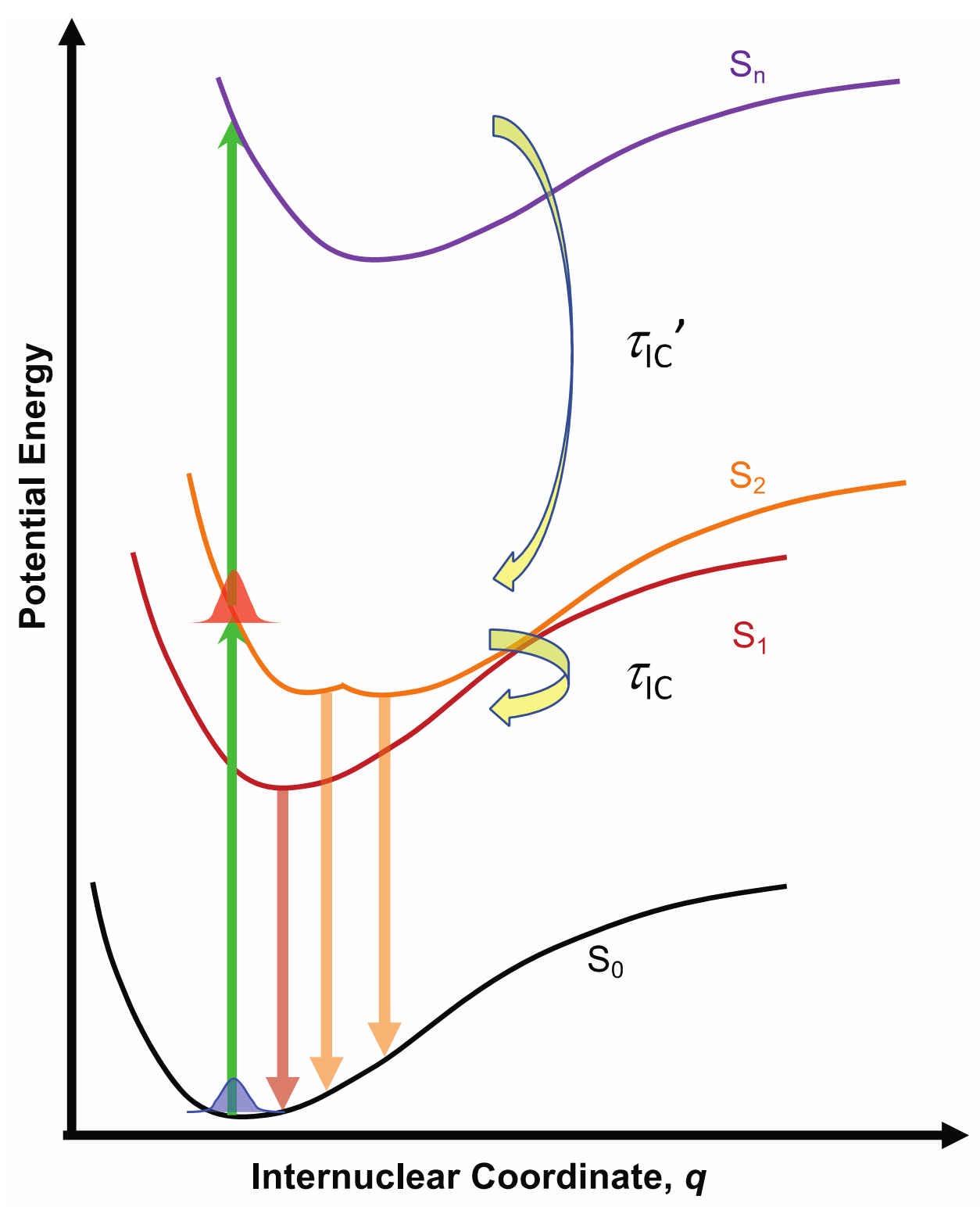


Figure 6.14. Schematic model representing potential energy curves that illustrate the different processes involved in the femtosecond chirped pulse experiments. As indicated in the theory section, two S_2 states were identified. The S_2 state under adiabatic representation can be considered as having a double well potential that leads to emission at two different wavelengths.

To simulate the chirp dependence results shown in Figure 6.9a we include the possibility of two-photon excitation from the FC region reached by the first photon (linear superpositions of both S_1 and S_2 vibronic states) to a higher excited state (see Figure 6.14), which if such an excitation relaxes preferentially to S_2 explains the chirp dependence and the power dependence of the S_2 fluorescence. When the pulses are TL, the probability of two-photon excitation is maximum, and as the chirp magnitude increases, the two-photon excitation is less probable. Two-photon excitation is proportional to pulse duration, thus, we set k_2 proportional to the inverse of the chirp-dependent pulse duration given by Eq. 6.1, such that for TL pulses k_2 decreases. We further note that the rate with which the molecular geometries associated with the S_{2L} and S_{2H} equilibrium, from which IC is no longer possible, is viscosity dependent. This explains why the observed chirp dependence shown in Figures 6.9a and b becomes broader as viscosity increases. Therefore, we made k_2 proportional to viscosity divided by pulse duration. The time-integrated S_1 and S_2 populations as a function of chirp mimic the behavior, as observed in the experiments, without the need to introduce higher excited states or additional relaxation constants.

When the laser is very weak, the effect of chirp on the pulses is smaller, and in the limit where nonlinear processes are no longer possible, chirp makes no difference. Because S_2 is nested within S_1 , and because of the presence of state S_1 , and evidenced by the overlapping absorption spectra in Figures 6.4a and b and illustrated in Figure 6.14, laser excitation populates both the S_1 and S_2 states. Empirically we found that S_{1_nat} is 3.54 times greater than S_{2_nat} . With these parameters, we were able to reproduce the chirp and viscosity dependence observed experimentally for methanol, ethanol and propanol, as shown in Figure 6.15. For the simulations shown, the only parameter that was changed was the viscosity of the solvent.

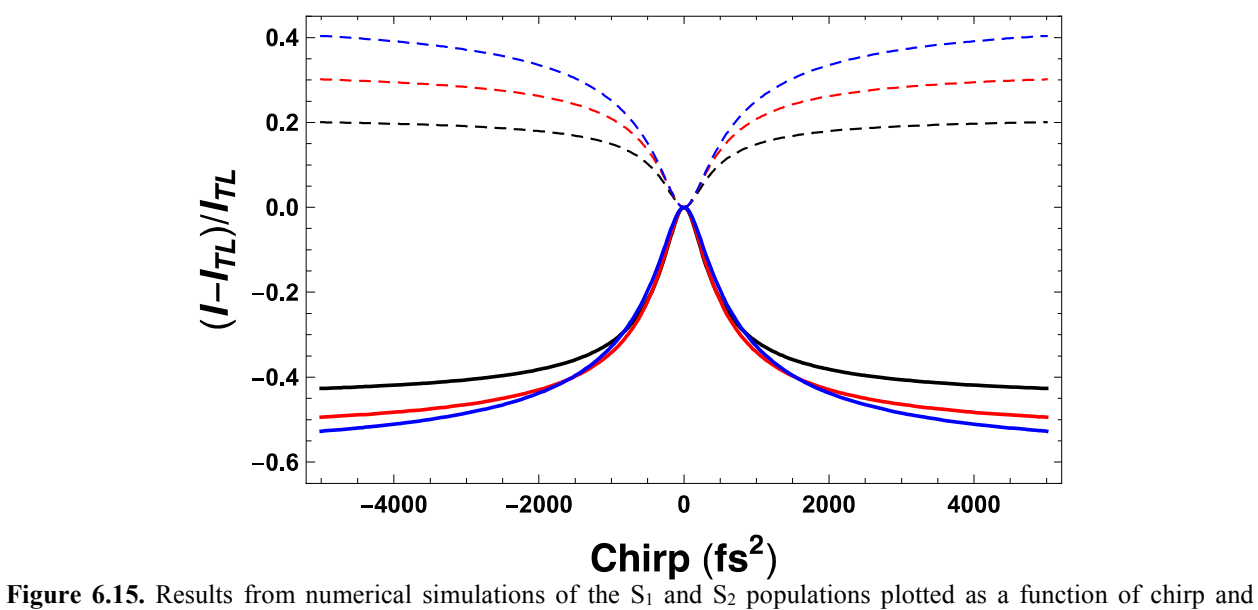


Figure 6.15. Results from numerical simulations of the S_1 and S_2 populations plotted as a function of chirp and viscosity. The viscosity of the solvent affects the rate k_2 , and this is reflected in the chirp dependence. Results shown for methanol (black), ethanol (red), and propanol (blue), where the only parameter changed in these simulations was the viscosity of the solvent.

Saturation of the S_2 FC region occurs under high laser intensity, near TL conditions. In this case, as the pulse duration increases, the wavepacket has time to move out of the FC region and S_2 can achieve greater population than observed with TL pulses. As pulse duration increases further, the behavior returns to the unsaturated case. Saturation was simulated by multiplying the S_2 population by a Gaussian function $\exp(-w^2)$, where $w = sk_2$. The saturation parameter s controls the extent of saturation. Because the rate constant k_2 is inversely proportional to pulse duration, we find that as pulse duration increases because of chirp, that saturation decreases. The population of S_2 is also increased by any population in the FC region of S_1 before it relaxes. This contribution increases as pulse duration increases at first but then decreases as that population relaxes and can no longer undergo two-photon exciation.

$$S_2 = e^{-w^2} \int_0^\infty S_2(t) dt + (1 - e^{-w^2}) \int_0^\infty S_1(t) S_{1_nat} dt + S_{2_nat}$$
 (6.4)

The saturation parameter *s* goes from zero to 27 in our simulations. The simulations as a function of laser intensity, using the viscosity of methanol, are presented in figure 6.16. At low intensities (blue line), the effect of chirp is minimal because two-photon excitation has a low probability. At optimum conditions we observe a large relative difference as a function of chirp (red line). Under saturation conditions (black line) we observe that the population in the S₂ state for increases above the TL value. The three conditions simulate the experimental data shown in Figure 6.10a. We did not include in our model the wavepacket motion in the S₂ state that results in the asymmetry visible in the IR140 data (Figure 6.10b, namely, greater fluorescence intensity for positively chirped pulses compared to negatively chirped pulses.

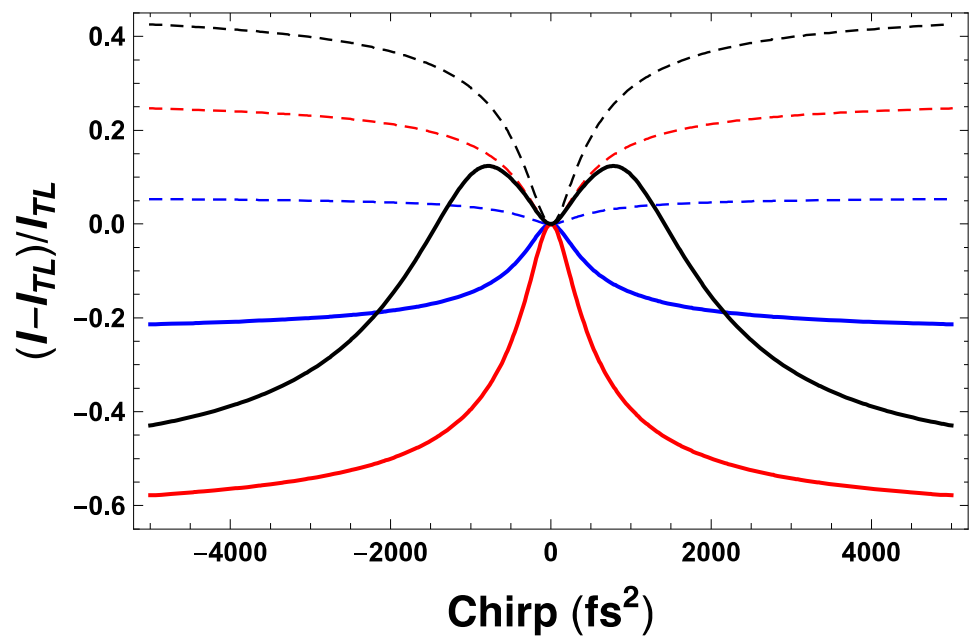


Figure 6.16. Results from numerical simulations of the S_1 and S_2 populations as a function of chirp for three different laser intensities: weak pulses (blue), higher intensity (red), and saturation (black); as described in the text.

6.4 Discussion

Results from steady state spectroscopy, including EEM spectra and fluorescence lifetime measurements in IR144 and IR140 in different solvents can be understood by taking advantage of the quantum calculations presented here. While emission from S₁ and S₂ states had been observed for both molecules before, here we report on a state we designate as S₁' that is bright in the sense of absorption but quickly decays to the bottom of the S₁ state. No evidence of S₁' fluorescence is observed in the EEM spectrum. Quantum calculations are able to predict this state and in addition find that it relaxes to the S_1 equilibrium geometry, consistent with experimental data. In addition, we report on two distinct molecular configurations for the S2 state. These correspond to two different states with different molecular structure. Because of their close proximity in energy, excitation from the ground state populates both of these states. We find that IR144 is more likely to emit from S₂^H and but IR140 is more likely to emit from S₂^L. The preference can be explained by realizing that S₂^H is associated with twisting of the amine substituent, which is more easily accomplished by IR144 than IR140. Conversely, the bulky amine substituent in IR140 does not twist substantially and emission from a configuration where the polymethine chain twists, corresponding to S_2^L , is preferred.

Fluorescence lifetime measurements report on the relatively long-lived S_2 states of these molecules, their dependence on viscosity, and their IC rate to the S_1 state. These measurements are later used to parametrize numerical simulations. The fluorescence decay from the S_2 states shows a biexponential behavior. We suggest that the biexponential decay arises from two sources. First, the initially excited 'hot' population in S_2 is able to undergo IC, and thus has a fast fluorescence decay. Upon vibrational cooling and likely structural change as discussed in the quantum

calculations, the relaxed S_2 state is much less likely to undergo IC and shows a fluorescence lifetime that is similar to the S_1 fluorescence lifetime.

Chirp dependence measurements obtained following excitation of the S₂ state are very different than those obtained following excitation of the S₁ state.^{3,233} The difference arises from two additional pathways. First, S₂ excitation can undergo IC to the S₁ state, and thus avoid depletion by negatively chirped pulses. Second, resonance two-photon excitation to a higher state provides an additional source of signal for TL pulses. In the particular case of IR144 and to some extent in IR140, excitation with intense TL pulses increased the ratio of S₂ emission. The corresponding nonlinear optical Albrecht diagrams corresponding to S₁ and S₂ excitation are provided in the introduction. In particular pathway 2⁻ in Figure 6.2 is responsible for the depletion observed for negative chirps. And pathway (TPE) in Figure 6.3 is responsible for the enhancement observed for TL pluses. This was confirmed by power dependence measurements and by fluorescence measurements under different laser excitation intensities.

The chirp dependence was found to broaden with solvent viscosity. This is because the initial motion of the wavepacket, primarily intramolecular vibrational motion, is constrained by solvent viscosity. Therefore, as viscosity increases the dependence on a fast chirp-rate, which varies inversely with chirp magnitude, is less stringent. Moreover, as viscosity increases, the wavepacket motion out of the FC region takes longer, facilitating the two-photon excitation pathway, which apparently is not available once the wavepacket has moved out of the FC region. We find that the slowdown is more pronounced for IR140 than for IR144, and this can be explained by the favored polymethine twist in IR144 as compared to amine substituent twist in IR140.

At higher intensities both molecules show saturation, such that one observes greater S_2 emission for chirped pulses than for TL pulses. Power dependence shows IR140 is much more

sensitive to saturation, as observed in the magnitude of the chirp effect under intense pulse excitation. Interestingly, the S_1 chirp dependent intensity does not show signs of saturation. We rationalize this observation by first noting that saturation depends on how the rate of excitation compares with the rate of wave packet motion out of the FC state. Direct excitation populates very high vibrational states in S_1 that undergo fast relaxation, competing favorably against saturation. The fraction of the population in S_2 that undergoes IC to S_1 avoids saturation. Therefore, the two main sources of population to S_1 show no sign of saturation.

We confirmed that the S_2/S_1 ratio is maximized for TL pulses, as had been observed before by our group. Most importantly, the enhanced S_2/S_1 ratio for TL pluses, as had already been reported by our group, can now be understood as a two-photon excitation originating from the FC region reached by the first photon, provided the wavepacket has not moved during the excitation process. This conclusion is reached by correlating multiple observations. First, two-photon 520 nm excitation (260 nm one-photon) leads to $S_2 \rightarrow S_0$ emission. Power dependence measurements of the S_2/S_1 ratio (Figure 6.11) are also consistent with two-photon excitation. The laser power dependence measurements are shown in Figure 6.17. Numerical simulations based on a kinetic model allowed us to test several alternative processes and their dependence on laser intensity, pulse chirp, and solvent viscosity. The overall scheme depicted in Figure 6.14, is the one was consistent with all our experimental observations.

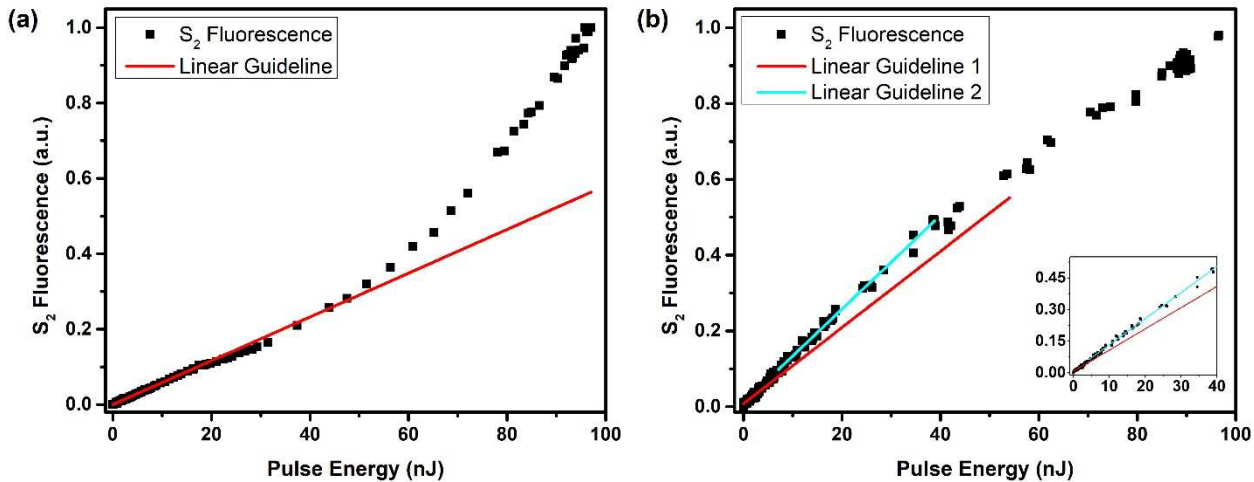


Figure 6.17. Laser intensity dependence of S_2 fluorescence upon 520 nm excitation for (a) IR144 and (b) IR140 in n-propanol.

One of the goals of this research was to take advantage of viscosity to slow intramolecular dynamics and enhance the population ratio S_2/S_1 . The greater the S_2/S_1 ratio the greater the probability to harness the energy provided by higher photon energies. Because in most molecules excitation of higher states leads to very fast relaxation to the bottom of the first excited state, according to Kasha's rule, one is not able to take advantage of the full energy content of photons. Being able to populate long-lived higher excited state is essential to enable novel photochemistry. For example, a cyanine derivative has recently been shown to undergo photodissociation following two-photon excitation to its second excited state. ²⁵⁸ One may extrapolate these results and imagine that capturing energy in higher excited states may lead to more efficient solar energy capture, especially systems containing cyanine compounds, ²²⁰ and perhaps theranostic applications whereby a compound excited to S_1 serves as fluorescent marker but when excited to S_2 it serves as a therapy agent.

6.5 Conclusions

In this study we have applied femtosecond pulse chirp and solvent viscosity to manipulate the rate of IC following S₂ excitation of IR144 and IR140. Steady state spectroscopy including excitation emission spectra and fluorescence lifetime emission, together with quantum calculations have revealed an excited state termed S₁, that promptly relaxes to S₁ but influences the IC process from S₂. In addition, we find that the S₂ state has two stable molecular configurations S₂^H and S₂^L associated with amine substituent twist or polymethine chain twist, respectively. We find that IR144 emits preferentially from S₂^H, while IR140 emits preferentially from S₂^L. Taking advantage of solvent viscosity and femtosecond pulse chirp we are able to manipulate the S₂/S₁ fluorescence ratio of IR144 from a minimum value of 0.01 for methanol with 5000 fs² chirp, to a maximum of 0.86 obtained for TL pulses. This overall change corresponds to almost two-orders of magnitude. The ability to control IC from upper excited states, may open exciting possibilities for the photochemical applications of cyanine dyes in imaging and photodynamic therapy. The results presented here may lead to future work on manipulating the lifetime of the upper excited states of similar polymethine dyes, other cyanine dyes and possibly other molecules such as carotenes.

Chapter 7 Human Serum Albumin Dimerization Enhances S₂ Emission of Bound Cyanine IR806

Cyanine molecules are important phototheranostic compounds given their high fluorescence yield in the near-infrared region of the spectrum. We report on the frequency and time-resolved spectroscopy of the S_2 state of IR806, which demonstrates enhanced emission upon binding to the hydrophobic pocket of human serum albumin (HSA). From excitation emission matrix spectra and electronic structure calculations, we identify the emission as one associated with a state having the polymethine chain twisted out of plane by 103° . In addition, we find that this configuration is significantly stabilized as the concentration of HSA increases. Spectroscopic changes associated with the S_1 and S_2 states of IR806 as a function of HSA concentration, as well as anisotropy measurements, confirm the formation of HSA dimers at concentrations greater than $10 \,\mu\text{M}$. These findings imply that the longer-lived S_2 state configuration can lead to more efficient phototherapy agents, and cyanine S_2 spectroscopy may be a useful tool to determine the oligomerization state of HSA.

This chapter has been adapted with permission from (*J. Phys. Chem. Lett.* **2022**, *13*, 1825-1832) Copyright © 2016, American Chemical Society.

7.1 Introduction and Background

Excitation to high-lying electronic excited states usually leads to internal conversion (IC) to the lowest excited state, as postulated by Kasha. ⁴⁴ Efforts to extend the lifetime of higher excited states, including increasing the solvent viscosity have been shown to decrease the rate of IC. ^{1,53,56} The combination of viscosity and nonlinear excitation has been shown to cause changes in the S₂/S₁ population ratio that are greater than an order of magnitude. ²⁵⁹ Here, the protein pocket of human serum albumin (HSA) is found to stabilize the S₂ state of cyanine IR806 in a geometry that delays the excited state non-radiative dynamics, resulting in a longer S₂ excited state lifetime. As the HSA concentration increases and protein dimers form, we find increased emission due to greater constraint of the molecular structure.

Heptamethine cyanine dyes are promising phototheranostic reagents given their high fluorescent yield and generation of singlet oxygen. 260-263 IR806 is a heptamethine cyanine dye capable of exhibiting extended conjugation through the polymethine group (Scheme 1a), allowing it to absorb and emit light in the IR region. IR806 is of interest due to its high extinction coefficient as well as quantum efficiency, giving it the potential to be used as a phototheranostic agent. Extending the lifetime of the S2 state of cyanines can lead to phototheranostic activity via direct excitation of the S2 state via two-photon excitation using near-IR laser pulses. The motivation for the use of IR806 can be derived from the similarities to the heptamethine dye IR125, also known as indocyanine green (Scheme 1b), the only near-IR FDA approved dye, which is extensively used for medical diagnostics including cardiac output measurements, liver function and ophthalmic angiography. Previous studies involving cyanine dyes have shown that these molecules bind with HSA, the most abundant protein in blood plasma. Previous shown that these molecules bind with HSA, the most abundant protein in blood plasma.

Scheme 7.1 Molecular structure of (a) IR806 and (b) IR125.

HSA consists of 585 amino acids with a molecular weight of $66.5 \text{ kDa}.^{277-279}$ In vivo HSA has a wide variety of functions in addition to maintaining plasma oncotic pressure, such as transporting steroids and the capability of binding to reactive oxygen species. ^{280–283} Thus, understanding the interactions of molecules with HSA is of great importance due to HSA's ability to allow binding and transporting a wide variety of molecules such as fatty acids, hormones, and a multitude of drugs. ^{284–286} X-ray crystallographic studies have shown that albumin has a heart-shaped tertiary structure, which changes to an ellipsoid in solution. ^{287,288} Hence, the tertiary and quaternary structure of HSA must be dependent on the overall concentration of HSA in solution, which would naturally alter the behavior of the protein; research has shown that reversible non-bonding dimers of HSA occur in concentrations as low as $10 \,\mu\text{M}$, ^{289,290} indicating that a significant portion of HSA could exist as dimers in the blood stream of a healthy individual where the concentration is between 526–753 μM . ²⁷⁸ Additionally, HSA dimers are a biomarker for oxidative stress and liver cirrhosis. ^{291,292} However, there is limited studies on the quantification of HSA occurring as dimers in the body.

The binding of IR806 with HSA has been experimentally confirmed in Awasthi et al.²⁷³ The two common ligand binding sites in HSA are the hydrophobic cavities in subdomain IIA and

IIIA. 272–276,293 The binding site in subdomain IIA exhibits hydrophobic interactions, which are strongly influenced by interactions with the hydrophobic sections of the binding dye.

In our recent studies of the higher excited states of IR144 and IR140, we found two S₂ states, which have distinctly different geometries, designated as S2^H and S2^L. ²⁵⁹ The geometry of S₂^H resembles a planar structure in the polymethine chain and fluoresces at a higher frequency. The geometry of S₂^L shows a 103-degree twist in the polymethine chain and fluoresces at a lower frequency. We find that IR806, when bound to HSA, adopts a distorted geometry. Based on spectroscopic data and calculations, we find that S₀ and S₁ states have energy minima corresponding to their planar geometries, thus the distorted geometry involves twisting distributed among several bonds. However, we find that the S₂^L state is stabilized when IR806 binds HSA. This observation is supported by an increase in the S₂^L fluorescence intensity and lifetime as the concentration of HSA increases. We present evidence for spectroscopic changes in IR806 bound to HSA occurring at concentrations where HSA reversible dimers form. This finding has two important consequences. First, a longer S₂ lifetime may enable the higher energy and hence more reactive state to act as an efficient phototheranostic species. Cyanine dyes can be designed accordingly to release therapy agents upon S_2 excitation. Second, the S_2 emission of IR806 shows conspicuous enhancement following HSA dimerization, in comparison to low HSA concentration. Therefore, it points to a spectroscopic method for quantifying the degree of aggregation of HSA, which has been linked to oxidative stress and liver cirrhosis.

7.2 Experimental and Theoretical Methods

IR806 (Sigma-Aldrich 543349) and human serum albumin protein (Sigma-Aldrich A3782) were purchased and used without any further purification. Phosphate buffered saline 10x (DOT Scientific Inc. DSP32060-1000) was diluted to 1x with deionized water and used as the solvent for all solutions. IR806–HSA samples of different molar ratios were freshly prepared by mixing the individual solutions. All solutions were prepared at room temperature (~ 298 K) and used within 8 minutes, which is the timeframe in which the absorption spectrum of the sample remains unchanged, indicating no reaction between the protein and the dye. All measurements were recorded in 1 cm quartz cuvettes.

Absorption and emission spectra were acquired using a Horiba Duetta spectrofluorometer. For time-resolved fluorescence measurements, a Ti:sapphire oscillator (Vitara-S, Coherent) producing pulses at 80 MHz centered at 800 nm was used to generate white light (WL) using a supercontinuum polarization maintaining photonic crystal fiber (FemtoWHITE 800, NKT Photonics). The WL was collimated and passed through a bandpass filter, transmitting pulses between 590 – 640 nm. The polarization was rotated with a half-wave plate to obtain vertically polarized pulses for excitation. A 16-channel photomultiplier time-correlated single-photon counting (TCSPC) system (SPC-830 TCSPC, Becker-Hickl, GmBH) was used to detect fluorescence from the samples. The fluorescence was acquired at parallel and perpendicular polarizations with respect to the vertically polarized excitation pulse, with the help of a polarizer, to obtain the isotropic decay component. Additional TCSPC data were acquired to record the rotational anisotropy behavior, described elsewhere, and we highlight the relevant details here. The light source for this instrument is a passively mode-locked Nd:YVO4 laser (Spectra-Physics Vanguard) that produces 13 ps pulses at 1064 nm with 80 MHz repetition rate. The second and

third harmonic outputs of this laser provide 2.5 W average power at 532 and 355 nm, respectively, with nominally the same 13 ps pulse width. The second harmonic output of this laser was used to excite a synchronously pumped cavity-dumped dye laser (Coherent 701-3) operating at 610 nm, which was used to excite our samples. A portion of the 700 nm pulse train was sent to a reference photodiode (B&H). Sample fluorescence was collected using a 40× reflecting microscope objective (Ealing) and sent to a polarization-selective beamsplitter (Newport). Each polarized emission component was polarization-scrambled and sent through a subtractive double monochromator (CVI Digikrom CM112) to a microchannel plate photomultiplier (Hamamatsu RG3809). The output of each detection channel was sent to one channel of a TCSPC system (B&H Simple Tau 152). Data were acquired and stored by using software written in-house using National Instruments LabVIEW.

Molecular docking simulations were carried out to determine the most favorable binding site of IR806 in HSA and gain insight into the changes in the structural features of IR806 upon binding. The methodology for molecular docking used in this work has been adapted from Nairat et al.'s work, and we highlight the main aspects here. The structure of the protein was adapted from the crystal structure of HSA in the protein data bank (PDB: 1AO6), which is dimeric in nature. The structure of the dye is adapted from the ground state optimized geometry from DFT calculations. The IR806 and HSA PDB files were introduced into the AutoDockTools (ADT), and polar hydrogens were added to both structures. ADT identified the rotatable bonds for the purpose of docking, and a grid box, big enough to contain the entire protein, was initialized to define the active space for the simulation. Docking was then carried out by using the Lamarckian Genetic Algorithm to obtain the 10 most favorable conformations with the highest binding affinity. Pymol was used to visualize the docked IR806 geometries in HSA.

Calculation of the ground and excited state structures of IR806 have been carried out using density functional theory (DFT) and the time-dependent extension of DFT (TD-DFT), respectively. The Gaussian 16 platform was utilized for the DFT and TD-DFT calculations. The geometry optimization of the different energy states was achieved at the CAM-B3LYP/6-311+G(d) level of theory. All the calculations were performed in the presence of a polarizable field of water, in order to simulate experimental conditions, using the continuum solvation model based on the solute electron density (SMD). The alkyl chains, off the nitrogen of the indole moiety on either side of the molecule, were replaced by methyl groups to conserve computational cost. This modification caused change in the transition energies of less than 1%. The ground and excited state geometry minimizations were accompanied by frequency calculations to ensure the stability of the states.

7.3 Results and Discussion

The normalized steady-state absorption of IR806 in buffer solution is shown in Figure 7.1a, which shows an absorption maximum for the first electronic excited state (S_1) at 12520 cm⁻¹, accompanied by a vibronic shoulder at 13600 cm⁻¹. Keeping the IR806 concentration constant at 5 μM, we increased the concentration of HSA, which resulted in a red shift of the S₁ absorption maximum. This is consistent with previous experiments, which show that a larger red shift of the S₁ absorption maximum indicates better protein-dye binding, with the 1:15 IR806-HSA solution showing a red shift of 200 cm⁻¹ in comparison to the unbound dye. The excitation–emission matrix (EEM) spectrum of IR806 in solution is shown in Figure 7.1b, and the EEM for a 1:15 IR806-HSA mixture is shown in Figure 7.1c. The emission maximum for S₁ shows a red-shift of 160 cm⁻¹ in the unbound dve compared to the IR806-HSA mixture. The EEM spectrum of IR806 reveals higher excited state emissions, which we shall label as S_2^H and S_2^L , which show excitation maxima at 16300 cm⁻¹ and 14880 cm⁻¹, respectively. The corresponding emission maxima for S₂^H and S₂^L are 15290 cm⁻¹ and 14130 cm⁻¹, respectively. It is worth noting that, although we are not able to identify the S₂^H and S₂^L absorption bands from the absorption spectra, mainly because of the strong S₁ absorption, we can determine excitation maxima from the EEM spectra.

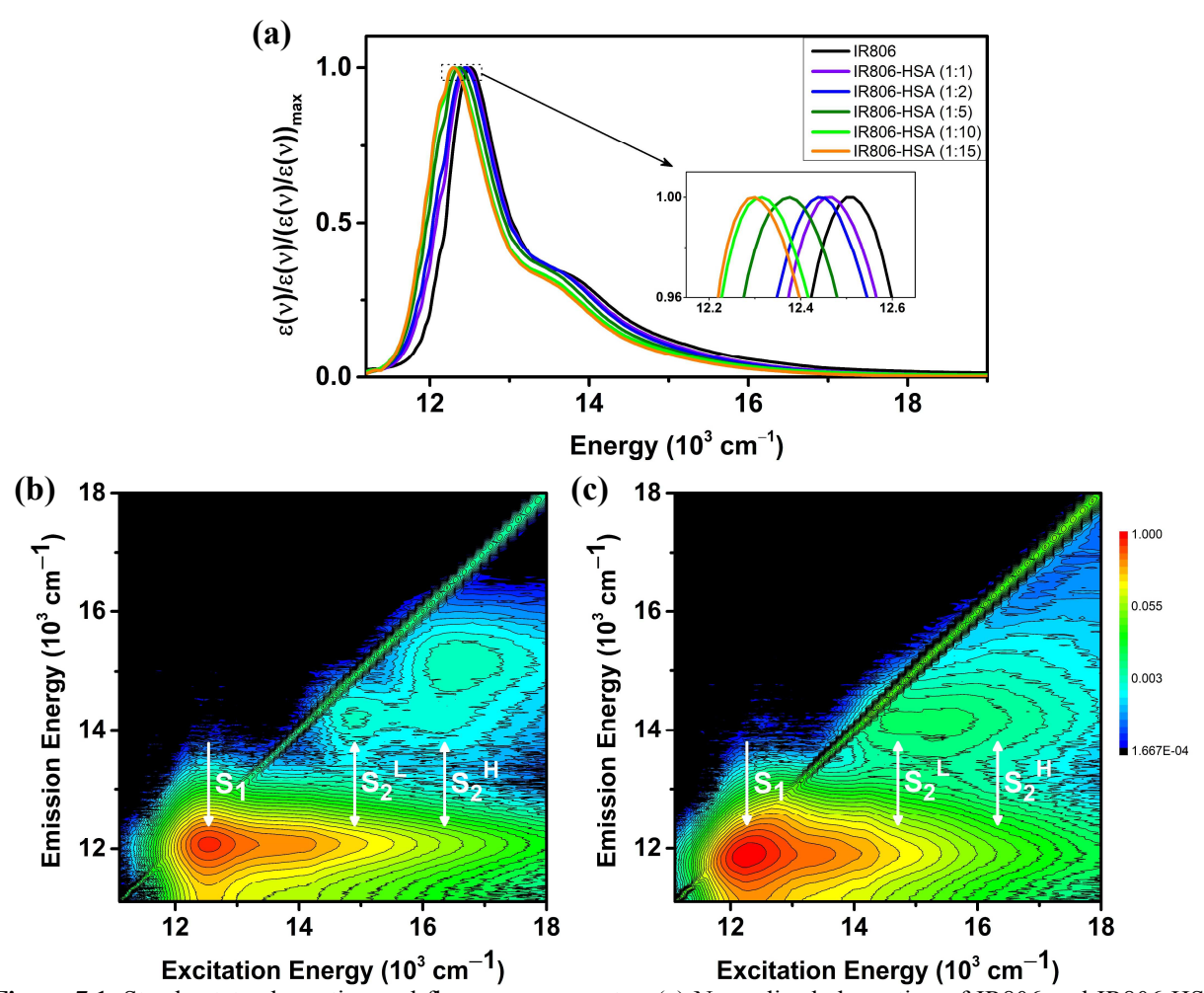


Figure 7.1. Steady-state absorption and fluorescence spectra. (a) Normalized absorption of IR806 and IR806-HSA samples prepared in pH 7.4 buffer. The IR806 concentration was kept constant at 5 μ M. (b) EEM spectrum of IR806 in the buffer. (c) EEM spectrum of IR806-HSA at 1:15 relative concentration. Please note that the scale for the z-axis in the EEM spectra is logarithmic.

The emission spectra following excitation at 16667 cm^{-1} , which is close to the absorption maximum of S_2^H , is shown as a function of HSA concentration in Figure 7.2a. For these measurements, the concentration of IR806 was fixed at 2 μ M and the integrated emission was normalized to a constant for all concentrations shown. We observe that emission from S_2^H is significantly higher in free IR806, with negligible emission from S_2^L . However, the emission from S_2^L increases upon IR806 binding to HSA, as can be seen in the 2 μ M HSA case. The S_2^L emission shows significant enhancement with the increase of HSA concentration, along with a noticeable

decrease in the S_2^H emission. With the further increase of the HSA concentration, beyond 10 μ M, we observe an even greater increase in the ratio of S_2^L to S_2^H emission, as shown in Figure 7.2b.

Fluorescence lifetime measurements were carried out on the IR806 and IR806-HSA solutions. Isotropic decay traces ($I_{\parallel}(t)+2I_{\perp}(t)$) of this excited state are shown in Figure 7.2c, which are plotted on a \log_{10} scale. The fluorescence, upon laser excitation centered at 16500 cm⁻¹ and detection at 14500 cm⁻¹, exhibited a biexponential decay. The deconvoluted lifetimes for the different solutions are given in Table 7.1. The presence of a biexponential decay indicates that a fraction of the population remains in S₂. In previous work from our group on IR144 and IR140, ^{1,259} we identified a change in the molecular structure associated with twisting in the polymethine chain in the S₂ state that causes a bottleneck, which prevents IC to S₁. The molecules that become twisted, namely the S₂^L state, have a much slower IC to S₁, and primarily exhibit S₂ \rightarrow S₀ fluorescence. Therefore, the fast component (π) of the biexponential corresponds to a portion of the S₂ population, which undergoes IC to the S₁ state, while the slow component (π) corresponds to a non-IC configuration that remains trapped in S₂. We rule out the possibility that the long-lived component is due to S₁ fluorescence given that the S₁ fluorescence lifetime (π) is shorter than 520 ps in the presence of HSA (see Figure 7.3).

Table 7.1 Fluorescence lifetimes obtained from time-correlated single photon counting experiments. The time constants are as defined by the fitting equation $f(t) = a \exp(-t/\tau_1) + (1-a) \exp(-t/\tau_2)$.

Samplea	а	$\tau_{\rm l} \ ({\rm ps})$	τ_2 (ps)	$ au_{\mathrm{avg}}\left(\mathrm{ps}\right)$	$ au_{ m OR} \left(m ps ight)$	$ au_3$
IR806	0.88	273 ± 20	1138 ± 107	380 ± 31	450 ± 49	261± 3
IR806-HSA (1:1)	0.84	286 ± 3	1296 ± 22	445 ± 6	550 ± 62	305 ± 5
IR806-HSA (1:15)	0.64	293 ± 9	1363 ± 70	673 ± 31		505 ± 10

 $^{^*\}tau_{\text{avg}} = a \tau_1 + (1 - a) \tau_2$

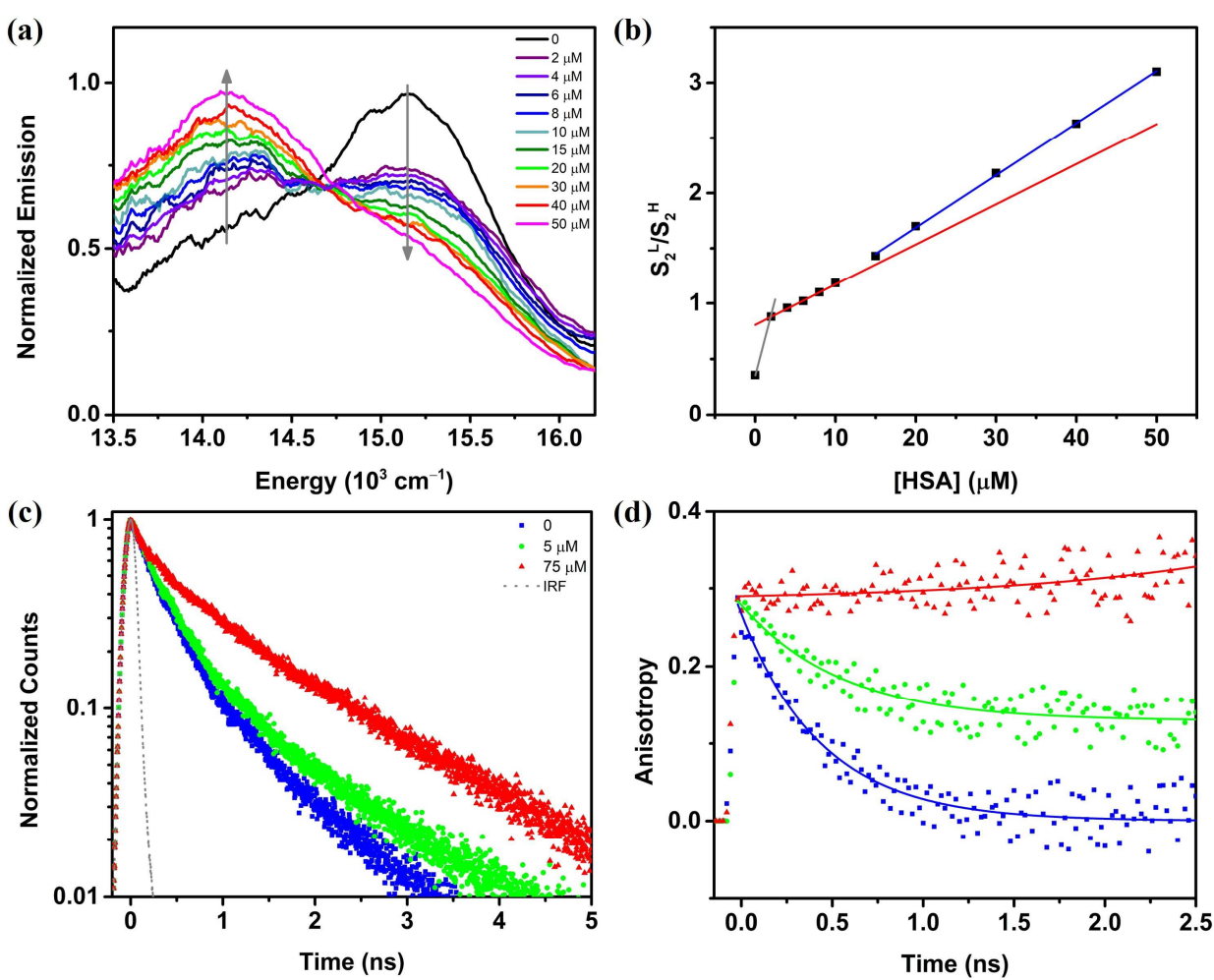


Figure 7.2. (a) Steady-state fluorescence of IR806 and IR806-HSA samples, with increasing HSA concentration, excited at 16667 cm⁻¹. The IR806 concentration was kept constant at 2 μ M. We normalized the data to keep the integrated emission under the two fluorescence bands constant. (b) The integrated fluorescence ratio of S_2^L/S_2^H , excited at 16667 cm⁻¹, as a function of the HSA concentration. Note the difference in slope for concentrations above 10 μ M, the concentration where dimerization becomes favorable. (c) The fluorescence decay of IR806 and IR806-HSA samples, with a constant IR806 concentration of 5 μ M, excited at 16500 cm⁻¹ and detected at 14500 cm⁻¹. (d) Rotational anisotropy decays associated with S_2 fluorescence for the samples in (c).

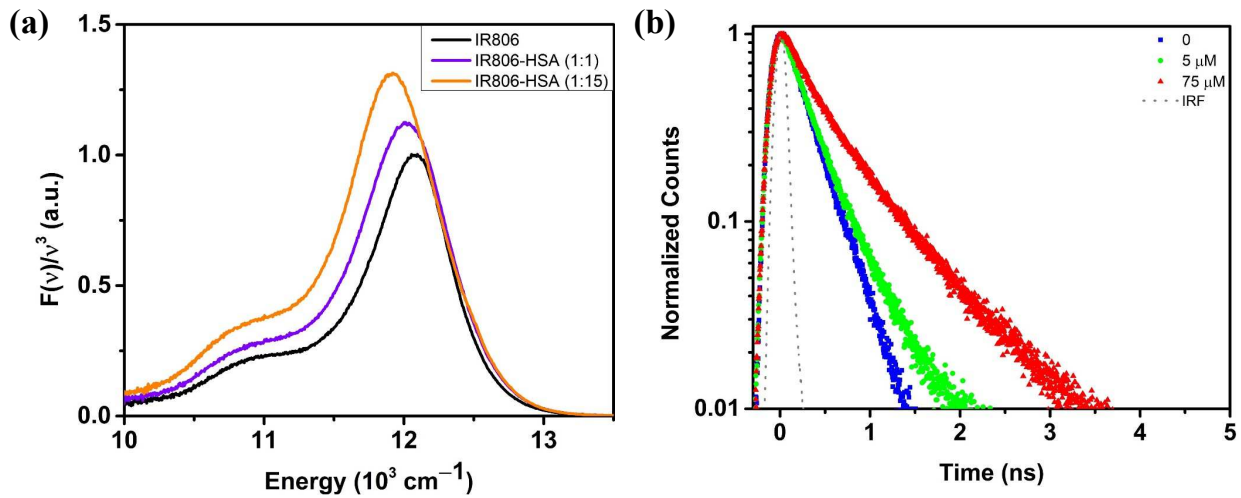


Figure 7.3. (a) Fluorescence following excitation at the absorption maximum for each solution. (b) The fluorescence decay of IR806 and IR806–HSA samples excited at 16500 cm^{-1} and detected at 12000 cm^{-1} . The concentration of IR806 was kept constant at $5 \mu M$.

The experimental rotational anisotropy decays R(t), which report on the ability of molecules to reorient in solution, are shown in Figure 7.2d for the same solutions in Figure 7.2c. The decays were fitted to single exponential functions to obtain the rotational anisotropy lifetime τ_{OR} . The solution containing IR806 showed a decay of 450 ± 49 ps, the solution with 5 μ M HSA showed a slower decay of 550 ± 62 ps. The solution containing 75 μ M HSA showed no discernible decay within the sub-nanosecond fluorescence lifetime. Given that reorientation time depends on molecular size, we conclude that IR806 binding to HSA slows its reorientation time, and when the concentration is high enough for the presence of dimers, it can no longer reorient during the fluorescence lifetime.

Molecular docking calculations of IR806 in HSA were carried out using AutoDockTools,²⁹⁴ which yielded the 10 most favorable conformations, the highest binding affinity being –9.2 kcal/mol. After analyzing the conformations, we infer that IR806 binds in the IIA subdomain of the protein primarily through hydrophobic interactions.^{274–277} Figure 7.4a shows IR806 non-covalently bound to the hydrophobic IIA pocket of HSA, with specifically the non-polar indoline groups on one end embedded into the pocket, while the charged sulfonate group extends out of the pocket. Another iteration of docking was carried out specifically in the IIA subdomain with the objective of obtaining the most likely conformation of IR806 in HSA. The IR806 geometry, upon binding with HSA, is shown in Figure 7.4b which exhibits an overall distortion in the polymethine chain, in comparison to the planar conformation in the unbound ground state conformation.^{274,275}

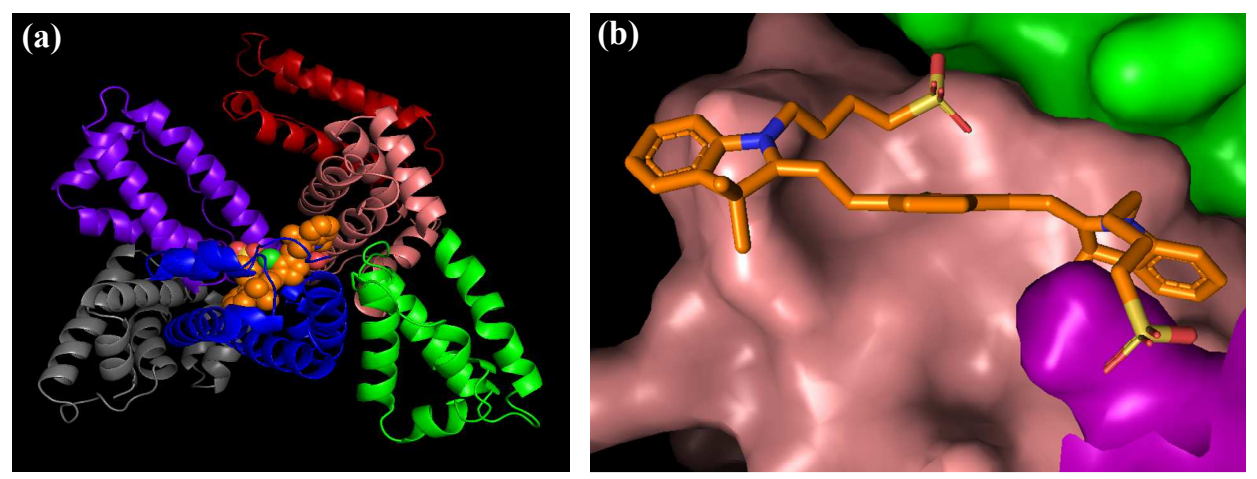


Figure 7.4. Molecular docking study of IR806. (a) IR806 (spheres) bound to HSA (ribbons). The different subdomains are depicted by different colors: IA - gray, IB - purple, IIA - blue, IIB - green, IIIA - salmon, and IIIB- red. The atoms of IR806 are shown by different colors as well: C - orange, Cl - green, O - red, S - yellow, and N - blue. (b) The geometry of IR806, when bound to HSA.

Electronic structure calculations using TD-DFT helped us understand the structural features of the ground and excited states of IR806. In spite of typically overestimating transition energies by almost an eV (8065 cm⁻¹) in TD-DFT calculations of cyanine dyes, the calculations are capable of accurately depicting the intricacies of the potential energy surface trajectories.^{251,252}

Several different ground state geometries were compared which revealed that the s-trans conformation is the most stable geometry. The ground state geometry (S_0 min) resembles a planar structure along the polymethine chain, the central cyclopentene ring, as well as the substituted aromatic indole groups on either side. The excited state optimizations were carried out to obtain the geometries responsible for the emission characteristics of IR806. Figure 7.5 highlights the results of our calculations with the different electronic states corresponding to the ground and excited state geometries, and the relevant transitions and the transition energies.

The vertical excitation (absorption) energy from the ground state to S_1 is 15647 cm⁻¹, which is 3146 cm⁻¹ higher than the experimental S_1 maximum of 12502 cm⁻¹. The optimized first excited state, which corresponds to the vibrationally cooled conformation in the S_1 electronic state, has been labelled S_1 min. The excited-state equilibrium geometry of S_1 min is very similar to the geometry at the FC point of the ground state. The emission energy from S_1 is calculated at 11937 cm⁻¹, which is in excellent agreement with the experimental value of 12018 cm⁻¹.

In line with the previous calculations of IR144 and IR140, there seems to be two distinct local minima on the S_2 PES that could be resolved through our calculations. The first minimum, S_2 min-1, boasts a geometry that is quite similar to the S_0 min and S_1 min geometries, specifically in terms of the planarity of their structures. The second minimum, S_2 min-2, on the contrary, displays a high degree of distortion. The polymethine chain of S_2 min-2 is twisted out of plane by 103° . The emission energies estimated from our calculations are 23712 and 20728 cm⁻¹ for S_2 min-1 and S_2 min-2 (experimental values are 15290 and 14130 cm⁻¹), respectively. Based on qualitative agreement with experiment, the minima S_2 min-1 and S_2 min-2 correspond to the emissive states, S_2 ^H and S_2 ^L, in line with Laboe et al.'s work.²⁵⁹

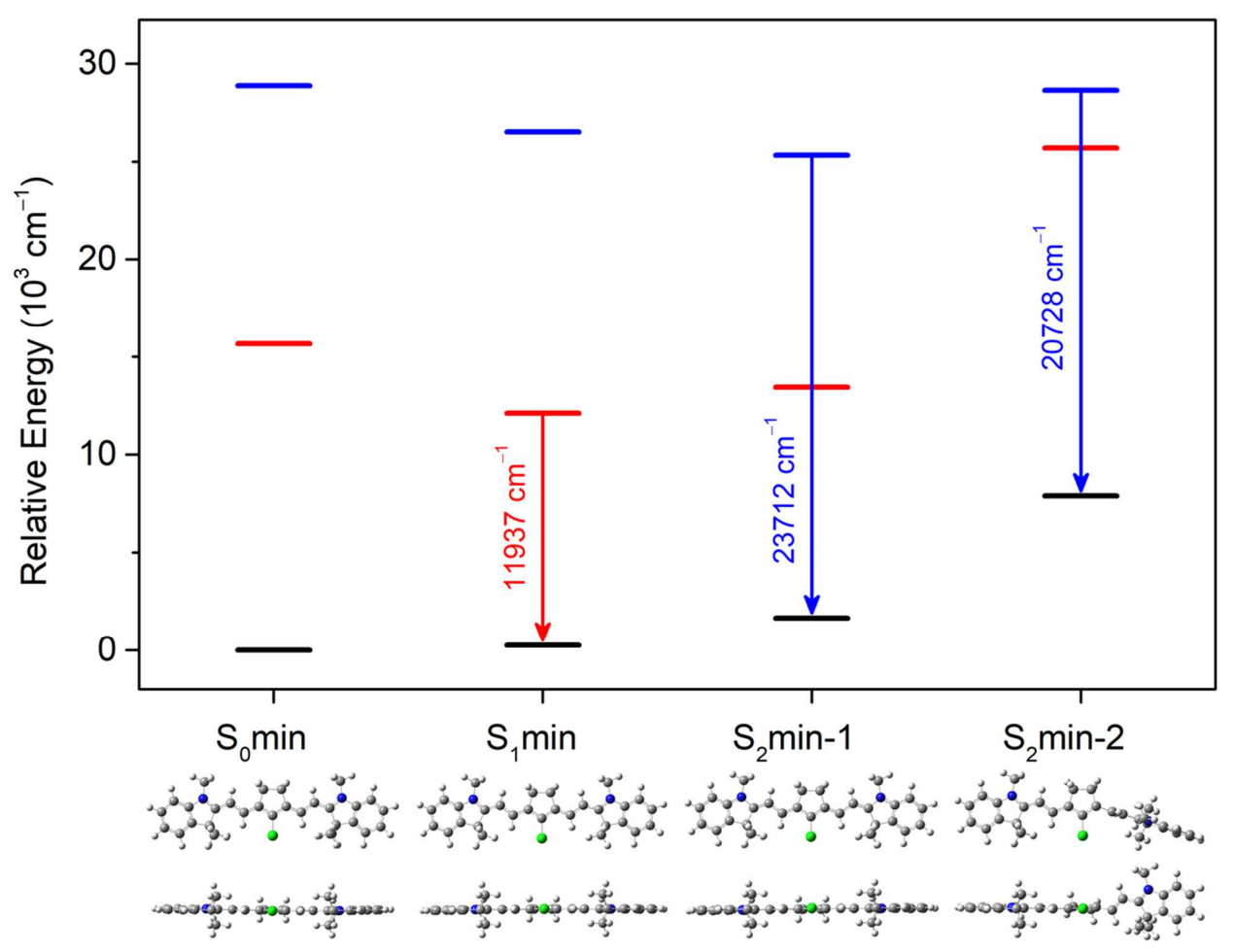


Figure 7.5. Results of the TD-DFT calculations showing energies for the different states corresponding to different geometries. The top row of molecular geometries depicts the molecules to be in the plane of paper while the bottom row is a visualization of the same system, with the Chlorine atom coming out of the plane of paper. The energies for S_0 , S_1 , and S_2 are shown in black, red, and blue, respectively.

Electronic structure calculations have helped us understand the structural features of the ground and excited states of IR806. While cis-trans isomers are known to contribute to the spectroscopy of cyanine dyes, ^{296,297} we did not consider the contribution of different cis-trans configurations for every carbon in the polymethine chain. Based on the energy difference for several different conformers (depicted in Figure 7.6), at room temperature, we expect the EEEE conformer to be 11 times more probable than the next lowest energy conformer EEEZ. Therefore, our calculations are limited to the all-trans (EEEE) isomer. We examined minimum energy configurations for multiple geometries starting from different twisting angles of the carbon atoms

closest to the center of the polymethine chain. We found that S_0 and S_1 always relaxed back to the planar geometry but found a configuration we call S_2^L that corresponds to a minimum with the polymethine chain twisted to 103-degrees. Emission from such a highly twisted geometry could populate the EEZE conformer and such a possibility has not been pursued here.

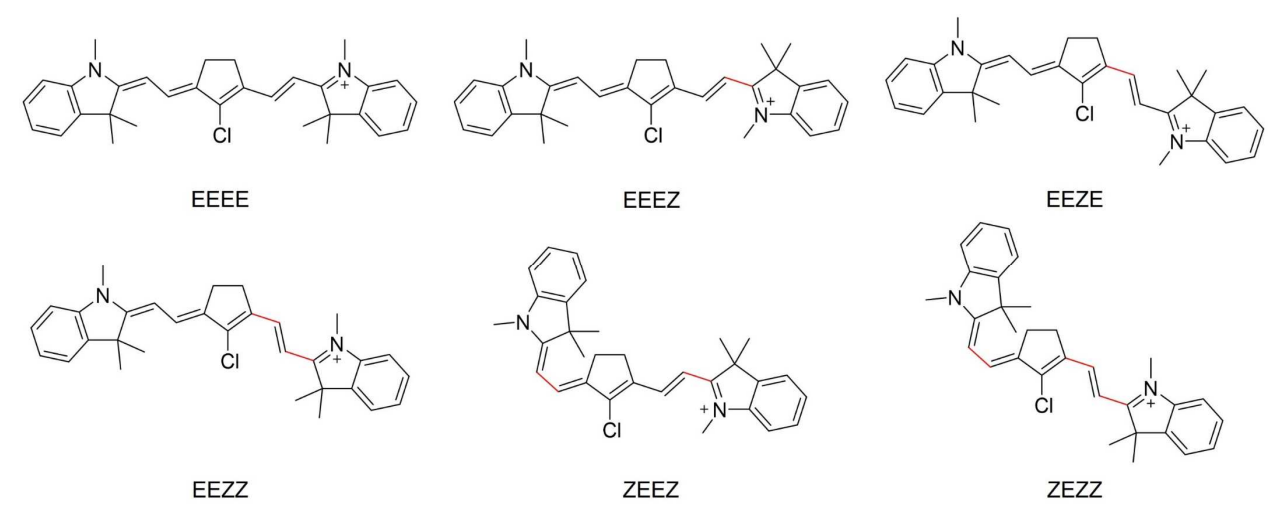


Figure 7.6. Principal IR806 isomers. The bonds in Z configuration are highlighted in red.

Non-covalent binding complex formation of HSA with IR806 manifests itself in the S₁ absorption spectrum with a red-shift in absorption (Figure 7.1).²⁷⁴ The fact that IR806 in solution shows negative solvatochromism, i.e., a red shift in the S₁ absorption spectrum with decreasing solvent polarity, is in line with a decrease in the dipole moment upon excitation to S₁.²³² This indicates that the binding of IR806 with HSA is primarily though non-polar interactions, similar to the binding behaviors of other cyanine dyes.^{274–276} The hydrophobic nature of the binding has also been captured in the docking studies of IR806 (Figure 7.4). Upon increasing the relative protein concentration, we see evidence of stronger protein-dye binding in the S₁ absorption spectrum of the 1:15 sample that is more red-shift in comparison to the 1:1 case (Figure 7.1a). The red-shift in absorption can thus be used as a gauge of protein-dye binding efficiency.

Free IR806 in solution shows two distinct absorptions from S_0 to S_2^H and S_2^L with absorption maxima at 16300 and 14900 cm⁻¹, respectively (Figure 7.7). In the presence of HSA in the 1:1 mixture, the S_2 absorption band becomes wider, more intense, and shifts to a lower frequency. We associate the relative loss of intensity in the high-frequency and increase in the lower-frequency band to a loss of planar structures in the ground state, resulting from binding to HSA. As the concentration of HSA increases, we see further shift to lower frequencies. This confirms that the bound IR806 adopts a twisted geometry in the ground state, in line with previous studies of cyanines binding with HSA.^{274,275}

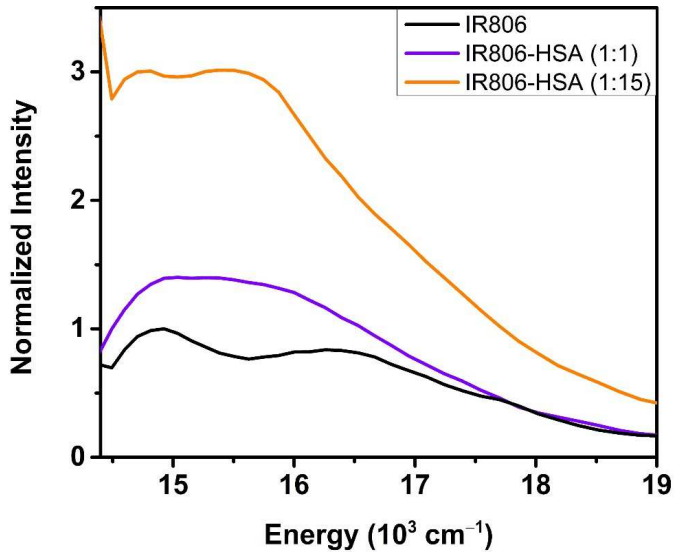


Figure 7.7. The excitation spectrum normalized for IR806 and IR806–HSA samples detecting fluorescence at 14190 cm $^{-1}$. The concentration of IR806 was kept constant at 5 μ M.

Free IR806 shows two conspicuous emissions from S_2^H and S_2^L . Upon binding to HSA, the S_2^L emission becomes favored, captured by the fluorescence spectra (Figure 7.2a) as well as the time-resolved fluorescence data (Figure 7.2c). Additionally, the emission from S_2^L shows significant enhancement upon increase in HSA concentration while S_2^H shows marked depletion, with an 8-fold increase in the S_2^L/S_2^H emission compared to free IR806 (Figure 7.2b). The fluorescence lifetime of the S_2 excited state shows a marked increase in the 75 μ M HSA sample

compared to the 5 μ M HSA sample, because of stronger IR806 binding. The distorted configuration that IR806 adopts when bound to HSA stabilizes the 103-degree twist in the polymethine chain that characterizes the S_2^L state. This conclusion is supported by similarities of the S_2^L geometry (corresponding to S_2 min-2 geometry) with the structure of the docked geometry of IR806 (Figure 7.4b). The enhanced emission signature can hence be used as an indication of binding.

We evaluated the spectroscopic changes in IR806 as a function of reversible HSA dimer formation. A study by Bhattacharya et al.²⁸⁹ suggests that HSA dimerization is more prevalent at concentrations above 10 µM. Chubarov et al. confirmed the reversible formation of HSA dimers, and gave the approximate equilibrium binding constant $K_D \sim 100 \, \mu M$. Based on those findings, we focused our study on HSA concentrations of 0 to 50 µM, while keeping a constant IR806 concentration. Based on the K_D value above, we expect dimer concentration to reach 10% when for solutions with 10 µM HSA. First, we verified that no aggregation takes place between dye molecules upon increasing the IR806 concentration from 1 µM to 5 µM. This was confirmed from the identical line shapes of the excitation spectra. Starting with S₂ state emission (Figure 7.2a), we find higher S_2^L and lower S_2^H emission, as the concentration of HSA increases. When the S_2^L/S_2^H emission ratio is plotted as a function of HSA concentration (Figure 7.2b), we observe a change in the slope occurring near 10 µM. We confirm the presence of dimers by the large increase in fluorescence lifetime and anisotropy decay observed for 75 µM HSA solutions (Figures 7.2c and d). We also looked at changes in the S₁ state spectroscopy, following excitation at its absorption maxima, for clues of dimer formation. We found that the fluorescence maxima red shifts as a function of increasing HSA concentration obtained at 2 and 5 µM IR806, respectively (Figures 7.8a and b). When the shift is plotted as a function of HSA concentration, we see a change in slope

near 10 μ M. Finally, when the raw S_1 emission intensity is plotted as a function of HSA concentration, we find a change in slope near 10 μ M (Figure 7.9). We attribute these spectroscopic changes to reversible HSA dimer formation consistent with the findings of Bhattacharya and Chubarov. We postulate that dimer formation leads to a more hydrophobic environment for IR806. Our findings indicate that spectroscopic changes in the S_1 and S_2 fluorescence of IR806 and perhaps other cyanines may be used as indicators for HSA oligomerization.

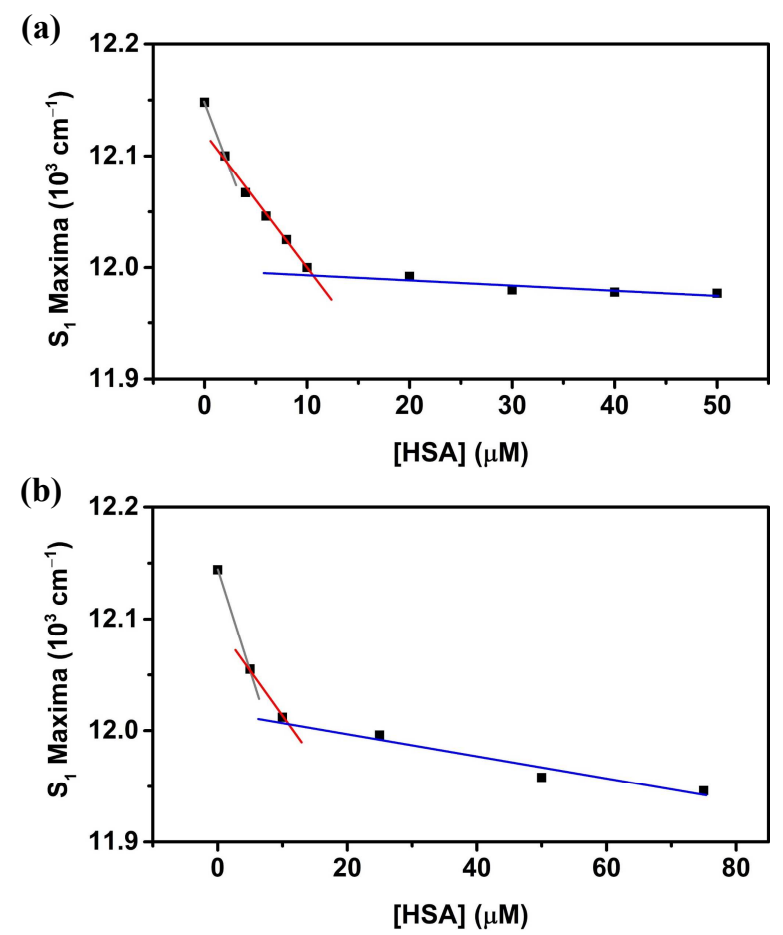
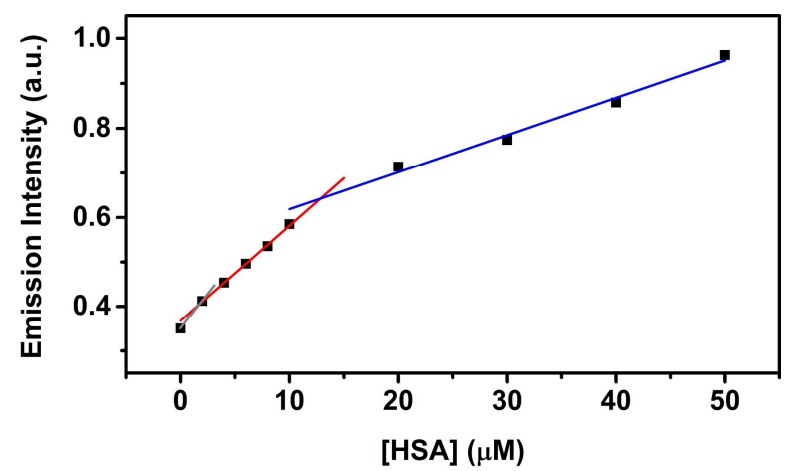


Figure 7.8. S_1 fluorescence maxima as a function of HSA concentration. IR806 concentration is kept constant at (a) 2 μ M and (b) 5 μ M.



[HSA] (μ M) Figure 7.9. S_1 integrated emission spectra at the emission maxima, as a function of HSA concentration. The data was obtained from raw spectra without normalization. IR806 concentration is kept constant at 2 μ M.

7.4 Conclusion

In this study we have explored changes in the spectroscopy of the cyanine IR806 as a function of HSA concentration in buffer solutions. Based on a spectroscopic shift in the S₁ absorption and emission, as well as changes in the S₂^L and S₂^H state emissions as a function of HSA concentration, we find that IR806 binds HSA. Protein docking calculations, together with an observed red shift of the S₁ absorption spectrum, lead us to conclude that binding takes place in the hydrophobic pocket (IIA subdomain) of HSA. From EEM spectra and electronic structure calculations, we identify the major emissive state of the IR806-HSA complex as one associated with a 103-degree twisted geometry labeled as S_2^L . As the concentration of HSA increases above 10 μM, we find a change in the rate of spectroscopic changes affecting absorption and emission to and from the S₁ and S₂ states that is consistent with the formation of reversible HSA dimers. The formation of dimers was further confirmed by reorientation anisotropy measurements at low and high HSA concentrations. Findings from our study have two important implications. First, the stabilization and hence longer lived high-energy S₂ state could enable the design of more effective phototherapy agents via formation of singlet oxygen or photo-release of therapy agents. Second, the dependence on HSA concentration indicates that cyanine S₂ spectroscopy may be used to quantify the oligomerization state of HSA. This is important given the fact that HSA dimerization has been utilized as a biomarker for numerous medical conditions related to oxidative stress.

Chapter 8 Summary and Future Outlook

The ability of the photobase FR0-SB to carry out ESPT from alcohols can be ascribed to the significantly higher dipole moment of the S_1 state, which allows the photobase molecule to abstract protons from *n*-alcohols C1 (methanol) through C8 (n-octanol). The rotational diffusion behavior of FR0-SB* and FR0-HSB⁺* are distinctly different and approximated by the modified DSE model in the slip and stick limits, respectively. The fluorescence lifetime of the excited states of both FR0-SB* and FR0-HSB⁺* correlate with the [-OH] and the dielectric constant of the solvent medium. The experimental data for a series of primary, secondary, and tertiary alcohols demonstrate that the efficiency of solvent proton abstraction by the electronically excited FR0-SB* species depends on the alcohol structure. Results indicate the formation of an intermediate [FR0-SB*···HOR] complex, which comprises of FR0-SB* interacting with a minimum of three alcohol molecules, a prerequisite for the ESPT reaction. The effective [FR0-SB*···HOR] complex formation is highly dependent on achieving spatial proximity and alignment of the alcohol's –OH group with the imine lone pair of FR0-SB*. To further understand the structural effects on the super photobasicity of FR0-SB, the FR0 precursor moiety has been investigated. The chargetransfer characteristic of the precursor FR0 has been studied by Capistran et al.²⁹⁸ Additionally. they have also examined the effect of cyclization of the amino group as well as the role of the aldehydic proton on the excited state dynamics of the precursor.²⁹⁹

TPE is advantageous as it allows control of chemical reactions with high spatial and temporal resolution. Upon examining the ESPT reactivity of **FR0**-SB following TPE, an enhancement of up to 62% was observed in comparison to isoenergetic OPE. Based on the excitation spectra, it can be concluded that the enhanced reactivity is caused by the differences in the solvent arrangement in the case of polar alcohols. Since TPE is highly dependent on the change

in dipole moment, with the change being highest for methanol, the enhancement in reactivity can be attributed to the stabilization of **FR0**-SB* from specific hydrogen bonding interactions with methanol molecules. TPE in non-centrosymmetric molecules such as **FR0**-SB can occur through virtual and dipole pathways. Spectrally shaped femtosecond laser pulses may be used to control the quantum interference between the virtual and dipole pathways, producing an enhancement of the TP excitation cross section by a factor of 1.75 in comparison to TL, when normalized to the SOPS intensity.

Fluorescence from S_2 may have applications in solar energy conversion and phototheranostics. The dynamics upon direct excitation to the S_2 state of IR144 and IR140 has been studied with the focus being obtaining higher S_2 emission. Femtosecond pulse chirp and solvent viscosity can be used to manipulate the rate of IC following S_2 excitation of IR144 and IR140. Using solvent viscosity and chirp, an overall control S_2/S_1 fluorescence ratio between 0.01-0.86 has been demonstrated. Additionally, experiments and quantum calculations reveal the presence of two S_2 configurations, S_2^H and S_2^L , with the main difference being the twist in the polymethine chain in S_2^L . Similar to IR144 and IR140, another heptamethine cyanine IR806 shows emissions from two different S_2 configurations, S_2^H and S_2^L , with similar geometric features. The spectroscopic changes of the S_2 states are utilized to detect the binding of IR806 with HSA. Results from experiments, protein docking, and quantum calculations have been used to validate the non-covalent dimer formation of HSA.

An outlook for future direction of research involving the photo reagents is presented in the subsections below.

8.1 Super Photobase for Precision Chemistry

The focus of the research has been to understand the photo physics of photobases in order to develop more active molecules for utilization in precision chemistry. The photobasicity of the cyclized amino group, that is the Schiff base of Ncy- $FR0^{299}$ (Ncy-FR0-SB), should be characterized to assess the effect of the restricted rotation of the electron-donating group on pK_a . Additionally, since the change in dipole moment is the primary reason for ESPT, a longer conjugation between the electron donor and the electron acceptor would lead to a higher change in dipole moment and subsequently a larger change in pK_a . A carbocyclized Schiff base, Ccy-FR0-SB, with a conjugation involving two additional methine groups between the amine and the imine groups, must be investigated. Initial tests on both Ncy-FR0-SB and Ccy-FR0-SB, recently synthesized by the Borhan group, have demonstrated a change in pK_a which is higher than that of FR0-SB.

The ESPT enhancement following TPE should be further explored to study and confirm the effect of solvation. The inhomogeneous broadening of the absorption of **FR0**-SB in alcoholic solvents provides an important aspect in the elucidation of the TP excited reactivity. This specific solvation effect in the excited state may be probed using ultrafast two-dimensional spectroscopy specifically by photon echo. 300–302 A comparison of the two-dimensional spectroscopy for OPE and TPE may be useful in revealing the enhancement in reactivity of the photobase **FR0**-SB.

The motivation for the development of more active photobase is to increase the efficiency of acid-base reactions in space and time. Progress towards practical photo reagents should be tested in the context of a chemical reaction in quantitative amounts to carry out time-controlled proton abstraction. A one-pot synthesis may be designed containing the photobase such that the photobase stays dormant but may be activated at a specific time, when necessary. A possible instance of this

application can be a base-mediated ether formation, similar to Williamson ether synthesis. Additionally, due to the reversible nature of fluorene-based super photobases, they can be utilized in a catalytic fashion for light-activated chemical reactions, similar to the applications of photoacids. The catalytic ESPT allows temporal control and modulation of the reaction kinetics by varying the intensity of the light. Further spatial control may be achieved using TPE in biological systems tagged with super photobase molecules to trigger localized proton abstraction. The abstraction of the systems tagged with super photobase molecules to trigger localized proton abstraction.

8.2 Excited Dynamics and Photochemistry of Cyanines

Cyanines are important molecules for solar energy conversion and biological imaging. The ability to stabilize the S₂ state opens up a range of applications in the already prevalent applications of solar cells and diagnostics. Stabilizing the S₂ excited state and increasing the excited state lifetime can allow for higher rate of photochemical reactions, leading to the successful release of the reactive agent (reactive oxygen species in cancer therapy) for cell death.³¹⁰ The ultrafast study of the S₂ dynamics of such cyanine molecules can reveal the underlying reaction mechanism and dynamics.

Photoconversion is a process that leads to the formation of new products that are emissive and is frequently encountered in fluorescence imaging.^{311–313} Photoconversion may also be used as a biomolecular tag, which includes green fluorescent proteins.^{314–316} Heptamethine cyanine dyes with absorption maxima in the near-IR region may undergo light-mediated conversion into pentamethine cyanines, which may further convert into trimethine cyanines, where both of them are emissive products. A detailed mechanistic study for the phototruncation process has been shown in the paper by Matikonda et al.³¹⁷ An ultrafast transient absorption study to understand the kinetics of the phototruncation process may be useful in depleting or enhancing the photoconversion process, depending on the application. Moreover, pulse shaping may be a useful tool in identifying the different modes that are favorable for either depleting or enhancing the photoconversion. This would involve the use of a near-IR beam to carry out TPE to the S₂ state of the cyanine dye and carrying out phase scans including chirp, sinusoidal, and pi-step.

APPENDIX

List of Publications

- (1) **Lahiri, J.**; Sandhu, S.; Levine, B. G.; Dantus, M. Human Serum Albumin Dimerization Enhances the S₂ Emission of Bound Cyanine IR806. *J. Phys. Chem. Lett.* **2022**, 1825–1832.
- (2) Laboe, M.;* Lahiri, J.;* Mohan T. M., N.; Liang, F.; Levine, B. G.; Beck, W. F.; Dantus, M. Linear and Nonlinear Optical Processes Controlling S₂ and S₁ Dual Fluorescence in Cyanine Dyes. J. Phys. Chem. A 2021, 125, 9770–9784. *equal contribution
- (3) **Lahiri, J.**; Yuwono, S. H.; Magoulas, I.; Moemeni, M.; Borhan, B.; Blanchard, G. J.; Piecuch, P.; Dantus, M. Controlling Quantum Interference between Virtual and Dipole Two-Photon Optical Excitation Pathways Using Phase-Shaped Laser Pulses. *J. Phys. Chem. A* **2021**, *125*, 7534–7544.
- (4) Lahiri, J.; Moemeni, M.; Kline, J.; Magoulas, I.; Yuwono, S. H.; Laboe, M.; Shen, J.; Borhan, B.; Piecuch, P.; Jackson, J. E.; Blanchard, G. J.; Dantus, M. Isoenergetic Two-Photon Excitation Enhances Solvent-to-Solute Excited-State Proton Transfer. *J. Chem. Phys.* 2020, 153, 224301.
- (5) Lahiri, J.; Moemeni, M.; Magoulas, I.; Yuwono, S. H.; Kline, J.; Borhan, B.; Piecuch, P.; Jackson, J. E.; Blanchard, G. J.; Dantus, M. Steric Effects in Light-Induced Solvent Proton Abstraction. *Phys. Chem. Chem. Phys.* **2020**, *22*, 19613–19622.
- (6) Lahiri, J.; Kline, J.; Dantus, M. Ultrafast Pulse Metrology for Industrial Applications. In *Frontiers in Ultrafast Optics: Biomedical, Scientific, and Industrial Applications XX*; Herman, P. R., Meunier, M., Osellame, R., Eds.; SPIE, **2020**; *11270*, 20.
- (7) **Lahiri, J.**; Moemeni, M.; Kline, J.; Borhan, B.; Magoulas, I.; Yuwono, S. H.; Piecuch, P.; Jackson, J. E.; Dantus, M.; Blanchard, G. J. Proton Abstraction Mediates Interactions between the Super Photobase FR0-SB and Surrounding Alcohol Solvent. *J. Phys. Chem. B* **2019**, *123*, 8448–8456.

BIBLIOGRAPHY

BIBLIOGRAPHY

- (1) Nairat, M.; Konar, A.; Lozovoy, V. V; Beck, W. F.; Blanchard, G. J.; Dantus, M. Controlling S₂ Population in Cyanine Dyes Using Shaped Femtosecond Pulses. *J. Phys. Chem. A* **2016**, *120*, 1876–1885.
- (2) Lahiri, J.; Moemeni, M.; Kline, J.; Magoulas, I.; Yuwono, S. H.; Laboe, M.; Shen, J.; Borhan, B.; Piecuch, P.; Jackson, J. E.; Blanchard, G. J.; Dantus, M. Isoenergetic Two-Photon Excitation Enhances Solvent-to-Solute Excited-State Proton Transfer. *J. Chem. Phys.* **2020**, *153*, 224301.
- (3) Konar, A.; Lozovoy, V. V; Dantus, M. Solvent Environment Revealed by Positively Chirped Pulses. *J. Phys. Chem. Lett.* **2014**, *5*, 924–928.
- (4) Weber, K. Über Die Enge Beziehung Der Fluorescenzauslöschung Zur Hemmung Photochemischer Reaktionen. *Zeitschrift für Phys. Chemie* **1932**, *15B*, 18–44.
- (5) Förster, T. Fluoreszenzspektrum Und Wasserstoffionen-Konzentration. *Naturwissenschaften* **1949**, *36*, 186–187.
- (6) Förster, T. Elektrolytische Dissoziation Angeregter Moleküle. *Zeitschrift für Elektrochemie und Angew. Phys. Chemie* **1950**, *54*, 42–46.
- (7) Förster, T. Die PH-Abhängigkeit Der Fluoreszenz von Naphthalinderivaten. Zeitschrift für Elektrochemie und Angew. Phys. Chemie 1950, 54, 531–535.
- (8) Weller, A. Fast Reactions of Excited Molecules. *Prog. React. Kinet.* **1961**, *1*, 187.
- (9) Solntsev, K. M.; Huppert, D.; Agmon, N. Photochemistry of "Super"-Photoacids. Solvent Effects. *J. Phys. Chem. A* **1999**, *103*, 6984–6997.
- (10) Solntsev, K. M.; Huppert, D.; Agmon, N.; Tolbert, L. M. Photochemistry of "Super" Photoacids. 2. Excited-State Proton Transfer in Methanol/Water Mixtures. *J. Phys. Chem. A* **2000**, *104*, 4658–4669.
- (11) Sheng, W.; Nairat, M.; Pawlaczyk, P. D.; Mroczka, E.; Farris, B.; Pines, E.; Geiger, J. H.; Borhan, B.; Dantus, M. Ultrafast Dynamics of a "Super" Photobase. *Angew. Chemie Int. Ed.* **2018**, *57*, 14742–14746.
- (12) Nachliel, E.; Ophir, Z.; Gutman, M. Kinetic Analysis of Fast Alkalinization Transient by Photoexcited Heterocyclic Compounds: POH Jump. *J. Am. Chem. Soc.* **1987**, *109*, 1342–1345.
- (13) Pines, E.; Huppert, D.; Gutman, M.; Nachliel, N.; Fishman, M. The POH Jump: Determination of Deprotonation Rates of Water by 6-Methoxyquinoline and Acridine. *J.*

- Phys. Chem. 1986, 90, 6366–6370.
- (14) Driscoll, E. W.; Hunt, J. R.; Dawlaty, J. M. Photobasicity in Quinolines: Origin and Tunability via the Substituents' Hammett Parameters. *J. Phys. Chem. Lett.* **2016**, *7*, 2093–2099.
- (15) Driscoll, E. W.; Hunt, J. R.; Dawlaty, J. M. Proton Capture Dynamics in Quinoline Photobases: Substituent Effect and Involvement of Triplet States. *J. Phys. Chem. A* **2017**, 121, 7099–7107.
- (16) Kucherak, O. A.; Didier, P.; Mély, Y.; Klymchenko, A. S. Fluorene Analogues of Prodan with Superior Fluorescence Brightness and Solvatochromism. *J. Phys. Chem. Lett.* **2010**, *I*, 616–620.
- (17) Pines, E.; Huppert, D. PH Jump: A Relaxational Approach. *J. Phys. Chem.* **1983**, *87*, 4471–4478.
- (18) Abbruzzetti, S.; Crema, E.; Masino, L.; Vecli, A.; Viappiani, C.; Small, J. R.; Libertini, L. J.; Small, E. W. Fast Events in Protein Folding: Structural Volume Changes Accompanying the Early Events in the N→I Transition of Apomyoglobin Induced by Ultrafast PH Jump. *Biophys. J.* **2000**, 78, 405–415.
- (19) Piatkevich, K. D.; Malashkevich, V. N.; Almo, S. C.; Verkhusha, V. V. Engineering ESPT Pathways Based on Structural Analysis of LSSmKate Red Fluorescent Proteins with Large Stokes Shift. *J. Am. Chem. Soc.* **2010**, *132*, 10762–10770.
- (20) Kwon, J. E.; Park, S. Y. Advanced Organic Optoelectronic Materials: Harnessing Excited-State Intramolecular Proton Transfer (ESIPT) Process. *Adv. Mater.* **2011**, *23*, 3615–3642.
- (21) Shen, J.-Y.; Chao, W.-C.; Liu, C.; Pan, H.-A.; Yang, H.-C.; Chen, C.-L.; Lan, Y.-K.; Lin, L.-J.; Wang, J.-S.; Lu, J.-F.; Chun-Wei Chou, S.; Tang, K.-C.; Chou, P.-T. Probing Water Micro-Solvation in Proteins by Water Catalysed Proton-Transfer Tautomerism. *Nat. Commun.* **2013**, *4*, 2611.
- (22) Piatkevich, K. D.; English, B. P.; Malashkevich, V. N.; Xiao, H.; Almo, S. C.; Singer, R. H.; Verkhusha, V. V. Photoswitchable Red Fluorescent Protein with a Large Stokes Shift. *Chem. Biol.* **2014**, *21*, 1402–1414.
- (23) White, W.; Sanborn, C. D.; Fabian, D. M.; Ardo, S. Conversion of Visible Light into Ionic Power Using Photoacid-Dye-Sensitized Bipolar Ion-Exchange Membranes. *Joule* **2018**, *2*, 94–109.
- (24) Göppert-Mayer, M. Über Elementarakte Mit Zwei Quantensprüngen. *Ann. Phys.* **1931**, *401*, 273–294.
- (25) Kaiser, W.; Garrett, C. G. B. Two-Photon Excitation in CaF₂:Eu²⁺. Phys. Rev. Lett. 1961,

- 7, 229–231.
- (26) Schawlow, A. L.; Townes, C. H. Infrared and Optical Masers. *Phys. Rev.* **1958**, *112*, 1940–1949.
- (27) Maiman, T. H. Stimulated Optical Radiation in Ruby. *Nature* **1960**, *187*, 493–494.
- (28) Denk, W.; Strickler, J. H.; Webb, W. W. Two-Photon Laser Scanning Fluorescence Microscopy. *Science* (80-.). **1990**, 248, 73–76.
- (29) Xu, C.; Zipfel, W.; Shear, J. B.; Williams, R. M.; Webb, W. W. Multiphoton Fluorescence Excitation: New Spectral Windows for Biological Nonlinear Microscopy. *Proc. Natl. Acad. Sci. U. S. A.* **1996**, *93*, 10763–10768.
- (30) Albota, M. A.; Xu, C.; Webb, W. W. Two-Photon Fluorescence Excitation Cross Sections of Biomolecular Probes from 690 to 960 Nm. *Appl. Opt.* **1998**, *37*, 7352.
- (31) Zipfel, W. R.; Williams, R. M.; Webb, W. W. Nonlinear Magic: Multiphoton Microscopy in the Biosciences. *Nat. Biotechnol.* **2003**, *21*, 1369–1377.
- (32) So, P. T. C.; Dong, C. Y.; Masters, B. R.; Berland, K. M. Two-Photon Excitation Fluorescence Microscopy. *Annu. Rev. Biomed. Eng.* **2000**, *2*, 399–429.
- (33) Clement, M.; Daniel, G.; Trelles, M. Optimising the Design of a Broad □ band Light Source for the Treatment of Skin. *J. Cosmet. Laser Ther.* **2005**, *7*, 177–189.
- (34) Skliutas, E.; Lebedevaite, M.; Kabouraki, E.; Baldacchini, T.; Ostrauskaite, J.; Vamvakaki, M.; Farsari, M.; Juodkazis, S.; Malinauskas, M. Polymerization Mechanisms Initiated by Spatio-Temporally Confined Light. *Nanophotonics* **2021**, *10*, 1211–1242.
- (35) Parthenopoulos, D. A.; Rentzepis, P. M. Three-Dimensional Optical Storage Memory. *Science (80-.).* **1989**, *245*, 843–845.
- (36) Kawata, S.; Kawata, Y. Three-Dimensional Optical Data Storage Using Photochromic Materials. *Chem. Rev.* **2000**, *100*, 1777–1788.
- (37) Dvornikov, A. S.; Walker, E. P.; Rentzepis, P. M. Two-Photon Three-Dimensional Optical Storage Memory. *J. Phys. Chem. A* **2009**, *113*, 13633–13644.
- (38) Albota, M.; Beljonne, D.; Brédas, J. L.; Ehrlich, J. E.; Fu, J. Y.; Heikal, A. A.; Hess, S. E.; Kogej, T.; Levin, M. D.; Marder, S. R.; McCord-Maughon, D.; Perry, J. W.; Röckel, H.; Rumi, M.; Subramaniam, G.; Webb, W. W.; Wu, X. L.; Xu, C. Design of Organic Molecules with Large Two-Photon Absorption Cross Sections. *Science* (80-.). 1998, 281, 1653–1656.
- (39) Pawlicki, M.; Collins, H. A.; Denning, R. G.; Anderson, H. L. Two-Photon Absorption and the Design of Two-Photon Dyes. *Angew. Chemie Int. Ed.* **2009**, *48*, 3244–3266.

- (40) Walowicz, K. A.; Pastirk, I.; Lozovoy, V. V.; Dantus, M. Multiphoton Intrapulse Interference. 1. Control of Multiphoton Processes in Condensed Phases. *J. Phys. Chem. A* **2002**, *106*, 9369–9373.
- (41) Lozovoy, V. V.; Pastirk, I.; Walowicz, K. A.; Dantus, M. Multiphoton Intrapulse Interference. II. Control of Two- and Three-Photon Laser Induced Fluorescence with Shaped Pulses. *J. Chem. Phys.* **2003**, *118*, 3187–3196.
- (42) M. Dela Cruz, J.; Pastirk, I.; V. Lozovoy, V.; A. Walowicz, K.; Dantus, M. Multiphoton Intrapulse Interference 3: Probing Microscopic Chemical Environments. J. Phys. Chem. A 2003, 108, 53–58.
- (43) Harris, D. A.; Shane, J. C.; Lozovoy, V. V.; Dantus, M. Automated Phase Characterization and Adaptive Pulse Compression Using Multiphoton Intrapulse Interference Phase Scan in Air. *Opt. Express* **2007**, *15*, 1932–1938.
- (44) Kasha, M. Characterization of Electronic Transitions in Complex Molecules. *Discuss. Faraday Soc.* **1950**, *9*, 14.
- (45) Turro, N. J.; Ramamurthy, V.; Cherry, W.; Farneth, W. The Effect of Wavelength on Organic Photoreactions in Solution. Reactions from Upper Excited States. *Chem. Rev.* **1978**, 78, 125–145.
- (46) Beer, M.; Longuet ☐ Higgins, H. C. Anomalous Light Emission of Azulene. *J. Chem. Phys.* **1955**, *23*, 1390–1391.
- (47) Viswanath, G.; Kasha, M. Confirmation of the Anomalous Fluorescence of Azulene. *J. Chem. Phys.* **1956**, *24*, 574–577.
- (48) Birks, J. B. The Photophysics of Azulene. Chem. Phys. Lett. 1972, 17, 370–372.
- (49) Murata, S.; Iwanaga, C.; Toda, T.; Kokubun, H. Fluorescence and Radiationless Transitions from the Second Excited States of Azulene Derivatives. *Berichte der Bunsengesellschaft für Phys. Chemie* **1972**, *76*, 1176–1183.
- (50) Müller, A.; Pflüger, E. Laser-Flashspectroscopy of Cryptocyanine. *Chem. Phys. Lett.* **1968**, 2, 155–159.
- (51) Tashiro, H.; Yajima, T. Direct Measurement of Blue Fluorescence Lifetimes in Polymethine Dyes Using a Picosecond Laser. *Chem. Phys. Lett.* **1976**, *42*, 553–557.
- (52) Kobayashi, T.; Nagakura, S. The Rates of Internal Conversion and Photoisomerization of Some Carbocyanine Dyes as Revealed from Picosecond Time-Resolved Spectroscopy. *Chem. Phys.* **1977**, *23*, 153–158.
- (53) Kasatani, K.; Sato, H. Viscosity-Dependent Decay Dynamics of the S2 State of Cyanine

- Dyes with 3, 5, and 7 Methine Units by Picosecond Fluorescence Lifetime Measurements. *Bull. Chem. Soc. Jpn.* **1996**, *69*, 3455–3460.
- (54) Oulianov, D. A.; Dvornikov, A. S.; Rentzepis, P. M. Optical Limiting and Picosecond Relaxation of Carbocyanines Upper Electronic States. *Opt. Commun.* **2002**, *205*, 427–436.
- (55) Rodríguez-Córdoba, W.; Noria, R.; Guarín, C. A.; Peon, J. Ultrafast Photosensitization of Phthalocyanines through Their Axial Ligands. *J. Am. Chem. Soc.* **2011**, *133*, 4698–4701.
- (56) Guarin, C. A.; Villabona-Monsalve, J. P.; López-Arteaga, R.; Peon, J. Dynamics of the Higher Lying Excited States of Cyanine Dyes. An Ultrafast Fluorescence Study. *J. Phys. Chem. B* **2013**, *117*, 7352–7362.
- (57) Snyder, S. H.; Axelrod, J.; Zweig, M. A Sensitive and Specific Fluorescence Assay for Tissue Serotonin. *Biochem. Pharmacol.* **1965**, *14*, 831–835.
- (58) Udenfriend, S. Fluorescence Assay in Biology and Medicine. In *Molecular Biology*; Elsevier, 1969.
- (59) Bradford, M. M. A Rapid and Sensitive Method for the Quantitation of Microgram Quantities of Protein Utilizing the Principle of Protein-Dye Binding. *Anal. Biochem.* **1976**, 72, 248–254.
- (60) Gerdes, H.-H.; Kaether, C. Green Fluorescent Protein: Applications in Cell Biology. *FEBS Lett.* **1996**, *389*, 44–47.
- (61) Kimura, S.; Noda, T.; Yoshimori, T. Dissection of the Autophagosome Maturation Process by a Novel Reporter Protein, Tandem Fluorescent-Tagged LC3. *Autophagy* **2007**, *3*, 452–460.
- (62) Bugaj, A.; Sieroń; Kawczyk-Krupka; Dariusz Straszak; Sebastian Kwiatek; Wojciech Latos; Sieron-Stoltny, K. The Role of Fluorescence Diagnosis in Clinical Practice. *Onco. Targets. Ther.* **2013**, *6*, 977.
- (63) Malval, J.-P.; Diemer, V.; Savary, F. M.; Jacques, P.; Allonas, X.; Chaumeil, H.; Defoin, A.; Carré, C. Excited State Proton Transfer in a 'Super' Photoacid Based on a Phenol-Pyridinium Biaryl Chromophore. *Chem. Phys. Lett.* 2008, 455, 238–241.
- (64) Finkler, B.; Spies, C.; Vester, M.; Walte, F.; Omlor, K.; Riemann, I.; Zimmer, M.; Stracke, F.; Gerhards, M.; Jung, G. Highly Photostable "Super"-Photoacids for Ultrasensitive Fluorescence Spectroscopy. *Photochem. Photobiol. Sci.* **2014**, *13*, 548–562.
- (65) Hunt, J. R.; Dawlaty, J. M. Photodriven Deprotonation of Alcohols by a Quinoline Photobase. *J. Phys. Chem. A* **2018**, *122*, 7931–7940.
- (66) Pillman, H. A.; Blanchard, G. J. Effects of Energy Dissipation on Motional Dynamics in

- Unilamellar Vesicles. J. Phys. Chem. B **2010**, 114, 13703–13709.
- (67) Kohn, W.; Sham, L. J. Self-Consistent Equations Including Exchange and Correlation Effects. *Phys. Rev.* **1965**, *140*, A1133–A1138.
- (68) Hohenberg, P.; Kohn, W. Inhomogeneous Electron Gas. *Phys. Rev.* **1964**, *136*, B864–B871.
- (69) Čížek, J. On the Correlation Problem in Atomic and Molecular Systems. Calculation of Wavefunction Components in Ursell □ Type Expansion Using Quantum □ Field Theoretical Methods. *J. Chem. Phys.* **1966**, *45*, 4256–4266.
- (70) Stanton, J. F.; Bartlett, R. J. The Equation of Motion Coupled □ cluster Method. A Systematic Biorthogonal Approach to Molecular Excitation Energies, Transition Probabilities, and Excited State Properties. *J. Chem. Phys.* **1993**, *98*, 7029–7039.
- (71) Hehre, W. J.; Ditchfield, R.; Pople, J. A. Self-Consistent Molecular Orbital Methods. XII. Further Extensions of Gaussian-Type Basis Sets for Use in Molecular Orbital Studies of Organic Molecules. *J. Chem. Phys.* **1972**, *56*, 2257–2261.
- (72) Hariharan, P. C.; Pople, J. A. The Influence of Polarization Functions on Molecular Orbital Hydrogenation Energies. *Theor. Chim. Acta* **1973**, *28*, 213–222.
- (73) Clark, T.; Chandrasekhar, J.; Spitznagel, G. W.; Schleyer, P. V. R. Efficient Diffuse Function-Augmented Basis Sets for Anion Calculations. III. The 3-21+G Basis Set for First-Row Elements, Li-F. *J. Comput. Chem.* **1983**, *4*, 294–301.
- (74) Fradelos, G.; Lutz, J. J.; Wesołowski, T. A.; Piecuch, P.; Włoch, M. Embedding vs Supermolecular Strategies in Evaluating the Hydrogen-Bonding-Induced Shifts of Excitation Energies. *J. Chem. Theory Comput.* **2011**, *7*, 1647–1666.
- (75) Włoch, M.; Lodriguito, M. D.; Piecuch, P.; Gour, J. R. Two New Classes of Non-Iterative Coupled-Cluster Methods Derived from the Method of Moments of Coupled-Cluster Equations. *Mol. Phys.* **2006**, *104*, 2149–2172.
- (76) Erratum. Mol. Phys. **2006**, 104, 1.
- (77) Piecuch, P.; Gour, J. R.; Włoch, M. Left-Eigenstate Completely Renormalized Equation-of-Motion Coupled-Cluster Methods: Review of Key Concepts, Extension to Excited States of Open-Shell Systems, and Comparison with Electron-Attached and Ionized Approaches. *Int. J. Quantum Chem.* 2009, 109, 3268–3304.
- (78) Piecuch, P.; Włoch, M. Renormalized Coupled-Cluster Methods Exploiting Left Eigenstates of the Similarity-Transformed Hamiltonian. *J. Chem. Phys.* **2005**, *123*, 224105.
- (79) Piecuch, P.; Włoch, M.; Gour, J. R.; Kinal, A. Single-Reference, Size-Extensive, Non-Iterative Coupled-Cluster Approaches to Bond Breaking and Biradicals. *Chem. Phys. Lett.*

- **2006**, *418*, 467–474.
- (80) Purvis, III, G. D.; Bartlett, R. J. A Full Coupled □ Cluster Singles and Doubles Model: The Inclusion of Disconnected Triples. *J. Chem. Phys.* **1982**, *76*, 1910–1918.
- (81) Piecuch, P.; Hansen, J. A.; Ajala, A. O. Benchmarking the Completely Renormalised Equation-of-Motion Coupled-Cluster Approaches for Vertical Excitation Energies. *Mol. Phys.* **2015**, *113*, 3085–3127.
- (82) Włoch, M.; Gour, J. R.; Kowalski, K.; Piecuch, P. Extension of Renormalized Coupled-Cluster Methods Including Triple Excitations to Excited Electronic States of Open-Shell Molecules. *J. Chem. Phys.* **2005**, *122*, 214107.
- (83) Yanai, T.; Tew, D. P.; Handy, N. C. A New Hybrid Exchange–Correlation Functional Using the Coulomb-Attenuating Method (CAM-B3LYP). *Chem. Phys. Lett.* **2004**, *393*, 51–57.
- (84) Casida, M. E. Time-Dependent Density Functional Response Theory for Molecules. In *Recent Advances in Density Functional Methods, Part 1*; Chong, D. P., Ed.; World Scientific, Singapore, 1995; pp 155–192.
- (85) Gordon, M. S.; Schmidt, M. W. Advances in Electronic Structure Theory. In *Theory and Applications of Computational Chemistry*; Dykstra, C. E., Frenking, G., Kim, K. S., Scuseria, G. E., Eds.; Elsevier, 2005; pp 1167–1189.
- (86) Piecuch, P.; Kucharski, S. A.; Kowalski, K.; Musiał, M. Efficient Computer Implementation of the Renormalized Coupled-Cluster Methods: The R-CCSD[T], R-CCSD(T), CR-CCSD[T], and CR-CCSD(T) Approaches. *Comput. Phys. Commun.* **2002**, *149*, 71–96.
- (87) Kowalski, K.; Piecuch, P. New Coupled-Cluster Methods with Singles, Doubles, and Noniterative Triples for High Accuracy Calculations of Excited Electronic States. *J. Chem. Phys.* **2004**, *120*, 1715–1738.
- (88) Humphrey, W.; Dalke, A.; Schulten, K. VMD: Visual Molecular Dynamics. *J. Mol. Graph.* **1996**, *14*, 33–38.
- (89) Chuang, T. J.; Eisenthal, K. B. Theory of Fluorescence Depolarization by Anisotropic Rotational Diffusion. *J. Chem. Phys.* **1972**, *57*, 5094–5097.
- (90) Debye, P. Polar Molecules. In *Polar Molecules*; New York, The Chemical Catalog Company, Inc., 1929; p 84.
- (91) Hu, C.; Zwanzig, R. Rotational Friction Coefficients for Spheroids with the Slipping Boundary Condition. *J. Chem. Phys.* **1974**, *60*, 4354–4357.
- (92) Perrin, F. Mouvement Brownien d'un Ellipsoide I. Dispersion Diélectrique Pour Des Molécules Ellipsoidales. *J. Phys. le Radium* **1934**, *5*, 497–511.

- (93) Edward, J. T. Molecular Volumes and the Stokes-Einstein Equation. *J. Chem. Educ.* **1970**, 47, 261.
- (94) Blanchard, G. J. A Study of the State-Dependent Reorientation Dynamics of Oxazine 725 in Primary Normal Aliphatic Alcohols. *J. Phys. Chem.* **1988**, *92*, 6303–6307.
- (95) Blanchard, G. J. Detection of a Transient Solvent-Solute Complex Using Time-Resolved Pump-Probe Spectroscopy. *Anal. Chem.* **1989**, *61*, 2394–2398.
- (96) Blanchard, G. J. Counterion-Dependent Reorientation Dynamics of an Oxazine in Polar Protic and Aprotic Solvents. *J. Phys. Chem.* **1991**, *95*, 5293–5299.
- (97) Yatsuhashi, T.; Inoue, H. Molecular Mechanism of Radiationless Deactivation of Aminoanthraquinones through Intermolecular Hydrogen-Bonding Interaction with Alcohols and Hydroperoxides. *J. Phys. Chem. A* **1997**, *101*, 8166–8173.
- (98) Ekimova, M.; Hoffmann, F.; Bekçioğlu-Neff, G.; Rafferty, A.; Kornilov, O.; Nibbering, E. T. J.; Sebastiani, D. Ultrafast Proton Transport between a Hydroxy Acid and a Nitrogen Base along Solvent Bridges Governed by the Hydroxide/Methoxide Transfer Mechanism. *J. Am. Chem. Soc.* 2019, 141, 14581–14592.
- (99) Hunt, J. R.; Dawlaty, J. M. Kinetic Evidence for the Necessity of Two Proton Donor Molecules for Successful Excited State Proton Transfer by a Photobase. *J. Phys. Chem. A* **2019**, *123*, 10372–10380.
- (100) Hunt, J. R.; Tseng, C.; Dawlaty, J. M. Donor-Acceptor Preassociation, Excited State Solvation Threshold, and Optical Energy Cost as Challenges in Chemical Applications of Photobases. *Faraday Discuss.* **2019**, *216*, 252–268.
- (101) Lahiri, J.; Moemeni, M.; Kline, J.; Borhan, B.; Magoulas, I.; Yuwono, S. H.; Piecuch, P.; Jackson, J. E.; Dantus, M.; Blanchard, G. J. Proton Abstraction Mediates Interactions between the Super Photobase FR0-SB and Surrounding Alcohol Solvent. *J. Phys. Chem. B* **2019**, *123*, 8448–8456.
- (102) Moog, R. S.; Maroncelli, M. 7-Azaindole in Alcohols: Solvation Dynamics and Proton Transfer. *J. Phys. Chem.* **1991**, *95*, 10359–10369.
- (103) Nakagawa, T.; Kohtani, S.; Itoh, M. Picosecond Fluorescence and Two-Step LIF Studies of the Excited-State Proton Transfer in Methanol Solutions of 7-Hydroxyquinoline and Methyl-Substituted 7-Hydroxyquinolines. *J. Am. Chem. Soc.* **1995**, *117*, 7952–7957.
- (104) Cui, Y.; Zhao, H.; Zhao, J.; Li, P.; Song, P.; Xia, L. The Excited-State Multiple Proton Transfer Mechanism of the 7-Hydroxyquinoline–(CH 3 OH) 3 Cluster. *New J. Chem.* **2015**, *39*, 9910–9917.
- (105) Hoffmann, F.; Ekimova, M.; Bekçioğlu-Neff, G.; Nibbering, E. T. J.; Sebastiani, D.

- Combined Experimental and Theoretical Study of the Transient IR Spectroscopy of 7-Hydroxyquinoline in the First Electronically Excited Singlet State. *J. Phys. Chem. A* **2016**, *120*, 9378–9389.
- (106) Fang, W.-H. Ab Initio Study of the Triple-Proton-Transfer Reactions of Ground and Excited States of 7-Hydroxyquinoline in Methanol Solution. *J. Am. Chem. Soc.* **1998**, *120*, 7568–7576.
- (107) Chou, P.-T.; Wei, C.-Y.; Chris Wang, C.-R.; Hung, F.-T.; Chang, C.-P. Proton-Transfer Tautomerism of 7-Hydroxyquinolines Mediated by Hydrogen-Bonded Complexes. *J. Phys. Chem. A* **1999**, *103*, 1939–1949.
- (108) Kim, T. G.; Topp, M. R. Ultrafast Excited-State Deprotonation and Electron Transfer in Hydroxyquinoline Derivatives. *J. Phys. Chem. A* **2004**, *108*, 10060–10065.
- (109) Kwon, O.-H.; Lee, Y.-S.; Yoo, B. K.; Jang, D.-J. Excited-State Triple Proton Transfer of 7-Hydroxyquinoline along a Hydrogen-Bonded Alcohol Chain: Vibrationally Assisted Proton Tunneling. *Angew. Chemie Int. Ed.* **2006**, *45*, 415–419.
- (110) Park, S.-Y.; Jang, D.-J. Accumulated Proton-Donating Ability of Solvent Molecules in Proton Transfer. *J. Am. Chem. Soc.* **2010**, *132*, 297–302.
- (111) Kang, B.; Ko, K. C.; Park, S.-Y.; Jang, D.-J.; Lee, J. Y. Solvent Effect on the Excited-State Proton Transfer of 7-Hydroxyquinoline along a Hydrogen-Bonded Ethanol Dimer. *Phys. Chem. Chem. Phys.* **2011**, *13*, 6332–6339.
- (112) Park, S.-Y.; Jang, D.-J. Excited-State Hydrogen Relay along a Blended-Alcohol Chain as a Model System of a Proton Wire: Deuterium Effect on the Reaction Dynamics. *Phys. Chem. Chem. Phys.* **2012**, *14*, 8885–8891.
- (113) Park, S.-Y.; Kim, H.-B.; Yoo, B. K.; Jang, D.-J. Direct Observation of Conformation-Dependent Pathways in the Excited-State Proton Transfer of 7-Hydroxyquinoline in Bulk Alcohols. *J. Phys. Chem. B* **2012**, *116*, 14153–14158.
- (114) Marenich, A. V.; Cramer, C. J.; Truhlar, D. G. Universal Solvation Model Based on Solute Electron Density and on a Continuum Model of the Solvent Defined by the Bulk Dielectric Constant and Atomic Surface Tensions. *J. Phys. Chem. B* **2009**, *113*, 6378–6396.
- (115) Cossi, M.; Barone, V. Time-Dependent Density Functional Theory for Molecules in Liquid Solutions. *J. Chem. Phys.* **2001**, *115*, 4708–4717.
- (116) Angulo, G.; Grampp, G.; Rosspeintner, A. Recalling the Appropriate Representation of Electronic Spectra. *Spectrochim. Acta A* **2006**, *65*, 727–731.
- (117) Serjeant, E. P.; Dempsey, B. *Ionisation Constants of Organic Acids in Aqueous Solution*; Pergammon Press, New York, 1979.

- (118) Reeve, W.; Erikson, C. M.; Aluotto, P. F. A New Method for the Determination of the Relative Acidities of Alcohols in Alcoholic Solutions. The Nucleophilicities and Competitive Reactivities of Alkoxides and Phenoxides. *Can. J. Chem.* **1979**, *57*, 2747–2754.
- (119) Jönsson, P. G. Hydrogen Bond Studies. CXIII. The Crystal Structure of Ethanol at 87 K. *Acta Crystallogr. Sect. B* **1976**, *32*, 232–235.
- (120) Derollez, P.; Hédoux, A.; Guinet, Y.; Danède, F.; Paccou, L. Structure Determination of the Crystalline Phase of {\it N}-Butanol by Powder X-Ray Diffraction and Study of Intermolecular Associations by Raman Spectroscopy. *Acta Crystallogr. Sect. B* **2013**, *69*, 195–202.
- (121) Janeček, J.; Paricaud, P. Size Distribution of Associated Clusters in Liquid Alcohols: Interpretation of Simulation Results in the Frame of SAFT Approach. *J. Chem. Phys.* **2013**, *139*, 174502.
- (122) Sillrén, P.; Swenson, J.; Mattsson, J.; Bowron, D.; Matic, A. The Temperature Dependent Structure of Liquid 1-Propanol as Studied by Neutron Diffraction and EPSR Simulations. *J. Chem. Phys.* **2013**, *138*, 214501.
- (123) Böhmer, R.; Gainaru, C.; Richert, R. Structure and Dynamics of Monohydroxy Alcohols—Milestones towards Their Microscopic Understanding, 100 Years after Debye. *Phys. Rep.* **2014**, *545*, 125–195.
- (124) Cirkel, S. A.; Boese, R. The Crystal Structure of Isopropanol. *Acta Crystallogr. Sect. A* **2004**, *60*, s205.
- (125) Konig, K. Multiphoton Microscopy in Life Sciences. J. Microsc. 2000, 200, 83–104.
- (126) Stosiek, C.; Garaschuk, O.; Holthoff, K.; Konnerth, A. In Vivo Two-Photon Calcium Imaging of Neuronal Networks. *Proc. Natl. Acad. Sci. U. S. A.* **2003**, *100*, 7319–7324.
- (127) Helmchen, F.; Denk, W. Deep Tissue Two-Photon Microscopy. *Nat. Methods* **2005**, *2*, 932–940.
- (128) Tu, H.; Liu, Y.; Turchinovich, D.; Marjanovic, M.; Lyngsø, J. K.; Lægsgaard, J.; Chaney, E. J.; Zhao, Y.; You, S.; Wilson, W. L.; Xu, B.; Dantus, M.; Boppart, S. A. Stain-Free Histopathology by Programmable Supercontinuum Pulses. *Nat. Photonics* **2016**, *10*, 534–540.
- (129) Saytashev, I.; Glenn, R.; Murashova, G. A.; Osseiran, S.; Spence, D.; Evans, C. L.; Dantus, M. Multiphoton Excited Hemoglobin Fluorescence and Third Harmonic Generation for Non-Invasive Microscopy of Stored Blood. *Biomed. Opt. Express* 2016, 7, 3449.
- (130) Murashova, G. A.; Mancuso, C. A.; Canfield, J. L.; Sakami, S.; Palczewski, K.; Palczewska,

- G.; Dantus, M. Multimodal Nonlinear Optical Imaging of Unstained Retinas in the Epi-Direction with a Sub-40 Fs Yb-Fiber Laser. *Biomed. Opt. Express* **2017**, *8*, 5228–5242.
- (131) Maruo, S.; Nakamura, O.; Kawata, S. Three-Dimensional Microfabrication with Two-Photon-Absorbed Photopolymerization. *Opt. Lett.* **1997**, *22*, 132.
- (132) Kawata, S.; Sun, H.-B.; Tanaka, T.; Takada, K. Finer Features for Functional Microdevices. *Nature* **2001**, *412*, 697–698.
- (133) Haske, W.; Chen, V. W.; Hales, J. M.; Dong, W.; Barlow, S.; Marder, S. R.; Perry, J. W. 65 Nm Feature Sizes Using Visible Wavelength 3-D Multiphoton Lithography. *Opt. Express* **2007**, *15*, 3426.
- (134) Lee, S.-H.; Moon, J. J.; West, J. L. Three-Dimensional Micropatterning of Bioactive Hydrogels via Two-Photon Laser Scanning Photolithography for Guided 3D Cell Migration. *Biomaterials* **2008**, *29*, 2962–2968.
- (135) Marino, A.; Filippeschi, C.; Mattoli, V.; Mazzolai, B.; Ciofani, G. Biomimicry at the Nanoscale: Current Research and Perspectives of Two-Photon Polymerization. *Nanoscale* **2015**, *7*, 2841–2850.
- (136) Kosower, E. M.; Huppert, D. Excited State Electron and Proton Transfers. *Annu. Rev. Phys. Chem.* **1986**, *37*, 127–156.
- (137) Arnaut, L. G.; Formosinho, S. J. Excited-State Proton Transfer Reactions I. Fundamentals and Intermolecular Reactions. *J. Photochem. Photobiol. A Chem.* **1993**, *75*, 1–20.
- (138) Formosinho, S. J.; Arnaut, L. G. Excited-State Proton Transfer Reactions II. Intramolecular Reactions. *J. Photochem. Photobiol. A Chem.* **1993**, *75*, 21–48.
- (139) Douhal, A.; Lahmani, F.; Zewail, A. H. Proton-Transfer Reaction Dynamics. *Chem. Phys.* **1996**, *207*, 477–498.
- (140) Agmon, N. Elementary Steps in Excited-State Proton Transfer. *J. Phys. Chem. A* **2005**, *109*, 13–35.
- (141) Carlos del Valle, J.; Domínguez, E.; Kasha, M. Competition between Dipolar Relaxation and Double Proton Transfer in the Electronic Spectroscopy of Pyrroloquinolines. *J. Phys. Chem. A* **1999**, *103*, 2467–2475.
- (142) Kohtani, S.; Tagami, A.; Nakagaki, R. Excited-State Proton Transfer of 7-Hydroxyquinoline in a Non-Polar Medium: Mechanism of Triple Proton Transfer in the Hydrogen-Bonded System. *Chem. Phys. Lett.* **2000**, *316*, 88–93.
- (143) Itoh, M.; Adachi, T.; Tokumura, K. Time-Resolved Fluorescence and Absorption Spectra and Two-Step Laser Excitation Fluorescence of the Excited-State Proton Transfer in the

- Methanol Solution of 7-Hydroxyquinoline. J. Am. Chem. Soc. 1984, 106, 850–855.
- (144) Solntsev, K. M.; Sullivan, E. N.; Tolbert, L. M.; Ashkenazi, S.; Leiderman, P.; Huppert, D. Excited-State Proton Transfer Reactions of 10-Hydroxycamptothecin 1. *J. Am. Chem. Soc.* **2004**, *126*, 12701–12708.
- (145) Nekipelova, T. D.; Gostev, F. E.; Kuzmin, V. A.; Sarkisov, O. M. Ultrafast Excited State Proton Transfer Dynamics of 1,2-Dihydroquinolines in Methanol Solution. *Photochem. Photobiol. Sci.* **2006**, *5*, 815.
- (146) Chang, K.-H.; Liu, Y.; Liu, J.; Peng, Y.-C.; Yang, Y.-H.; Li, Z.-B.; Jheng, R.-H.; Chao, C.-M.; Liu, K.-M.; Chou, P.-T. Catalytic ☐ Type Excited ☐ State N−H Proton- Transfer Reaction in 7 ☐ Aminoquinoline and Its Derivatives. *Chem. A Eur. J.* **2019**, *25*, 14972–14982.
- (147) Bardez, E. Excited-State Proton Transfer in Bifunctional Compounds. *Isr. J. Chem.* **1999**, *39*, 319–332.
- (148) Matsumoto, Y.; Ebata, T.; Mikami, N. Structure and Photoinduced Excited State Keto-Enol Tautomerization of 7-Hydroxyquinoline-(CH 3 OH) n Clusters. *J. Phys. Chem. A* **2002**, *106*, 5591–5599.
- (149) Penedo, J. C.; Lustres, J. L. P.; Lema, I. G.; Rodríguez, M. C. R.; Mosquera, M.; Rodríguez-Prieto, F. Solvent-Dependent Ground- and Excited-State Tautomerism in 2-(6'-Hydroxy-2'-Pyridyl)Benzimidazole. *J. Phys. Chem. A* **2004**, *108*, 6117–6126.
- (150) Liu, Y.-H.; Mehata, M. S.; Liu, J.-Y. Excited-State Proton Transfer via Hydrogen-Bonded Acetic Acid (AcOH) Wire for 6-Hydroxyquinoline. *J. Phys. Chem. A* **2011**, *115*, 19–24.
- (151) Park, S.-Y.; Kim, Y.; Lee, J. Y.; Jang, D.-J. Ground-State Proton Transport along a Blended-Alcohol Chain: Accelerated by Accumulated Proton-Donating Ability. *J. Phys. Chem. B* **2012**, *116*, 10915–10921.
- (152) Fang, H.; Kim, Y. Hydrogen-Bonded Channel-Dependent Mechanism of Long-Range Proton Transfer in the Excited-State Tautomerization of 7-Hydroxyquinoline: A Theoretical Study. *Theor. Chem. Acc.* **2017**, *136*, 28.
- (153) Lahiri, J.; Moemeni, M.; Magoulas, I.; Yuwono, S. H.; Kline, J.; Borhan, B.; Piecuch, P.; Jackson, J. E.; Blanchard, G. J.; Dantus, M. Steric Effects in Light-Induced Solvent Proton Abstraction. *Phys. Chem. Chem. Phys.* **2020**, *22*, 19613–19622.
- (154) Gordon, M. S.; Slipchenko, L.; Li, H.; Jensen, J. H. The Effective Fragment Potential: A General Method for Predicting Intermolecular Interactions. In *Annual Reports in Computational Chemistry*; Spellmeyer, D. C., Wheeler, R., Eds.; Elsevier, 2007; Vol. 3, pp 177–193.

- (155) Barca, G. M. J.; Bertoni, C.; Carrington, L.; Datta, D.; De Silva, N.; Deustua, J. E.; Fedorov, D. G.; Gour, J. R.; Gunina, A. O.; Guidez, E.; Harville, T.; Irle, S.; Ivanic, J.; Kowalski, K.; Leang, S. S.; Li, H.; Li, W.; Lutz, J. J.; Magoulas, I.; Mato, J.; Mironov, V.; Nakata, H.; Pham, B. Q.; Piecuch, P.; Poole, D.; Pruitt, S. R.; Rendell, A. P.; Roskop, L. B.; Ruedenberg, K.; Sattasathuchana, T.; Schmidt, M. W.; Shen, J.; Slipchenko, L.; Sosonkina, M.; Sundriyal, V.; Tiwari, A.; Galvez Vallejo, J. L.; Westheimer, B.; Włoch, M.; Xu, P.; Zahariev, F.; Gordon, M. S. Recent Developments in the General Atomic and Molecular Electronic Structure System. *J. Chem. Phys.* **2020**, *152*, 154102.
- (156) Sakurai, J. J.; Napolitano, J. Modern Quantum Mechanics, 2nd ed.; Addison-Wesley, 2011.
- (157) Bräunlich, P. Multiphoton Spectroscopy. In *Progress in Atomic Spectroscopy*; Hanle, W., Kleinpoppen, H., Eds.; Springer US: Boston, MA, 1979; pp 777–827.
- (158) Meath, W. J.; Power, E. A. On the Importance of Permanent Moments in Multiphoton Absorption Using Perturbation Theory. *J. Phys. B At. Mol. Phys.* **1984**, *17*, 763–781.
- (159) Jagatap, B. N.; Meath, W. J. On the Competition between Permanent Dipole and Virtual State Two-Photon Excitation Mechanisms, and Two-Photon Optical Excitation Pathways, in Molecular Excitation. *Chem. Phys. Lett.* **1996**, *258*, 293–300.
- (160) Dick, B.; Hohlneicher, G. Importance of Initial and Final States as Intermediate States in Two□photon Spectroscopy of Polar Molecules. *J. Chem. Phys.* **1982**, *76*, 5755–5760.
- (161) Birge, R. R.; Murray, L. P.; Zidovetzki, R.; Knapp, H. M. Two-Photon, ¹³C and Two-Dimensional ¹H NMR Spectroscopic Studies of Retinyl Schiff Bases, Protonated Schiff Bases and Schiff Base Salts: Evidence for a Protonation Induced Ππ* Excited State Level Ordering Reversal. *J. Am. Chem. Soc.* **1987**, *109*, 2090–2101.
- (162) Callis, P. R. TWO-PHOTON-INDUCED FLUORESCENCE. *Annu. Rev. Phys. Chem.* **1997**, *48*, 271–297.
- (163) Drobizhev, M.; Meng, F.; Rebane, A.; Stepanenko, Y.; Nickel, E.; Spangler, C. W. Strong Two-Photon Absorption in New Asymmetrically Substituted Porphyrins: Interference between Charge-Transfer and Intermediate-Resonance Pathways. *J. Phys. Chem. B* **2006**, *110*, 9802–9814.
- (164) Alam, M. M.; Chattopadhyaya, M.; Chakrabarti, S. On the Origin of Large Two-Photon Activity of DANS Molecule. *J. Phys. Chem. A* **2012**, *116*, 11034–11040.
- (165) Meath, W. J. On the Optimization, and the Intensity Dependence, of the Excitation Rate for the Absorption of Two-Photons Due to the Direct Permanent Dipole Moment Excitation Mechanism. *AIP Adv.* **2016**, *6*, 075202.
- (166) Reichardt, C. Solvatochromic Dyes as Solvent Polarity Indicators. *Chem. Rev.* **1994**, *94*, 2319–2358.

- (167) Kawski, A.; Bojarski, P. Comments on the Determination of Excited State Dipole Moment of Molecules Using the Method of Solvatochromism. *Spectrochim. Acta Part A Mol. Biomol. Spectrosc.* **2011**, *82*, 527–528.
- (168) Hosoi, H.; Yamaguchi, S.; Mizuno, H.; Miyawaki, A.; Tahara, T. Hidden Electronic Excited State of Enhanced Green Fluorescent Protein. *J. Phys. Chem. B* **2008**, *112*, 2761–2763.
- (169) Kamarchik, E.; Krylov, A. I. Non-Condon Effects in the One- and Two-Photon Absorption Spectra of the Green Fluorescent Protein. *J. Phys. Chem. Lett.* **2011**, *2*, 488–492.
- (170) Moran, A. M.; Egolf, D. S.; Blanchard-Desce, M.; Kelley, A. M. Vibronic Effects on Solvent Dependent Linear and Nonlinear Optical Properties of Push-Pull Chromophores: Julolidinemalononitrile. *J. Chem. Phys.* **2002**, *116*, 2542–2555.
- (171) Moca, R.; R. Meech, S.; A. Heisler, I. Two-Dimensional Electronic Spectroscopy of Chlorophyll a: Solvent Dependent Spectral Evolution. *J. Phys. Chem. B* **2015**, *119*, 8623–8630.
- (172) Rumble, C. A.; Breffke, J.; Maroncelli, M. Solvation Dynamics and Proton Transfer in Diethylaminohydroxyflavone. *J. Phys. Chem. B* **2017**, *121*, 630–637.
- (173) Tokumura, K.; Itoh, M. Two-Photon-Induced Excited-State Proton Transfer Process in Methanol Solution of 7-Hydroxyquinoline. *J. Phys. Chem.* **1984**, *88*, 3921–3923.
- (174) Peng, L. W.; Dantus, M.; Zewail, A. H.; Kemnitz, K.; Hicks, J. M.; Eisenthal, K. B. Stepwise Solvation of the Intramolecular-Charge-Transfer Molecule p (Dimethylamino)Benzonitrile. *J. Phys. Chem.* **1987**, *91*, 6162–6167.
- (175) Meshulach, D.; Silberberg, Y. Coherent Quantum Control of Two-Photon Transitions by a Femtosecond Laser Pulse. *Nature* **1998**, *396*, 239–242.
- (176) Lozovoy, V. V.; Pastirk, I.; Walowicz, K. A.; Dantus, M. Multiphoton Intrapulse Interference. II. Control of Two- and Three-Photon Laser Induced Fluorescence with Shaped Pulses. *J. Chem. Phys.* **2003**, *118*, 3187–3196.
- (177) Lozovoy, V. V.; Dantus, M. Systematic Control of Nonlinear Optical Processes Using Optimally Shaped Femtosecond Pulses. *ChemPhysChem* **2005**, *6*, 1971–2000.
- (178) Pastirk, I.; Cruz, J. M. Dela; Walowicz, K. A.; Lozovoy, V. V.; Dantus, M. Selective Two-Photon Microscopy with Shaped Femtosecond Pulses. *Opt. Express* **2003**, *11*, 1695–1701.
- (179) Lozovoy, V. V.; Xu, B.; Shane, J. C.; Dantus, M. Selective Nonlinear Optical Excitation with Pulses Shaped by Pseudorandom Galois Fields. *Phys. Rev. A* **2006**, *74*, 041805.
- (180) Schelhas, L.; Shane, J.; Dantus, M. Advantages of Ultrashort Phase-Shaped Pulses for Selective Two-Photon Activation and Biomedical Imaging. *Nanomedicine*

- Nanotechnology, Biol. Med. 2006, 2, 177–181.
- (181) Ogilvie, J. P.; Débarre, D.; Solinas, X.; Martin, J.-L.; Beaurepaire, E.; Joffre, M. Use of Coherent Control for Selective Two-Photon Fluorescence Microscopy in Live Organisms. *Opt. Express* **2006**, *14*, 759–766.
- (182) Isobe, K.; Suda, A.; Tanaka, M.; Kannari, F.; Kawano, H.; Mizuno, H.; Miyawaki, A.; Midorikawa, K. Multifarious Control of Two-Photon Excitation of Multiple Fluorophores Achieved by Phase Modulation of Ultra-Broadband Laser Pulses. *Opt. Express* **2009**, *17*, 13737–13746.
- (183) Labroille, G.; Pillai, R. S.; Solinas, X.; Boudoux, C.; Olivier, N.; Beaurepaire, E.; Joffre, M. Dispersion-Based Pulse Shaping for Multiplexed Two-Photon Fluorescence Microscopy. *Opt. Lett.* **2010**, *35*, 3444–3446.
- (184) Kondo, A. E.; Meath, W. J. Two□color Multiphoton Transitions in Molecular Beam Electric Resonance Studies: Rotating Wave versus Floquet, and On□ versus Off□ resonance, Calculations. *J. Chem. Phys.* **1996**, *104*, 8312–8320.
- (185) Dudovich, N.; Dayan, B.; Gallagher Faeder, S. M.; Silberberg, Y. Transform-Limited Pulses Are Not Optimal for Resonant Multiphoton Transitions. *Phys. Rev. Lett.* **2001**, *86*, 47–50.
- (186) Honig, B.; Jortner, J.; Szöke, A. Theoretical Studies of Two□Photon Absorption Processes. I. Molecular Benzene. *J. Chem. Phys.* **1967**, *46*, 2714–2727.
- (187) Webman, I.; Jortner, J. Energy Dependence of Two□Photon□Absorption Cross Sections in Anthracene. *J. Chem. Phys.* **1969**, *50*, 2706–2716.
- (188) Shapiro, M.; Brumer, P. Laser Control of Product Quantum State Populations in Unimolecular Reactions. *J. Chem. Phys.* **1986**, *84*, 4103–4104.
- (189) Zhu, L.; Kleiman, V.; Li, X.; Lu, S. P.; Trentelman, K.; Gordon, R. J. Coherent Laser Control of the Product Distribution Obtained in the Photoexcitation of HI. *Science* (80-.). **1995**, 270, 77–80.
- (190) Chen, Z.; Brumer, P.; Shapiro, M. Coherent Radiative Control of Molecular Photodissociation via Resonant Two-Photon versus Two-Photon Interference. *Chem. Phys. Lett.* **1992**, *198*, 498–504.
- (191) Chen, Z.; Brumer, P.; Shapiro, M. Multiproduct Coherent Control of Photodissociation via Two Photon versus Two-Photon Interference. *J. Chem. Phys.* **1993**, *98*, 6843–6852.
- (192) Meshulach, D.; Silberberg, Y. Coherent Quantum Control of Multiphoton Transitions by Shaped Ultrashort Optical Pulses. *Phys. Rev. A* **1999**, *60*, 1287–1292.

- (193) Präkelt, A.; Wollenhaupt, M.; Sarpe-Tudoran, C.; Baumert, T. Phase Control of a Two-Photon Transition with Shaped Femtosecond Laser-Pulse Sequences. *Phys. Rev. A* **2004**, 70, 063407.
- (194) Weiner, A. M. Femtosecond Pulse Shaping Using Spatial Light Modulators. *Rev. Sci. Instrum.* **2000**, *71*, 1929–1960.
- (195) Silberberg, Y. Quantum Coherent Control for Nonlinear Spectroscopy and Microscopy. *Annu. Rev. Phys. Chem.* **2009**, *60*, 277–292.
- (196) Lozovoy, V. V.; Pastirk, I.; Dantus, M. Multiphoton Intrapulse Interference IV Ultrashort Laser Pulse Spectral Phase Characterization and Compensation. *Opt. Lett.* **2004**, *29*, 775–777.
- (197) Xu, B.; Gunn, J. M.; Cruz, J. M. Dela; Lozovoy, V. V.; Dantus, M. Quantitative Investigation of the Multiphoton Intrapulse Interference Phase Scan Method for Simultaneous Phase Measurement and Compensation of Femtosecond Laser Pulses. *J. Opt. Soc. Am. B* **2006**, *23*, 750–759.
- (198) Pastirk, I.; Zhu, X.; Martin, R. M.; Dantus, M. Remote Characterization and Dispersion Compensation of Amplified Shaped Femtosecond Pulses Using MIIPS. *Opt. Express* **2006**, *14*, 8885.
- (199) Xu, B.; Coello, Y.; Lozovoy, V. V.; Harris, D. A.; Dantus, M. Pulse Shaping of Octave Spanning Femtosecond Laser Pulses. *Opt. Express* **2006**, *14*, 10939–10944.
- (200) Dantus, M.; Lozovoy, V. V.; Pastirk, I. MIIPS Characterizes and Corrects Femtosecond Pulses. *Laser Focus World* **2007**, *43*, 101–104.
- (201) Zhu, X.; Gunaratne, T. C.; Lozovoy, V. V.; Dantus, M. In-Situ Femtosecond Laser Pulse Characterization and Compression during Micromachining. *Opt. Express* **2007**, *15*, 16061–16066.
- (202) Lozovoy, V. V.; Xu, B.; Coello, Y.; Dantus, M. Direct Measurement of Spectral Phase for Ultrashort Laser Pulses. *Opt. Express* **2008**, *16*, 592–597.
- (203) Coello, Y.; Lozovoy, V. V.; Gunaratne, T. C.; Xu, B.; Borukhovich, I.; Tseng, C.; Weinacht, T.; Dantus, M. Interference without an Interferometer: A Different Approach to Measuring, Compressing, and Shaping Ultrashort Laser Pulses. *J. Opt. Soc. Am. B* **2008**, *25*, A140-150.
- (204) Pestov, D.; Lozovoy, V. V.; Dantus, M. Single-Beam Shaper-Based Pulse Characterization and Compression Using MIIPS Sonogram. *Opt. Lett.* **2010**, *35*, 1422–1424.
- (205) Lee, D.-I.; Goodson, T. Entangled Photon Absorption in an Organic Porphyrin Dendrimer. *J. Phys. Chem. B* **2006**, *110*, 25582–25585.

- (206) Upton, L.; Harpham, M.; Suzer, O.; Richter, M.; Mukamel, S.; Goodson, T. Optically Excited Entangled States in Organic Molecules Illuminate the Dark. *J. Phys. Chem. Lett.* **2013**, *4*, 2046–2052.
- (207) Saleh, B. E. A.; Jost, B. M.; Fei, H.-B.; Teich, M. C. Entangled-Photon Virtual-State Spectroscopy. *Phys. Rev. Lett.* **1998**, *80*, 3483–3486.
- (208) Harpham, M. R.; Süzer, O.; Ma, C.-Q.; Bäuerle, P.; Goodson, T. Thiophene Dendrimers as Entangled Photon Sensor Materials. *J. Am. Chem. Soc.* **2009**, *131*, 973–979.
- (209) Guzman, A. R.; Harpham, M. R.; Süzer, O.; Haley, M. M.; Goodson, T. G. Spatial Control of Entangled Two-Photon Absorption with Organic Chromophores. *J. Am. Chem. Soc.* **2010**, *132*, 7840–7841.
- (210) Burdick, R. K.; Varnavski, O.; Molina, A.; Upton, L.; Zimmerman, P.; Goodson, T. Predicting and Controlling Entangled Two-Photon Absorption in Diatomic Molecules. *J. Phys. Chem. A* **2018**, *122*, 8198–8212.
- (211) Mohanty, J.; Palit, D. K.; Mittal, J. P. Photophysical Properties of Two Infrared Laser Dyes-IR-144 and IR-140: A Picosecond Laser Flash Photolysis Study. *Proc. Indian Natl. Sci. Acad.* **2000**, *66*, 303–315.
- (212) Zhang, H.; Zhang, S.; Lu, C.; Jia, T.; Wang, Z.; Sun, Z. Single-Photon Fluorescence Enhancement in IR144 by Phase-Modulated Femtosecond Pulses. *Chem. Phys. Lett.* **2011**, *503*, 176–179.
- (213) Goswami, D.; Das, D. K.; Makhal, K. Solvent Effect on Dual Fluorescence and the Corresponding Excited State Dynamics BT Reviews in Fluorescence 2017; Geddes, C. D., Ed.; Springer International Publishing: Cham, 2018; pp 145–160.
- (214) Ballou, B.; Ernst, A. L.; Waggoner, S. A. Fluorescence Imaging of Tumors In Vivo. *Current Medicinal Chemistry*. 2005, pp 795–805.
- (215) Huang, B.; Jones, S. A.; Brandenburg, B.; Zhuang, X. Whole-Cell 3D STORM Reveals Interactions between Cellular Structures with Nanometer-Scale Resolution. *Nat. Methods* **2008**, *5*, 1047–1052.
- (216) Pansare, V. J.; Hejazi, S.; Faenza, W. J.; Prud'homme, R. K. Review of Long-Wavelength Optical and NIR Imaging Materials: Contrast Agents, Fluorophores, and Multifunctional Nano Carriers. *Chem. Mater.* **2012**, *24*, 812–827.
- (217) Zhang, Z.; Berezin, M. Y.; Kao, J. L. F.; D'Avignon, A.; Bai, M.; Achilefu, S. Near-Infrared Dichromic Fluorescent Carbocyanine Molecules. *Angew. Chemie Int. Ed.* **2008**, *47*, 3584–3587.
- (218) Li, D.-H.; Schreiber, C. L.; Smith, B. D. Sterically Shielded Heptamethine Cyanine Dyes

- for Bioconjugation and High Performance Near ☐ Infrared Fluorescence Imaging. *Angew. Chemie Int. Ed.* **2020**, *59*, 12154–12161.
- (219) Sayama, K.; Tsukagoshi, S.; Mori, T.; Hara, K.; Ohga, Y.; Shinpou, A.; Abe, Y.; Suga, S.; Arakawa, H. Efficient Sensitization of Nanocrystalline TiO2 Films with Cyanine and Merocyanine Organic Dyes. *Sol. Energy Mater. Sol. Cells* **2003**, *80*, 47–71.
- (220) Zhao, Y.; Meek, G. A.; Levine, B. G.; Lunt, R. R. Near-Infrared Harvesting Transparent Luminescent Solar Concentrators. *Adv. Opt. Mater.* **2014**, *2*, 606–611.
- (221) Zhang, J.; Moemeni, M.; Yang, C.; Liang, F.; Peng, W.-T.; Levine, B. G.; Lunt, R. R.; Borhan, B. General Strategy for Tuning the Stokes Shifts of near Infrared Cyanine Dyes. *J. Mater. Chem. C* **2020**, *8*, 16769–16773.
- (222) Delaey, E.; van Laar, F.; De Vos, D.; Kamuhabwa, A.; Jacobs, P.; de Witte, P. A Comparative Study of the Photosensitizing Characteristics of Some Cyanine Dyes. *J. Photochem. Photobiol. B Biol.* **2000**, *55*, 27–36.
- (223) Conceição, D.; Ferreira, D.; Ferreira, L. Photochemistry and Cytotoxicity Evaluation of Heptamethinecyanine Near Infrared (NIR) Dyes. *Int. J. Mol. Sci.* **2013**, *14*, 18557–18571.
- (224) Shindy, H. A. Fundamentals in the Chemistry of Cyanine Dyes: A Review. *Dye. Pigment.* **2017**, *145*, 505–513.
- (225) Bricks, J. L.; Kachkovskii, A. D.; Slominskii, Y. L.; Gerasov, A. O.; Popov, S. V. Molecular Design of near Infrared Polymethine Dyes: A Review. *Dye. Pigment.* **2015**, *121*, 238–255.
- (226) Gunaratne, T. C.; Zhu, X.; Lozovoy, V. V; Dantus, M. Symmetry of Nonlinear Optical Response to Time Inversion of Shaped Femtosecond Pulses as a Clock of Ultrafast Dynamics. *Chem. Phys.* **2007**, *338*, 259–267.
- (227) Bardeen, C. J.; Yakovlev, V. V; Squier, J. A.; Wilson, K. R. Quantum Control of Population Transfer in Green Fluorescent Protein by Using Chirped Femtosecond Pulses. *J. Am. Chem. Soc.* **1998**, *120*, 13023–13027.
- (228) Yakovlev, V. V; Bardeen, C. J.; Che, J.; Cao, J.; Wilson, K. R. Chirped Pulse Enhancement of Multiphoton Absorption in Molecular Iodine. *J. Chem. Phys.* **1998**, *108*, 2309–2313.
- (229) Mishima, K.; Hayashi, M.; Lin, J. T.; Yamashita, K.; Lin, S. H. A Numerical Study on Vibronic and Vibrational Dynamics Generated by Chirped Laser Pulses in the Presence of Relaxation Processes. *Chem. Phys. Lett.* **1999**, *309*, 279–286.
- (230) Fainberg, B. D.; Narbaev, V. Chirped Pulse Excitation in Condensed Phases Involving Intramolecular Modes Studied by Double-Sided Feynman Diagrams for Fast Optical Dephasing. *J. Chem. Phys.* **2000**, *113*, 8113–8124.

- (231) Misawa, K.; Kobayashi, T. Wave-Packet Dynamics in a Cyanine Dye Molecule Excited with Femtosecond Chirped Pulses. *J. Chem. Phys.* **2000**, *113*, 7546–7553.
- (232) Nairat, M.; Webb, M.; Esch, M. P.; Lozovoy, V. V; Levine, B. G.; Dantus, M. Time-Resolved Signatures across the Intramolecular Response in Substituted Cyanine Dyes. *Phys. Chem. Chem. Phys.* **2017**, *19*, 14085–14095.
- (233) Konar, A.; Lozovoy, V. V; Dantus, M. Solvation Stokes-Shift Dynamics Studied by Chirped Femtosecond Laser Pulses. *J. Phys. Chem. Lett.* **2012**, *3*, 2458–2464.
- (234) Liebel, M.; Kukura, P. Lack of Evidence for Phase-Only Control of Retinal Photoisomerization in the Strict One-Photon Limit. *Nat. Chem.* **2017**, *9*, 45–49.
- (235) Brühl, E.; Buckup, T.; Motzkus, M. Experimental and Numerical Investigation of a Phase-Only Control Mechanism in the Linear Intensity Regime. *J. Chem. Phys.* **2018**, *148*, 214310.
- (236) Lozovoy, V. V; Dantus, M. Laser Control of Physicochemical Processes; Experiments and Applications. *Annu. Reports Sect.* "C" (*Physical Chem.* **2006**, *102*, 227.
- (237) Mukamel, S. Principles of Nonlinear Optical Spectroscopy; Oxford University Press, 1995.
- (238) Lee, D.; Albrecht, A. C. Advances in Infrared and Raman Spectroscopy; Clark, R. J. H., Hester, R. E., Eds.; Wiley-Heyden: Chichester, U.K., 1985.
- (239) Grimberg, B. I.; Lozovoy, V. V; Dantus, M.; Mukamel, S. Ultrafast Nonlinear Spectroscopic Techniques in the Gas Phase and Their Density Matrix Representation. *J. Phys. Chem. A* **2002**, *106*, 697–718.
- (240) Cerullo, G.; Bardeen, C. J.; Wang, Q.; Shank, C. V. High-Power Femtosecond Chirped Pulse Excitation of Molecules in Solution. *Chem. Phys. Lett.* **1996**, *262*, 362–368.
- (241) Nahmias, O.; Bismuth, O.; Shoshana, O.; Ruhman, S. Tracking Excited State Dynamics with Coherent Control: Automated Limiting of Population Transfer in LDS750. *J. Phys. Chem. A* **2005**, *109*, 8246–8253.
- (242) Sharafy, S.; Muszkat, K. A. Viscosity Dependence of Fluorescence Quantum Yields. *J. Am. Chem. Soc.* **1971**, *93*, 4119–4125.
- (243) Loutfy, R. O.; Arnold, B. A. Effect of Viscosity and Temperature on Torsional Relaxation of Molecular Rotors. *J. Phys. Chem.* **1982**, *86*, 4205–4211.
- (244) Lozovoy, V. V; Rasskazov, G.; Pestov, D.; Dantus, M. Quantifying Noise in Ultrafast Laser Sources and Its Effect on Nonlinear Applications. *Opt. Express* **2015**, *23*, 12037.
- (245) Birks, J. B.; Dyson, D. J.; Flowers, B. H. The Relations between the Fluorescence and

- Absorption Properties of Organic Molecules. *Proc. R. Soc. London. Ser. A. Math. Phys. Sci.* **1963**, 275, 135–148.
- (246) Methanol Dynamic and Kinematic Viscosity https://www.engineeringtoolbox.com/methanol-dynamic-kinematic-viscosity-temperature-pressure-d 2093.html.
- (247) Ethanol Dynamic and Kinematic Viscosity https://www.engineeringtoolbox.com/ethanol-dynamic-kinematic-viscosity-temperature-pressure-d_2071.html.
- (248) Pang, F.-M.; Seng, C.-E.; Teng, T.-T.; Ibrahim, M. H. Densities and Viscosities of Aqueous Solutions of 1-Propanol and 2-Propanol at Temperatures from 293.15 K to 333.15 K. *J. Mol. Liq.* **2007**, *136*, 71–78.
- (249) Tsierkezos, N. G.; Molinou, I. E. Densities and Viscosities of Ethylene Glycol Binary Mixtures at 293.15 K. *J. Chem. Eng. Data* **1999**, *44*, 955–958.
- (250) Segur, J. B.; Oberstar, H. E. Viscosity of Glycerol and Its Aqueous Solutions. *Ind. Eng. Chem.* **1951**, *43*, 2117–2120.
- (251) Adamo, C.; Jacquemin, D. The Calculations of Excited-State Properties with Time-Dependent Density Functional Theory. *Chem. Soc. Rev.* **2013**, *42*, 845–856.
- (252) Le Guennic, B.; Jacquemin, D. Taking Up the Cyanine Challenge with Quantum Tools. *Acc. Chem. Res.* **2015**, *48*, 530–537.
- (253) Ufimtsev, I. S.; Martinez, T. J. Quantum Chemistry on Graphical Processing Units. 3. Analytical Energy Gradients, Geometry Optimization, and First Principles Molecular Dynamics. *J. Chem. Theory Comput.* **2009**, *5*, 2619–2628.
- (254) Isborn, C. M.; Luehr, N.; Ufimtsev, I. S.; Martínez, T. J. Excited-State Electronic Structure with Configuration Interaction Singles and Tamm–Dancoff Time-Dependent Density Functional Theory on Graphical Processing Units. *J. Chem. Theory Comput.* **2011**, *7*, 1814–1823.
- (255) Seritan, S.; Bannwarth, C.; Fales, B. S.; Hohenstein, E. G.; Isborn, C. M.; Kokkila ☐ Schumacher, S. I. L.; Li, X.; Liu, F.; Luehr, N.; Snyder, J. W.; Song, C.; Titov, A. V; Ufimtsev, I. S.; Wang, L.-P.; Martínez, T. J. TeraChem: A Graphical Processing Unit ☐ accelerated Electronic Structure Package for large ☐ scale Ab Initio Molecular Dynamics. *WIREs Comput. Mol. Sci.* **2021**, *11*, e1494.
- (256) Barone, V.; Cossi, M. Quantum Calculation of Molecular Energies and Energy Gradients in Solution by a Conductor Solvent Model. *J. Phys. Chem. A* **1998**, *102*, 1995–2001.
- (257) Lange, A. W.; Herbert, J. M. A Smooth, Nonsingular, and Faithful Discretization Scheme for Polarizable Continuum Models: The Switching/Gaussian Approach. *J. Chem. Phys.*

- **2010**, *133*, 244111.
- (258) Rodríguez-Romero, J.; Guarin, C. A.; Arroyo-Pieck, A.; Gutiérrez-Arzaluz, L.; López-Arteaga, R.; Cortés-Guzmán, F.; Navarro, P.; Peon, J. Fluorophore Release from a Polymethinic Photoremovable Protecting Group Through a Nonlinear Optical Process. *ChemPhotoChem* **2017**, *1*, 397–407.
- (259) Laboe, M.; Lahiri, J.; Mohan T. M., N.; Liang, F.; Levine, B. G.; Beck, W. F.; Dantus, M. Linear and Nonlinear Optical Processes Controlling S₂ and S₁ Dual Fluorescence in Cyanine Dyes. *J. Phys. Chem. A* **2021**, *125*, 9770–9784.
- (260) Hilderbrand, S. A.; Kelly, K. A.; Weissleder, R.; Tung, C.-H. Monofunctional Near-Infrared Fluorochromes for Imaging Applications. *Bioconjug. Chem.* **2005**, *16*, 1275–1281.
- (261) Shi, C.; Wu, J. B.; Pan, D. Review on Near-Infrared Heptamethine Cyanine Dyes as Theranostic Agents for Tumor Imaging, Targeting, and Photodynamic Therapy. *J. Biomed. Opt.* **2016**, *21*, 50901.
- (262) Li, Y.; Zhou, Y.; Yue, X.; Dai, Z. Cyanine Conjugates in Cancer Theranostics. *Bioact. Mater.* **2021**, *6*, 794–809.
- (263) Bilici, K.; Cetin, S.; Aydındogan, E.; Yagci Acar, H.; Kolemen, S. Recent Advances in Cyanine-Based Phototherapy Agents. *Front. Chem.* **2021**, *9*, 1–15.
- (264) Gorka, A. P.; Nani, R. R.; Zhu, J.; Mackem, S.; Schnermann, M. J. A Near-IR Uncaging Strategy Based on Cyanine Photochemistry. *J. Am. Chem. Soc.* **2014**, *136*, 14153–14159.
- (265) Nani, R. R.; Gorka, A. P.; Nagaya, T.; Kobayashi, H.; Schnermann, M. J. Near-IR Light-Mediated Cleavage of Antibody–Drug Conjugates Using Cyanine Photocages. *Angew. Chemie Int. Ed.* **2015**, *54*, 13635–13638.
- (266) Nani, R. R.; Gorka, A. P.; Nagaya, T.; Yamamoto, T.; Ivanic, J.; Kobayashi, H.; Schnermann, M. J. In Vivo Activation of Duocarmycin–Antibody Conjugates by Near-Infrared Light. *ACS Cent. Sci.* **2017**, *3*, 329–337.
- (267) Shi, L.; Yan, C.; Guo, Z.; Chi, W.; Wei, J.; Liu, W.; Liu, X.; Tian, H.; Zhu, W. H. De Novo Strategy with Engineering Anti-Kasha/Kasha Fluorophores Enables Reliable Ratiometric Quantification of Biomolecules. *Nat. Commun.* **2020**, *11*, 1–3.
- (268) Demchenko, A. P.; Tomin, V. I.; Chou, P.-T. Breaking the Kasha Rule for More Efficient Photochemistry. *Chem. Rev.* **2017**, *117*, 13353–13381.
- (269) Cherrick, G. R.; Stein, S. W.; Leevy, C. M.; Davidson, C. S. Indocyanine Green: Observations on Its Physical Properties, Plasma Decay, and Hepatic Extraction. *J. Clin. Invest.* **1960**, *39*, 592–600.

- (270) Alander, J. T.; Kaartinen, I.; Laakso, A.; Pätilä, T.; Spillmann, T.; Tuchin, V. V.; Venermo, M.; Välisuo, P. A Review of Indocyanine Green Fluorescent Imaging in Surgery. *Int. J. Biomed. Imaging* **2012**, *2012*.
- (271) Boni, L.; David, G.; Mangano, A.; Dionigi, G.; Rausei, S.; Spampatti, S.; Cassinotti, E.; Fingerhut, A. Clinical Applications of Indocyanine Green (ICG) Enhanced Fluorescence in Laparoscopic Surgery. *Surg. Endosc.* **2015**, *29*, 2046–2055.
- (272) Berezin, M. Y.; Lee, H.; Akers, W.; Nikiforovich, G.; Achilefu, S. Ratiometric Analysis of Fluorescence Lifetime for Probing Binding Sites in Albumin with Near-Infrared Fluorescent Molecular Probes. *Photochem. Photobiol.* **2007**, *83*, 1371–1378.
- (273) Awasthi, K.; Nishimura, G. Modification of Near-Infrared Cyanine Dyes by Serum Albumin Protein. *Photochem. Photobiol. Sci.* **2011**, *10*, 461–463.
- (274) Nairat, M.; Konar, A.; Kaniecki, M.; Lozovoya, V. V; Dantus, M. Investigating the Role of Human Serum Albumin Protein Pocket on the Excited State Dynamics of Indocyanine Green Using Shaped Femtosecond Laser Pulses. *Phys. Chem. Chem. Phys.* **2015**, *17*, 5872–5877.
- (275) Tian, R.; Zeng, Q.; Zhu, S.; Lau, J.; Chandra, S.; Ertsey, R.; Hettie, K. S.; Teraphongphom, T.; Hu, Z.; Niu, G.; Kiesewetter, D. O.; Sun, H.; Zhang, X.; Antaris, A. L.; Brooks, B. R.; Chen, X. Albumin-Chaperoned Cyanine Dye Yields Superbright NIR-II Fluorophore with Enhanced Pharmacokinetics. *Sci. Adv.* **2019**, *5*, 1–12.
- (276) Du, B.; Qu, C.; Qian, K.; Ren, Y.; Li, Y.; Cui, X.; He, S.; Wu, Y.; Ko, T.; Liu, R.; Li, X.; Li, Y.; Cheng, Z. An IR820 Dye–Protein Complex for Second Near ☐ Infrared Window and Photoacoustic Imaging. *Adv. Opt. Mater.* **2020**, *8*, 1901471.
- (277) He, X. M.; Carter, D. C. Atomic Structure and Chemistry of Human Serum Albumin. *Nature* **1992**, *358*, 209–215.
- (278) Peters Jr., T. All About Albumin, 1st Editio.; Elsevier: Orlando, Florida, 1995.
- (279) Sugio, S.; Kashima, A.; Mochizuki, S.; Noda, M.; Kobayashi, K. Crystal Structure of Human Serum Albumin at 2.5 Åresolution. *Protein Eng. Des. Sel.* **1999**, *12*, 439–446.
- (280) Kunkel, H. G.; Labby, D. H.; Ahrens, E. H.; Shank, R. E.; Hoagland, C. L. The Use of Concentrated Human Serum Albumin in the Treatment of Cirrhosis of the Liver 1. *J. Clin. Invest.* **1948**, *27*, 305–319.
- (281) Thorn, G. W.; Armstrong, S. H. Chemical, Clinical, and Immunological Studies on the Products of Human Plasma Fractionation; the Use of Salt-Poor Concentrated Human Serum Albumin Solution in the Treatment of Chronic Bright's Disease. *J. Clin. Invest.* **1945**, *24*, 802–828.

- (282) Caraceni, P.; Tufoni, M.; Bonavita, M. E. Clinical Use of Albumin. *Blood Transfus.* **2013**, *11*, 20894.
- (283) Taverna, M.; Marie, A.-L.; Mira, J.-P.; Guidet, B. Specific Antioxidant Properties of Human Serum Albumin. *Ann. Intensive Care* **2013**, *3*, 4.
- (284) Sudlow, G.; Birkett, D. J.; Wade, D. N. The Characterization of Two Specific Drug Binding Sites on Human Serum Albumin. *Mol. Pharmacol.* **1975**, *11*, 824–832.
- (285) Sudlow, G.; Birkett, D. J.; Wade, D. N. Albumin. Mol. Pharmacol. 1976, 12, 1052-1061.
- (286) Berde, C. B.; Hudson, B. S.; Simoni, R. D.; Sklar, L. A. Human Serum Albumin. Spectroscopic Studies of Binding and Proximity Relationships for Fatty Acids and Bilirubin. *J. Biol. Chem.* **1979**, *254*, 391–400.
- (287) Ferrer, M. L.; Duchowicz, R.; Carrasco, B.; De La Torre, J. G.; Acuña, A. U. The Conformation of Serum Albumin in Solution: A Combined Phosphorescence Depolarization-Hydrodynamic Modeling Study. *Biophys. J.* **2001**, *80*, 2422–2430.
- (288) Akdogan, Y.; Reichenwallner, J.; Hinderberger, D. Evidence for Water-Tuned Structural Differences in Proteins: An Approach Emphasizing Variations in Local Hydrophilicity. *PLoS One* **2012**, *7*, e45681.
- (289) Bhattacharya, A.; Prajapati, R.; Chatterjee, S.; Mukherjee, T. K. Concentration-Dependent Reversible Self-Oligomerization of Serum Albumins through Intermolecular \$β\$-Sheet Formation. *Langmuir* **2014**, *30*, 14894–14904.
- (290) Chubarov, A.; Spitsyna, A.; Krumkacheva, O.; Mitin, D.; Suvorov, D.; Tormyshev, V.; Fedin, M.; Bowman, M. K.; Bagryanskaya, E. Reversible Dimerization of Human Serum Albumin. *Molecules* **2021**, *26*, 108.
- (291) Ogasawara, Y.; Namai, T.; Togawa, T.; Ishii, K. Formation of Albumin Dimers Induced by Exposure to Peroxides in Human Plasma: A Possible Biomarker for Oxidative Stress. *Biochem. Biophys. Res. Commun.* **2006**, *340*, 353–358.
- (292) Naldi, M.; Baldassarre, M.; Nati, M.; Laggetta, M.; Giannone, F. A.; Domenicali, M.; Bernardi, M.; Caraceni, P.; Bertucci, C. Mass Spectrometric Characterization of Human Serum Albumin Dimer: A New Potential Biomarker in Chronic Liver Diseases. *J. Pharm. Biomed. Anal.* **2015**, *112*, 169–175.
- (293) Zhong, D.; Douhal, A.; Zewail, A. H. Femtosecond Studies of Protein-Ligand Hydrophobic Binding and Dynamics: Human Serum Albumin. *Proc. Natl. Acad. Sci. U. S. A.* **2000**, *97*, 14056–14061.
- (294) Sanner, M. F. Python: A Programming Language for Software Integration and Development. *J. Mol. Graph. Model.* **1999**, *17*, 57–61.

- (295) Hervé, M.; Brédy, R.; Karras, G.; Concina, B.; Brown, J.; Allouche, A.-R.; Lépine, F.; Compagnon, I. On-the-Fly Femtosecond Action Spectroscopy of Charged Cyanine Dyes: Electronic Structure versus Geometry. *J. Phys. Chem. Lett.* **2019**, *10*, 2300–2305.
- (296) Wang, D.; Jiang, H.; Yang, H.; Liu, C.; Gong, Q.; Xiang, J.; Xu, G. Investigation on Photoexcited Dynamics of IR-140 Dye in Ethanol by Femtosecond Supercontinuum-Probing Technique. *J. Opt. A Pure Appl. Opt.* **2002**, *4*, 155–159.
- (297) Silori, Y.; Seliya, P.; De, A. K. Ultrafast Excited-State Dynamics of Tricarbocyanine Dyes Probed by Two-Dimensional Electronic Spectroscopy: Polar Solvation vs Photoisomerization. *J. Phys. Chem. B* **2020**, *124*, 6825–6834.
- (298) Capistran, B. A.; Yuwono, S. H.; Moemeni, M.; Maity, S.; Vahdani, A.; Borhan, B.; Jackson, J. E.; Piecuch, P.; Dantus, M.; Blanchard, G. J. Excited-State Dynamics of a Substituted Fluorene Derivative. The Central Role of Hydrogen Bonding Interactions with the Solvent. *J. Phys. Chem. B* **2021**, *125*, 12242–12253.
- (299) Capistran, B. A.; Yuwono, S. H.; Moemeni, M.; Maity, S.; Vahdani, A.; Borhan, B.; Jackson, J. E.; Piecuch, P.; Dantus, M.; Blanchard, G. J. Intramolecular Relaxation Dynamics Mediated by Solvent–Solute Interactions of Substituted Fluorene Derivatives. Solute Structural Dependence. *J. Phys. Chem. B* **2021**, *125*, 12486–12499.
- (300) Pastirk, I.; Lozovoy, V. V; Dantus, M. Femtosecond Photon Echo and Virtual Echo Measurements of the Vibronic and Vibrational Coherence Relaxation Times of Iodine Vapor. *Chem. Phys. Lett.* **2001**, *333*, 76–82.
- (301) Jonas, D. M. Two-Dimensional Femtosecond Spectroscopy. *Annu. Rev. Phys. Chem.* **2003**, *54*, 425–463.
- (302) Maiuri, M.; Garavelli, M.; Cerullo, G. Ultrafast Spectroscopy: State of the Art and Open Challenges. *J. Am. Chem. Soc.* **2020**, *142*, 3–15.
- (303) Das, A.; Banerjee, T.; Hanson, K. Protonation of Silylenol Ether via Excited State Proton Transfer Catalysis. *Chem. Commun.* **2016**, *52*, 1350–1353.
- (304) Das, A.; Ayad, S.; Hanson, K. Enantioselective Protonation of Silyl Enol Ether Using Excited State Proton Transfer Dyes. *Org. Lett.* **2016**, *18*, 5416–5419.
- (305) Zhang, X.; Hu, S.; Ma, Q.; Liao, S. Visible Light-Mediated Ring-Opening Polymerization of Lactones Based on the Excited State Acidity of ESPT Molecules. *Polym. Chem.* **2020**, *11*, 3709–3715.
- (306) Zhang, X.; Ma, Q.; Jiang, Y.; Hu, S.; Li, J.; Liao, S. Visible Light-Regulated Organocatalytic Ring-Opening Polymerization of Lactones by Harnessing Excited State Acidity. *Polym. Chem.* **2021**, *12*, 885–892.

- (307) Gutman, M.; Nachliel, E.; Gershon, E.; Giniger, R.; Pines, E. The PH Jump: Kinetic Analysis and Determination of the Diffusion-Controlled Rate Constants. *J. Am. Chem. Soc.* **1983**, *105*, 2210–2216.
- (308) Wan, P.; Shukla, D. Utility of Acid-Base Behavior of Excited States of Organic Molecules. *Chem. Rev.* **1993**, *93*, 571–584.
- (309) Abbruzzetti, S.; Crema, E.; Masino, L.; Vecli, A.; Viappiani, C.; Small, J. R.; Libertini, L. J.; Small, E. W. Fast Events in Protein Folding: Structural Volume Changes Accompanying the Early Events in the N→I Transition of Apomyoglobin Induced by Ultrafast PH Jump. *Biophys. J.* **2000**, 78, 405–415.
- (310) Atchison, J.; Kamila, S.; Nesbitt, H.; Logan, K. A.; Nicholas, D. M.; Fowley, C.; Davis, J.; Callan, B.; McHale, A. P.; Callan, J. F. Iodinated Cyanine Dyes: A New Class of Sensitisers for Use in NIR Activated Photodynamic Therapy (PDT). *Chem. Commun.* **2017**, *53*, 2009–2012.
- (311) Robinson-Duggon, J.; Mariño-Ocampo, N.; Barrias, P.; Zúñiga-Núñez, D.; Günther, G.; Edwards, A. M.; Greer, A.; Fuentealba, D. Mechanism of Visible-Light Photooxidative Demethylation of Toluidine Blue O. *J. Phys. Chem. A* **2019**, *123*, 4863–4872.
- (312) Butkevich, A. N.; Bossi, M. L.; Lukinavičius, G.; Hell, S. W. Triarylmethane Fluorophores Resistant to Oxidative Photobluing. *J. Am. Chem. Soc.* **2019**, *141*, 981–989.
- (313) Helmerich, D. A.; Beliu, G.; Matikonda, S. S.; Schnermann, M. J.; Sauer, M. Photoblueing of Organic Dyes Can Cause Artifacts in Super-Resolution Microscopy. *Nat. Methods* **2021**, *18*, 253–257.
- (314) Wiedenmann, J.; Ivanchenko, S.; Oswald, F.; Schmitt, F.; Röcker, C.; Salih, A.; Spindler, K.-D.; Nienhaus, G. U. EosFP, a Fluorescent Marker Protein with UV-Inducible Green-to-Red Fluorescence Conversion. *Proc. Natl. Acad. Sci.* **2004**, *101*, 15905–15910.
- (315) Betzig, E.; Patterson, G. H.; Sougrat, R.; Lindwasser, O. W.; Olenych, S.; Bonifacino, J. S.; Davidson, M. W.; Lippincott-Schwartz, J.; Hess, H. F. Imaging Intracellular Fluorescent Proteins at Nanometer Resolution. *Science* (80-.). 2006, 313, 1642–1645.
- (316) Jradi, F. M.; Lavis, L. D. Chemistry of Photosensitive Fluorophores for Single-Molecule Localization Microscopy. *ACS Chem. Biol.* **2019**, *14*, 1077–1090.
- (317) Matikonda, S. S.; Helmerich, D. A.; Meub, M.; Beliu, G.; Kollmannsberger, P.; Greer, A.; Sauer, M.; Schnermann, M. J. Defining the Basis of Cyanine Phototruncation Enables a New Approach to Single-Molecule Localization Microscopy. *ACS Cent. Sci.* **2021**, *7*, 1144–1155.